MODIFICATION OF INDIUM-TIN OXIDE SURFACES: ENHANCEMENT OF SOLUTION ELECTRON TRANSFER RATES AND EFFICIENCIES OF ORGANIC THIN-LAYER DEVICES

By

Chet Edward Carter

A Dissertation Submitted to the Faculty of the

DEPARTMENT OF CHEMISTRY

In Partial Fulfillment of the Requirements
For the Degree of

DOCTOR OF PHILOSOPHY

In the Graduate College

UNIVERSITY OF ARIZONA

2 0 0 6

THE UNIVERSITY OF ARIZONA
GRADUATE COLLEGE

As members of the Dissertation Committee, we certify that we have read the dissertation prepared by Chet E. Carter

entitled: MODIFICATION OF INDIUM-TIN OXIDE SURFACES: ENHANCEMENT OF SOLUTION ELECTRON TRANSFER RATES AND EFFICIENCIES OF ORGANIC THIN-LAYER DEVICES

and recommend that it be accepted as fulfilling the dissertation requirement for the Degree of Doctor of Philosophy

Neal R. Armstrong_____ Date: 04-11-06

Dennis H. Evans_____ Date: 04-11-06

S. Scott Saavedra_____ Date: 04-11-06

Dominic V. McGrath_____ Date: 04-11-06

Final approval and acceptance of this dissertation is contingent upon the candidate's submission of the final copies of the dissertation to the Graduate College.

I hereby certify that I have read this dissertation prepared under my direction and recommend that it be accepted as fulfilling the dissertation requirement.

Neal R. Armstrong _____ 04-11-06 _____
Dissertation Director Date

STATEMENT BY AUTHOR

This dissertation has been submitted in partial fulfillment of requirements for an advanced degree at The University of Arizona and is deposited in the University Library to be made available to borrowers under rules of the Library.

Brief quotations from this dissertation are allowable without special permission, provided that accurate acknowledgment of source is made. Requests for permission for extended quotation from or reproduction of this manuscript in whole or in part may be granted by the head of the major department or the Dean of the Graduate College when in his or her judgment the proposed use of the material is in the interests of scholarship. In all other instances, however, permission must be obtained from the author.

SIGNED: Chet E. Carter

TABLE OF CONTENTS

TABLE OF CONTENTS (*CONTINUED*)

TABLE OF CONTENTS (*CONTINUED*)

TABLE OF CONTENTS (*CONTINUED*)

TABLE OF CONTENTS (*CONTINUED*)

TABLE OF CONTENTS (*CONTINUED*)

LIST OF ACRONYMS

TPD……N,N’-diphenyl-N,N’-(3-methylphenyl)-1,1’-biphenyl-4,4’-diamine
DE……..Diffraction Efficiency
ITO…….Indium Tin Oxide
Alq_3……..... 8-hydoxyquinoline-aluminum complex
OLED…….……Organic Light Emitting Diode
OPV……Organic Photovoltaic Cell
XPS…….……X-Ray Photoelectron Spectroscopy
UPS…….……Ultraviolet Photoelectron Spectroscopy
AFM……...……Atomic Force Spectroscopy
$Fc(COOH)_2$……Ferrocene Dicarboxylic Acid
3-TAA…….3-thiophene acetic acid
(p-OMe)$_2$-TPD-X_2…..(6-{4-[{4'-[[4-(5-Carboxy-pentyloxy)-phenyl]-(4-methoxy-phenyl)-amino]-biphenyl-4-yl}-(4-methoxy-phenyl)-amino]-phenoxy}-hexanoic acid,
HBC-$(C_3COOH)_6$…..hexa-carboxylic acid derivative of hexabenzocoronene
PANI……...……Polyanaline
PEDOT……...Polyethylenedioxythiophene
EC……...Electrochemically Grown
TBAHFP……Tetrabutylammonium-hexafluorophosphate

LIST OF FIGURES

CHAPTER 1

LIST OF FIGURES *(CONTINUED)*

CHAPTER 2

LIST OF FIGURES *(CONTINUED)*

LIST OF FIGURES *(CONTINUED)*

CHAPTER 3

LIST OF FIGURES *(CONTINUED)*

LIST OF FIGURES *(CONTINUED)*

LIST OF FIGURES *(CONTINUED)*

CHAPTER 4

LIST OF FIGURES *(CONTINUED)*

LIST OF FIGURES *(CONTINUED)*

CHAPTER 5

LIST OF FIGURES *(CONTINUED)*

LIST OF FIGURES *(CONTINUED)*

CHAPTER 6

LIST OF TABLES

ABSTRACT

This dissertation has focused on the study of the ITO/organic heterojunction and the chemistries therein, and proposes appropriate strategies that enhance the interfacial physical and electronic properties for more efficient charge injection with application to organic thin-layer devices. We focused on four major aspects of this work: ***i*)** To characterize the ITO surface and understand the chemistries that may be pertinent to interaction with adjacent organic layers in a device configuration. This developed into a working model of the ITO surface chemistry and provided a foundation for modification strategies. Characterization of the electronic properties of the surface indicated that less than 5% of the geometrical surface area is responsible for the bulk of current flow while the rest is electrically inactive. Likely, this is due to the build up of an $In(OH)_X$ type species which is isolating in nature. ***ii*)** To determine the extent to which these chemistries are variable and propose circumstances where compositional changes can occur and characterize the resulting change in surface chemistry. It is shown that the surface chemistry of ITO is heterogeneous and possible very dynamic with respect to the surrounding environment. Solution pretreatments and plasma based etching had substantial effects on the surface chemistry. In particular, the amount of $In(OH)_X$ material present. ***iii*)** To propose a strategy for modification of the interface which leads to enhanced physical and/or electrical properties. Modification of ITO surfaces by small molecules containing carboxylic acid functionalities is investigated. To accomplish this, a protocol for solution electrochemical probing was developed utilizing

ferrocene/ferrocenium as the probe. Enhancements in the electron transfer rate coefficient were realized after modification of the ITO electrode. The enhancements are found to stem from a light etching mechanism which removes a portion of $In(OH)_X$ material and exposes a larger electrically active area. Additionally, an elecro-catalytic effect was observed with some of the modifiers used increasing k_{eff} further. ***iv)*** Apply these modifications to the development of model organic light emitting diodes (OLEDs) and organic photovoltaic devices (OPVs). Selected modification strategies including small molecule chemisorption and conductive polymer overlayers were utilized in OLED and OPV devices. Enhancements seen in solution electrochemical experiments are indicative of the enhancements seen for solid state devices. Modifications resulted in substantially lower leakage currents (3 orders of magnitude in some cases) as well as nearly doubling the efficiency. Also noted, the best devices utilized a combonation of small molecule chemisorption and polymer overlayers.

An additional chapter describes the creation and characterization of electrochemically grown polymer nano-structures based on blazed angle diffraction gratings. The discussion details the micro-contact printing process and the electro-catalytic growth of the conductive polymers PANI and PEDOT to form diffraction grating structures in their own right. The resulting diffraction efficiency of these structures is shown to be sensitive to environmental conditions outlining possible uses as chemical sensors. This is demonstrated by utilizing these structures as working pH and potentiometric sensors based on the changing diffraction efficiency.

CHAPTER 1

INTRODUCTION

1.1 INTRODUCTION

In recent years, an increasing effort has been concentrated on the development and further enhancement of organic thin layer technologies such as organic light emitting diodes (OLEDs) and organic photovoltaic cells (OPVs) .[1-21] This interest has been fueled by the advantages organic materials offer over their current inorganic based counterparts. These merits are widespread and include: ***i)*** A large variety of organic dyes available for device applications creating the possibility of emission tuned OLED structures in order to emit at predetermined wavelengths, as well as the development of high absorptivity and broad band absorption spectra for OPVs;[7,8,11,13] ***ii)*** The ability to fabricate devices on flexible substrates for inexpensive and non-traditional applications;[1-3] ***iii)*** Lightweight construction, combined with an ultra-thin device geometry leads to an end-product which is extremely portable; ***iv)*** Displays constructed in this manner have the potential to be brighter, and more power-efficient than current display technologies; ***v)*** Do not suffer from the angle viewing problems associated with current LCD or other backlit displays. Moreover, the materials and fabrication process can be solution based, substantially decreasing manufacturing costs creating the potential for truly disposable electronics.

This effort has resulted in organic materials being incorporated into several consumer end, electronic products such as automobile radios, digital cameras, PDAs, and

wireless telephones, with the first generation of large area displays now surfacing.[20] However, organic device technology is still far from mature. Many aspects of these devices hamper the mainstream commercialization of this technology in high quality displays and/or solar panels capable of withstanding prolonged use. These aspects currently include relatively short lifetimes and low efficiencies when compared to similar technologies currently on the market. The causes of these shortcomings, particularly those which govern the efficiency, brightness, and lifetime, are still poorly understood. Many investigators suspect the instability of organic materials in oxygen rich environments,[21,22] poor interface compatibility,[24-26] and excessive heat[27,28] may lead to characteristic dark spots and delamination which can be found after continued device service.[29-31] While those aspects that govern efficiencies and operating voltages are attributed to energy alignment problems and organic material purity.[32-33]

In an effort to address these problems, many studies have been conducted to ascertain the chemistries and energy pathways that take place within a device including the alignment of energy levels at the organic/organic and organic/electrode heterojunctions,[32-33] and the movement of charge across the interior of the device.[34-35] Other studies are concerned with producing new materials, tailored for specific device proposes such as bandgap tuning, emission wavelength, and mobility properties.[36-40] However, aside from thermodynamic considerations, there has been little study of the chemistries that take place across electrode/organic heterojuctions. Typically, the junction is only considered as a thermodynamic problem where charge injection is dictated solely by the position of the electrode potential and the molecular orbitals of the

organic layers. This is especially problematic when considering the transparent conducting oxide (TCO) material, used as the anode in these devices. The most common of these, tin doped indium-oxide (ITO), has a relatively low conductivity compared to other metal electrode materials[41-44] and exhibits a more complex surface chemistry than pristine electrodes.

This dissertation is focused on the study of the ITO/organic heterojunction and the chemistries therein, and proposes appropriate strategies that enhance the interfacial physical, and electronic properties for more efficient charge injection with application to organic thin-layer devices. We focused on four major aspects of this work: ***i*)** To characterize the ITO surface and understand the chemistries that may be pertinent to interaction with adjacent organic layers in a device configuration. ***ii*)** To determine the extent to which these chemistries are variable and propose circumstances where compositional changes can occur and characterize the resulting change in surface chemistry. ***iii*)** To propose a strategy for modification of the interface which leads to enhanced physical and/or electrical properties; and ***iv*)** apply these modifications in the development of model organic thin-layer devices and characterize the enhancements observed in relation to the modification of the electrode/organic interface.

1.2 ORGANIC THIN-LAYER DEVICES

1.2.1 Organic Light Emitting Diodes (OLED)

The concept of the modern OLED can be traced back to the early 1960's, when Pope and others first reported on the electroluminescent behavior of single crystal anthracene.[46] These first devices required extremely high drive voltages for device operation, up to 6000 volts. This combined with a relatively weak electroluminescence led to declining interest in the practicality of this type of technology.[45-48] Over the next two decades, several groups introduced materials and fabrication methods that made light production in this manner more reasonable. This was demonstrated when researchers at Kodak, Tang and Van Slyke,[48] incorporated a thin-layer geometry, utilizing new organic materials, constructing a two layer, vapor deposited device, based on a 8-hydoxyquinoline-aluminum complex (Alq_3), and N,N'-diphenyl-N,N'-(3-methylphenyl)-1,1'-biphenyl-4,4'-diamine (TPD), which cut the required drive voltage to ca. 10 volts and produced a significantly higher light emission. This technology has continued to mature; however, the TPD/Alq_3 device developed at Kodak remains the model against which new advances are compared.

Current OLED technology has diverged into two main classes. The first of these is based on small-molecules similar to those described and championed by Kodak. These utilize one or more thin layers of small organic molecules, generally vapor deposited in high vacuum on a TCO base and capped with a metallic cathode. Variations of these

types of devices are plentiful and are described by a number of sources.[46,48-49]

The second class is a polymer-based OLED, pioneered by Friend and coworkers, Heeger and coworkers and by Cambridge Display Technology (Cambridge, U.K.) which consists of a body of conductive polymer in similar geometries, generally incorporating dopant molecules to assist in an active role, i.e. charge transport or light emission. Again, these devices are constructed on a TCO base and capped with a vapor deposited metallic cathode. Many variations of this class also exist and are described thoroughly in the literature.[50-52] Regardless of class, the general workings of the device can be explained in a similar manner. The work presented here utilizes small molecule devices exclusively, and as such, limits the background discussion to that geometry.

Figure 1.1 outlines the design and geometry of the ITO/TPD/Alq_3/Al thin layer device, previously described, in a cross sectional view. Typically, thin layers (10-100 nm) of the organic molecules (TPD and Alq_3) are deposited on a transparent base coated with a thin TCO layer (ITO). This allows for the transmission of a photon out of the device (for OLEDs), and also serves as the bottom electrical contact, typically the anode. These devices have traditionally been constructed on a glass support, although recently polymeric materials used as a base include the advantage of flexibility and durability. This bottom contact is typically made with ITO as the TCO material which exhibits the best combination of electrical conductivity and optical transparency available from the limited number of transparent conducting materials currently known. A second electrode is vapor deposited on top of the organic layer(s), sandwiching the assembly between the two electrodes to complete the device. The composition of this top electrode has been

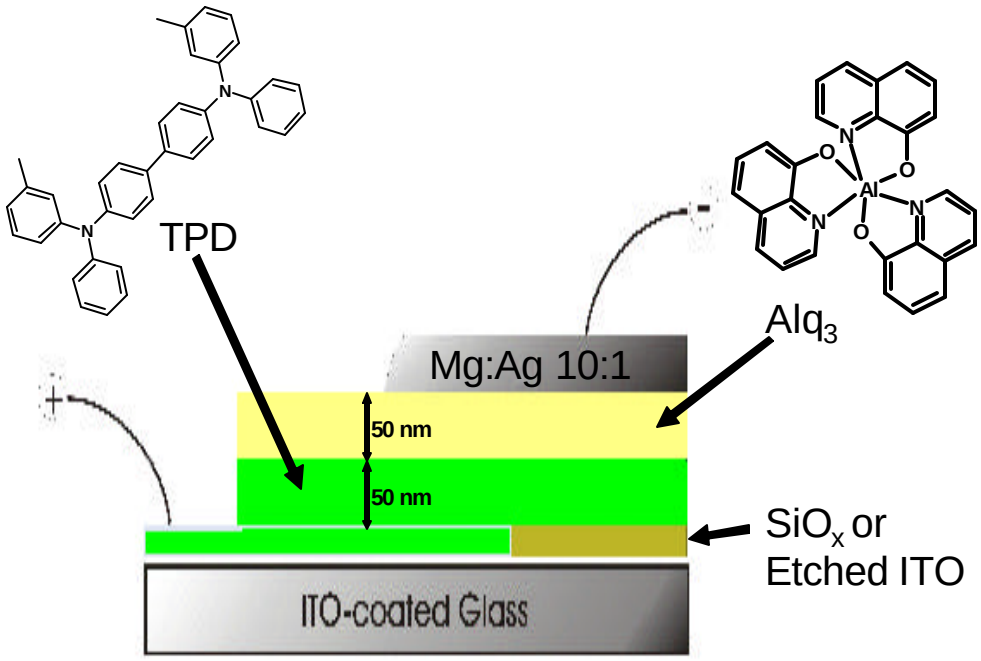

Figure 1.1 Schematic of the OLED device first developed by Tang *et al.* at Kodak Inc. ITO coated glass is used as the bottom contact while a masked layer of SiO_x, or etched channel creates a contact pad to prevent accidental "punch-through" electrode contact. This is followed by vapor deposited films consisting of 50 nm TPD (HTL) and 50 nm Alq_3 (ETL and emission). The whole assembly is capped with ca. 100 nm of 10:1 magnesium:silver cathode.

variable throughout the development of OLEDs although a co-deposition of Ag and Mg routinely provides an acceptable low work-function contact.[53]

Geometries of this type of OLED are not strictly defined; devices with multiple layers have been developed to take advantage of specific material attributes. Typically, a material with good hole transport properties is deposited nearest the anode to facilitate hole transport (e.g. TPD), while those materials with good electron transport characteristics are placed nearest the cathode (e.g. Alq_3). Emission is either carried out by one of these materials, (e.g. Alq_3), separate emission layers,[54-55] or dopants can be added.[56,57] Light production in these structures is usually described in terms of an energy band diagram and is shown in Figure 1.2. The diagram shown in the figure represents a cross sectional profile of the same device, operating in forward bias, with the relevant thermodynamic energy levels indicated; HOMO and LUMO for organic materials, and the Fermi-level for metallic entities.

During the operation of the device, a bias is placed across the two electrodes by an external source. When the bias exceeds the internal energy barriers, electrons are injected from the cathode, while simultaneously, holes are injected from the anode, into the adjacent organic materials. These charges, which now reside on the organic molecules within each layer (TPD^+ and Alq_3^-), migrate in the presence of the applied electric field toward the interior of the device. Migration continues until the density of each carrier is large enough to place opposing charge carriers in a proximity where they may recombine (ideally near the organic/organic interface), giving off excess energy as a photon. The

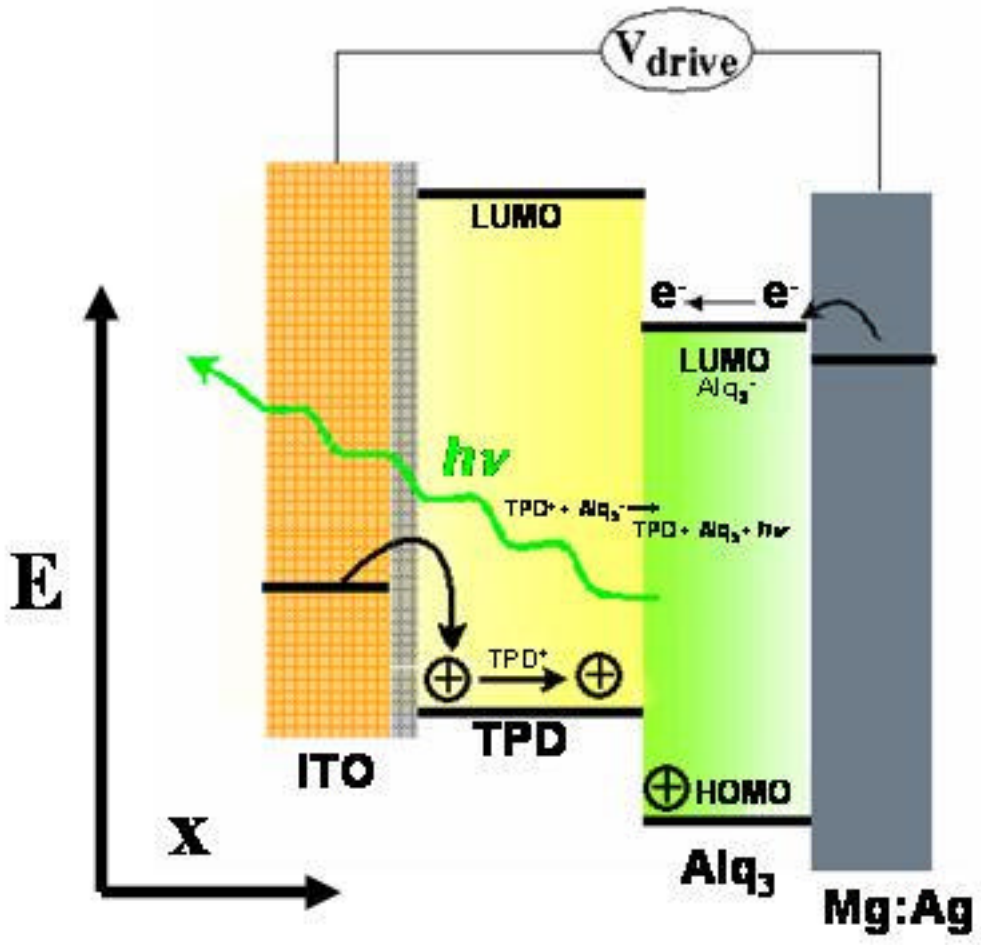

Figure 1.2 Energy band diagram of a typical OLED thin layer device. Electrons are injected from the cathode under forward bias and migrate in the presence of the electric field toward the center. Holes are injected from the anode side and likewise migrate toward the opposite electrode. Charge carriers in close proximity recombine giving off excess energy as light which exits the device through the transparent electrode.

light is then transmitted through the transparent side of the device to where it may be observed by a viewer. The wavelength of the emitted photon is determined by the bandgap of the recombined carriers and can be tailored by using materials with different HOMO/LUMO energy combonations.[52] Presently, OLED emission spans nearly the entire visible spectrum, with luminescence values of up to 140,000 cd/m^2,[57] power efficiencies of up to 40 lm/W,[58] and operating voltages from 3-10V[59] have been reported.

Additionally, OLEDs based on this structure operating under DC potentials can be described as a simple diode, modeled by an RC circuit which describes the fundamental processes of operation. Figure 1.3 describes this as a simplified RC circuit diagram depicting the basic OLED thin-layer device as described above. The major components of this circuit include a light emitting diode, a power source to drive the circuit, and two resistor elements. The first element, a resistor in parallel with the diode (R_P), represents the shunt resistance of the device and models those processes which lead to current flow without production of light (i.e. leakage current). This includes defects in the organic films which lead to cathode/anode shorts, and regions where charge flows through the organic layers without radiative products. Ideally, this term should be infinitely large to maximize current flow through the diode. Pinholes and other shorts at the ITO/organic interface, however, often render this term much less than desired.

The resistor in series with the diode, represents the series resistance (R_S), and describes the summation of resistances which limit current flow under forward bias, including contact resistances, resistances due to low rates of charge transport, and resistances due to low conductivity in the thin film electrodes. In the ideal case, this term

should approach zero, however low mobilities and contact resistances generally increase this term substantially.

Current density/voltage (J/V) behavior of these devices can be described relative to diode-like behavior according to the Schottky equation (1).

$$J = J_0\left(e^{\frac{V}{nV_T}} - 1\right) \quad (1)$$

Where J is the current density; J_0 is the reverse saturation current (current in reverse bias); V is the applied bias; n represents the diode quality factor, which for ideal diode behavior approaches 1.0; and V_T is the voltage generated or applied across the organic device. The general form of this equation can be modified slightly to reflect the effects due to limitations of less then ideal devices, i.e. the shunt and series resistance values, represented by Equations (2) and (3) respectively:

$$J = J_0(e^{\frac{V}{nV_T}} - 1) - \frac{V}{R_p} \quad (2)$$

$$V = nV_T \ln\left(\frac{I}{I_0}\right) + IR_S \quad (3)$$

Equations (2) and (3) allow for empirical calculations of both R_S and R_P based on the J/V characteristics of a completed device.

Performance of these types of devices are usually judged by the current density/voltage (J/V) behavior, luminosity/voltage behavior (L/V), total light output, and lifetime measurements which can be used to calculate other performance parameters such

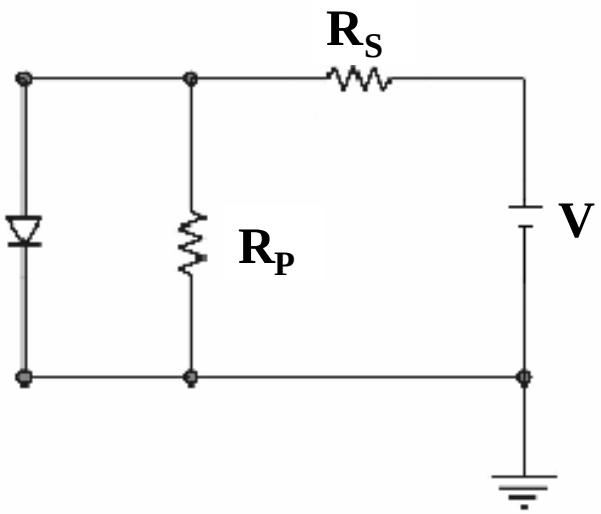

Figure 1.3 Simple RC circuit model of an OLED thin-layer device. Elements include a light emitting diode, a source of drive voltage (V), and two resister elements; the series resistance (R_S) which describes the resistance to current flow across the device, and the shunt resistance (R_P) which describes current flow that is not associated with light production. In the ideal case, R_S would approach zero, and R_P would be infinitely large.

as device quantum efficiency, voltage required to obtain a predetermined light output, and overall brightness.

1.2.2 Organic Photovoltaic Devices (OPV)

OPVs can be described in a similar manner to OLEDs, with a similar device geometry.[60-62] Figure 1.4 illustrates an OPV device developed by Forrest and co-workers[60] based on vapor deposited layers of Buckminster fullerene (C_{60}) and copper phthalocyanine (CuPc) organic layers with a hole blocking layer of bathocuproine (BCP). The geometry of this type of device is similar to those described for the OLED as shown in the figure. In general one or more organic layers are deposited on a TCO base and similarly are capped with a metallic anode. Again, each layer is picked based on the particular characteristic of the material i.e. charge mobility, ease of charge separation, and absorptivity being some of the most important factors. Other layers may be added to achieve a specialized purpose, in this case BCP is used to block exiton migration to the top metallic electrode.

The behavior of these devices is also similar to OLED device structures. In this case, a photon is transmitted through the transparent side of the device and is absorbed within the layers of organic material, on the interior of the device, as shown in Figure 1.5. The absorption process leads to an electron excitation on the organic molecules which is subsequently separated (at open circuit) from the excited molecule by a built-in electric

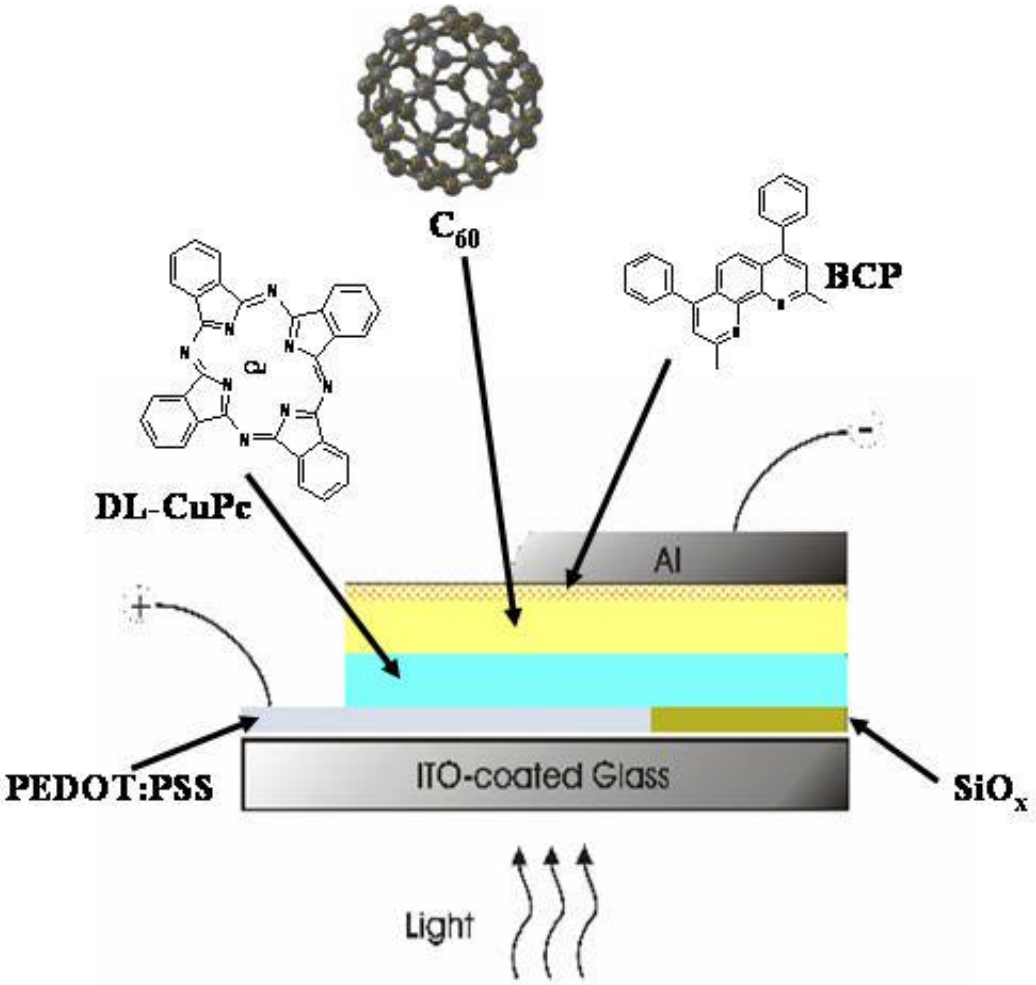

Figure 1.4 Cross sectional schematic of the OPV device described by Forrest. ITO coated glass is used as the bottom contact and a masked layer of SiO_x or heavily etched ITO channel creates a contact pad to prevent accidental "punch through" shorts. This is followed by vapor deposited films consisting of 20 nm CuPC, 40 nm C_{60} and 10nm BCP respectively. The whole assembly is then capped with an aluminum electrode as the top contact.

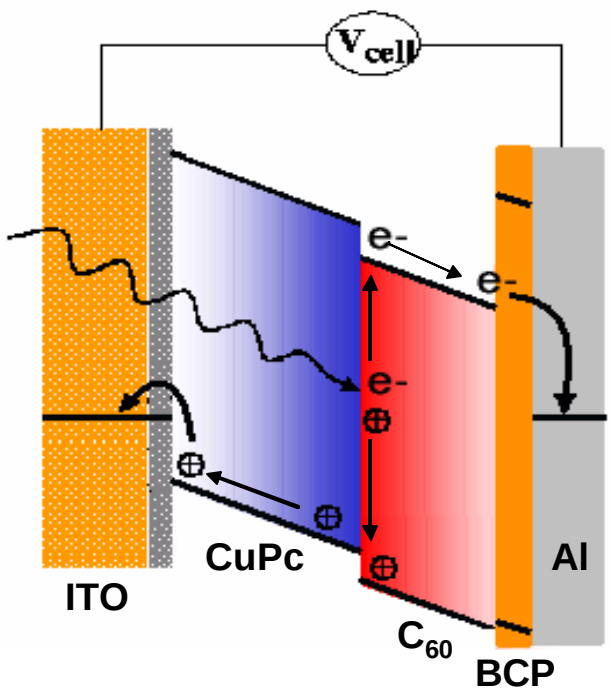

Figure 1.5 Energy band diagram of typical OPV device. Light enters the cell through the transparent side (ITO) where it excites an electron on a molecule within the interior of the device. Generated exitons are separated by an electric field and migrate toward the electrodes where they are collected and produce a photo current and voltage.

field, generated as the Fermi energy of the opposing electrodes reach equilibrium or conversely with an applied electric field. The separated charges then migrate toward the appropriate electrodes where they are collected and produce a load current. Device performance is generally expressed by the open circuit photovoltage (V_{OC}), the short circuit photocurrent (J_{SC}) and the device fill factor (FF) which is the fraction of theoretical power obtained.

A similar argument to the OLED equivalent circuit can be made for an equivalent RC circuit that describes an OPV. Thin film OPV cells can be modeled as in Figure 1.6 as a photo active diode and two resistor elements. The resistor elements R_s and R_p are the same as those listed for the OLED circuit and are governed by the same limitations. However, rather than driving current through the diode, in an OPV charge is moving toward the load. In this case, the current density/voltage (J/*V*) response of such cells can been modeled with respect to the circuit as Equation 4:

$$J = \frac{1}{1+R_S/R_P}\left[J_0 \left\{ \exp\left(\frac{V - JR_S A}{nV_T}\right) - 1 \right\} - \left(J_{ph} - \frac{V}{R_P A}\right) \right] \qquad (4)$$

Where R_s and R_p are the usual resistances and A is the device area. At the zero-current state, the open circuit photovoltage, V_{OC} can be written as:

$$V_{OC} = nV_T \ln\left(1 + \frac{J_{ph}}{J_0} - \frac{V_{OC}}{J_0 R_P A} \right) \qquad (5)$$

while the product of the short circuit photocurrent, J_{SC} and R_S can be written as:

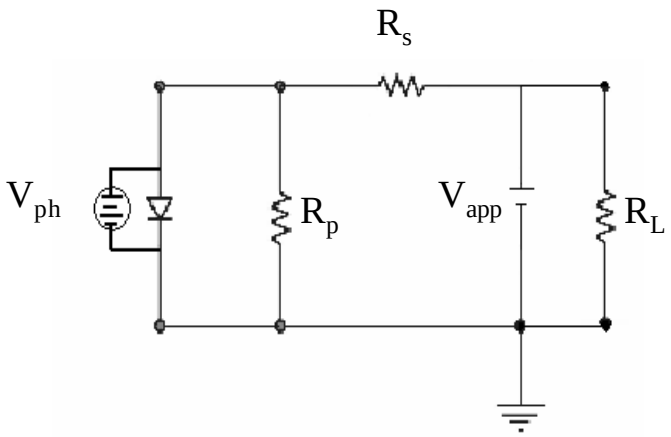

Figure 1.6 Simple RC equivalent circuit for an OPV device behaving as a photo active diode. The circuit shows the shunt resistance (R_P), series resistance (R_S), as well as the load resistance (R_L) applied voltage source (V_{app}), and a photo diode with a photo voltage (V_{ph})

$$J_{SC}R_S = -\frac{nV_T}{A}\ln\left(1+\frac{J_{ph}}{J_0}+(1+\frac{R_S}{R_P})\frac{J_{SC}}{J_0}\right) \qquad (6)$$

Described in these equations, successful device characteristics maximize R_P by limiting inappropriate current paths attributed to pin-holes and energy traps found in poor quality films. Lowering of V_{OC} values can also arise from pin-holes, which short-circuit the PV cell, and through traps within the material and at the anode and cathode interfaces. The major loss of photovoltaic power through lowered J values originates from high values of R_S.

These descriptions show the importance of the parameters of R_S and R_P in the aspect of describing the behavior of both OLED and OPV devices. It then follows that efforts to enhance the performance of these types of devices should be centered on understanding the chemical origins of these terms as well as the conditions that may affect them.

1.3 MOTIVATION

It is clear that the use of ITO can be problematic and represents one of the more limiting aspects of organic thin-layer technology. This limitation of ITO is partially illustrated by observing its electrochemical behavior with a simple electroactive probe molecule when compared to a more common electrode such as platinum. Figure 1.7

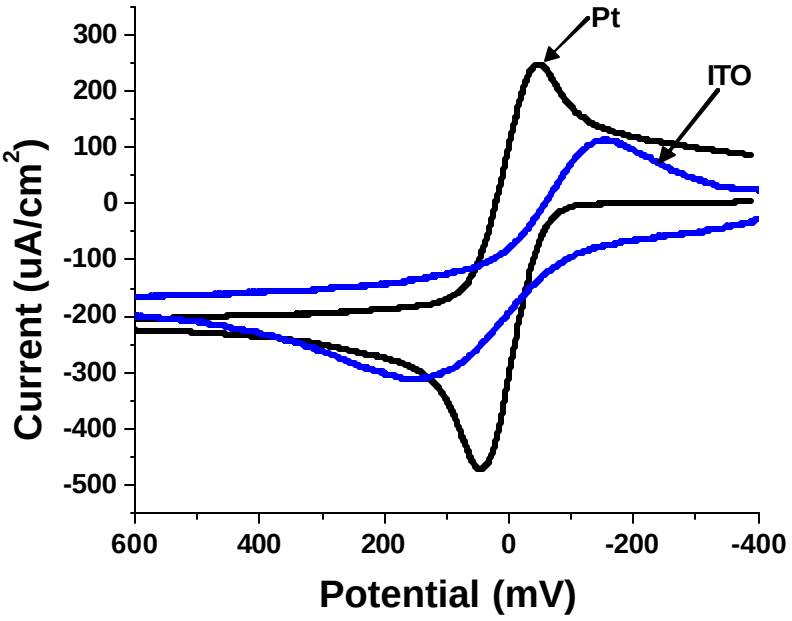

Figure 1.7 Voltammetric characterization of two different electrode materials, Pt and ITO, using ferrocene/ferrocenium as a redox probe. The ITO sample shows broad anodic and cathodic peaks with large overpotentials giving rise to a ΔE_p of 368 mV at 0.01V/s, which corresponds to an estimated k_{et} value of ca. 6.0×10^{-4} cm s^{-1}. The voltammetry for the Pt electrode shows a more reversible system with peak difference of ca. 98 mV, corresponding to a k_{et} value of ca. 7.0×10^{-2} cm s^{-1}.

ferrocene/ferrocenium (Fc/Fc^{+}) for these two electrodes with respect to each other (0.01 V/s, 0.250M $LiClO_4$ in acetonitrile, normalized for area). The figure shows very broad anodic/cathodic peaks corresponding to the ITO electrode when compared to Pt indicating a more complex surface with a large variance in available energy states. Further, the anodic/cathodic peak separation is large, ca. 0.3 Volts. These overpotentials indicate that ITO cannot be assumed as a simple electrode undergoing outer sphere electron transfer; clearly other factors are important when utilizing ITO for charge injection.

In OLED and OPV devices, the series resistance is understood to be the sum of many factors and can be broken into component terms where $R_S = R_\mu + R_{ITO} + R_{CT}$. However, most researchers assume the resistance due to charge mobility (R_m) is the major factor comprising R_S, and dominates all other terms that may contribute. In this manner, factors such as the resistance to charge injection (R_{ct}) and resistance intrinsic to the TCO (R_{ITO}), are typically neglected. Estimations of R_{ct} based on solution electrochemical studies and electron transfer theory indicate this factor may be much higher than previously expected, and potentially rival R_m as a major contributor to R_S.

The resistance a thin-film device experiences due to the mobility of the carriers present in the organic layers (R_m) can be approximated based on the mobility and concentration of the appropriate carriers according to the equation:

$$\frac{1}{R_m} = \frac{FA}{d}|z|m\,C \qquad (7)$$

where F is Faraday's constant, A is the device area, d is the thickness of the organic layer, z is the charge of the carrier, μ is the mobility of the charge, generally found through time-of-flight measurements, and C is the concentration of carriers in the device. This expression can be evaluated using the current/voltage behavior of a typical OLED device, near its onset bias to estimate the actual concentration of charge carriers. The resulting resistance value calculated for a typical TPD/Alq_3 OLED device is ca. 1.0 Ω of resistance (1cm^2 area, 100nm thick, current density of 0.1mA/cm^2).

Alternatively, a measure of how well charge may be passed with respect to a particular electrode can be approximated by calculating the charge transfer resistance (R_{ct}). The calculation of this value utilizes the exchange current density of the electrode at high solute concentrations and according to solution electrochemistry and may be approximated according to equation 8:

$$R_{ct} = \frac{RT}{nFi_o} \qquad (8)$$

Where R, T, F and i_o are the gas constant, temperature, Faraday's constant, and exchange current density respectively. The exchange current density described here is related to the amount of electron transfer activity at equilibrium and inherent to the rate of the electron transfer. A large value indicates fast electron transfer kinetics, while a low i_o indicates a slow transfer process. The value can be estimated using the Butler-Volmer equation for electrochemical processes rearranged to represent a Tafel plot. The value can be

generated in solution for an arbitrary redox event by plotting the log of the current vs. the overpotential according to equation 9.

$$\log i = \frac{anFh}{RT} + \log i_0 \qquad (9)$$

where the constants have their usual meanings, η is the overpotential, α is the electron transfer coefficient for the redox process, and i is the observed current during the potential cycle. When calculated using a ferrocene/ferrocenium redox process on an ITO electrode, the resulting i_o is ca. 1.7 x10^{-3} A/cm^2, extrapolating for concentrations approaching that present in a completed device, and results in an estimated charge transfer resistance ca. 25Ω cm^{-1}. It should be noted, that the exchange current density utilized here has been extrapolated to concentrations similar to that of a completed device, the value of which may not be strictly correct. However, the approximated charge injection resistance, at the very least is comparable to that of the mobility resistance, and as such, cannot be neglected. This comparable resistance value indicates a more complex electrode behavior than previously thought when utilizing ITO as an electrode in these devices. This also indicates that the interface itself is susceptible to consideration for optimizing a device as a whole.

To this end, the ITO/organic interface and electron transfer processes can be categorized into five major factors that are thought to be important for the successful injection of charge, for application to thin layer device technology: ***i)*** The inherent internal resistance of ITO (R_{ITO}). The resistive nature of ITO complicates its use as an electrode material by inserting an additional, largely unknown, resistive factor that

changes the conductivity of the material and must be accounted for. Undoubtedly, energy is lost by trying to drive charge through this resistive medium. However, little can be done to change this attribute when using commercially obtained ITO samples aside from decreasing devices area substantially ***ii)*** The relative wettability of ITO. The amount of intimate contact between the electrode material and the adjacent organic layer is a concern for transporting large amounts of charge across the interface. If large areas are left open, due to compatibility differences, charge transport is forced to focus toward isolated contact areas where the organic layer and electrode are in more intimate contact. This may manifest as a limited overall electron injection (higher R_S), and substantial pinhole formation (lower R_P). This may also lead to other problems such as delamination, Joule heating, and device shorting. ***iii)*** Active sites of transport across an ITO electrode. It has been clearly demonstrated that ITO is heterogeneous with respect to surface energy across its surface and is ultimately comprised of sites of high electrical activity surrounded by larger less active areas. The population of these electrically active regions may influence the charge that can be passed across the interface in a given amount of time. Low populations of electrically active sites would lead to a lower observable current flow (higher R_S) than the initial design may suggest. ***iv)*** Electron transfer kinetics. Injecting charge into an organic layer requires the oxidation/reduction of those molecules closely associated with the transport site, on the organic side. This redox process is not instantaneous and likely follows the mechanisms outlined by Marcus theory. The time required for each event is then a function of the mechanism a particular system establishes through the specific chemical interaction of the electrode surface and the

redox molecules involved. Unfavorable interactions can be detrimental in the efficient injection of charge, leading to a low overall rate coefficient and poor device properties (increased R_S); while more favorable interactions may increase the apparent electron transfer rates (substantially lower R_S). ***v)*** The thermodynamics associated with charge injection. Many factors fall under this classification, electrode work-function and redox potentials of the organic material are important parameters in the evaluation of charge transport.

The extent to which each of these factors effect the injection of charge into a device is largely unknown; likely a combination of these factors represents the observed transfer characteristics. However, an estimation of the most important factors could direct research efforts to achieve the maximum chance for success when searching for possible enhancements of charge transfer. Additionally, efforts to improve on one factor may influence other factors in a positive or negative manner. The final aim of this dissertation is to provide for an understanding of how efforts to enhance electron transfer at this interface may alter the factors that are involved in charge transfer and demonstrate this through the completion of a series of organic thin-layer devices which document the enhancements found for each factor.

The foundations of these studies are set in Chapter 2 which examines the ITO material fully. This chapter describes the crystal structure and defect chemistry that produces the unique properties ITO exhibits. The discussion is focused on the composition and structure of the near surface (upper 2-3 nm) of the material which interfaces with the organic layers. Described here is a working model of the ITO surface

and how the surface chemistry is variable with respect to chemical influences and pretreatments. The conclusion of this chapter examines the electronic nature of the ITO surface and suggests less that 5% of the geometrical surface area is involved with charge injection. Additionally, the electrically active area can be influenced by different pretreatments of the ITO surface including piranha etching, RCA treatments, plasma treatments and solvent washes.

Chapter 3 extents these discussions by further characterizing the electrical properties of ITO, establishing a protocol of electrochemical probing to evaluate the electrode with respect to different pretreatments, or the lack thereof. Additional evidence for the heterogeneity and small active area of the surface are also presented. The discussion introduces the modification of ITO by small molecules incorporated with carboxylic acid functional groups and conductive polymer overlayers (spin cast and electrochemically grown) which are both shown to have substantial improvements over unaltered ITO substrates. Also described here is the mechanism for each modification and the rational behind the apparent electrical improvements observed electrochemically.

The studies are drawn to a conclusion in Chapter 4 which describes the construction and evaluation of OLED and OPV devices based on the more successful pretreatment and modification strategies previously evaluated. The characterization of these devices show a dramatic decrease in the reverse bias leakage current upon modification with respect to unaltered ITO as well as nearly doubling the quantum efficiency. The rational for the apparent enhancements are also discussed in addition to the electrically active surface area.

An additional chapter, Chapter 5, describes the creation and characterization of electrochemically grown polymer nano-structures based on blazed angle diffraction gratings. The discussion details the micro-contact printing process and the electro-catalytic growth of the conductive polymers PANI and PEDOT to form diffraction grating structures in their own right. Further discussion illustrates the diffraction efficiency of these structures and conditions when it may change (changes in refractive index or absorptivity) outlining possible uses as chemical sensors. The chapter is concluded with the evaluation of these structures as both working pH sensors and potentiometric sensors based on the changing diffraction efficiency.

CHAPTER 2

TIN DOPED INDIUM OXIDE (ITO): STRUCTURE AND REACTIVITY

2.1 INTRODUCTION

Currently, tin doped indium oxide (ITO) thin films are the primary transparent conducting oxide (TCO) electrode utilized in organic thin-layer devices such as organic light emitting diodes (OLEDs), organic photovoltaic devices (OPVs), and as the transparent indicator electrode in electroactive integrated optical waveguides (EA-IOW).[1,2] Devices of this type generally require a large optical gap and operate at relatively high current densities, and consequently require high rates of charge injection to achieve satisfactory device performance.[3-7] In this capacity, ITO surpasses other known TCO materials by providing the best combination of conductivity, optical transmission, and ease of lithographic processing through chemical etching techniques.

However, the use of ITO is still problematic. Manufacturing conditions, processing conditions (cleaning), and storage conditions of ITO films are widely variable. Consequently, the resulting oxide surface is heterogeneous with respect to its compositional, chemical, and electrical properties. This surface heterogeneity is of particular concern in organic thin layer devices where organic layers must interface (form a heterojuction) with the adjacent organic material. This also severely complicates working with ITO, as an electrode, rendering comparisons of device measurements from

system to system difficult and, depending on the state of the electrode, negatively impacts on its physical and electrical properties.

This variable nature of ITO, combined with an intrinsic chemical incompatibility with many of the organic materials developed for device use, as well as a chemical instability while under high current loads, have led to increasing problems with ITO as device technology becomes more advanced. These problems include the erratic operation, development of high charge injection barriers, electrically dead areas appearing with sustained device use, and physical delamination at the ITO/organic interface. In an effort to control these problems, many studies have responded with several empirically derived solution and gas phase pretreatment procedures aimed at altering the nature of the terminating oxide and hence, the inherent properties of ITO.

The majority of these strategies dealt with decreasing the surface roughness, or controlling the observed workfunction of an ITO film. Modification strategies currently include the addition of a surface dipole layer,[8-11] and/or coating the electrode with a thin layer of metal[12] or conductive polymer.[13,14] Other strategies include utilizing cross-linked triarylamine-siloxane layers,[15] reactions of organometallic species such as zirconium oxide or phenoxy-tin complexes to achieve specific surface functionalities,[16,17] as well as the addition of monolayers of surfactant across the electrode surface.[18] Regardless of the technique, all of these modifications seek to alter the fundamental interface properties of ITO/organic heterojunctions. However, with limited success in these studies, control of the surface chemistry of ITO is still largely unknown. In order to successfully change the surface and interfacial properties of a device reliably, the surface composition and

structure of ITO must first be adequately understood and described. Once a model has been constructed, reasonable alterations may be proposed to achieve the desired goal.

The exact surface composition of most commercially available ITO is still uncertain[3,19,20] and possibly very dynamic, even among the same suppliers. DC-magnetron and RF-sputter processes create an oxide film that has a high oxygen defect concentration. It is thought that these defect sites play a key role in both the optical and electrical properties of the material.[21] Understanding of both the surface morphology and chemical state of the oxide is important for predicting how the material will behave in any given system. Also, a better understanding in this area is essential for the development of how the organic/ITO interface behaves with respect to: ***i)*** physical compatibility or wetting of an organic molecule to the oxide, ***ii)*** the mechanism for charge transfer and the rates at which it occurs, and ***iii)*** the type and impact modification strategies will have on both (*i*) and (*ii*). In this regard, the extent of the chemistries found on ITO and how they can be changed with various modification techniques are explored.

2.2 BULK MORPHOLOGY AND CRYSTAL STRUCTURE

Currently, a wide variety of processes exist for the deposition of ITO, in a thin-film form, onto glass or polymeric support substrates.[22-28] These processes include: reactive DC sputtering, RF sputtering, plasma assisted electron beam evaporation and more recently dip coating the substrate with an indium carboxylate salt followed by high

temperature pyrolysis[29] and novel sol-gel processes.[30] DC sputtering from a tin doped In_2O_3 target is the most common deposition technique for large area preparations. Thin layers (100-500 nm) are generally deposited on a glass or polymeric substrate as a support with certain desirable properties, such as low resistively values and high optical transmittance, being highly interrelated and strongly dependent on the growth conditions.[31-35] Several parameters can be altered during the deposition process to influence the structural, electronic, and optical properties of the prepared film, including: the surrounding gas composition, target composition, substrate temperature, input power, and annealing time.[31-33] The resulting composition as well as microstructure is shown to have a significant effect on the characteristics of ITO films[34-35] and play a major role when considering device structure and design.

2.2.1 Crystal Lattice and Bixbyite Unit Cell

X-ray diffraction (XRD) and transmission electron microscopy (TEM) investigations have shown the bulk structure of most ITO films to consist primarily as a mixture of crystallographic forms of In_2O_3.[36] The basic crystal structure of most commercially available ITO is a cubic, C-type, rare-earth sesquioxide of In_2O_3 referred to as bixbyite, shown in Figure 2.1. Bixbyite is a member of the Ia3 space group (number

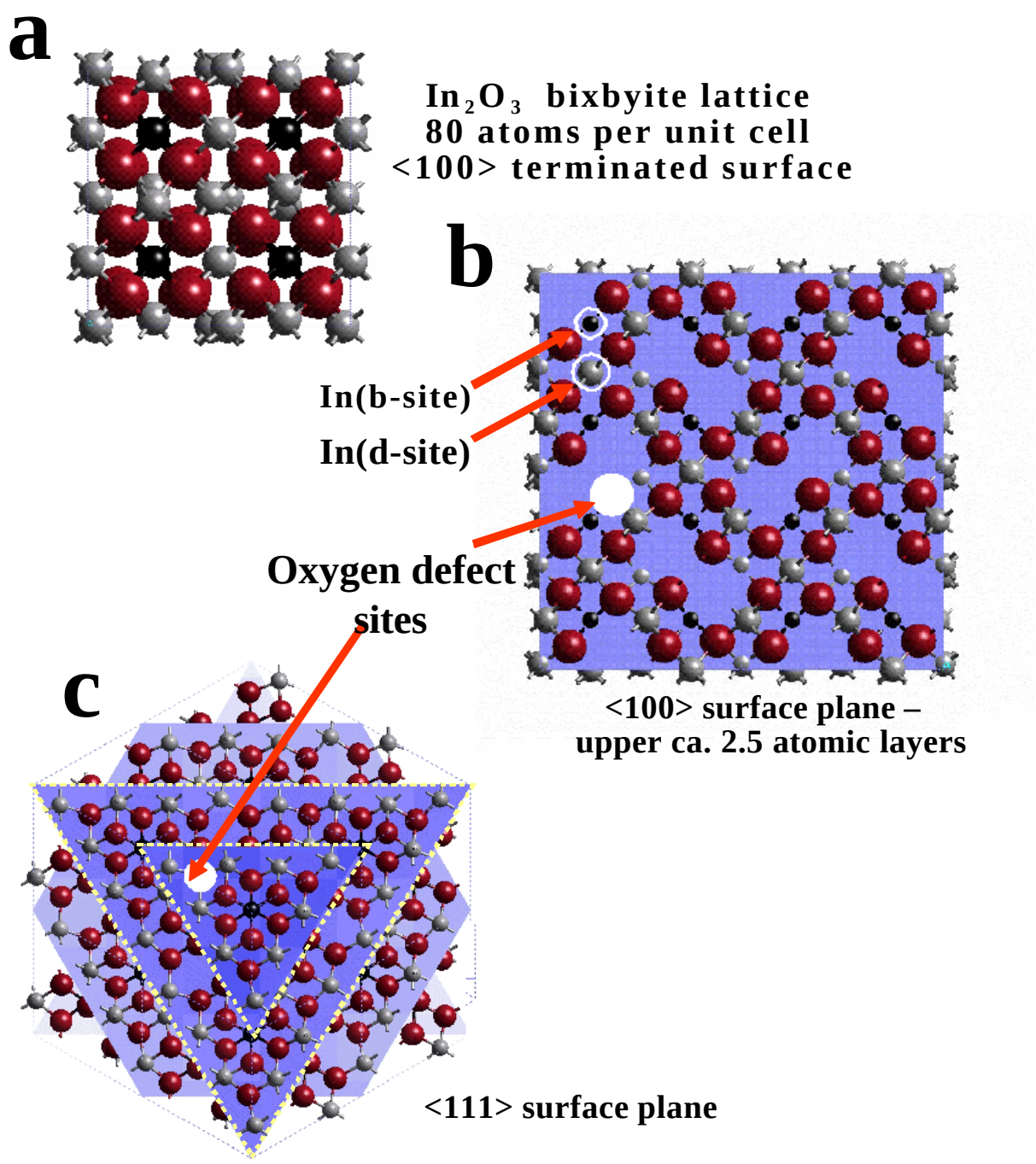

Figure 2.1 Crystal structure of the bixbyte lattice. (a) the <100> plane of for In_2O_3 parent, (b) the <100> surface plane of ITO based on the same unit cell but exhibiting oxygen defect sites, doped tin atoms and different indium sites. c) the <100> surface plane of ITO.

206), with a lattice parameter of 10.117 Å. The structure can be obtained by removing one fourth of the anions from the fluorite structure, and allowing for small shifts of the remaining ions.[38] The unit cell of bixbyite is also complex, including 80 total constituent atoms, two differing indium sites, many sites devoid of interstitial oxygen atoms; and with ITO, additional oxygen vacancy defects, and an indium-to-tin doping ratio of ca. 10:1. This type of structure is unique in that other close-packed structures in this family (rocksalt, spinel) lack such empty interstitial oxygen sites. The complexity of this material also creates a uniquely strained system. Stress measurements reveal that these types of films experience large amounts of internal stress, where compressive stresses have been measured up to ca. 2.2 GPa.[32]

The empty interstitial oxygen positions dictate that metal cations reside at two non-equivalent six-fold symmetry positions giving rise to the 'b' and 'd' sites according to Figure 2.1b. Each unit cell in the lattice consists of 8 'b' site and 24 'd' site cation positions. The b-site indium cations shown here are bounded by six equidistant oxygen atoms at a distance of 2.18Å, and lie roughly in the corners of a cube with structural oxygen vacancies along one body-diagonal. This can be viewed more readily in Figure 2.2. The 'd' site position is also bounded by six oxygen atoms, but at three different distances: 2.13 Å, 2.19 Å, and 2.23Å making up the corners of a distorted cube which leaves two oxygen vacancies along one face-diagonal. This larger distance is attributed to unequal distribution of repulsive forces among the oxygen anions that form the coordination polyhedron.

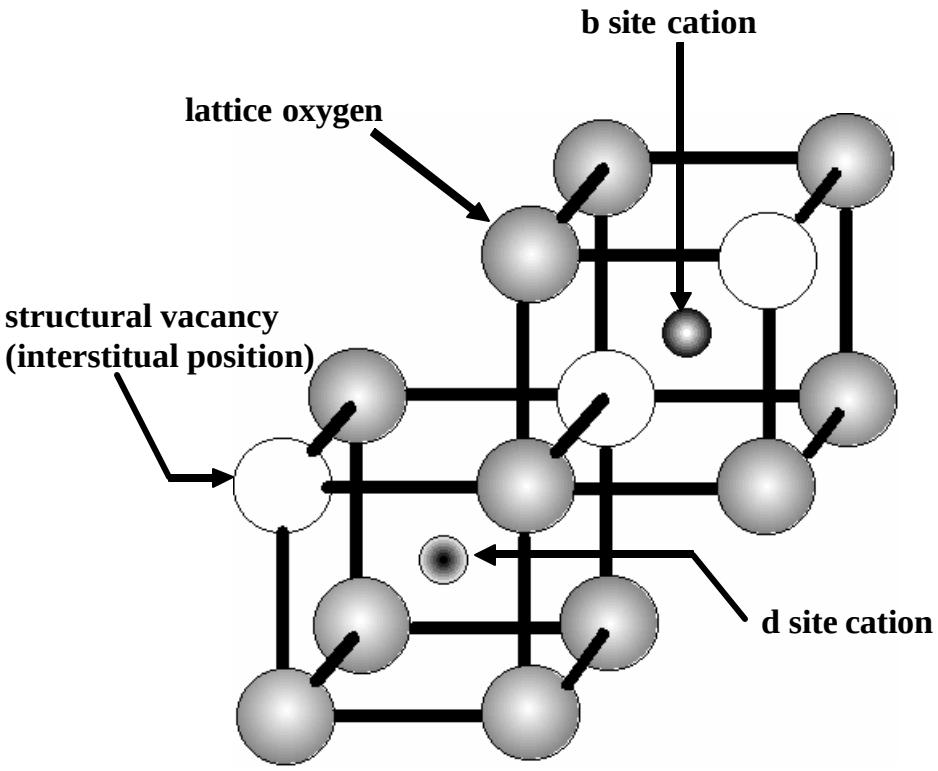

Figure 2.2 Portion of the ITO unit cell which contains 'b' site cation and 'd' site cation positions. The b-site indium cations are bound by six equidistant oxygen atoms at a distance of 2.18Å, and lie roughly in the corners of a cube with structural oxygen vacancies along one body-diagonal. The 'd' site position is also bounded by six oxygen atoms, but at three different distances: 2.13 Å, 2.19 Å, and 2.23Å making up the corners of a distorted cube which leaves two oxygen vacancies along one face-diagonal

Additionally, ITO is manufactured with structural oxygen atoms removed from the bulk lattice (in addition to interstitial oxygen vacancies), and doped tin atoms that take up random positions normally occupied by indium, although the 'b' site is preferred due to the smaller ionic radius of tin.[10,11,12]

2.2.2 Topological Structure

Figure 2.3 shows the typical topology of a commercially available ITO sample as imaged by scanning probe microscopy (AFM) methods. Although the exact surface structure is sensitive to deposition type and conditions, most of these films can be described in the same manner. XRD studies have shown the {222} and {400} reflections are mainly observed with a ratio of ca. 3.3:1, this is consistent with random distribution of exposed <100> and <111> faces of the bixbyite lattice. It has also been shown that sputter-deposited films tend to be more <100> in character and that this low-index face will generally increase in prominence as the film increases in thickness (greater than 450nm), while electron beam deposited materials show a predominance of the <111> face. [37] As shown in Figure 2.1, the <100> plane on the lattice can exhibit open rectangular spaces one atomic layer deep with an aspect ratio of ca. 0.8Å to 4.9Å. Similar lattice openings, with differing geometric spacing are revealed in the <111> plane. Regardless of deposition type, ITO growth is characterized by a polycrystalline nature dominated by a grain-like structure, which ranges in size from 200-400nm. Sputter-

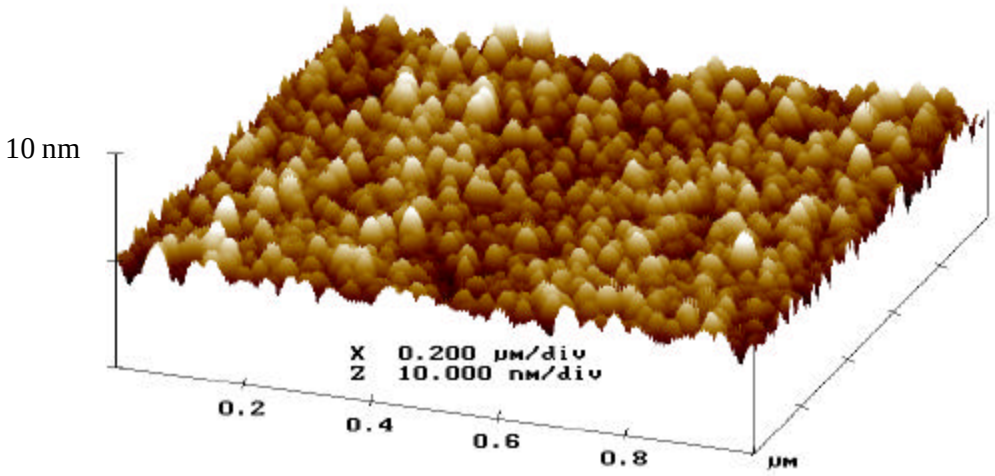

Figure 2.3 Topological features of ITO characterized by AFM show a polycrystalline structure dominated by a grain-like structure, which ranges in size from 200-400nm. Sputter-deposited films also consist of subgrain regions, visible here, 10-30nm in diameter. Overall roughness depends on the deposition but generally falls 0.8-1.6 nm RMS roughness. Image is 1x1µm with a 10nm height scale.

deposited films also consist of subgrain regions, visible in Figure 2.3, 10-30 nm in diameter. Studies have also shown that the size of these subgrains tends to remain constant as film thickness changes.[37] Measured surface roughness may vary from supplier to supplier but is generally in the range of 0.8-1.6 nm RMS roughness.

2.3 ELECTRICAL AND OPTICAL PROPERTIES

It is well known that undoped In_2O_3 exhibits n-type conductivity due to the presence of the aforementioned oxygen defect sites.[39-41] To achieve this property, the lattice must undergo a mechanism to establish these vacancies and is accomplished when a neutral oxygen atom decomposes upon reduction to supply free electrons for conduction according to the equation.

$$O_O^X \longrightarrow \frac{1}{2} O_{2(g)} + V_0 + 2e^- \qquad (1)$$

Where O_o^x represents a neutral structural oxygen atom within the lattice and V_o represents the newly formed oxygen vacancy that acts as doubly ionized donor and can contribute two electrons to the electrical conductivity of the material. The process generally takes place during the annealing process during film fabrication, and the resulting structure can be represented by substituting in the formula to account for the defect population: (In_2O_{3-x}). In addition to supplying electrons for conduction, the

oxygen vacancy defects allow for O^{2-} ion mobility.[45] However, this aspect of conductivity is negligible when compared to the overall electronic conduction and is typically neglected.

The conductivity of ITO can be increased further by doping the oxide material with a metal having a valance of IV or greater; Sn is doped in at high levels to create the Sn doped In_2O_3 represented by the formula: $In_{2-x}Sn_xO_{3-2x}$. In this case, the presence of Sn greatly increases the carrier density by creating a charge imbalance within the lattice that must be compensated by either the oxygen interstitial atoms surrounding the site (in the oxidized case) or by free electrons (in the reduced case) in order to maintain charge neutrality. According to a model developed by Subbarao, De Witt, and later Frank and Kostlin,[42,40,43] the cation sites in the lattice are completely filled, and interstitial oxygen anions are situated near some of the ordered structural vacancy sites of the lattice. These oxygen interstitial anions then compensate the charge of the ionized donor, Sn^{3+}. The defect causes a loosely bound cluster between the adjacent atoms which may decompose upon reduction as shown.

$$Sn_2O_i \longrightarrow \frac{1}{2}O_{2(g)} + 2Sn_{(s)} + 2e^- \qquad (2)$$

Where O_i represents interstitial oxygen atoms bound to tin. The electrons that charge compensate the Sn^{4+}/In^{3+} species are then responsible for the increased conductivity in the reduced ITO material and due to the disparity of charge between Sn^{4+} and In^{3+}, each dopant atom may contribute one electron to the conductance band. Typical conductivity

values of ITO[44] have been measured to be 5000-10,000 S cm^{-1} (resistivity of $2x10^{-4}$ Ω cm) with a carrier densities between $3.0x\ 10^{20}$ to $7.5\ x\ 10^{20}$ cm^{-1} and mobility measurements of ca. 41 $cm^2\ V^{-1}\ s^{-1}$ placing it as a semiconductor by category.

To establish the overall conductivity, other factors must be evaluated. Electrical conductivity (s) is dependant on both the concentration (*N*) and mobility of free carries (μ) according to the equation:

$$s = N\mu e \qquad (3)$$

In an effort to obtain the highest electrical conductivity, a maximum of carrier concentration and mobility should be realized. Both oxygen defect sites and Sn doping realize a substantial increase in the number of carriers. However, it has been shown that mobility and carrier concentration in degenerate semiconductors are not independent terms but governed by the relation

$$m \propto N^{-\frac{3}{2}} \qquad (4)$$

Therefore, doping concentrations and mobility values must be balanced in order to maximize the conductivity of the material and not compromise the optical nature of the films. It has been reported that the optimum conductivity values for ITO is 5000-10000 S cm^{-1} based on theoretical calculations.[45-46]

2.3.1 Defect Structure of ITO

ITO conductivity is shown to be based on the culmination of oxygen defect sites and Sn doping in order to supply free carriers within the bulk. However, the conductivity

values that are observed in practice are somewhat lower than expected. It is thought that this lower conductivity is due to a variety of additional defects incorporated throughout the lattice. To date, four major types of defect structures have been identified and account for the lower conductivities observed. ***i)*** The removal of structural oxygen atoms upon annealing (V_o) as described above, where reduction leads to the characteristic n type behavior and providing the bulk of the conductivity. ***ii)*** The lattice incorporates an ionizable complex where two Sn^{4+} ions become loosely bound to an interstitial oxygen anion forming the defect [Sn_2O_i]. This interstitial defect may also dissociate on annealing under reducing conditions which results in the afore mentioned tin doping responsible for additional conductivity. ***iii)*** Sn atoms substituting near two neighboring indium atoms strongly binds an additional oxygen, forming a neutral complex which consists of two Sn^{4+} and the surrounding oxygen atoms creating Sn_2O_4. And ***iv)*** an associate of the two above mentioned defects. $(Sn_2O_i)(Sn_2O_4)^x$ respectively. The latter two defect sites inhibit mobility by introducing non-uniform crystalline behavior, and decreases conductivity by trapping electrons keeping them from obtaining the conduction band.

2.3.2 Band Structure of ITO as a "Degenerate Semiconductor"

ITO is many times mistaken as a metallic electrode for use in organic electronic devices. In reality, ITO is a wide gap, highly degenerate n-type semiconductor with a

carrier concentration of ca. 5 x10^{20} cm^{-3} compared to 10^{23} electrons/cm^3 for a typical metal. Because ITO is a semiconductor, many difficulties must be overcome when utilizing the material as a general electrode. Though many studies and theoretical models have dealt with microscopic aspects of the electronic structure, few have tried to approach this in a density of states argument due to the complexity of the ITO unit cell. Recently, a few studies have taken both theoretical[45] and experimental[46] approaches for a better model. These studies have shown that the In: 5s antibonding orbitals with small impurity bands of O: 2s antibonding orbitals and Sn: 5s/O: 2s antibonding orbitals predominantly make up the character of the conduction bands of indium oxide and tin oxide respectively. However, the orbitals responsible for the conduction band of the doped material (ITO) are predominately In: 5s/O: 2p antibonding, with a small admixture of Sn: 5s/O: 2s antibonding orbitals. The deviation from the parent oxides is reasonable if one concedes that the oxygen atom is compensating for excess charge from the Sn and a mixing of orbitals occurs. Figure 2.4 shows a simplified band diagram resulting from these studies that can be constructed for ITO.

Stoichiometric indium oxide should have a filled valence band that is primarily oxygen 2*p* in character with the In: 3*d* band residing just below the valence band edge. The conduction band is comprised primarily of the In: 5*s* band ca. 3.5 eV above. The next higher band is the In: 5*p* band. However, indium oxide generally lacks stoichiometry due to the aforementioned oxygen defect sites throughout the lattice. If vacancy concentrations are large, an O: 1s impurity band forms and overlaps the bottom of the conduction band producing a degenerate state.

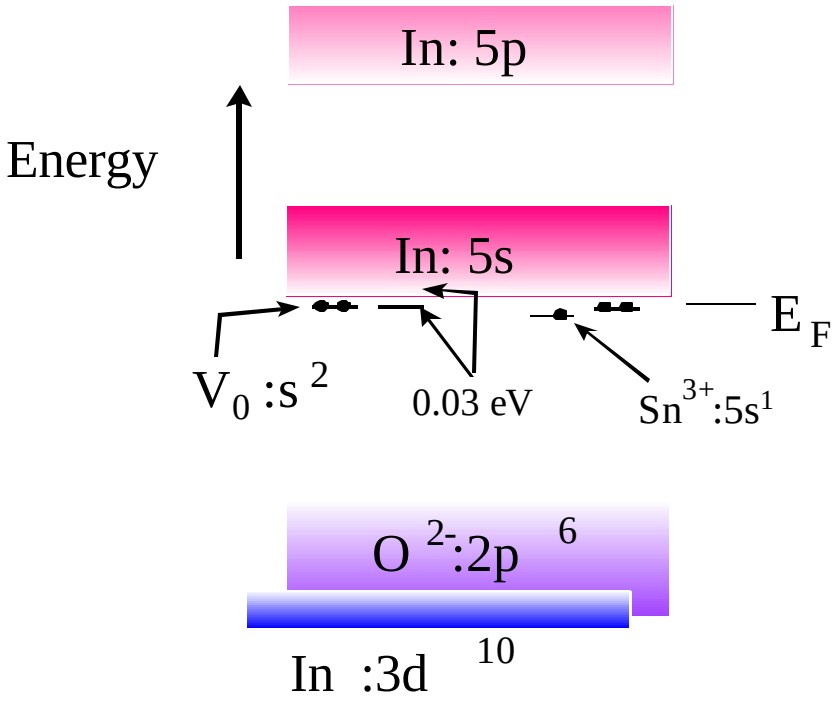

Figure 2.4 Simplified band structure for ITO showing the contribution of each element to make up the wide gap, highly degenerate n-nype material. Principle orbitals contributing to the character of the conduction band are Sn 5s/O 2p antibonding with a small mixture of Sn 5s/O 2s antibonding orbitals.

Sn, doping into the lattice, substitutes for a fraction of the bulk indium atoms. This results in n type doping by providing an electron into the conduction band due to the formation of an additional impurity band with s-like symmetry, overlapping the conduction band. The conduction band itself changes character from predominantly In: 5*s*/O: 2s to characteristically Sn: 5*s*/O: 2*p* with a small admixture of Sn: 5*s*/O: 2*s*. The gap may also change in energy depending on the doping load of the material. In general, a larger gap is observed with higher Sn concentrations.

2.3.3 Absorption Spectrum

Figure 2.5 shows a typical optical transmission spectrum for an ITO sample in the visible wavelength band. Depending on the thickness, the transmission of ITO varies in the visible region between 80-90% throughout the band and exhibits a refractive index of approximately 2.0 throughout the visible range. The large optical gap seen here makes ITO extremely useful for the input/output of light for use in organic electronic devices as there is minimal absorbance in the visible range. Typically, ITO has a band gap of ca. 3.5 eV leading to an absorption edge in the blue ca. 350 nm shown by the sudden absorbance at that wavelength.

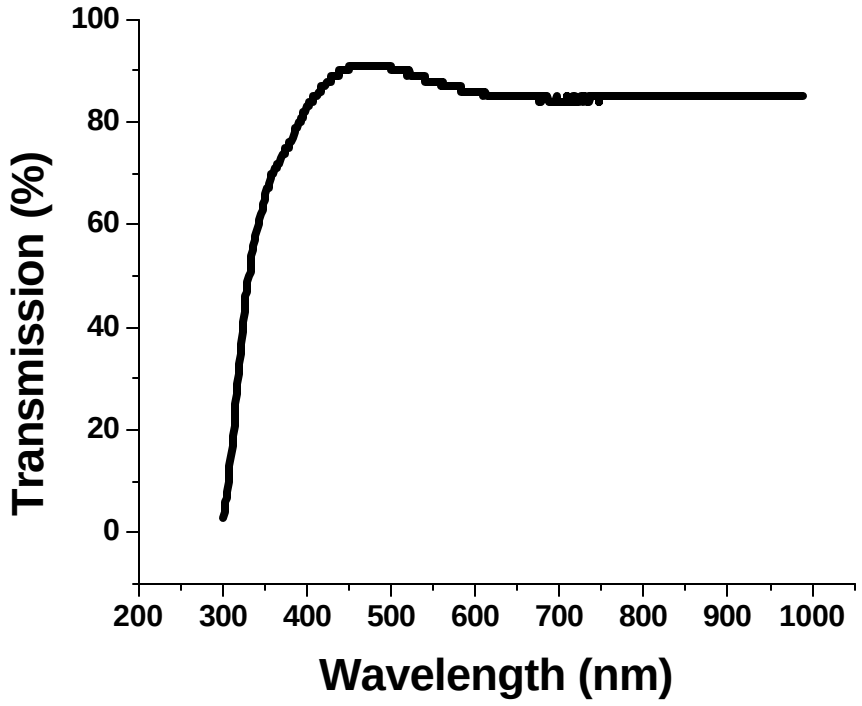

Figure 2.5 Optical characteristics of commercially obtained ITO thin films (Colorado Concept Coatings, Longmont Co). Optical transmission is relatively constant throughout the visible region reaching nearly 95%. The absorption edge in the blue ca. 350 nm results from a bandgap of ca. 3.5 eV

2.4 SURFACE CHARACTERIZATION OF ITO FILMS

Evaluation of the chemical and physical properties of ITO is crucial to understanding how this TCO interacts with other materials in a device configuration. While the crystal structure of ITO has been well studied, the terminus of the lattice which interacts with device organics is largely unknown. This thin surface can be problematic to study conventionally and hence requires surface sensitive techniques such as contact angle measurements, X-ray photoelectron spectroscopy (XPS), and ultraviolet photoelectron spectroscopy (UPS).

2.4.1 Axis Symmetric Drop Shape Analysis

In many active devices such as OLEDs and OPVs, ITO is coupled with an adjacent thin layer of organic material, which most often is extremely hydrophobic in nature. This interaction between the somewhat hydrophilic surface of ITO and the adjacent layer becomes important for a device to maintain satisfactory performance. Microscopic delamination of the organic film often results from improper consideration of wettability differences which reduces effective contact area and may lead to larger incompatibility issues such as large areas becoming detached with long term usage. Despite the importance of interfacial compatibility between the two materials, the wetting

process of an organic moiety on an ITO surface is still poorly understood and is most commonly estimated by simple measurements of solvent droplet contact angles, using either water or some other low vapor pressure liquid, on the solid surface.

Contact angles of liquids on surfaces, are used as an empirical parameter to quantify the interfacial compatibility or wettability of the liquid on the solid. Then, by examining the nature of the solvent used, (hydrophobic/hydrophilic) predictions of how other materials will behave on the surface can be made. The wetting ability of a liquid or small molecule is a function of the surface energies of the materials involved. When the liquid encounters the surface of an ITO sample, the adhesive forces between the liquid and the ITO surface will compete against the cohesive forces within the liquid droplet. Liquids where cohesive forces cannot compete with the strong attraction forces of the sample surface tend to spread over the ITO material, reducing the angle of contact. This type of surface (e.g. clean ITO) with respect to the specific liquid (e.g. water) is termed a high energy surface. Liquids where strong cohesive forces compete effectively with the adhesive forces of the surface generally tend to bead-up or form a droplet when in contact with the sample. Because this surface lacks the energy to separate the intermolecular bonds within the wetting material, this type of surface is low energy and is characterized by a large contact angle. Figure 2.6 shows water contact angles for two such surfaces. The measured angle shown in figure 2.6a is moderate and indicates a low energy surface more suitable for the wetting of organic materials. Alternatively, Figure 2.6b shows a low contact angle indicating high energy surface with respect to the water. In general it is difficult to obtain suitable wettability from high energy surfaces (with respect to

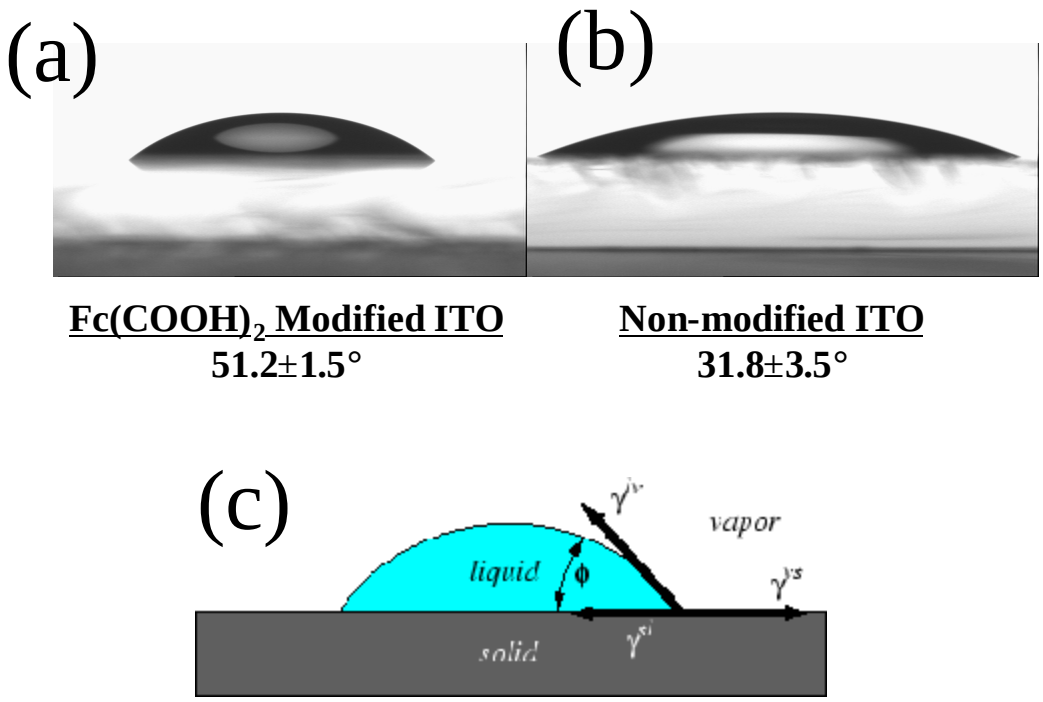

Figure 2.6 Water contact angles of two energetically different surfaces, the $Fc(COOH)_2$ modified ITO surface (a) shows a greater contact angle and represents a low energy surface with respect to water. The non-modified ITO sample (b) shows a shallow contact angle and represents a high energy surface with respect to water. Contact angle is taken from the base of the drop and tangent to the outside edge as shown in (c), as well as the forces involved; contact angle is indicated by ϕ, while γ_{lv}, γ_{vs}, and γ_{sl} represent to cohesive forces between solid, liquid and vapor respectively.

water), such as ITO with organic materials; although there have been are numerous studies for converting high energy into low energy surfaces. This is mostly accomplished by modification schemes developed especially for ITO systems.[47]

The measurement process and the resulting contact angle can be described mathematically through the use of Young's Equation shown below, where the interface is constrained to be a flat surface.

$$\gamma_{vs} \cos \phi = (\gamma_{vs} - \gamma_{sl})/ \gamma_{lv} \qquad (5)$$

where γ_{vs}, γ_{sl}, γ_{lv} represent the surface tension of the vapor-solid, solid-liquid, and liquid-vapor interfaces respectively and ϕ is the contact angle as shown in Figure 2.6c and defined to be $0° \leq \phi \leq 180°$.

Contact angles on most surfaces are not only influenced by the interfacial forces, according to Young´s equation, but also by many other phenomena, such as surface roughness, chemical heterogeneity, adsorption layers, molecular orientation, and swelling of the solid. Because a surface such as ITO exhibits many of these factors, these effects have to be considered when predicting cohesion between the ITO surface and the molecules of interest. Wetting characteristics are also largely responsible for the material's ability to fill a void. Liquids are often pulled into surface defects by capillary action. The capillary force driving the liquid into the crack is a function of the surface tension of the liquid-gas interface, the contact angle, and the size of the defect opening.

This can be critical for highly porous or rough surfaces where driving force for the capillary action can be expressed as the following

$$\text{Capillary Force} = 2\pi r\sigma_{lv}\cos\phi \qquad (6)$$

Where: r = radius of the crack opening, σ_{lv} = liquid-vapor surface tension, and ϕ = contact angle. Since pressure is the force over a given area, it can be written that the pressure developed, or capillary pressure, is expressed as:

$$\text{Capillary Pressure} = (2\sigma_{lv}\cos\phi)/r \qquad (7)$$

with the variables the same as those listed above. These equations are only strictly defined for a cylindrical defect, but the relationships of the variables are the same for any flaw with a noncircular cross section. Capillary pressure equations only apply when there is simultaneous contact of the liquid along the entire length of the opening. This leads to lower than expected angles when utilizing rough materials but are minimal with ITO due to the relatively low surface roughness of ca. 2.0 nm, but may be substantial for the deposition of organic layers on organic or modified surfaces and the deposition of cathodic materials.

Because the exact surface tensions and forces are rarely known, the most common strategy to estimate relative wettability is to use contact angle measurements with pure test liquids, (such as water) in order to obtain information on the solid-liquid interfacial region. These thermodynamic parameters can be applied in an inverse manner to predict wetting and adhesion properties of polymers or small molecules on ITO as well as the

effect of subsequent surface modifications. Thermodynamically relevant contact angles on ITO surfaces can be precisely determined using a contact angle/ interfacial tension technique such as Axis symmetric Drop Shape Analysis (ADSA).

Measurements carried out on ITO samples can be erratic based on the conditions/pretreatments the sample is exposed to prior to analysis. Generally, samples cleaned with surfactant/water followed by an EtOH rinse exhibit a modest contact angle of ca. 31° ± 3.5° using water as the liquid, showing ITO to be a fairly low energy surface with respect to organic materials, while those recently subjected to plasma etching conditions can exhibit angles of less than 3°. This indicates a severe problem with current device manufacturing techniques which often specifies organic deposition directly after plasma etching. These small angles suggest that the freshly cleaned/plasma etched surface is incompatible with molecules of an organic nature and will possibly lead pinholes and delamination effects as the junction tries to reorganize to lower energy.

2.4.2 X-Ray Photoelectron Spectroscopy

TCO films can be studied by a wide variety of techniques. However, very few can provide information about the terminus of the crystal lattice which determines the nature of the interaction with adjacent materials. X-ray photoelectron spectroscopy (XPS) is one technique that is adapted for this purpose extremely well. The XPS technique is highly surface specific due to the short inelastic mean free path which limits the escape range

that the photoelectrons possess when they are ejected from the atoms within the solid. The technique takes advantage of the photoelectron process where the energy of the incoming photon is given by the Planck relation:

$$\boldsymbol{E} = \boldsymbol{h}\,\mathrm{n} \qquad (8)$$

Where *h* is Planck's constant (6.62×10^{-34} J s) and ν is the frequency of the radiation in hertz. The impinging photon is absorbed by a specific atom in a molecule or solid, leading to its ionization by the emission of an inner core level electron of that atom.

$$\mathbf{A_{(core)}} + \boldsymbol{h}\mathrm{n} \;\text{®}\; \mathbf{A_{(core)}^{+}} + \mathbf{e^{-}}$$

Because the core atomic orbitals of each atom requires a different energy to overcome atomic cohesive forces, the emitted photoelectrons will have kinetic energies based on the identity of the orbitals from which they came, and hence identifies the atom itself.

Usually the range of scanning energies is ca. 0 - 1250 eV or 0 - 1480 eV, depending on the radiation source used. The photoelectrons leaving the sample are collected and analyzed by kinetic energy. An XPS spectrum for a typical sample of ITO is shown in Figure 2.7. The figure shows the photoemission peaks that arise from the experiment allowing for the identification of atoms present within the sampling depth. ITO, when examined in this manner exhibits the presence of oxygen, indium, tin, and carbon atoms.

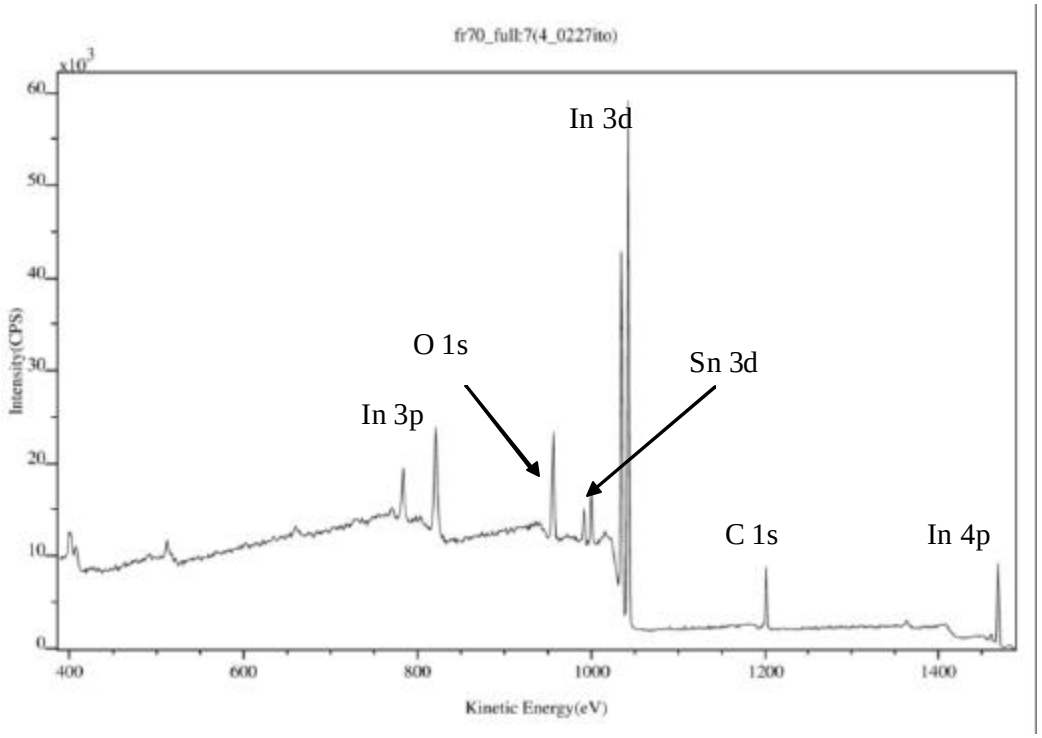

Figure 2.7 X-Ray Photoelectron Spectroscopy (XPS) spectrum of a typical ITO sample, obtained commercially (Colorado Concept Coatings, Longmont Co), after light solution cleaning. Atoms identified include In, O, Sn, and a substantial amount of carbon contamination.

It is also convenient to discuss photoemission events in terms of energy required to emit the electron (binding energy) and the following equation is commonly used for converting between the recorded electron kinetic energy and the binding energy, taking into account the work function of the spectrometer (Φ_W).

$$\mathbf{KE} = \boldsymbol{h}\nu - \mathbf{BE} - \Phi_W \qquad \mathbf{(9)}$$

The peak areas can also be used to determine the composition of the surface based on the intensities and area of each individual peak. In this manner, the relative composition of the sample (within the sampling depth) can be ascertained.

The exact binding energy of an electron depends not only upon the orbital level from which photoemission is occurring, but also upon ***i)*** the formal oxidation state of the atom and ***ii)*** the local chemical and physical environment the atom exists in. Changes in either of these conditions give rise to small shifts in the peak positions observed in a sample. Atoms of a higher positive oxidation state generally exhibit a higher binding energy due to the extra coulombic interactions between the emitted electron and the atomic core. The ability to discriminate between different oxidation states and chemical environments is one of the major strengths of the XPS technique used to study a TCO such as ITO. This aspect is demonstrated in Figure 2.8a. The figure depicts the oxygen 1s peak of a commercial ITO sample. The peak shape can be fit by assuming a minimum of 4 different chemical environments present for the oxygen atom. The number of components is generally justified based on the current understanding of the particular

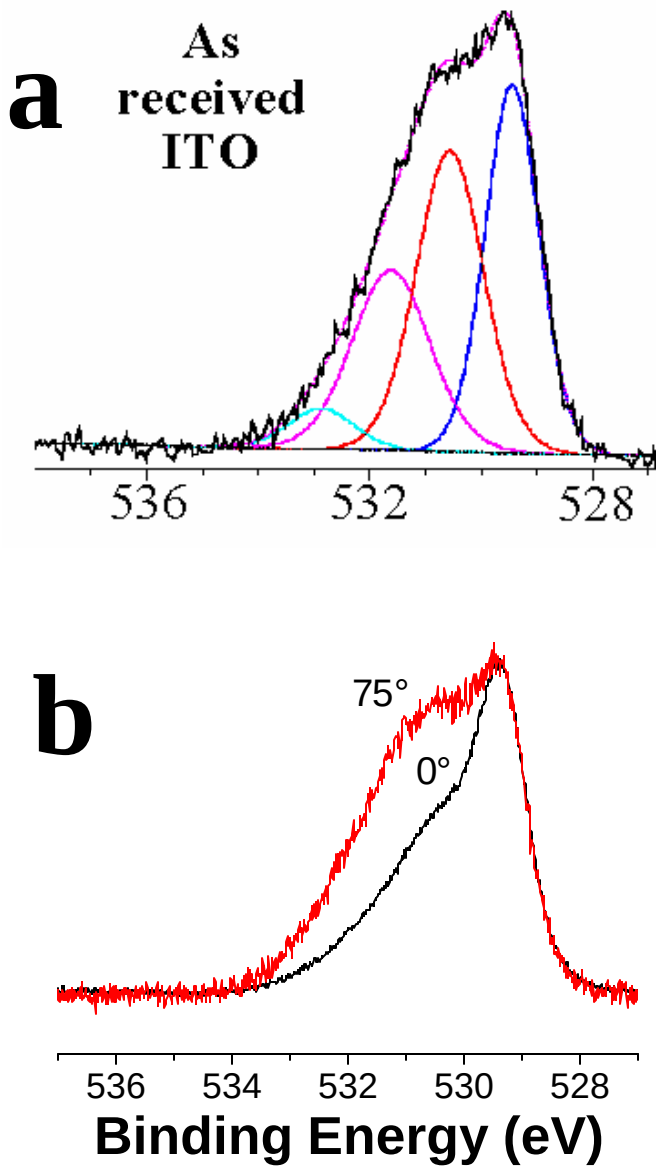

Figure 2.8 XPS results shown for the emission energy corresponding to the oxygen 1s orbitals. (a) shows the contribution of at least four separate oxidation states of oxygen in an ITO sample while (b) indicates the changing nature the sample at the near surface as resolved by high angle XPS (75° rotation of sample).

surface and is discriminately evaluated for its presence, or lack thereof. In this case, the oxygen component of the material is thought to consist mainly of native oxide material In_20_{3-x}, oxygen atoms adjacent to defect sites, a hydroxide of indium and/or the oxy-hydroxide and a fourth peak likely due to the other described defect sites, (SnO_2) or surface contamination elements (assignments and justification of these components are discussed below). Combining this information with the oxidation states of other atoms present as well as comparing observed emission energies against those of known samples enables accurate identification of the individual peaks present, and hence the surface moieties that contribute to the ITO surface. By accurately describing the atoms present in the near surface, a model of the surface can be developed and an understanding of how these surfaces may interact with adjacent organic materials in a thin layer device can be elucidated.

As already mentioned, XPS is inherently surface sensitive based on the relatively short inelastic mean free path, which for most samples averages to be ca. 2-5 nm in depth. The degree of surface sensitivity of an electron-based technique such as XPS may be varied by collecting photoelectrons emitted at different emission angles to the surface plane of the sample according to equation 10.

$$I = I_0 \exp(-d/\lambda \cos\theta) \qquad (10)$$

Where I represents the collected emission intensity, I_0 is the initial radiation intensity, d is the depth of sampling, λ is the inelastic mean free path, and θ is the angle of the sample with respect to the analyzer normal. This approach may be used to perform analysis of

the sample by indicating any variation of chemical state or composition with depth. The technique is especially useful for the study of TCOs with application to thin layer devices due to the coupling of the oxide surface with organic species where bulk conditions are not necessarily present. Figure 2.8b illustrates the use of the angle resolved experiment. In this case a sample of ITO is analyzed using the conventional XPS geometry and the emission spectrum is recorded (O 1s). During a subsequent experiment, the same sample is analyzed again with a 75° take off angle. The results when comparing the two oxygen emission peaks clearly indicate a differing chemical environment exists at the near surface of the sample than from the bulk of the lattice. In these studies it allows for the construction of a detailed surface model which extends the bulk lattice and describes how it terminates (detailed below).

2.4.3 Ultraviolet Photoelectron Spectroscopy

The use of other electron spectroscopies especially ultraviolet photoelectron spectroscopy (UPS) is very common in the study of TCOs. Typically, UPS is used to characterize properties such as effective workfunction, ionization potentials, and median orbital positions such as the HOMO or a nonspecific density of states. UPS is a traditional electron spectroscopy where the source of radiation is normally a noble gas discharge lamp, frequently a He-discharge lamp emitting He I radiation of energy 21.2 eV. This energy of radiation is only capable of ionizing electrons from valence levels of

most elements or molecules. Workfunction is normally calculated by comparing the width of electron emission energies with respect to the input radiation energy according to the equation:

$$F_{eff} = h\nu - w_F \qquad (11)$$

For molecular adsorbates, ionization potentials can be estimated from the kinetic energy of the leading edge (high kinetic energy cutoff) of the highest feature in the UPS spectrum, with respect to the Fermi energy, correcting for shifts in vacuum level, if necessary. HOMO energies are estimated from the median energy of the ionization peak of the highest band, again correcting for shifts in vacuum level, if necessary.

The workfunction of a material such as ITO has been shown to be altered by the chemisorption of a molecule with a specific interface dipole.[49,56] There are reports of "workfunction tuning" by the application of reactive moieties containing functional groups such as -COOH, -COCl, $-SO_2Cl$ and $-PO_2Cl_2$.[49] The large dipole introduced at the surface can change the effective workfunction of ITO and cause adjacent materials to experience a different electric field when coupled with ITO, an important aspect of the design and implementation of certain electrical devices such as OPVs.

In these systems, an adjustment of equilibrium vacuum levels occur when charge transfer events take place between the two species. It is important to understand when this type of behavior is occurring in order to be effective at predicting how ITO behaves, from an electronic point of view, when coupled with other molecules or thin films. Figure 2.9 shows the shift in the vacuum level of ITO after submersion in EtOH. In this case, the observed workfunction is increased by ca. 0.74eV

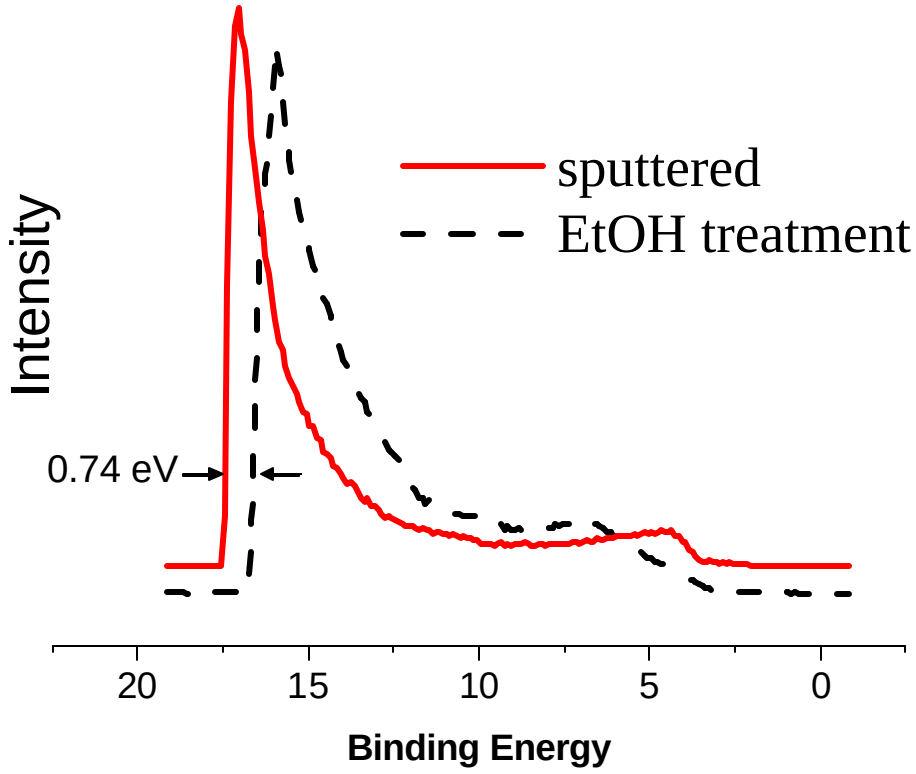

Figure 2.9 UPS spectrum of commercially available ITO samples. Argon sputtered samples which have been exposed to EtOH solutions in atmospherically controlled conditions show a 0.74eV shift in the apparent vacuum level. This suggests a build-up of hydroxide moieties on the electrode surface after solvent exposure.

Likely, immersion into a solvent containing trace amounts of water can change the surface chemistry of the ITO substantially, and is discussed fully in Chapter 3. However, this is not the case with all adsorbates. The size and nature of the shift seems to depend on many factors and traditionally it is difficult to predict these electronic interface properties from the bulk values. In any case, UPS is a valuable tool for observing this type or lack-of energy shift and determining what effects to expect from an ITO sample.

2.5 SURFACE COMPOSITION AND MODEL

X-ray photoelectron spectroscopy studies have been beneficial in elucidating the actual surface composition of ITO, extending the bulk and detailing how it terminates. Previous studies have documented at least two separate forms of oxygen atoms present on the surface of ITO. In addition, only one form in indium has routinely been observed[50-51] leading to simplistic understanding of the ITO surface. These studies have generally been made using a non-monochromatic Mg excitation radiation source that exhibits a radiation distribution width of ca. 0.7 eV. The implementation of a monochromatic Al radiation source, used in these studies, cuts the distribution peak nearly in half, down to ca. 0.4 eV. The difference in the radiation peak distributions has enabled much more detailed studies for the analysis of the types of atoms present in the surface structure of ITO. With this narrower source, there is now evidence for at least four separate forms of oxygen atoms, and at least two forms of both indium and tin atoms

which also need to be incorporated into the surface model described. This is reasonable, as it's likely that the terminus of the material would exhibit a different chemical state from the bulk lattice, which already known to exhibit at least two chemical environments for oxygen atoms.

In order to effectively construct a reasonable surface model of how ITO terminates, there needs to be a better understanding of which type atoms are present, and how many chemical states each of these atoms exist in. The type of atoms present in the bulk lattice of ITO has been previously investigated[36] and is thoroughly described above.

Utilizing angle resolved XPS techniques, the ITO terminus is known to consist predominantly of oxygen, with small amounts of indium and doping levels of tin. Carbon is also present and thought to be a constant contaminant that likely persists throughout the lattice. The chemical states of each type of atom comprising the surface chemistry of ITO can be identified by careful studies using XPS and incorporating monochromatic Al radiation. Figure 2.10 describes the basic method of utilizing the high resolution photoemission spectra of an ITO sample and identifying element peaks with respect to those of chosen standards, of which the chemical state of each atom is well known. Standards chosen for this study include those materials likely to exist in the sample such as: Indium metal, In_2O_3, "InOOH" electrochemically prepared as an intermediate between the oxide and the hydroxide species, and $In(OH)_3$. It should be noted that the exact composition of the "InOOH" intermediate is not precisely known in so much as the ratio of oxide like atoms to hydroxide-like atoms have yet to be determined. For this reason, the species is referred to in quotations.

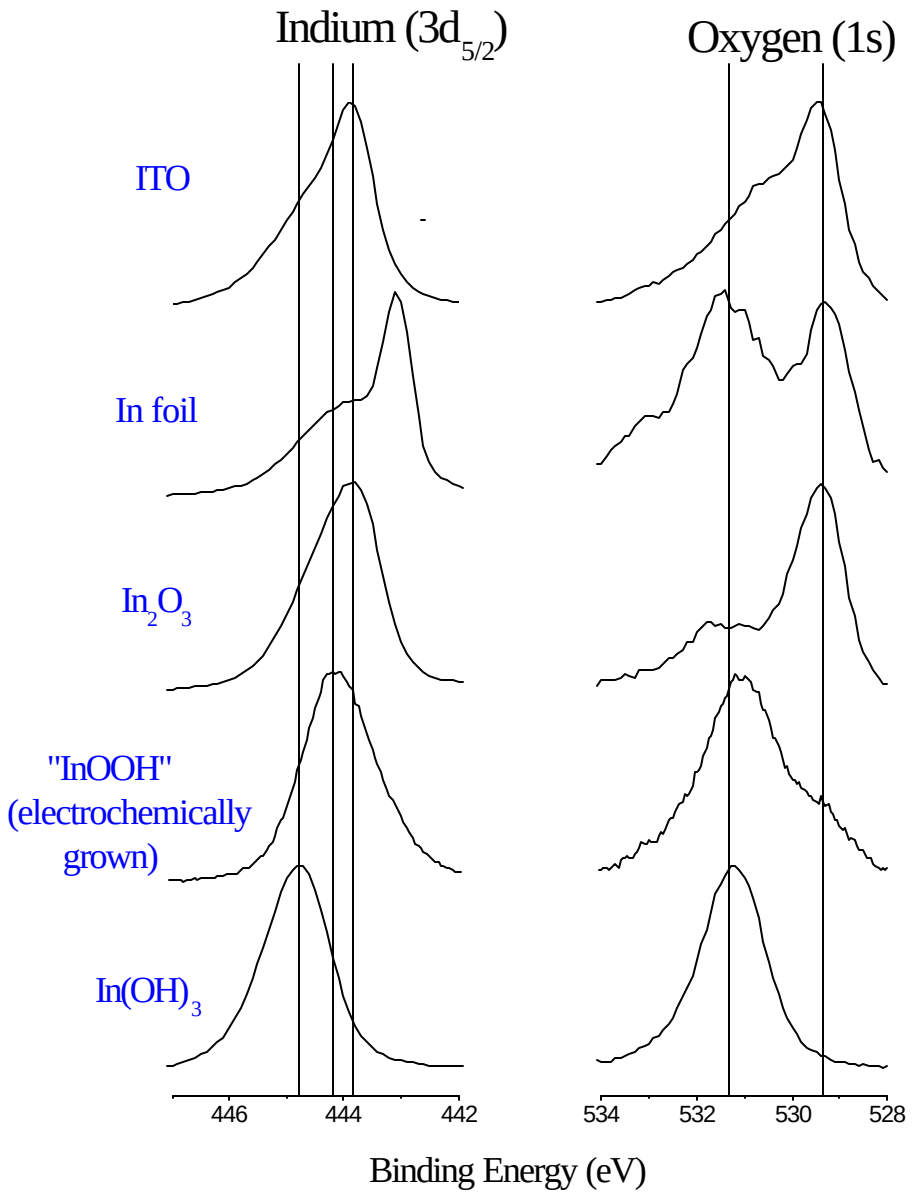

Figure 2.10 Elucidation of various oxidation states from the oxygen 1s and indium 3d orbitals of commercially available ITO. The emission spectra are identified by comparing the discrete binding energy positions with those of known standards.

The photoemission of each standard is carefully taken, and the resulting spectra are broken down into known compositional components by introducing an analysis where each oxidation state within the sample is assigned to a single component peak (70% Gaussian, 30% Lorenztian). For example, the O: 1s spectrum obtained for the In_2O_3 standard comprises one oxygen component that may be present in ITO, atoms in a similar chemical state (with respect to O: 1s orbitals of ITO), should then occur at similar binding energy. Once component species are found, they are assumed to occur at that energy and fixed for the duration of the analysis. Component states are then compared to the photoemission obtained for ITO samples, where the contribution is increased or lowered to obtain a "best-fit scenario," where the compilation of the component peaks match the resulting ITO sample spectrum. Those components that contribute in a significant manner to the overall fitted emission, can be taken as present in the ITO material, while those that do not match are discarded. In this way, each component can be identified as well as the extent of its total contribution.

The photoemission of the major atoms present in ITO is shown in Figure 2.11. Oxygen 1s peak analysis for these standards indicate at least four states of oxygen are present, as indicated in the figure. The major contributor is the natural oxide (In_2O_{3-X}) shown by component A. For component B, the binding energy shift for is too small for assignment to one of the hydroxide forms; therefore, given the density of oxygen vacancy defect sites in the lattice, it is not surprising to assign this component respectively. In the model described by Frank and Kostlin, oxygen atoms adjacent to these defect sites donate some electron density toward the indium atoms to help stabilize the structure as

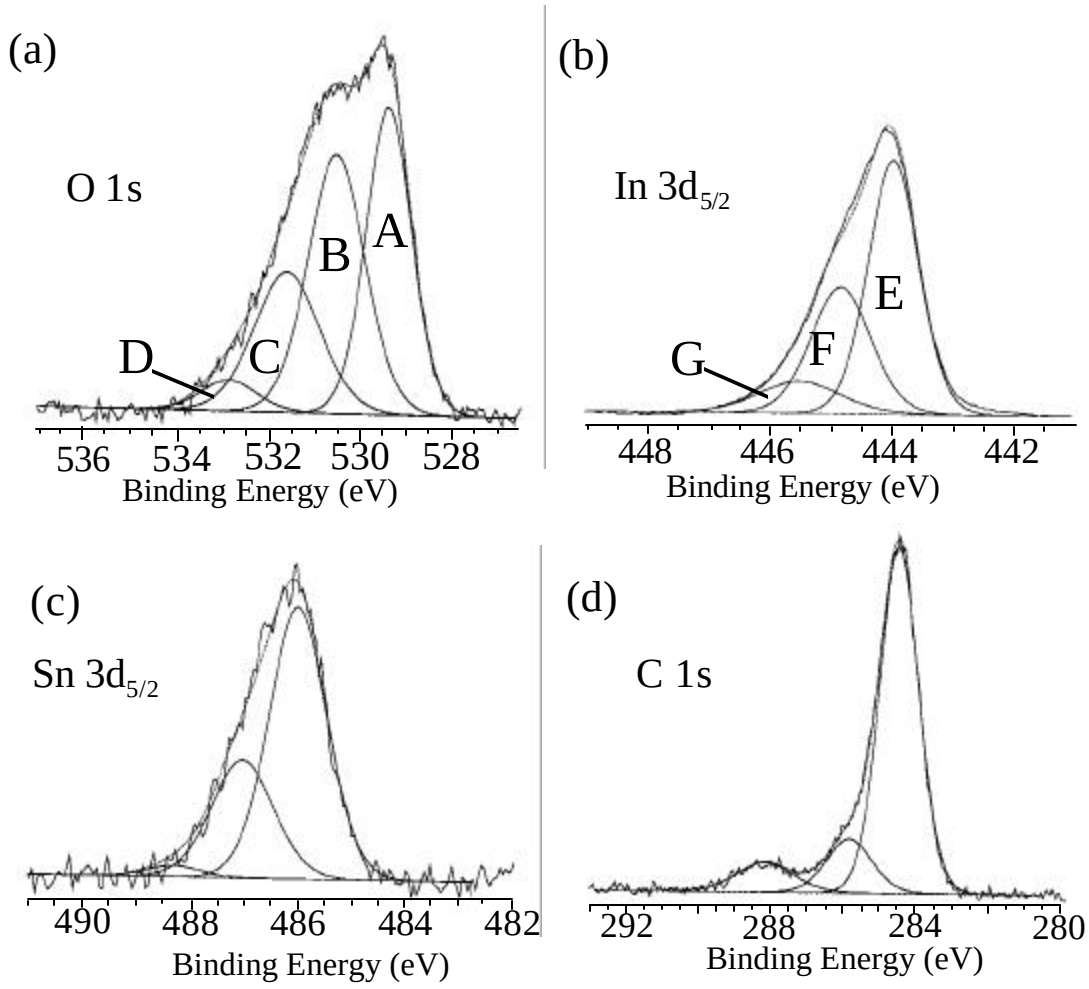

Figure 2.11 Assigning the number and character of oxidation states for each orbital (a) O 1s includes at least 4 different oxidation states corresponding to 'A' the In_2O_3 structure oxygen atoms, 'B' is oxygen sites that are adjacent to oxygen deficiency sites, 'C' hydroxide and or the oxy-hydroxide form while an additional component 'D' is interjected to improve the fitting of the O 1s peak and may be due to defects or contaminants. (b) In 3d contributes 3 states while (c) Sn 3d and (d) C 1s also show 3 oxidation states. Component height and width is subject to the oxidation states brought about by the pre-treatment used.

previously described. This donation of electron density creates the loosely bound cluster and appears to cause the O 1s peak to shift towards higher binding energies while stabilizing indium. Therefore, large chemical shifts in the In 3d spectra associated with these defects are not observed (see below). Component C can be correlated to the hydroxide and/or oxy-hydroxide as the binding energy shift works well for either standard. The last component, C can be attributed to those other defect sites described, or possible unknown contaminants.

The photoemission for indium $3d_{5/2}$ peaks (shown in Figure 2.11 b) indicate three distinct chemical states to coexist in the samples examined. These include: In_2O_3 (E), InOOH and/or $In(OH)_3$ as one entity (F), and a component that can be attributed to errors in peak fitting or a contaminant. In either case, it was not found to be significant. Indium peaks can also be fit with a metallic In^0 component on the low binding energy side, although the contribution is negligible in these studies. The Sn $3d_{5/2}$ peak is evaluated similar to the In $3d_{5/2}$ and is presumed to arise from similar entities, SnO_2 and Sn(OH)-like species along with a third unidentified component. C 1s photoemissions show evidence for three types of contamination present likely arising from alkane chain-like carbons, and carbon oxides.

By comparing the photoemission peaks arising from the given standards to those arising from ITO, it is clear that the majority of the ITO structure is made up of the oxide In_2O_{3-x}, however, the shoulder on the high binding energy side of the In $3d_{5/2}$ peak can be determined to consist mainly of the $In(OH)_3$ species. The O 1s photoemission data for the standards compared to the ITO sample indicate that both forms, the oxide and the

hydroxide, are present with agreement that the bulk of the structure is made up of the In_2O_3. The presence of "InOOH" can not be confirmed or ruled out exclusively on this data as the In $3d_{5/2}$ peak can be fit with, or without utilizing this position while peak fitting. However, it is probable that this moiety does exist to some extent in the regions surrounding defect sites terminating in the near surface.

Based on the results of this XPS work, a surface model of ITO can be constructed utilizing the observed chemical states of the atoms present and is shown in Figure 2.12. This model extends from the bulk crystal structure, which is represented by the oxide lattice in the lower part of the Figure. Some features of the bulk structure shown are the repeating oxide lattice, positions of tin doping, and the absence of oxygen atoms to create the structural defect sites. Other defect sites occur at low concentrations and are not pictured, but understood to exist. The lattice terminates in mostly the oxide form with occasional defect sites where the oxide is broken providing surface hydroxide groups. Also indicated by the model, an $In(OH)_x$-like species is abundantly present on the surface of ITO. There is some suggestion that this material does not exist as the single $In(OH)_3$ complex but rather a polymeric form with a lattice that extends throughout the surface and gives rise to both the hydroxide and oxy-hydroxide moieties.[61] Also, it's thought that this species is not covalently bonded into the ITO structure but due to its extremely low solubility ($K_{sp} = 10^{-37}$) remains chemisorbed to the surface despite any cleansing efforts.[62] It is likely that this hydroxide species arises from hydroxylation of the lattice in the presence of water.

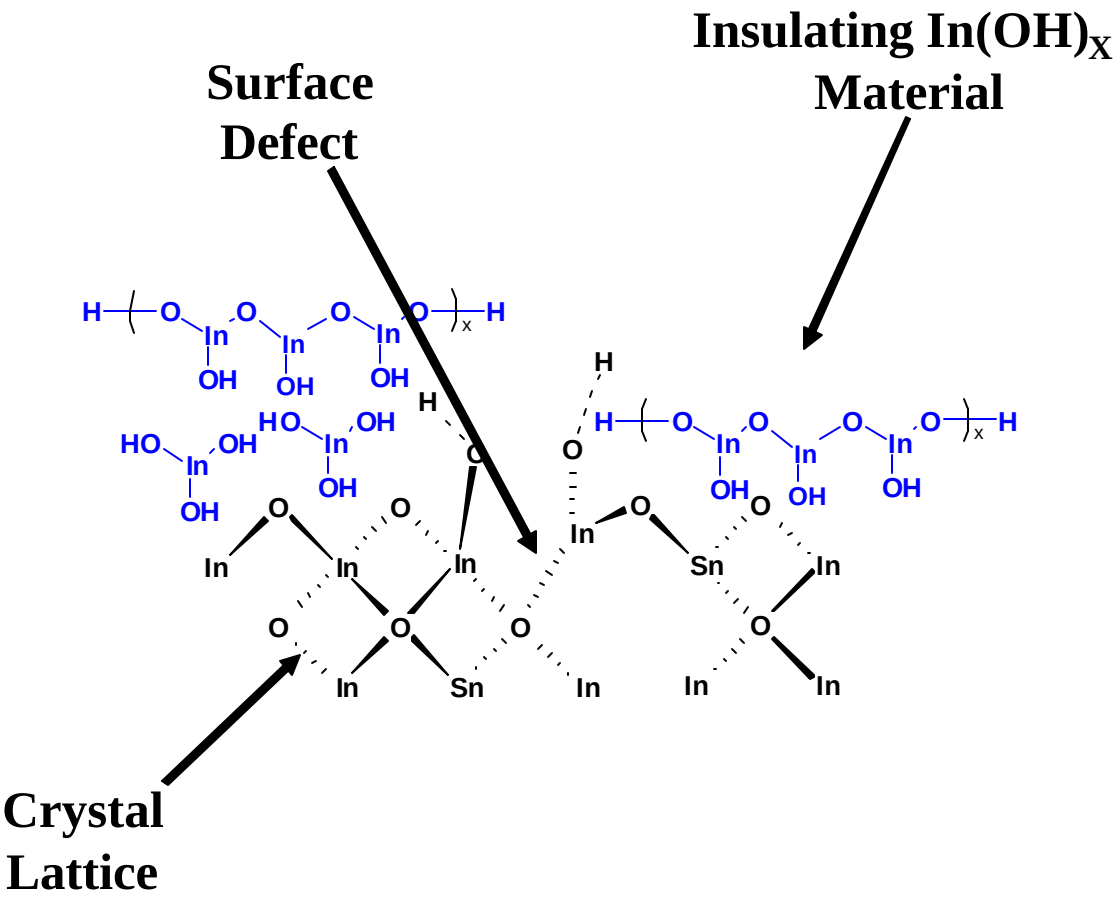

Figure 2.12 Proposed surface model of ITO concluded through assigning oxidation states in XPS studies. Bulk crystal lattice terminates as unbroken structure, with sites of defects leading to surface hydroxides and presumable where electrical activity occurs. Surface $In(OH)_x$ species, most likely the hydrolysis product of In_2O_3 and polymeric in form coverers a large portion (up to 75%) of the surface by it low solubility product.

$$In_2O_3 + XH_2O \longrightarrow 2In(OH)_X \qquad (12)$$

Other sources have attributed the formation of this species to the exposure of indium metal to water vapor upon film formation:[63]

$$2In_2 + 6H_2O \longrightarrow 2In(OH)_X + 3H_2 \qquad (13)$$

Regardless of the origin, the material has been found on every sample in copious amounts. Angle resolved XPS (Figure 2.8b), where tilting the sample during analysis increases the surface sensitivity, limits the detection of this material to the near surface region or the upper 2 nm. Other reports have also described the presence of this material and its origins associated with ITO materials.[64]

In summery, an ITO thin film consists of the bulk material, a bixbyite lattice that incorporates oxygen defect sites, Sn doping sites, and other minor defects in random distributions. Upon reaching the near surface, the lattice terminates in a combination of oxygen atoms in the oxide form, surface hydroxides where the lattice is broken, and the presence of $In(OH)_x$ material chemisorbed throughout the near surface region.

2.6 PRETREATMENT EFFECTS ON ITO SUBSTRATES

It has been reported that exposing ITO to certain treatments, have had dramatic effects on the chemical composition, the electrical properties and the optical properties of the sample. In fact, many strategies currently exist for “tuning” ITO for a desired purpose.[4,8-11] These range from solution or gas phase treatments in an attempt to control

work function values [8-11] to a reaction of organometallic species such as zirconium oxides or phenoxytin complexes to add specific surface functionalities[16-17]. Some previous studies have utilized photoelectron spectroscopies, including XPS and UPS, to follow changes in work function and surface composition which result when various cleaning treatments and pretreatment procedures are used on ITO. These include soaking the ITO in acid or base solutions[4, 8-11] a standard RCA cleaning solution treatment[4,11] and a wide variety of plasma treatments.[4,8,11,52] Unfortunately, many of these studies have focused entirely on changes in ITO work function, mainly for organic electronic device applications where anode work function is believed to be the most important factor to consider for a TCO.[8-11] Using high resolution XPS the changing surface composition, due to these treatments, may be elucidated.

A description of how the surface chemistry may change in response to a chemical environment is important in understanding ITO and potentially to determine the most constructive route in modification techniques in order to tailor the material to a desired use, or what would be the most beneficial chemistries for TCOs in general. The results described here are from pretreatments selected primarily due to the documented change in work function and/or the change in the amount of adsorption/covalent attachment of molecules to the ITO surface. These include "piranha" acid treatment, adapted from Wilson and Schiffrin[65] which consists of three steps: (1)heating the ITO in 10mM solutions of NaOH for 4 hours at 80º C, (2) soaking sampling in 4:1 H_2SO_4:H_2O_2 for 1 minute, and (3) heating the ITO to ca. 160º C for 2 hours; the RCA treatment, heating ITO samples in a 1:1:5 solution of NH_4OH:H_2O_2:H_2O for 30 minutes at 80º C followed

by thoroughly rinsing with water and drying in nitrogen; air plasma etching, where samples are placed under 60 watt plasma for 15 minutes; and vacuum sputtering under argon ions at 750eV for 45 minutes at $6.5x10^{-7}$ torr.

The change in chemical state of ITO samples was monitored by photoemission elemental peaks from XPS analysis which were subsequently fitted with the minimum amount of components that indicated a reasonable fit between the experimental data and the resulting fit. Peak position assignments were based off rational developed by the series of standards previously described. Once individual component peak positions were established, the position was fixed and only the heights of the component peaks were allowed to fluctuate during subsequent fitting. This insured a constant binding energy separation between each component in each fitting scheme. Additionally, the amount of change brought about by each treatment is based on an initial measurement of ITO described above and marked as received.

In the analysis of the as received ITO, the components of each peak can again be fit by the application previously described and shown in Figure 2.11. Results on the effects of pretreatments are illustrated in Figure 2.13 which shows the XPS photoemission spectra at 75° take off angle, before and after, with respect to each pretreatment selected. These results are also summarized in numerical form in Table 2.1. Only subtle differences were noticed in the In ($3d_{5/2}$) and Sn ($3d_{5/2}$) component peaks before and after each of the pretreatment procedures and are not shown. The most significant compositional changes were observed with the O (1s) peak shapes. Fitting

Sample	In: $3d_{5/2}$	O: 1s	Sn: $3d_{5/2}$
ITO	443.9 444.9 445.9	529.5 530.6 531.8	485.8 486.8 487.7
In^0	443.2	531.5 529.4	-
In_2O_3	443.8	529.5 531.4	-
"InOOH"	444.3	531.2 529.1	-
$In(OH)_3$	444.8	531.3	-
Heated $In(OH)_3$	444.9 444.3	531.6 529.8	-

Table 2.1 Emission energy values for the determined component peaks derived from each orbital. Samples include ITO and Related Indium Oxide/Hydroxide Standards for component determination.

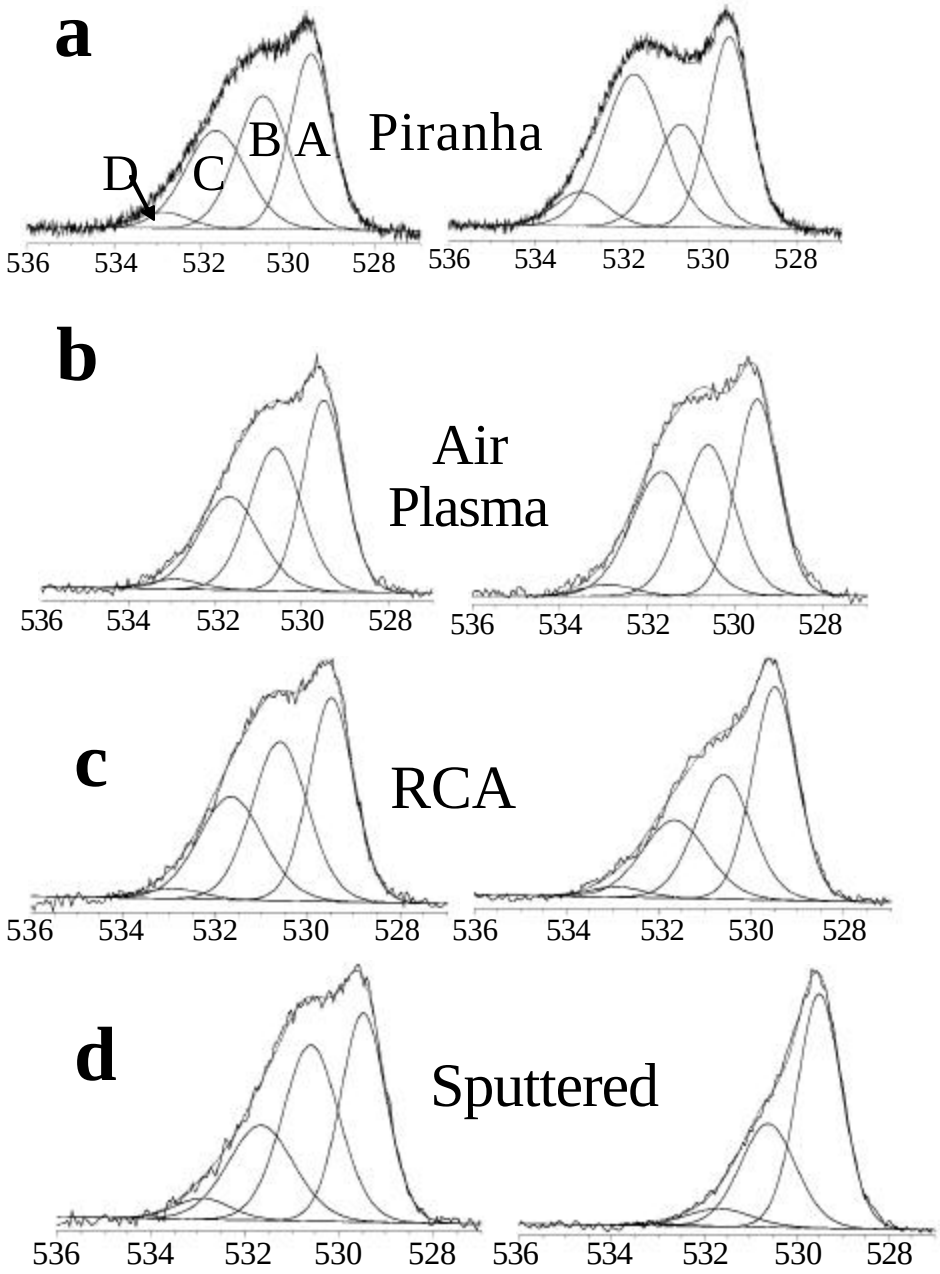

Figure 2.13 Effect of pretreatments on the O 1s orbital of ITO, shown as before and after for each sample. These include (a) Piranha treatment, (b) Air plasma etched, (c) RCA treatment, and (d) argon ion sputtered.

analysis shows that much of the changes are accredited to changes in components ‘B’ and ‘C’ as shown in Figure (2.13). Following the treatment procedure described for piranha etching, the oxygen component ‘C’ peak, the piranha treatment dramatically increases the relative surface hydroxide coverage on the sample. The air plasma etching also indicates a small increase in the surface hydroxide coverage. However, the RCA treatment results in a small decrease in this component as compared to the initial sample. Vacuum sputtered ITO shows a decrease in both ‘B’ and ‘C’ components indicating a lower coverage of hydroxide and defect sites. This seems to be consistent with removal of the uppermost layers of material and in an UHV environment where the surface that has yet to be reacted with any atmospheric moieties. Exposing these sputtered samples to atmospheric conditions for a short time e.g. 10 min followed by reexamination show the O (1s) components previously shown to decrease, have returned to the initial levels with hydroxide coverages approximately equivalent to those seen for the piranha treated samples.[66]

These studies suggest that the hydroxylation of In_2O_{3-x} can be enhanced by acidic conditions that exist in the piranha treatment as well as the air plasma procedure. This behavior has also been noted in the literature.[59,71] Basic treatments such as those encountered in the RCA treatment may help to remove surface hydroxide concentrations, perhaps by interacting with defect sites and deprotonating the hydroxide group where the oxygen is left to collapse back into the oxide structure. These studies show that the surface of ITO is very dynamic and further, can be changed based on the chemical environment a sample is exposed to.

While in these studies, the piranha treatment led to large amounts of surface hydroxide, this scenario would be poor from an electronic device point of view. The $In(OH)_x$ material is known to be an insulator an would lead to restrictions in charge injection (higher R_S) between electrode and adjacent organic. They do suggest, however, that searching for specific pretreatments or modification schemes is beneficial in the ability to alter the surface chemistry for maximal benefits either functional or electronic. Specifically, those techniques that target the removal, or greatly decrease the $In(OH)_x$ material coverage may lead to better electrode behavior.

2.7 REACTIVE SURFACE AREA

Despite its widespread use in existing and emerging technologies, ITO is still poorly understood, especially regarding how the surface chemistries affect its electrical properties. There has been some recent evidence that the surface conductivity of ITO is not entirely homogeneous. Work conducted by Liau and coworkers,[54] where the authors utilized a conductive tip AFM probe to map the surface conductivity of an ITO sample, clearly show an ITO surface conductivity that is patchy in nature where some areas have near zero conductivity and appear to be electronically dead while other areas conduct very well and are more electronically active. More recent work[72] has mapped the conductivity in a histogram fashion as shown in Figure 2.14. This Figure describes the

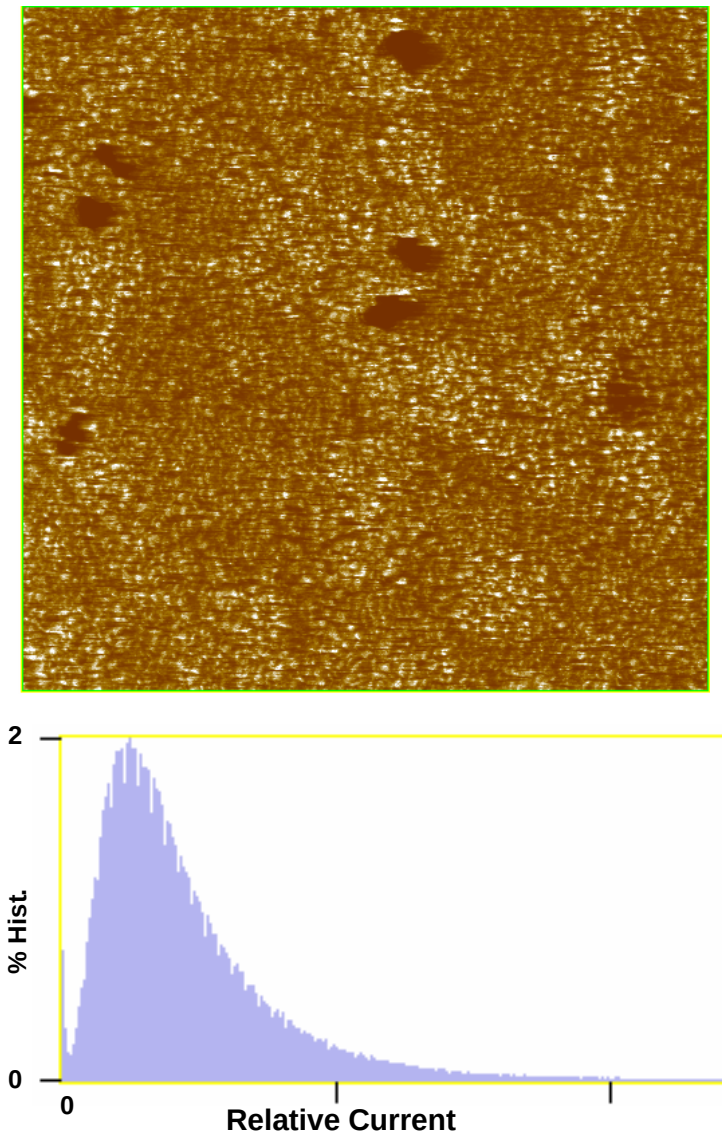

Figure 2.14 Conducting tip AFM (a) 2 x 2 µm image of an ITO sample showing the conductivity map with respect to surface position. It is clear ITO exhibits a heterogeneous surface consisting of highly conductive sites, and electrically dead sites. (b) Histogram of the current flow with respect to the above image. This illustrates the heterogeneity of the surface further and indicates the poor electrical behavior of ITO as more than 95% of the surface lies below the median current.

conductivity map of an ITO sample as a function of surface position. The image clearly indicates a distribution of activity across the sample (lighter regions being more conductive). When plotted in a histrogram form, nearly 95% of the surface lies below the median current (i.e. the current at exactly 50% of the maximum achieved), while a small portion of the surface lies outside the normal, expected distribution for activity. This portion is indicated by the high current tail and accounts for approximately 2% of the surface.

To further document this heterogeneity in electrical activity, other experiments[56] and previous work by Wrighton and coworkers[57] and Zotti and coworkers[58] show that a variety of molecules readily chemisorb to ITO surfaces. It has recently been shown that a ferrocene derivative, ferrocene dicarboxylic acid [$Fc(COOH)_2$], can chemisorb to ITO surfaces from polar solvents, presumably through hydrogen bonding interactions with the surface hydroxyl groups.[55] The adsorbed molecules can then be followed electrochemically, where the apparent molecular coverage can then be determined.

Combined with differing samples of pretreated ITO, these chemisorbed ferrocene-like molecules can show significant sensitivity to coverage with respect to the pretreatment conditions and hence, the surface chemistry present on an ITO sample. Figure 2.15 and Table 2.2 summarize the results of $Fc(COOH)_2$ on ITO samples as received and those prepared by the surface treatments described above. Typical $Fc(COOH)_2$ coverages range from 2.2×10^{-11} moles/cm^2 for the piranha treated ITO to 1.8×10^{-10} moles/cm^2 for the air plasma treated ITO. In either case, these results indicate somewhat less than the coverage expected[58] for a close packed monolayer of

$Fc(COOH)_2$, just 5% for piranha treated ITO and a maximum of 44% for the air plasma treated ITO.

Separate XPS studies of $Fc(COOH)_2$ chemisorption on high surface area, vacuum dried In_2O_3 powders, In_2O_3 powders and $In(OH)_3$ powders[59] clearly show that the concentration of adsorbed $Fc(COOH)_2$ scales with the relative hydroxide concentration available to those samples. However, this is not the case with ITO sample coverage determined electrochemically. The RCA pretreated ITO sample and the vacuum sputtered sample show nearly the same adsorbed $Fc(COOH)_2$ concentrations but the surface hydroxide concentrations are 20% and 8.5% respectively. Additionally, XPS based studies indicate a relatively constant intensity of Fe ($2p_{3/2}$) photoemission between all the ITO pretreatment samples indicating each sample should possess close to the expected compact monolayer. The less than expected $Fc(COOH)_2$ coverage determined electrochemically indicates that up to 95% of ITO's geometrical area may be unsuitable for charge transfer, depending on the pretreatment used. This magnitude of unusable area shows the severe limitations ITO may possess as an electrode.

These results suggest that hydroxide sites introduced into the ITO surface structure by means of surface pretreatments do not necessarily produce sites where the additionally bound $Fc(COOH)_2$ will be electrochemically active. It is thought that much of the increase in surface hydroxide is expressed as additional $In(OH)_x$ material confined to the surface. If this is the case, any additional $Fc(COOH)_2$ is expected to be electrochemically inactive due to the insulating nature of the hydroxide species. $In(OH)_3$

Pre-Treatment	Relative Hydroxide Concentration	Adsorbed Fc(COOH)2 mol/cm^2 (%ML)	Electron transfer rate (s^{-1})
As-received	25%	0.7 ± 0.3 (17%)	0.7 ± 0.2
Piranha	~38%	0.2 ± 0.1 (5%)	0.167 ± 0.006
Air Plasma	31%	1.8 ± 0.9 (44%)	0.7 ± 0.2
RCA	20%	1.3 ± 0.4 (32%)	0.8 ± 0.2

Table 2.2 Relative hydroxide concentration, concentration of adsorbed $Fc(COOH)_2$, and electron transfer rate as a function of pretreatment procedure.

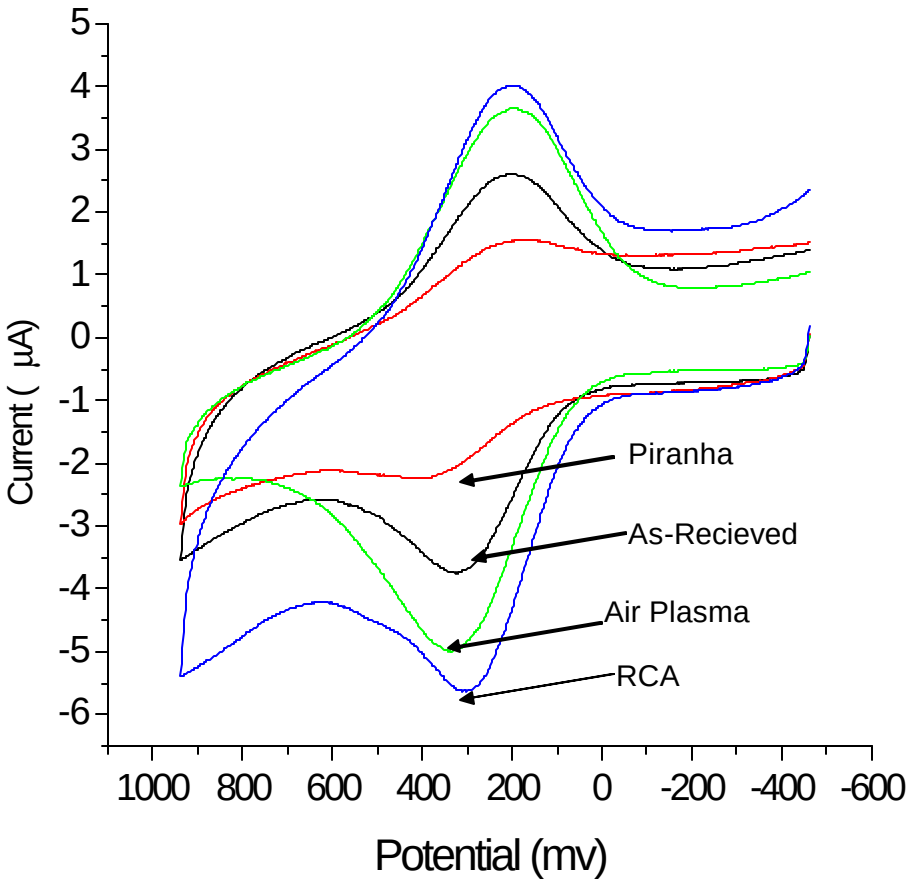

Figure 2.15 Cyclic voltammetry of adsorbed ferrocene dicarboxylic acid ($Fc(COOH)_2$) on pretreated samples of ITO. Piranha cleaned ITO indicated the lowest coverages 2.2 x 10^{-11} moles/cm^2 as well as the slowest electron transport kinetics 0.167 s^{-1} , while the plasma etched ITO shows the largest coverage 1.8 x 10^{-10} moles/cm^2 and the RCA treatment shows the fastest electron transfer kinetincs at 0.84 s^{-1} .

is a known insulator and any species absorbed directly to it would be isolated from the conductive surface of the ITO. In other words, high surface concentration of hydroxide may indeed lead to high concentrations of absorbed $Fc(COOH)_2$. However, these new sites for adsorption may be located in electrochemically dead regions, apparently increased by the creation of new $In(OH)_x$ material, resulting in a low measured degree of $Fc(COOH)_2$ adsorption (measured electrochemically). However, even if an excess of $In(OH)_x$ is responsible for increased electrode inactivity, the active electrode area of ITO is still bounded by an upper limitation. Examining the vacuum sputtered sample, the relative hydroxide concentration is the lowest at ca. 8.5% the calculated coverage of electroactive $Fc(COOH)_2$ is only 35%.

Unfortunately, electrochemical measurements cannot be conducted in a vacuum; and samples retrieved after sputtering are particularly reactive resulting in surfaces similar to the piranha treated samples after ca. 10 minutes. It is speculated that there are two issues governing the surface conductivity of ITO. Figure 2.12 illustrates these two possibilities which may arise to limit the surface conductivity of ITO. First, the presence of the insulating $In(OH)_x$ groups, cover large areas of the ITO surface creating a layer which isolates any adjacent molecules from transferring charge between ITO and itself. This could be especially true if the adsorbing molecule relies on hydrogen bonding to chemisorb to the sample, such as the case with $Fc(COOH)_2$. This would actually have the effect of drawing the adsorbate away from the ITO surface and fasten to the insulating $In(OH)_x$. Second, ITO must possess and rely on defect sites in the near surface in order to carry out charge transfer processes. This is shown as active sites in the figure and is

characterized by a break in the oxide lattice. $Fc(COOH)_2$ must come in close contact with an active site before charge transfer can occur. This possibility has merit due to conductivity of ITO is due to defect sites. This evaluation agrees with the electrochemical studies in which increased amounts of surface oxide decreased the measured amount of $Fc(COOH)_2$. Undoubtedly some pretreatments such as the piranha, encourage the addition of the insulating $In(OH)_x$ species which cover the surface defect sites and reduce observed conductivity toward adsorbed $Fc(COOH)_2$.

This type of behavior is not isolated to ITO, work conducted by Comninellis and coworkers[60] show a similar trend for the presence of active site populations using boron doped diamond electrodes that have been modified with active sites consisting of sp^3 hybridized carbon and is discussed below.

2.8 ELECTRON TRANSFER KINETICS

Rates of charge transfer can be determined by observing the electrochemistry of the chemisorbed ferrocene derivative $Fc(COOH)_2$. Electron transfer rates for this surface confined redox species can be calculated in the same manner as reported by Laviron.[68] Utilizing the typical cyclic voltammetry observed on ITO for a given pretreatment (Figure 2.15), calculated electron transfer rate constants can range from 0.167 s^{-1} for the piranha pretreatment samples to 0.84 s^{-1} for the RCA pretreatment. Estimated redox potentials, defined by the midpoint of the cyclic voltammogram varied from 0.22 volts to

0.34 volts vs. ferrocene/ferrocinium^{+} redox couple. It is thought that the apparent difference is due to heterogeneity in the sites available for chemisorption and the relative stability of $Fc(COOH)_2$ at these sites. As discussed above, electron transfer in ITO relies on an active site, presumably a near surface defect site. Hence, adsorbates near these active sites would require less overpotential for the redox event while distance from the site may require more overpotential to oxidize the species. Additionally, the presence of $In(OH)_x$ may decrease the site availability and further remove electroactive species from the active sites. Subsequent voltammetric scans produced votammograms which were typically smaller and narrower than the initial scans, and were ca. 20-25% of the original chemisorbed material, showing a slightly elevated electron transfer rate which seems to indicate the material loss is from sites furthest from the active sites.

The chemical state of the surface has a dramatic effect on the electron transfer rates as indicated by examining the samples undergoing pretreatments. Table 2.2 lists the electron transfer rates correlated with surface hydroxide concentrations found thorough XPS. Electron transfer rates seem to be inversely proportional to the amount of hydroxide on the sample surface. The sputter cleaned sample is disregarded for this evaluation due to the unknown surface conditions that exist after the sample is removed from vacuum. The pretreatment that gives rise to the largest surface concentration of relative hydroxide is the piranha acid etching with a relative hydroxide concentration of 40-50%. This type of surface also gives rise to the lowest calculated electron transfer rates at 0.17 s^{-1}. On the other hand, the surface with the smallest hydroxide coverage generated the fastest electron transfer rates at 0.8 s^{-1} with the others falling in between

these two extremes. This is further evidence that with ITO the finite number of active electron transfer sites become blocked by the formation of the insulating $In(OH)_x$ material during selected pretreatments.

There is precedence for this type of behavior in studies using boron doped diamond (BDD). Researchers Comninellis and coworkers[60] have clearly shown that electron transfer rates are directly tied to the number of accessible active sites on an electrode surface. BDD electrodes have a finite number of sp^3 hybridized carbon atoms, which in this case, act as active sites for the redox couple $Fe(CN)_6^{4-}/Fe(CN)_6^{3-}$. Using a procedure to increase the amount of sp^3 hybridized carbon atoms/active sites the observed voltammogram shows a significant increase in electron transfer rates as judged by the anodic/cathodic peak separation distances. Utilizing their technique to further increase the amount of active sites, the authors saw a further increase the electron transfer rates. To further illustrate this point, the authors were able to anodically strip active sites from the BDD electrode and observe the electron transfer rates plummet as indicated by a large increase in anodic/cathodic peak separation. This seems to a similar situation that arises with ITO electron transfer rates. Initially, ITO exhibits a moderate kinetic behavior with respect to the absorbed $Fc(COOH)_2$. However, following pretreatment processing which increases the amount of $In(OH)_x$ observed, the material covers a population of the surface active sites restricting the sites available for electron transfer. The result of this, is the decrease in the observed electron transfer rates suggesting a blocking of the active sites available on the ITO surface.

2.9 CONCLUSIONS

The heterogeneity of surface chemistries found on ITO samples is substantial. It is clear that reactivity of defects in the oxide structure, the quality of the vacuum system used to produce the ITO film, and the type of laboratory ambient the oxide surface sees when first removed from the ITO fabrication chamber, play a critical role in determining surface composition and reactivity. However, ITO remains dynamic in its compositional form which can be changed by a variety of conditions. Through careful XPS studies and component analysis, a working model of how ITO the lattice terminates can be constructed. This model can be used to ascribe various properties of ITO and elucidate how it may behave in an electronic device setting. Additionally, this model is used to help describe charge injection of the electrode and the limitations thereof.

It has been found that simple solution treatments (Piranha and RCA) and plasma etching procedures; which have been developed by a number of research groups to increase work the function, decrease contaminant levels, and enhance overall performance of ITO and related TCO anode surfaces, have been shown to substantially change the ITO surface chemistry, and depending on the treatment undergone, detrimentally impact the electrode. Upon closer inspection, some treatments can lead to the hydrolysis of the ITO surface which can contribute to a significant amount of $In(OH)_x$ like material being present on the electrode. This material is known to be insulating and may lead to an overall decrease in the observed electrical activity. This hydrolysis product is presumed to cover a population of ITO's active sites available for electron

transfer, rendering them inaccessible to normal redox events. This limitation is expressed in kinetic studies of adsorbed probes on ITO showing an inverse relationship between the amount of $In(OH)_x$ material on the surface and the electron transfer rate constant. The behavior is similar to boron doped diamond in which active sites can be added or removed from the material and show a corresponding increase or decrease in the electron transfer rate respectively. Additionally, current treatments where $In(OH)_x$ is expected to decrease still show substantial amounts of the product leading to an upper limit of observed activity. However, surface histograms indicate small population of very active sites exist throughout the sample. Presumably, these represent the active sites which are unhindered by $In(OH)_x$. This is encouraging as specific modification of the surface may expose a greater number of these sites, substantially increasing the electrode activity.

Clearly, with the use of the developed surface model, a procedure for the pretreatment of ITO that addresses the limitations described is needed. Ideally, this procedure may influence ITO in two ways. ***i)*** increase the electrically active site population of ITO by creating more surface defects ***ii)*** reduce the amount of the hydrolysis product on the surface to expose more ITO active sites making them available for charge transfer.

CHAPTER 3

ITO ELECTRODE MODIFICATIONS AND CHARGE TRANSFER

3.1 INTRODUCTION

The use of ITO as the anode in OLEDs and OPVs still presents a number of challenges in the development of these new technologies. This has inspired a number of studies which investigate possible improvement of these "less than ideal" TCO surfaces with respect to organic thin-film devices.[1-36] A majority of these studies include pretreatments and cleaning techniques, direct chemical modifications of the ITO surface, and covering of the surface with various conducting polymer thin films. Generally these modification efforts have been designed to alter the morphology of the surface, increase the effective work function of the ITO film, and increase its wettability by non-polar organic layers[2-8,15,18,20,27-31] to enhance device properties.

Many of these strategies also seek to add a molecular or polymeric component to the electrode.[5,9,13,26,29-37] The most commonly used of these strategies involves several steps: detergent and solvent based cleaning, followed by oxygen- or air-plasma etching, and spin casting and annealing of a thin layer of conductive polymer prior to the completion of the OLED or OPV device architecture. The most widely used of these conducting polymer layers is the proprietary material PEDOT:PSS (trade name Baytron P, H.C. Starck Inc.), which is a polyelectrolyte consisting of oligomers of poly(3,4-diethoxy-thiophene) and higher molecular weight strands of poly(styrene-sulfonate),

although other blends are being introduced.[37] Devices utilizing this film generally show higher current flow under forward bias, and lower leakage currents under reverse bias versus devices built on ITO alone. However, there is still considerable speculation why ITO electrodes utilizing this PEDOT:PSS overlayer exhibit the favorable charge injection properties they do. PEDOT:PSS is thought to mainly planarize the ITO surface and make it slightly hydrophobic in order to enhance its interaction with organic thin films. Its use, however, may be problematic in that its ionic composition can be difficult to control, and PEDOT:PSS presents a somewhat acidic microenvironment to the ITO/CP interface, leading to in-situ etching of the ITO material.[38-44] The aqueous dispersion of PEDOT:PSS used for device processing is quite acidic due to the high loading of PSS in its acidic form. In the presence of water, PSS may dissociate, attacking ITO and etching the material.

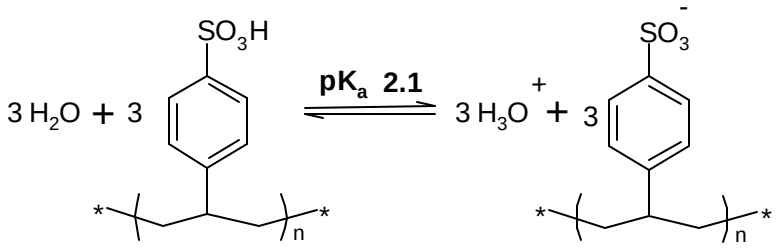

(1)

$$3H_3O^+ + In(OH)_3 \rightleftharpoons In^{3+} + 6\ H_2O \qquad (2)$$

This etching process has led to the migration of indium atoms into the adjacent organic layers which results in declining device efficiency by contaminating the organic material.

Moreover, the material does not wet organic substrates without high loadings of binders or complex formulation. Unfortunately, this causes a decrease in the conductivity of the resulting film limiting the acceptable thickness.

Other modifications of the ITO material are known to affect device operation and performance in a positive manner, and have been recently correlated with changes in the ITO surface chemistry.[1,2,4,14-20,25,30,31] This includes several solution based cleaning procedures such as plasma etching (air and oxygen), RCA treatments comprised of heating the ITO in a 1:1:5 solution of NH_4OH : H_2O_2 : H_2O for 30 minutes at 80°C, and piranha etched ITO which consists of three steps: (1) heating the ITO in a 10 mM solution of NaOH for 4 hours at 80°C, (2) soaking the ITO in piranha (4:1 H_2SO_4: H_2O_2) for 1 minute, and (3) heating the ITO to ca. 160°C for 2 hours. A less obvious modification, which has already been discussed, includes small carboxylic acid-based redox probes, such as ferrocene dicarboxylic acid ($Fc(COOH)_2$), which have the ability to chemisorb to the ITO surface from polar solvents such as ethanol. The carboxylic acid functionalities are believed to adsorb to oxide surfaces, such as ITO, through electrostatic and/or hydrogen bonding interactions or by the formation of coordination complexes to form a stable adsorbed layer.[45-46] It follows that simple chemisorption of these small molecules can be used to create a molecular component at the electrode surface whose polarity and redox properties are easily controlled.

Alternatively, modification methods can be applied together. For example, both the surface coverage (determined voltammetrically in a less polar solvent like acetonitrile) and the rate of oxidation/reduction of adsorbed $Fc(COOH)_2$ have been

shown to be sensitive to solution based pre-treatment and cleaning procedures used to prepare the ITO electrode.[1,2,14-16,19,20,25,30] The purpose of this chapter is to ascertain the effect these modification strategies may have on electron transfer dynamics, and the likelihood they may lead to positive enhancements when utilized in the construction of organic thin-layer devices.

3.2 CHARGE TRANSFER KINETICS

In order to effectively ascertain if these modification strategies will have any influence on a completed device, the development of a method which isolates each component of the total observed charge transfer rate in the device is essential. Currently, studies interested with interfacial charge injection processes in OLEDs and OPVs utilize measurements based on completed thin-layer devices and project results back to the interfacial properties, typically neglecting other factors which may contribute to the measurements. This approach is problematic in that many factors ultimately combine to give rise to the total observed charge injection. Interface chemistries are complex and there is currently no way to assign observed current to a particular factor from device measurements alone. Therefore, in order to accurately describe the effects of a particular modification process, testing must be conducted in such a way that components such as electron transfer kinetics, wettability, material impurity, complementary electrode effects, and device geometry can be measured independently.

It is widely assumed that charge transfer events that occur in these types of thin-film devices undergo outer-sphere-like electron transfer, in which no appreciable adsorption occurs before charge transfer can progress. It is also understood that after a modification process is completed, the modifiers are incorporated as part of the electrode and do not change the fundamental charge transfer mechanism. If this premise is true, a simple outersphere redox probe in a solution electrochemical environment, such as the ferrocene/ferrocinium (Fc/Fc^+) redox couple, should be able to probe the surface of the electrode and provide information on electrode charge injection. Fc/Fc^+ was chosen as a probe based on its well behaved electrochemistry, its current use as a standard in many electroanalytical processes, and the fact it is believed to undergo outersphere electron transfer with most electrodes.

This use of a solution redox couple is advantageous in that it eliminates many of the components that are variable when characterizing the device as a whole. Rate information can be extracted by examining probe molecules directly on the (modified) electrode through solution electrochemistry as outlined by Nicholson *et al.* [47,55] according to Equation 3 and shown in Figure 3.1.

$$y = \frac{\left(\frac{D_o}{D_R}\right)^{\frac{a}{2}} k_{et}}{\left(p D_O \frac{nF}{Rt} v\right)^{\frac{1}{2}}} \qquad (3)$$

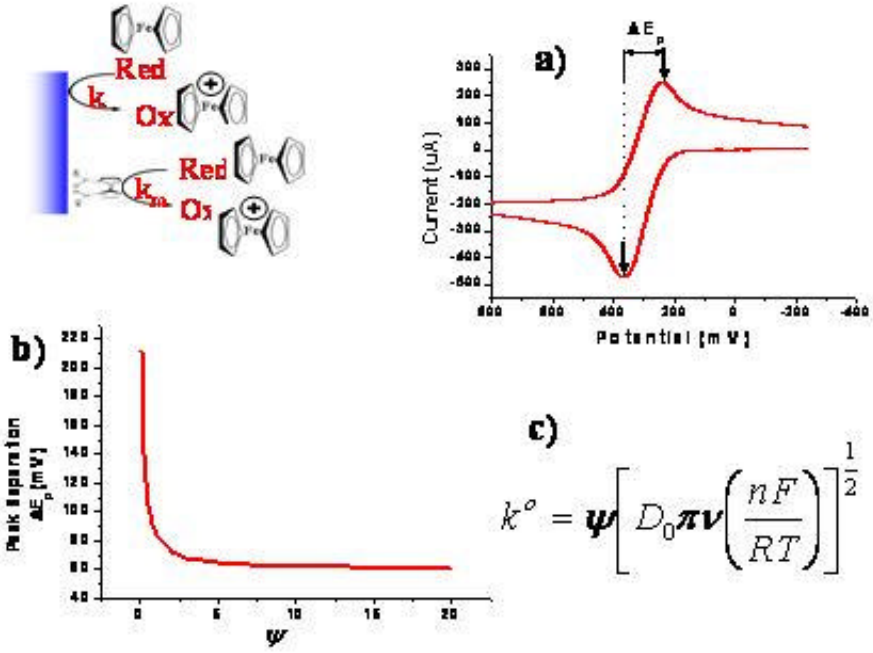

Figure 3.1 Nicholson treatment for the voltammetric response of a ferrocene probe molecule on an ITO surface, utilizing the difference in cathodic/anodic peak separations (ΔE_p) to estimate the effective electron transfer rate coefficient. (a) Anodic/cathodic peak separations are measured at a series of given sweeprates, and (b) compared with numerical solutions relating ΔE_p to ψ. The corresponding rate coefficient can then be estimated from the equation (c).

Where D_O, D_R correspond to the diffusion constants for the probe in the oxidized and reduced form respectively, α is the charge transfer coefficient, n is the scan rate of the potential wave, and k_{et} is the electron transfer rate coefficient. The method described by Nicholson offers a convenient way to estimate the electron transfer rate coefficient for these types of systems. A typical cyclic voltammogram for Fc/Fc^+ is observed in Figure 3.1a. The wave shape and separation of the of the cathodic/anodic peak potentials are functions of several variables, including the rate coefficient (k_{et}). Values of k_{et} can be extracted using numerical solution methods which create a relation between the difference in cathodic and anodic peak positions $\Delta E_p = (E_{p,a}-E_{p,c})$ and the term y (Figure 3.1b) assuming semi-infinite linear diffusion conditions. Estimates of k_{et} extracted from ΔE_p values at several different sweeprates, can give rise to a realistic average value for k_{et}.

Variations in k_{et} with electrode material can be demonstrated by comparing the voltammetry of Fc/Fc^+ on as-recieved ITO verses a more common electrode material, such as platinum. Figure 3.2, shows the solution cyclic wave voltammetry of Fc/Fc^+ on both surfaces, normalized for electrode area. Observing each voltammogram, the resulting waves are dramatically different. The ITO sample shows broad anodic and cathodic peaks with large overpotentials giving rise to a ΔE_p of ca. 365 mV at 0.01 V s^{-1} which corresponds to an estimated k_{et} value of ca. 6.0×10^{-4} cm s^{-1}. However, the voltammetry for the Pt electrode shows ca. 40% increase in the normalized peak current, and a more sharply defined reversible system with a peak potential difference of only ca. 98 mV at the same sweep rate, corresponding to a k_{et} value of ca. 7.0×10^{-1} cm s^{-1}, a

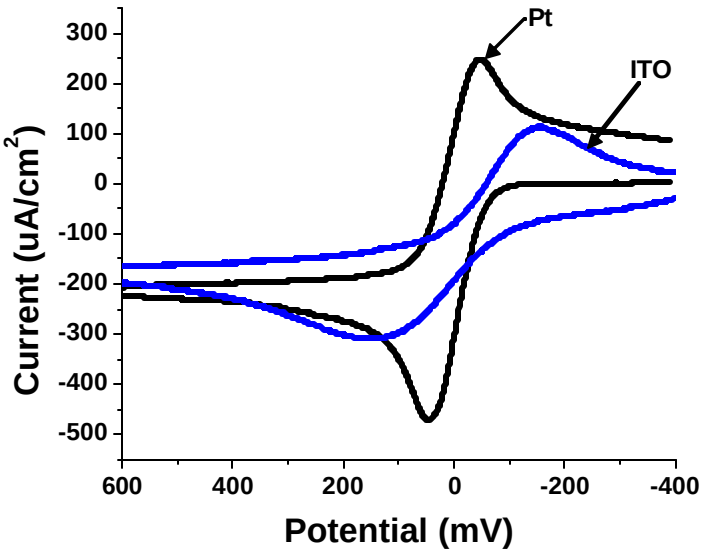

Figure 3.2 Voltammetric characterization of two different electrode materials, Pt and ITO, using ferrocene/ferrocenium as a redox probe. The ITO sample shows broad anodic and cathodic peaks with large overpotentials giving rise to a ΔEp of 368 mV at 0.01V/s, which corresponds to an estimated k_{et} value of ca. 6.0×10^{-4} s^{-1}. The voltammetry for the Pt electrode shows a more reversible system with peak a difference of ca. 98 mV, corresponding to a k_{et} value of ca. 7.0×10^{-2} s^{-1}.

difference of nearly three orders of magnitude between the ITO and Pt electrodes. Other common electrode materials (gold, carbon) give electron transfer rates[48] similar to that of Pt, between ca. 0.1 and 10 cm s^{-1}.

The apparent difference in electrode behavior shown by the Fc/Fc^{+} probe on ITO vs. Pt, prompted the use of another probe to verify the apparent poor kinetic behavior of ITO. N,N'-Diphenyl-N,N'-bis(3-methylphenyl)-1,1'-diphenyl-4,4'-diamine (TPD) was chosen because of its extensive use in organic electronic devices, and its well known electrochemical behavior.[56] The results of this comparison can be viewed in Figure 3.3. This figure shows the voltammetric response of TPD on clean ITO versus a Pt electrode (normalized for the same area). The voltammogram for TPD on ITO again demonstrates a large overpotential at the first oxidation peak and substantially lower currents (ca. 43%) with respect to the Pt, and corresponds with an apparent difference of the effective k_{et} (first oxidation step) from 6.1 x 10^{-2} cm s^{-1} for TPD on Pt to 0.25 x 10^{-4} cm s^{-1} for the TPD on ITO.

The apparent difference in the measured electron transfer properties when using ITO vs. other electrode materials is substantial. Normalized current flow is greater with traditional electrode materials indicating the resistive nature of ITO, also assuming the redox process proceeds via an outersphere electron transfer, the intrinsic electron transfer rate coefficient is not changed by switching electrodes. One possible explanation for the observed difference is that much of the surface of the ITO is not electrically active with respect to the solution probe, a characteristic that likely carries over to solid state devices. This characteristic is not uncommon with the use of exotic electrode surfaces, and other

cases have been thoroughly documented in the literature.[49-52] Assuming ITO can be modeled as a partially blocked electrode, which is reasonable given the amount of insulating $In(OH)_x$ found on the surface, the fraction of surface area covered by an insulating material can be calculated according to Equation 4.

$$k_{eff} = k^{\circ}(1-q) \qquad (4)$$

Where k_{eff} represents the electron transfer rate coefficient calculated for the blocked electrode, i.e. the rate constant found for the Fc/Fc^+ redox couple on ITO surfaces, and $k°$ represents the intrinsic homogenous electron transfer rate constant for the unimpeded redox reaction. i.e. the rate constant found on unblocked electrodes such as Pt. Using the values previously determined, the fraction of the surface of ITO blocked (or inactive) accounts for more than 99% the total surface area. i.e. the currents generated in Figure 3.2 on ITO arise from ca. 1% of the geometric electrode area.

The substantial inactive area of ITO, combined with the heterogeneous nature of the surface, clearly demonstrate some of the challenges when using ITO as an electrode material, especially where high current densities are needed. Such a small active area may be adequate for applications where only minimal current densities are needed (e.g. potentiometric sensors), however in applications where large current densities are needed (OPVs, OLEDs, etc…) the active area is insufficient and may lead to substantial problems with ITO use, including joule heating and imbalanced device charge injection. ITO, however, still represents the "best" TCO available and its use in applications where photons must be coupled in/out of the adjacent organic films is unavoidable.

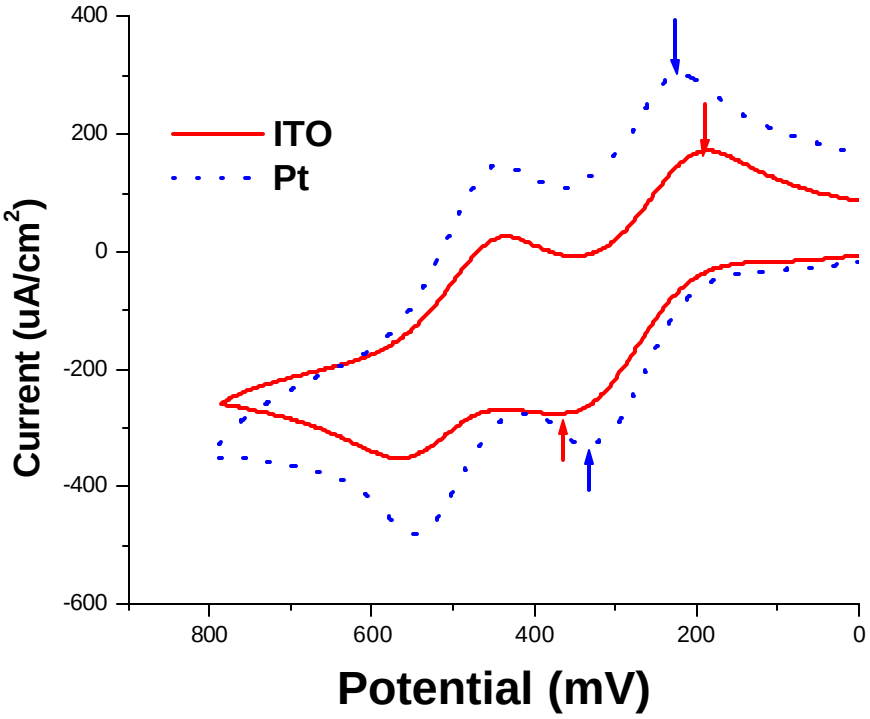

Figure 3.3 Voltammetric characterization of two different electrode materials, Pt and ITO, using TPD/TPD$^+$ as a redox probe. The ITO sample shows broad anodic and cathodic peaks with large overpotentials, which corresponds to an estimated k_{et} value of ca. 0.25 x 10^{-4} cm s^{-1}. The voltammetry for the Pt electrode shows a more reversible system with smaller peak separations, corresponding to estimated k_{et} value of ca. 6.1 x 10^{-2} cm s^{-1}.

The use of ITO as an electrode is also complicated by the heterogeneous nature of the material. This is not only true microscopically as previously discussed, but also on an individual sample level. Studies have shown that calculated rate constants can differ up to an order of magnitude on samples from different suppliers, samples from the same supplier but different batch numbers, and even between individual sheets of the same batch numbers. It is likely that the amount of inactive surface material, presumably polymeric $In(OH)_x$ and carbonaceous material, forms at different rates depending on the surrounding environments. Some studies have shown that freshly sputtered ITO samples exhibit low levels of these materials while certain cleaning agents enhance the amount of material found on the surface.[1,2, 14,16, 19-20, 25,30] It is therefore very important to select ITO samples carefully, from the same sheet in adjacent placements, with similar optical properties (reflectivities) in order to minimize variation in measurements due to the sample's homogeneity alone.

3.3 SMALL MOLECULE MODIFICATION

The surface composition of ITO can be influenced by a variety of methods. In particular, the type and nature of cleaning agents exposed to the surface can dramatically change the composition. To this end, the method described above can be applied to ITO samples which correspond to solution based modifications known to induce changes in the ITO surface chemistries. These include air plasma etching (Harrick plasma cleaner

Model PDC-32G, 60 watts for 15 minutes), RCA treatment, and piranha etched ITO with respect to as-recieved ITO surfaces. Figure 3.4 shows the resulting voltammetric characterization using Fc/Fc^+ as a redox probe on each of these samples. All samples show a broad voltammetric response with wide peak separations at 0.015 V/s scan rate. Solvent cleaned ITO (not pictured) and piranha treated samples were nearly identical and had the widest peak separations at ca. 330mV while the air plasma etched sample had $?E_p$ value of 272 mV and the RCA treated sample had the smallest $?E_p$ at ca. 214 mV. These values correspond to calculated electron transfer rate coefficients of ca. 7.8×10^{-4} cm s^{-1}, 8.2×10^{-4} cm s^{-1} and 9.4×10^{-4} cm s^{-1} respectively, showing a small increase in the rate coefficient for the RCA exposed sample while the piranha etched sample displayed the lowest rate coefficient. This complements previous studies[1,30] conducted with the adsorbed probe molecule $Fc(COOH)_2$, which shows the same general trend in rate constants with respect to surface conditions. Similar arguments to these studies can be made here for the difference in the apparent electron transfer rate coefficients observed. The piranha treated sample was shown to have the highest loading of $In(OH)_x$ material through XPS studies, and corresponds to the lowest electron transfer rate coefficient. Likewise, the RCA treated sample had the lowest loading of material and corresponds to the highest electron transfer rates. This suggests that the loading of the $In(OH)_x$ material plays an integral role in charge injection processes and must be minimized for enhanced electrode function (discussed below). Even though k_{eff} shows a small increase for some of

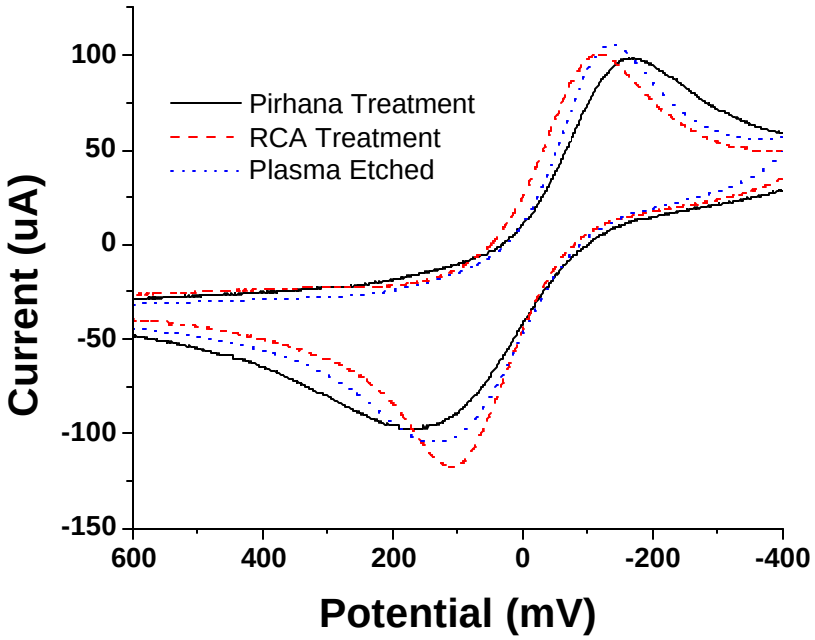

Figure 3.4 Resulting voltammetric ferrocene/ferrocenium characterization waves of ITO pretreatments at .015 V/s. Pretreatments include: air plasma etching, RCA treatment, and piranha etching corresponding to calculated *ket* values of 7.8 x 10^{-4} cm s^{-1}, 8.2x10^{-4} cm s^{-1} and 9.4x10^{-4} cm s^{-1} respectively. This compliments the trend found with rate studies of adsorbed $Fc(COOH)_2$.

these pretreatments, the fraction of blocked area remains high. Initially, more than 99% of the surface (as-received ITO) is thought to be blocked or inactive. Pretreatments described here decrease this blockage by only ca. 0.2% suggesting that the bulk of the current is carried by less than 2% of the total surface area.

3.3.1 *Surface Modification*

It has already been shown that carboxylic acid-based small molecules such as $Fc(COOH)_2$ readily chemisorb to oxide surfaces, and have been previously used as surface probes to follow the electrochemical activity of ITO electrodes. An extension of this philosophy is to utilize the probe molecule directly as the modifying entity, along with other carboxylic-acid based small molecules. The modifiers described here include a variety of acid functionalized molecules including: ferrocene dicarboxylic acid, ($Fc(COOH)_2$) **[1]**; a modified version of the hole transport agent, TPD (4,4'-Bis(*m*-tolylphenamino)biphenyl) functionalized with two *para*-methoxy substituents and two six-carbon alkoxy side chains, terminated in carboxylic acids (6-{4-[{4'-[[4-(5-Carboxy-pentyloxy)-phenyl]-(4-methoxy-phenyl)-amino]-biphenyl-4-yl}-(4-methoxy-phenyl)-amino]-phenoxy}-hexanoic acid, ($(p\text{-}OMe)_2$-TPD-X_2) **[2];** 3-thiophene acetic acid, (3-TAA) **[3]**; a hexa-carboxylic acid derivative of hexabenzocoronene, (HBC-$(C_3COOH)_6$) **[4]**; all shown schematically in Figure 3.5. $Fc(COOH)_2$ was selected because of the

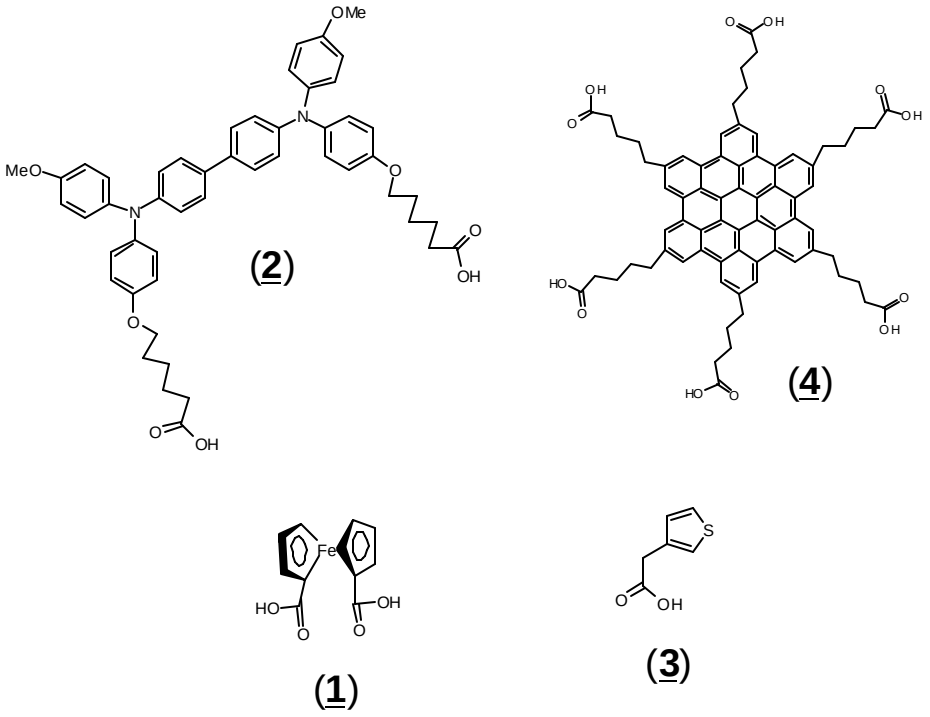

Figure 3.5 Schematic views of small molecule modifiers: ferrocene dicarboxylic acid $Fc(COOH)_2$ (**1**), (6-{4-[{4'-[[4-(5-Carboxy-pentyloxy)-phenyl]-(4-methoxy-phenyl)-amino]-phenoxy}-hexanoic acid (p-$OMe)_2$-TPD-X_2 (**2**), 3-thiophene acetic acid (3-TAA) (**3**), and a hexa-carboxylic acid derivative of hexabenzocoronene, HBC-$(C_3COOH)_6$ (**4**).

success in using this molecule as a probe to determine the fraction of electroactive sites on the ITO surface previously described. 3-TAA is one of a few thiophene derivative probes under evaluation as a "nucleation site" for electropolymerized thiophene polymers grown on the ITO surface.[53] (*p*-OMe)$_2$-TPD-X$_2$ was selected to be more compatible with current device materials, and to provide a surface species more easily oxidized than TPD,[53,56-57] and HBC-(C$_3$COOH)$_6$ was chosen due to its large aromatic core and its six carboxylic side functionalities as, making it capable of adsorbing parallel to the electrode surface.

Each of these molecules is thought to modify the surface of an ITO electrode through interactions involving their acid functional groups and the oxide nature of the ITO surface. Successful modification has the potential to enhance aspects of the ITO/organic interface important for the overall injection of charge including: the relative wettability of ITO, device stability, and the thermodynamic properties associated with charge injection such as work function. The modification techniques required to chemisorb a small molecule modifier onto the ITO surface are similar for each molecule, and are described in detail in Appendix A2.1. Because the adsorption seems to primarily involve electrostatic interactions, hydrogen bonding and/or the formation of a metal-carboxylate like complex between ITO surface groups and the carboxylic acid functionalities, the mechanism for adsorption of each of the different modifiers is likely very similar. The effects of the modification process can be followed electrochemically in order to determine the surface coverage of each species. Figure 3.6 shows the voltammetric characterization (in 0.25M LiClO$_4$/acetonitrile) for two of these adsorbed

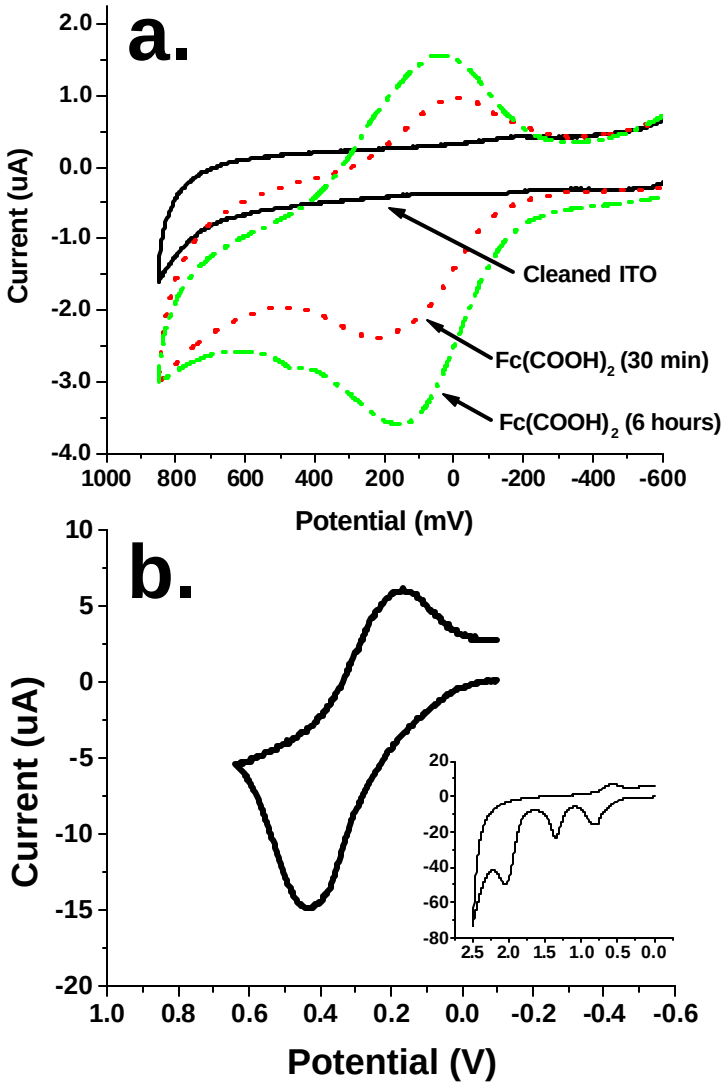

Figure 3.6 Voltammetric characterization of the adsorbed small molecule modifiers $Fc(COOH)_2$ and $(p\text{-}OMe)_2$-TPD-X_2. **a)** $Fc(COOH)_2$ is shown for two separate adsorbed coverages with respect to a background scan and show broad quasi-reversible behavior with an E° of ca. 0.1 V vs. Fc/Fc^+ **b)** The first oxidation of adsorbed $(p\text{-}OMe)_2$-TPD-X_2 showing a quasi-reversible behavior with an E° of ca. 0.3 V vs. Fc/Fc^+. Two more irreversible oxidation events can be seen at higher potentials (inset) with peaks potentials of ca. 1.3 V and 1.9 V vs. Fc/Fc^+ respectfully.

modifier molecules, $Fc(COOH)_2$ and $(p\text{-}OMe)_2$-TPD-X_2. The voltammetric response for the adsorbed $Fc(COOH)_2$, (Figure 3.6a) which shows two different coverages (immersion times) with respect to a background, is quite broad, with a full width at the base of the voltammetric peak of ca. 0.6 volts, and a midpoint potential of ca. 0.1 volts vs. Fc/Fc^+. The broadness of the peak suggests a heterogeneous surface environment for electron transfer (as previously discussed), while the difference in coverage between the immersion times indicate a strong time correlation for modification. Figure 3.6b similarly shows the voltammetric characterization for the adsorbed $(p\text{-}OMe)_2$-TPD-X_2. This modifier also shows a broad voltammetric response with an E_0 of ca. 0.3 V and a base width of ca. 0.7 volts. p-$(OMe)_2$-TPD-X_2 likewise showed voltammetric peaks which increased with immersion time in a similar manner to $Fc(COOH)_2$. Two other oxidation events were observed at higher potentials, with the first peak at ca. 1.3 volts vs. Fc/Fc^+, and the second seen at ca. 1.9 volts vs. Fc/Fc^+, both irreversible. The reduction process to return to the neutral state, however, had no appreciable overpotential, and allowed us to estimate the E° for the first oxidation/reduction potential of surface confined p-$(OMe)_2$-TPD-X_2, E° = ca. 0.3 volts vs. Fc/Fc^+; ca. 0.1 volts positive of the E° for the oxidation/reduction of solution TPD. However, the molecule loses much of the chemically reversible voltammetric behavior that the solution form of TPD displays, retaining semi-reversibility only at the first oxidation potential. HBC-$(C_3COOH)_6$ and 3-TAA were similarly chemisorbed in the same manner to ITO surfaces, for the same immersion times. The voltammetric characterization of adsorbed 3-TAA, shows a single irreversible voltammetric oxidation peak at ca. 1.0 volts versus Fc/Fc^+, which was used to

determine its maximal electroactive surface coverage to be ca. 5.2 $x10^{-11}$ mol cm^{-1}, close to that seen for $Fc(COOH)_2$. The voltammetric behavior of HBC-$(C_3COOH)_6$ is also similar with an E° for the first oxidation of 0.2 volts vs. Fc/Fc^+.

From these studies, it is clear that a substantial time dependence is present for the modification step to establish a steady state surface coverage. Figure 3.7 indicates that even after long absorption times (approx. 6 hours) the process has not reached a steady state. The elapsed time is unexpected and indicates a more complex mode of adsorption than simple electrostatics or hydrogen bonding. Modification times are equally long for the other modifiers tested. Figure 3.7 shows the apparent coverage (moles/cm^2) of $Fc(COOH)_2$/ITO and (p-OMe)$_2$-TPD-X_2/ITO as a function of immersion time in a 0.01 M modifier/EtOH solution used for chemisorption, as calculated from an integration of the voltammetric responses for the oxidation wave. An estimated compact monolayer of $Fc(COOH)_2$ would correspond to ca. $3.0x10^{-10}$ moles/cm^2, assuming a molecular diameter of 4.1 ? and an ITO roughness of approximately 1.1-1.2 nm rms.[1,2,46]

Based on the voltammetric response, the apparent calculated coverage for $Fc(COOH)_2$ rises sharply after immersion in the modification solution, then increases slowly between 75 and 200 minutes before maximizing after ca. 250 minutes, achieving a steady state voltammetric response. The steady state coverage, however only accounts for ca. 1 x 10^{-11} to 5 x 10^{-11} moles/cm^2 or ca. 3 to 19% of the coverage expected for a compact monolayer of the modifier. Other sources of ITO, and with variations in cleaning procedures, coverages of $Fc(COOH)_2$ ranging from 3% to ca. 50% of a compact monolayer have been observed. However, observed coverages do not seem to correlate

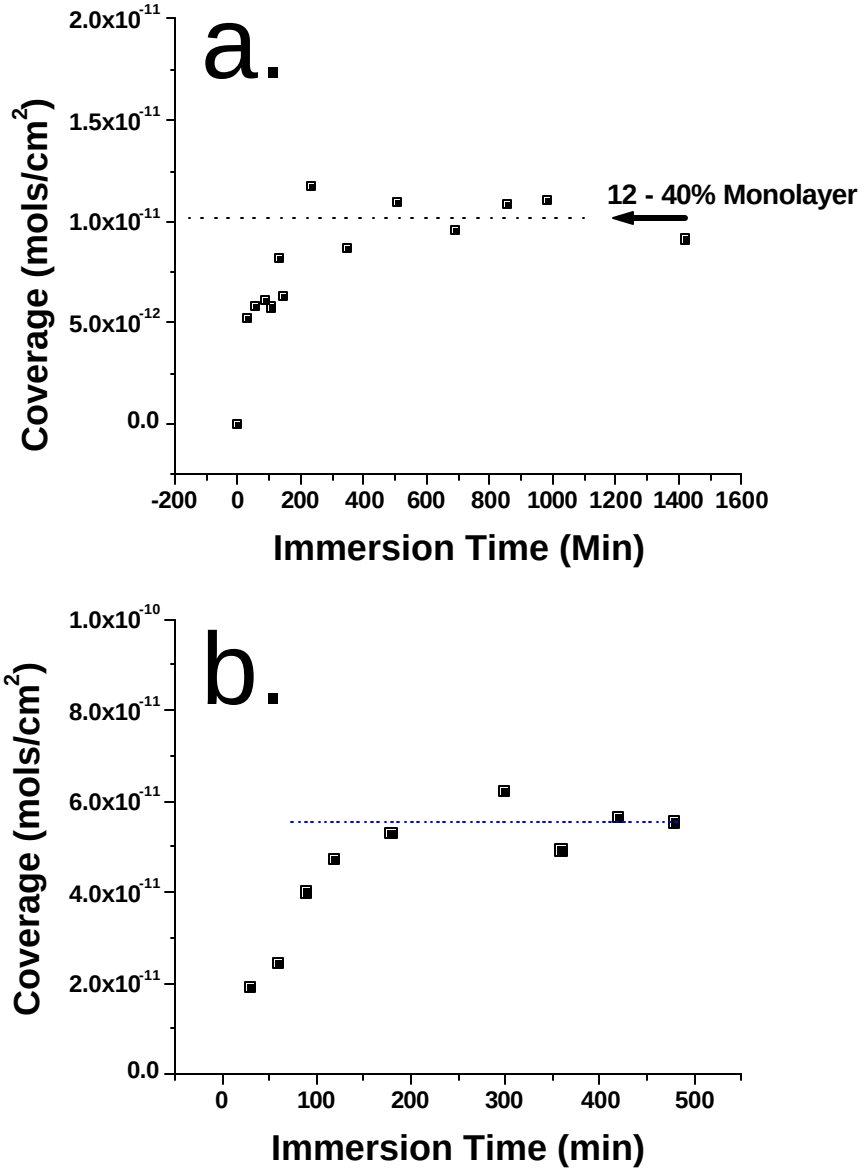

Figure 3.7 Immersion time/adsorption profiles of small molecule modifiers (a) $Fc(COOH)_2$ and (b) (p-$OMe)_2$-TPD-X_2. Initially, a large increase in modifier coverage is observed followed by a slower increase before reaching steady state at ca. 250 minutes. The long modification time suggests a more elaborate mechanism than simple hydrogen bonding or electrostatic absorption.

with the addition of hydrogen bonding sites (i.e. OH groups). This behavior is counter to the proposed adsorption model and was verified by XPS studies.[1]

In these studies, XPS characterization of ITO surfaces resulted in low intensities owing to the low coverages and partial spectral overlap of the In: 3p photoemission. To increase emission intensities, $Fc(COOH)_2$ was absorbed onto high area powders of dried In_2O_3 (160°, 20 hours), as-received In_2O_3, and $In(OH)_3$ powders (e.g. samples increasing in relative hydrogen bonding/hydroxide concentration) and analyzed for the Fe 2p / In 3p ratio. These studies clearly show that the concentration of adsorbed $Fc(COOH)_2$ does indeed scale with the relative hydroxide concentration, a behavior absent with electrochemical studies.

This suggests that only a fraction of the adsorbed material on an ITO surface is electrochemically active, and that the remainder must be adsorbed at or near "electrically inactive" sites.[23] The idea that larger modifier coverages are present than measured voltammetrically is also supported by water contact angles, measured after each modification step. Initially, contact angles of ITO samples are low, 5-31º depending on the cleaning procedures. However, after a short immersion time (ca. 10 minutes), angles have increased substantially to more hydrophobic levels ca. 65º with little to no change observed for longer immersion times, even though coverage is increasing based on the voltammetric data. According to this data, the slow increase in modifier activity measured seems not to be a function of increased actual coverage, but rather increased activity of the ITO surface.

AFM characterization of small molecule modified ITO samples have shown no appreciable difference in rms roughness, no added topographic differences which might be attributed to aggregated materials adsorbed to the ITO surface and no changes in 4-point probe resistance values versus those seen for unmodified ITO. This supports the assumption of a single monolayer of adsorbed material and rules out the possibility of large scale polymerization or hydrogen bonding networks, as recently reported for some materials.[59,60]

The combination of broad voltammertic profiles and increasing electrochemical activity with immersion time, suggests a more complex modification scheme than previously thought. If this process can be fully understood and modeled successfully, the concepts may be enhanced and applied toward engineering a more useful TCO electrode material for organic electronics. To this end, a model has been developed as a rational for the increase in activity observed over long immersion times.

3.3.2 Absorption Model

Figure 3.8 summarizes the proposed state of an as-received ITO surface. The surface of the ITO electrode is thought to consist of the oxide material with exposed Sn doping sites; interstitial oxygen vacancies; and additional oxygen site defects, which may be hydrolyzed, introducing terminal hydroxyl groups into the structure. It is these surface defects and/or dopant sites which are primarily responsible for electron transfer into the

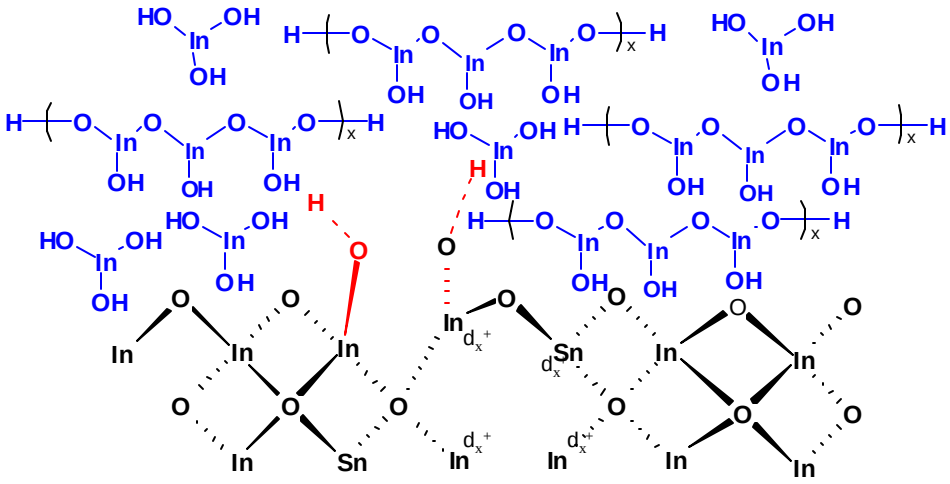

Figure 3.8 Proposed initial state of the ITO surface. Important factors include: the oxide lattice, featuring oxygen defect sites, Sn doping positions, interstitial oxygen vacancies, additional oxygen site defects, and surface defects where the lattice is broken introducing terminal hydroxyl groups. Also shown is the polymer-like $In(OH)_X$ material that is known to be abundantly present on the surface covering an estimated 66% of electron transport sites.

oxide lattice.[58,61-64] The figure also shows that polymeric $In(OH)_x$ like species covers a majority of the surface of the electrode, although there is undoubtedly a considerable variation in thickness.

According to calculated modifier coverages, a "best case" scenario indicates at least 66% (likely more) of the available surface defects may be buried under this insulating material, rendering them inaccessible for redox events. XPS and contact angle studies suggest that the coverage of modifier (likely) saturates quickly on the ITO surface, but the electroactivity of these adsorbed molecules increases slowly as a result of chemical transformations to the ITO surface. This suggests that the surface chemistry of ITO is sufficiently altered during the modification process to allow a greater number of the modifier species electrical contact with the surface active sites. The observed increases in modifier coverage can be explained by a process which ***i)*** lightly etches the $In(OH)_x$-like material to reduce the thickness, or expose a larger population of electrically active sites. ***ii)*** Interacts with the surface in a manner which aids in the creation of more electrically active sites; ***iii)*** a combination of *i* and *ii*.

To elucidate what could be happening, the $Fc(COOH)_2$ modification solution was analyzed for traces of indium, which would indicate a removal of material from the oxide surface. ICP-AES studies on the modification solutions were inconclusive. i.e emission for free indium in the sample failed to achieve a signal-to-noise ratio of 3. With an observed change in the modifier loading of only ca. 15% of a compact monolayer over the entire 8 hour modification period, the etching process is likely very light, releasing only a small amount of material into the solution. It is unlikely that such small

concentrations can be seen without pre-concentration steps. This prompted additional studies where ca. 3.0 grams of In_2O_3 powder (450 m^2 surface area, ca. 150 m^2 per gram) was exposed to $Fc(COOH)_2$ in a similar manner to the modification methods described above. In_2O_3 powders have been shown to be similar in composition to ITO but provide high surface areas to maximize the $In(OH)_x$ material that may potentially be lost to solution. After sufficient elapsed time to achieve equilibrium had passed, (approximately 8 hours) the solution was collected, double filtered, and exposed to gold samples which had previously been modified with an alkane-thiol carboxylic acid, ($SH(CH_2)_{12}COOH$). The carboxylic acid functionalized SAM was utilized to complex with, and pre-concentrate, any indium or indium carboxylate-like complex present in the modification solution, capturing the etched material in the thin film suitable for analysis by XPS. The gold samples were allowed to soak overnight in the collected modification solutions before rinsing with ethanol and placing under vacuum. The results of this study are shown by the XPS spectra of the SAM covered gold substrates after immersion in modification solutions collected over powder exposed to $Fc(COOH)_2$ as well as a control group where the powder was exposed to EtOH only. The emission of the In: 3d peaks corresponding to the sample exposed to $Fc(COOH)_2$ clearly indicate indium is present in the modification solution. This is in contrast with no emission observed for the ethanol control. The presence of indium in the modification solution but not the control group suggests that the loss of indium from the In_2O_3/(ITO) surface is due to the modifier-surface interactions and not simply a washing of the surface. Likely, the acid functionalities of the modifier are complexing with indium lifting it from the surface.

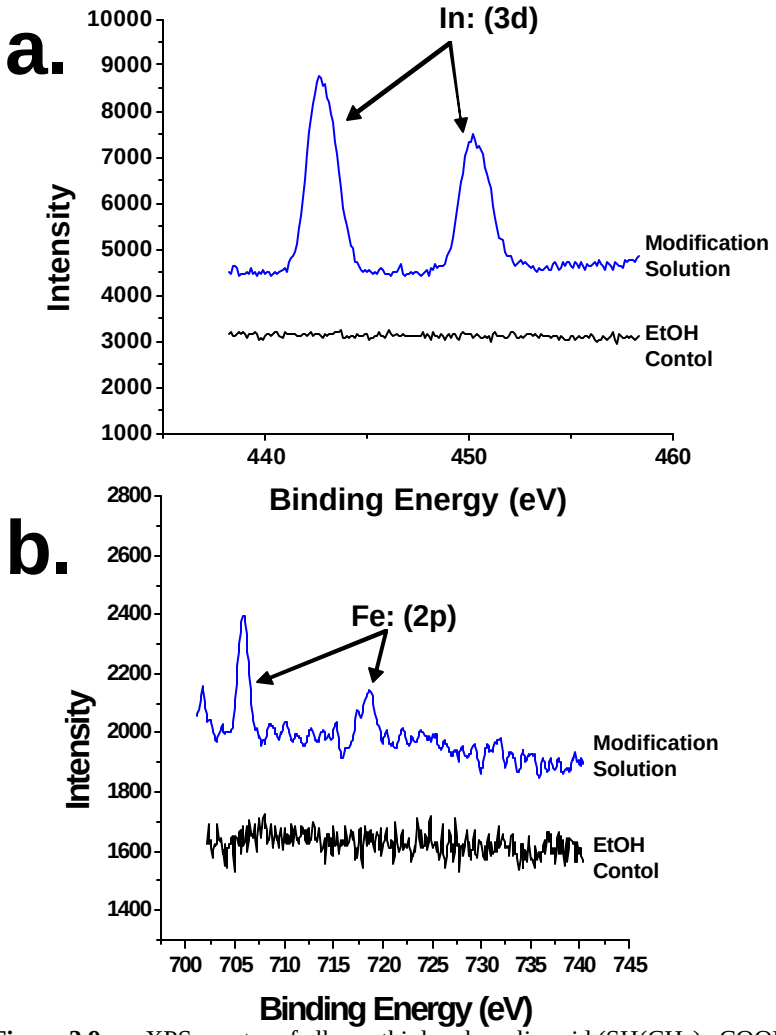

Figure 3.9 XPS spectra of alkane-thiol carboxylic acid ($SH(CH_2)_{12}COOH$) SAMs absorbed on gold slides after an 8 hour exposure to filtered modification solutions (taken after modification of ITO by neat EtOH and 0.01 M $Fc(COOH)_2$/EtOH over In_2O_3 powders (3.0g, 450 m^2)). **(a)** Indium 3d binding energy positions for the EtOH only sample and after exposure to filtered $Fc(COOH)_2$ modification solution, showing presence of indium and **(b)** Iron 2p photoemission for the same samples, suggesting an etching type mechanism is possable.

This is reasonable to suggest as indium-oxalate complex species have been reported in the literature[65-68] and have substantial formation constants, with values of ca. 10^{15} recorded. The Fe(2p) peak in Figure 3.9a and 3.9b also indicates that $Fc(COOH)_2$ is bound to the SAM modified Au surface after exposure to the solution. This may indicate further two ligand (tetra dentate) complex formation between the $Fc(COOH)_2$, indium and the alkane-thiol functionality, but more likely simply shows hydrogen bonding interactions of $Fc(COOH)_2$ can be quite stable on hydrophilic surfaces such as those formed by the alkane-thiol on gold and ITO surfaces.

Figure 3.10 suggests a mechanism for the etching of ITO surfaces with modifiers functionalized with carboxylic acids. We envision that $Fc(COOH)_2$ is in dynamic equilibrium with the ITO surface when adsorbed from the EtOH solution (which contains ca. 5% water). Adsorption via electrostatic interactions or hydrogen bonding to the $In(OH)_x$ network is unlikely to disrupt the $In(OH)_x$ network, and likely little of the electoactive fraction of $Fc(COOH)_2$ seen in the first few minutes of adsorption is bound in that fashion – i.e. the electoactive $Fc(COOH)_2$ seen first is likely bound at, or adjacent to an exposed defect or dopant site and is readily available for oxidation/reduction. The formation of mono or bidentate oxalate-like complex between $Fc(COOH)_2$ and In^{3+}, however, would necessitate breaking of bonds in the $In(OH)_x$ network and (likely) slow dissolution of this network of insulating species.

There is evidence for this type of carboxylic acid-metal complexation on other oxide surfaces. This is illustrated most readily by the adsorption of myristic and succinic acid on Al_2O_3.[69-70] Adsorption of either of these acids necessitates the complexation

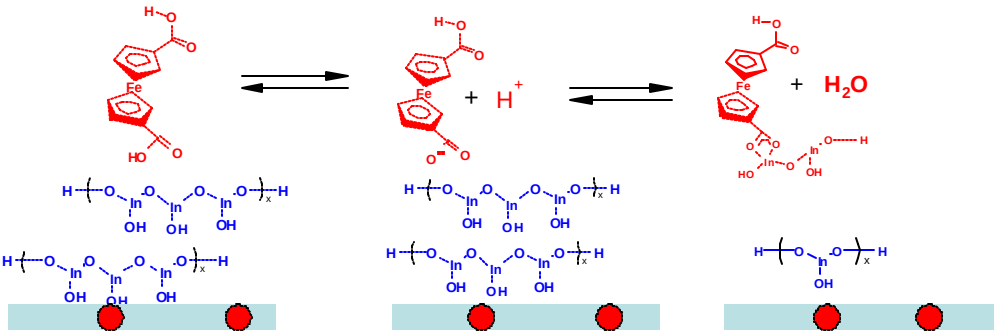

Figure 3.10 Proposed mechanism for light etching of the polymeric $In(OH)_X$ type material present on the surface of ITO. Initially, a dynamic equilibrium is established by the acid functionalities of the modifier. Deprotonation allows for coordination complexes to form necessitating the breakage of In-O bonds. In(OH)x material is removed from the surface by repeated complex formations and the breaking of the network into smaller chains where it can be washed away, exposing additional active sites on the surface (red dots).

between the functional acids and the surface aluminum species. The process consumes surface bound hydroxyl groups (either surface defects or hydroxides) liberating water and forming a stable complex. This is likely similar to what is seen here except complexation with the $In(OH)_X$ network results in smaller chain sizes susceptible to washing away.

Figure 3.11 is a depiction of the state of the surface after the etching process has reached equilibrium. The loss of the $In(OH)_x$ material has lead to the exposure of (or reduction in insulator thickness to) previously inaccessible sites of activity. Eventually, the less stable $In(OH)_x$ material is etched and/or rearranged from the surface and the relatively weak etchant can no longer increase access to buried active sites, and the steady state is reached. However, it should be noted that even after long immersion times, an abundant amount of the $In(OH)_x$ is still present on the surface. It is likely that a majority of the active sites remain buried and inaccessible to electrical activity. The general mechanism described is thought to apply to all the small molecule modifiers discussed here as the carboxylic acid functionality is what primarily interacts with the surface and the adsorption profiles are similar.

3.3.3 Charge Transfer Kinetics

The evaluation of these surfaces can be extended further to characterize the surfaces of ITO modified by the small molecules described above. Figure 3.12, Figure 3.13 and Table 3.1 summarize the cyclic voltammetric redox behavior of the solution probe

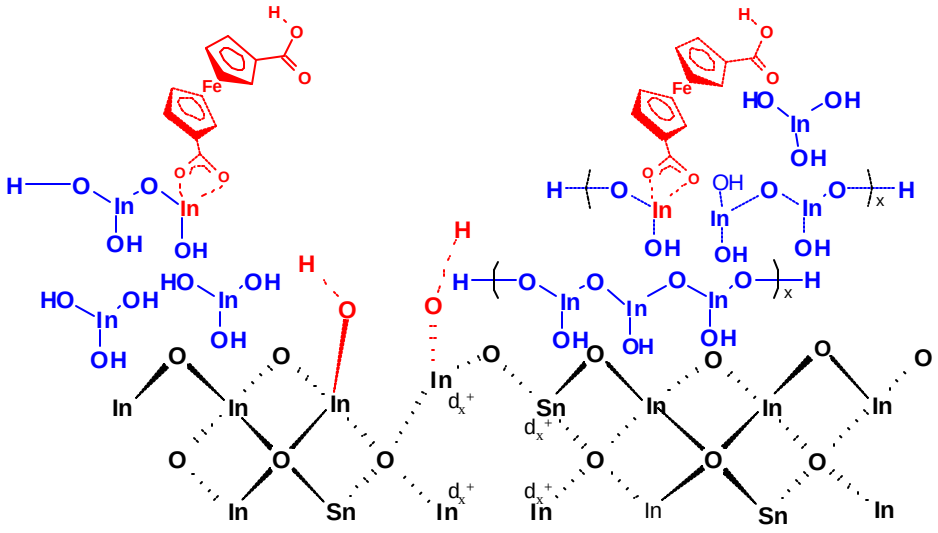

Figure 3.11 Proposed composition of the ITO surface after light etching by the $Fc(COOH)_2$ modifier. Significant breakup of the $In(OH)_X$ material has resulted in the removal of smaller, unstable portions of the structure and leads to the uncovering (or thinning of the layer to) previously inaccessible active charge injection sites. The increased population of sites leads to an increase in the observed electroactive $Fc(COOH)_2$ by ca. 20 to 30% of a compact monolayer (0.5×10^{-11} mol cm^{-1}).

molecules Fc/Fc^+ and TPD/TPD^+ utilized on clean and modified ITO surfaces. Acetonitrile was the chosen solvent for these experiments, as the solution probes have high solubility and the chemisorbed small modifier molecules have only limited solubility in this solvent. Also, supporting electrolyte concentrations were kept high (0.25 M $LiClO_4$) to minimize solution resistance effects on voltammetric peak separation.

Although the oxidation/reduction reactions of both of these molecules are presumed to be outer sphere electron transfer processes, there is an observed strong dependence of electrode surface composition to the corresponding voltammetric behavior. Hence, the electron transfer rate coefficients measured on these surfaces cannot be attributed to changes in the electron transfer mechanism. Rather, changes in the coefficient arise from changing electrode surface conditions. This phenomenon is well known and described as a blocked or limited active site electrodes in many sources.[50-52] The observed rate can be described as an effective rate coefficient (k_{eff}) which is understood to arise from surface conditions only.

Figures 3.12a and 3.12b show the cyclic voltammograms of the Fc/Fc^+ redox couple (0.015 V/s, 0.250 M TBAHFP) on non-modified ITO electrodes as well as ITO modified by the small molecule modifiers $Fc(COOH)_2$, 3-TAA, (*p*-OMe)$_2$-TPD-X_2, and HBC-$(C_3COOH)_6$. All voltammograms show a small amount of hysteresis between the anodic and cathodic peaks, this effect seems to be exaggerated with modification by the TPD derivative (*p*-OMe)$_2$-TPD-X_2 and $Fc(COOH)_2$. This behavior is consistent with the proposed surface, where discrete active sites may mimic an array of micro-electrodes.

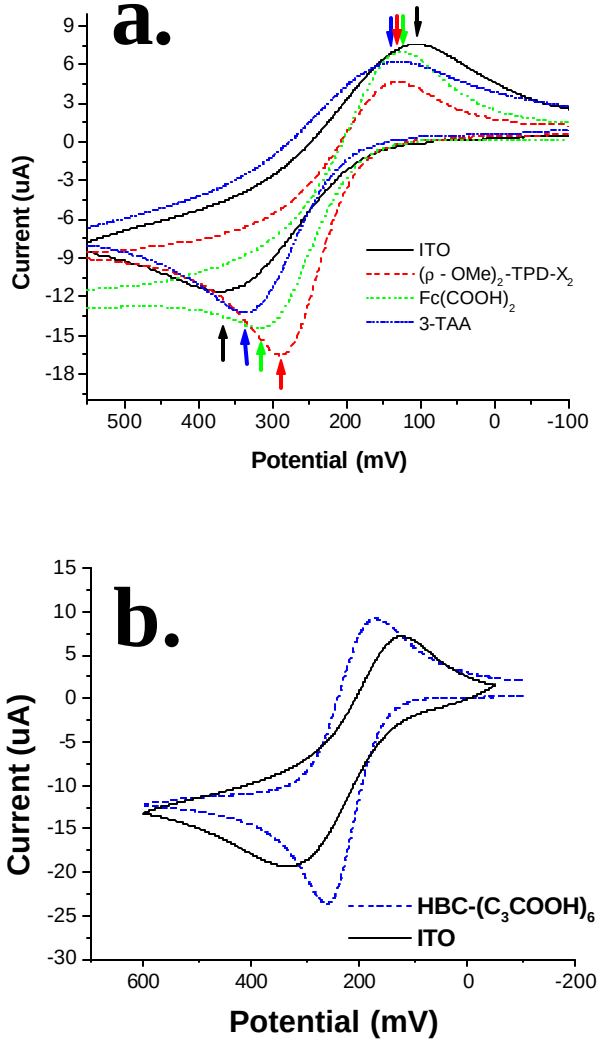

Figure 3.12 Voltammetric characterization of ITO modified by small molecules $Fc(COOH)_2$, 3-TAA, HBC-$(C3COOH)_6$, and (*p*-OMe)$_2$-TPD-X_2 using ferrocene/ferrocenium as a redox probe at .015 V/s compared to that of unaltered ITO. Upon modification, voltammogram peak separations decrease greatly. HBC-$(C_3COOH)_6$ with (*p*-OMe)$_2$-TPD-X_2 show the largest reduction followed by 3-TAA and $Fc(COOH)_2$ resulting in effective electron transfer rate constants of: $5.1x10^{-4}$ cm s^{-1}, $5.3x10^{-4}$ cm s^{-1}, $3.9x10^{-4}$ cm s^{-1} and $3.3x10^{-4}$ cm s^{-1} respectively compared to 6.0 x 10^{-5} cm s^{-1} for bare ITO.

The histeresis is normal and indicates the redox species diffusing out of the electrified solution layer on the return sweep. However, excessive oxidation currents seen for (*p*-OMe)$_2$-TPD-X$_2$ and Fc(COOH)$_2$ indicate other factors may be contributing to the charge passed. Peak widths remain broad, ca. 0.3 to 0.4 volts, and anodic/cathodic peak separations (? E_p) are large. Unmodified ITO samples are the largest, ? E_p = 0.271 V, which also corresponds to the lowest effective electron transfer rates at ca. $k_{eff} = 6.0x10^{-4}$ cm s^{-1}. Upon selected modifications, voltammogram peak separations decrease greatly. HBC-(C_3COOH)$_6$ with (*p*-OMe)$_2$-TPD-X$_2$ show the largest reduction, ? E_p = 0.156 V and ? E_p = 0.147 V respectfully, followed by Fc(COOH)$_2$?Ep = 0.189 V and 3-TAA ? E_p = 0.214 V, resulting in effective electron transfer rate constants of $5.1x10^{-3}$ cm s^{-1}, $5.3x10^{-3}$ cm s^{-1}, $3.9x10^{-3}$ cm s^{-1} and $3.3x10^{-3}$ cm s^{-1} respectively. The increase in the effective rate coefficient with respect to the non-modified sample is significant and can be nearly a factor of 10 for those samples modified with (*p*-OMe)$_2$-TPD-X$_2$ or HBC-(C_3COOH)$_6$.

Figure 3.13 shows the voltammetric characterization of modified and non-modified ITO electrodes using a different probe molecule, TPD/TPD^+, which is also believed to exhibit outer sphere electron transfer. The voltammetric response of TPD is determined in a similar manner to the Fc/Fc^+ probe, with the same small molecule modifiers, minus HBC-(C_3COOH)$_6$. Once again, significant differences were seen for ITO and those modified with Fc(COOH)$_2$, 3-TAA and (p-OMe)$_2$-TPD-X$_2$. As before, (p-OMe)$_2$-TPD-X$_2$ provided the largest increase in effective electron transfer rates, showing an estimated effective electron transfer coefficients of $k_{eff} = 7.8 \times 10^{-3}$ cm

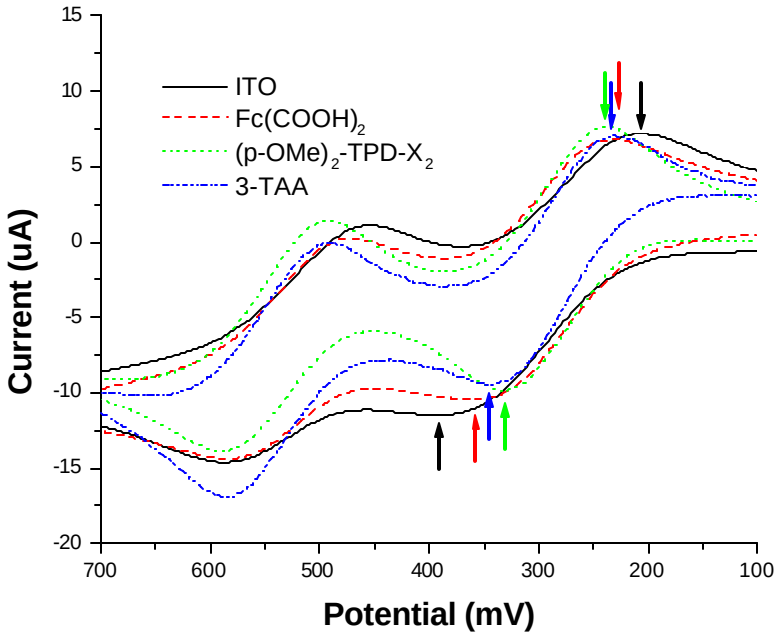

Figure 3.13 Voltammetric characterization of ITO modified by small molecules $Fc(COOH)_2$, 3-TAA, and $(p\text{-}OMe)_2$-TPD-X_2 using TPD as a redox probe at sweep-rates of 0.015 V/s. The same general trends can be seen as with the other probe, $(p\text{-}OMe)_2$-TPD-X_2 show the largest reduction followed by 3-TAA and $Fc(COOH)_2$ with values of k_{et} = 7.8 x 10^{-4} cm s^{-1}, 5.5 x 10^{-4} cm s^{-1}, 2.1 x 10^{-4}cm s^{-1} and 3.1 x 10^{-4} cm s^{-1} respectively.

ITO Sample (modification)	Fc/Fc+ x 10^{-3}	TPD/TPD+ x 10^{-4}
Unmodified ITO	0.6	0.21
$Fc(COOH)_2$	3.9	3.1
$(p\text{-}OMe)_2\text{-}TPD\text{-}X_2$	5.3	7.8
3-TAA	3.3	5.5
$HBC\text{-}(C_3COOH)_6$	5.1	

Table 3.1 Effective electron transfer rate coefficients for modified ITO samples as well as unaltered ITO for two probe molecules Fc/Fc^+ and TPD/TPD^+

s^{-1} increased from k_{eff} = 2.1 x 10^{-4} for the ITO while 3-TAA and $Fc(COOH)_2$ lie somewhere in the middle with k_{eff} values of 5.5 x 10^{-3} and 3.1 x 10^{-3} respectively.

At least a partial amount of the increases in the apparent k_{eff} can be attributed to light etching of the ITO surface. However, this does not explain the excessive oxidation current seen by $(p\text{-}OMe)_2\text{-}TPD\text{-}X_2$ or $HBC\text{-}(C_3COOH)_6$. An alternate explanation may be a catalytic process brought about by the oxidized surface modifier with the solution probe. The adsorbed modifier may act as a charge transfer mediator, where the adsorbed modifier is oxidized slightly before the Fc/Fc^+ probe during the voltammetric sweep. The oxidized species is then able to mediate the oxidation of the probe molecule directly according to equation 5 and 6.

$$Fc(COOH)_{2(s)} \rightleftharpoons Fc(COOH)_2^+{}_{(s)} + e^- \qquad k_{eff} \qquad (5)$$

$$Fc + Fc(COOH)_2^+{}_{(s)} \rightleftharpoons Fc^+ + Fc(COOH)_{2(s)} \qquad k_{cat} \qquad (6)$$

Similar relationships can be written for adsorbed $(p\text{-}OMe)_2\text{-}TPD\text{-}X_2$ and $HBC\text{-}(C_3COOH)_6$ where the estimated E° is positive of that for Fc/Fc+ by ca. 0.2 volts, however the voltammetric peak width (for oxidation of the adsorbed species) is broad, and oxidation of ca. 60% of the electroactive adsorbed $Fc(COOH)_2$ occurs before the peak potential for oxidation of solution ferrocene, i.e. the surface-confined redox active modifier can act to mediate charge transfer to solution Fc/Fc^+.[71-72] This is illustrated in Figure 3.14. The top frame shows the oxidation voltammetric wave for the solution Fc/Fc^+ probe. The next two frames illustrate the fractional coverage of the electoactive

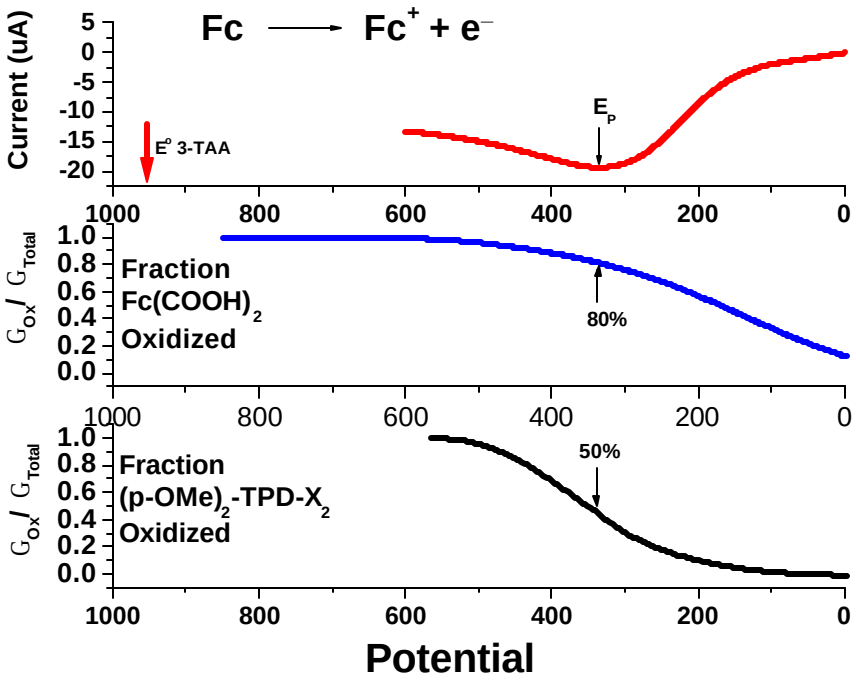

Figure 3.14 Linear sweep voltammogram (0.15 V/s) of the oxidation of the solution probe molecule Fc/Fc^+ compared to the fraction of adsorbed surface modifier in the oxidized form with respect to potential. The adsorbed modifier oxidation peaks are sufficiently broad that ca. 80% of the $Fc(COOH)_2$ and 50% of the $(?\text{-}OMe)_2\text{-}TPD\text{-}X_2$ are oxidized before the Fc/Fc^+ peak potential. This suggests the possibility that the adsorbed modifier may act as an electron transfer mediator in an electrocatalytic process. Additionally, the redox potential of adsorbed 3-TAA is well positive that of the probe molecule and is not expected to be electrocatalytic.

adsorbed modifier in the oxidized state with respect to the applied potential. At the potential where the oxidation of Fc shows a measurable current, the fraction of oxidized modifier is already ca. 30%, and nearly 60% oxidized at the Fc/Fc^+ peak potential. This suggests that there is sufficient modifier in the oxidized state to act as an electron transfer mediator. The width of the oxidation peak for the $(p\text{-}OMe)_2\text{-}TPD\text{-}X_2$ is similarly broad. The fraction of adsorbed modifier in the oxidized state is ca. 15% by the onset of the oxidation of Fc and ca. 50% oxidized by the Fc/Fc^+ peak potential. Similar voltammetric results were obtained for the $HBC\text{-}(C_3COOH)_6$ modifier where the E° is slightly (ca. 0.2 V) positive of that for Fc solution probe.

Briefly, these surface modifiers may act to mediate electron transfer to both Fc/Fc^+ and TPD/TPD^+ probes which is beneficial in transferring charge. This is true for all the presented modifiers except 3-TAA. The redox potential of the 3-TAA modifier occurs well positive that of the probe molecule ca. 1.0V vs. Fc/Fc^+, (Figure 3.14). Because no oxidized 3-TAA modifier is present during the oxidation of Fc or TPD, it is unlikely that adsorbed 3-TAA can act as a redox mediator. The increase in charge passed while utilizing this modifier over plain ITO, may be due solely to the enhancement in surface active sites brought about by the etching of the electrode. This allows for a rough estimation of the magnitude of the enhancement in electroactivity due to etching, as well as the proposed electrocatalytic mechanism. Assuming the increase in the oxidation of Fc on 3-TAA modified ITO is due to etching alone, the peak current is ca. 17% larger than that for ITO alone. This increase must be true for all the surfaces modified in this way, as the mechanism for etching is likely similar. When using modifiers with the potential for

electrocatalysis, the peak currents are shown to increase up to ca. 33% over that of the etched surface alone, and ca. 50% greater than the unaltered ITO alone.

Because the rate increase for the 3-TAA modifier is attributed to etching without the complication of an electrocatalytic effect, the magnitude of the etching effect with respect to surface active sites can be estimated. Previously it was estimated that more than ca. 99% of the surface was blocked (or inactive). Following etching, the coverage of blocked surface area is reduce to ca. 96% or an increase in surface activity of ca. 3%. The seemingly small increase in surface active area illustrates how little etching this modification brings about, but also demonstrates the potential to activate the ITO surface further.

Other etching procedures currently being explored utilize more harsh conditions i.e. 5.5 M aqueous HI. Conducting tip AFM studies indicate a substantially increased electroactive surface on HI-etched verses non-etched ITO alone. However, similar voltammetric studies to those presented above have been inconclusive. It is thought that water present in the preparation solvents (modification and electrochemical solutions) passivates the newly etched and activated surface quickly re-forming surface bound $In(OH)_X$, and leaving a sample similar to the initial state.

Alternatively, it is possible to follow the change in effective electron transfer rate of the Fc/Fc^+ probe molecule with increasing active surface area (electroactivity of the modifier), ie. large etching times. Figure 3.15 shows the profile of the calculated rate

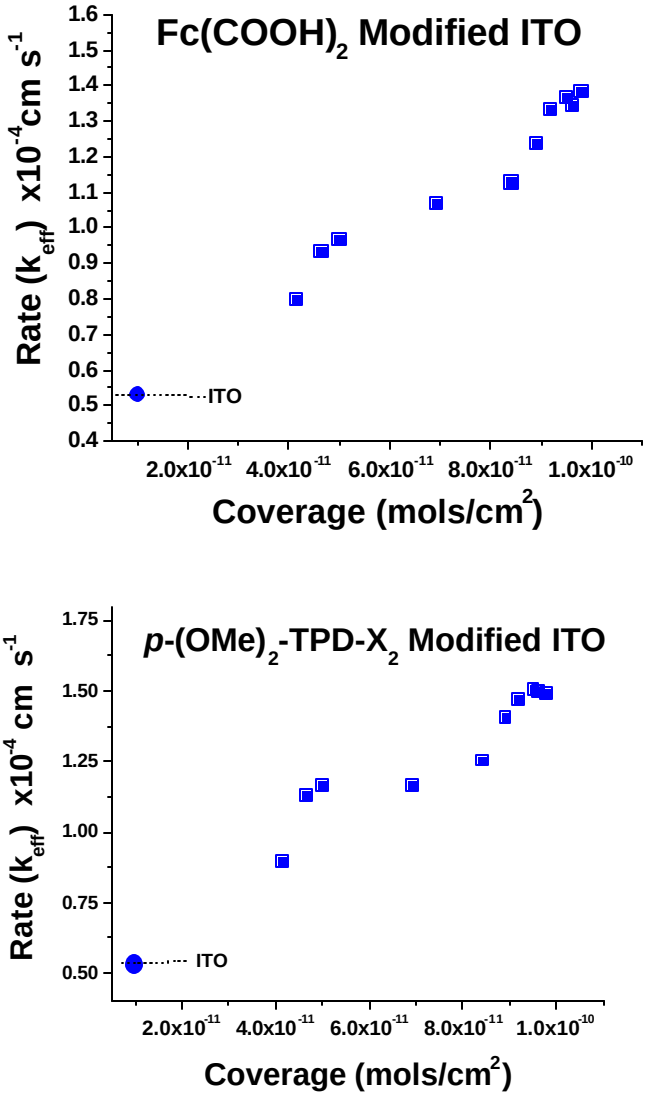

Figure 3.15 Adsorbed modifier coverage (mol/cm^2) vs. effective electron transfer rate constant (k_{eff}) with respect to small molecule modifiers (a) $Fc(COOH)_2$ and (b) $(p\text{-}OMe)_2\text{-}TPD\text{-}X_2$, with the rate of unaltered ITO shown in the lower left. The large initial increase followed by the unusual step-like feature is indicative of three apparent processes: a mediation effect (the initial increase) followed by slow ITO etching and a step due to the formation of an In(COO-X) like complex.

constant change (k_{eff}) with respect to the electroactive surface coverage of the small molecule modifiers: $Fc(COOH)_2$ and $(p\text{-}OMe)_2\text{-}TPD\text{-}X_2$. An initial non-modified ITO, reference is also shown in the lower left of the figure to illustrate the change in effective rate after short modification times. In both cases, a somewhat steep increase in rate occurs shortly after modification begins, and accounts for nearly 25% of the total increase. After this initial jump, the rate coefficient gradually increases with added modifier loading until a step-like feature occurs at loading levels of ca. $9x10^{-11}$ mols/cm^2. At this point, the rate seems to increase sharply by another ca. 30% of the total increase before finally reaching a steady state for the duration of the experiment, ca. 1.5×10^{-3} cm s^{-1}.

The step-like increase in electron transfer rate versus modifier coverage can be explained by a series of events that occur during the modification process. First there is an abrupt increase in the k_{eff} with the lowest measured coverage of modifier achieved in just a few minutes of solution exposure. We hypothesize that the initial chemisorption places mediator molecules in close proximity to the most electoactive sites on the clean ITO surface. We postulate that the initial enhancement in k_{eff} comes about from simple redox mediation involving those most active sites. Prolonged exposures to a solution of these chemisorbing small molecules clearly produces additional subtle changes in ITO surface composition including release of free indium from that surface. This process takes hours but eventually more than doubles the surface coverage of electroactive small molecules, and further enhances k_{eff}. Both because the number of electroactive sites has apparently increased, and because the coverage of active mediators has increased.

After long modification times, coverages of ca. $9x10^{-11}$ mol cm^{-1} and greater, enough material has been removed to allow for a more intimate contact between the modifier and the oxide bound In groups (either by relief of steric hindrance or by removal of thin layers of $In(OH)_X$ covering the parent oxide). It is postulated that previous to this point, complex formation between the modifier and In moieties have involved the $In(OH)_X$ material exclusively. At this point, mono or bi-dentate complexes begin to form on the parent oxide itself. Figure 3.16 depicts the different proposed binding configurations for $Fc(COOH)_2$ on the ITO surface as opposed to chemisorbing to the $In(OH)_X$ material. This is similar to the structures previously discussed involving the chemisorption of myristic and succinic acid on Al_2O_3[81-85] which is similar enough to In_2O_3 for accurate comparisons.

Further evidence of the formation of this complex can be found utilizing time resolved FTIR studies of the modification process on In_2O_3 powders, shown in Figure 3.17. In these studies, In_2O_3 powders underwent the same surface modification protocols used for the surface modification of ITO, for the same adsorption times. Throughout the modification process, samples were subjected to FTIR spectroscopy at given time increments to represent a time resolved progression of the etching by the modifier. The bottom most spectrum on the graph is the FTIR absorbance spectrum for the modifier $Fc(COOH)_2$ suspended in a KBr pellet in the 1200 – 1800 cm^{-1} range. The large peak shown at 1626 cm^{-1} can be ascribed to the carbonyl stretching vibration $?_{(C=O)}$ of the carboxylic acid functionality.[86] The peak visible at 1480 cm^{-1} is likely due to the COH bending vibrations, 1410 cm^{-1} is the $?_{(C-H)}$ ring mode while the peak at 1300 cm^{-1} is

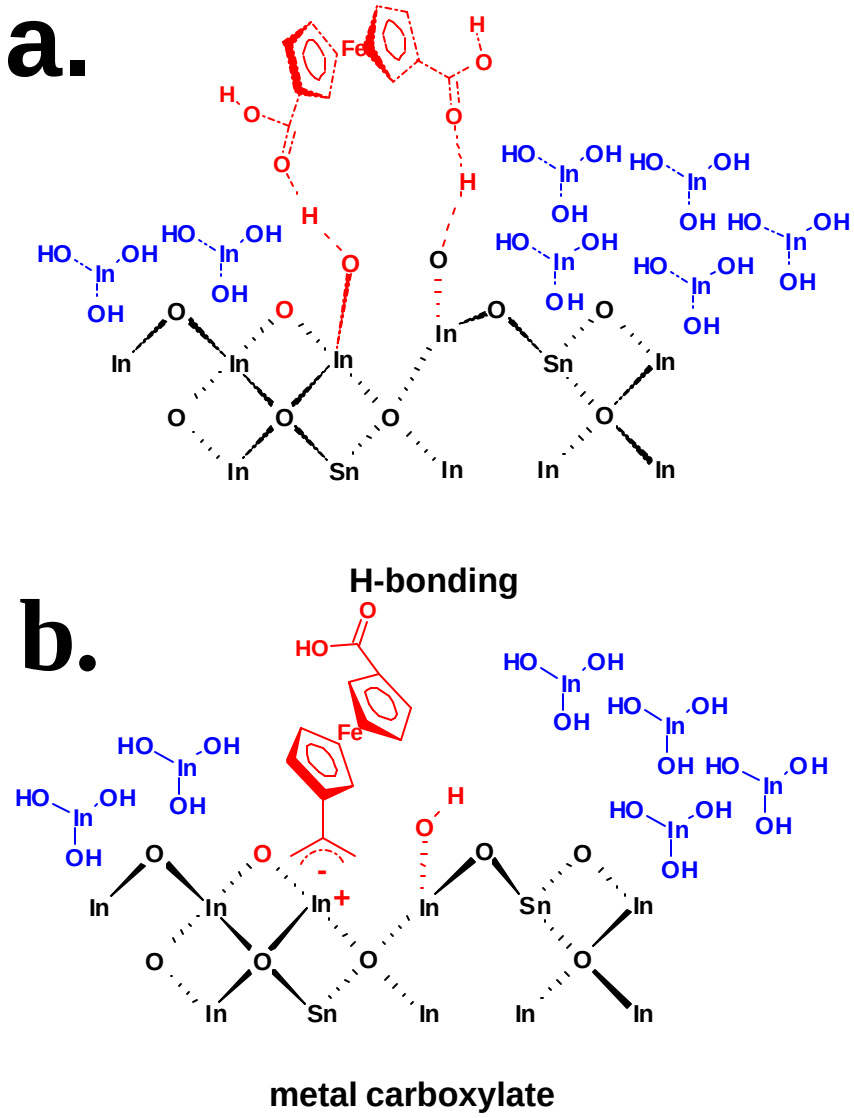

Figure 3.16 Proposed depiction showing the different ways modifier may interact with the surface active sites. **(a)** Interaction through hydrogen bonding and **(b)** coordination complex formation, which may be single or bi-dentate.

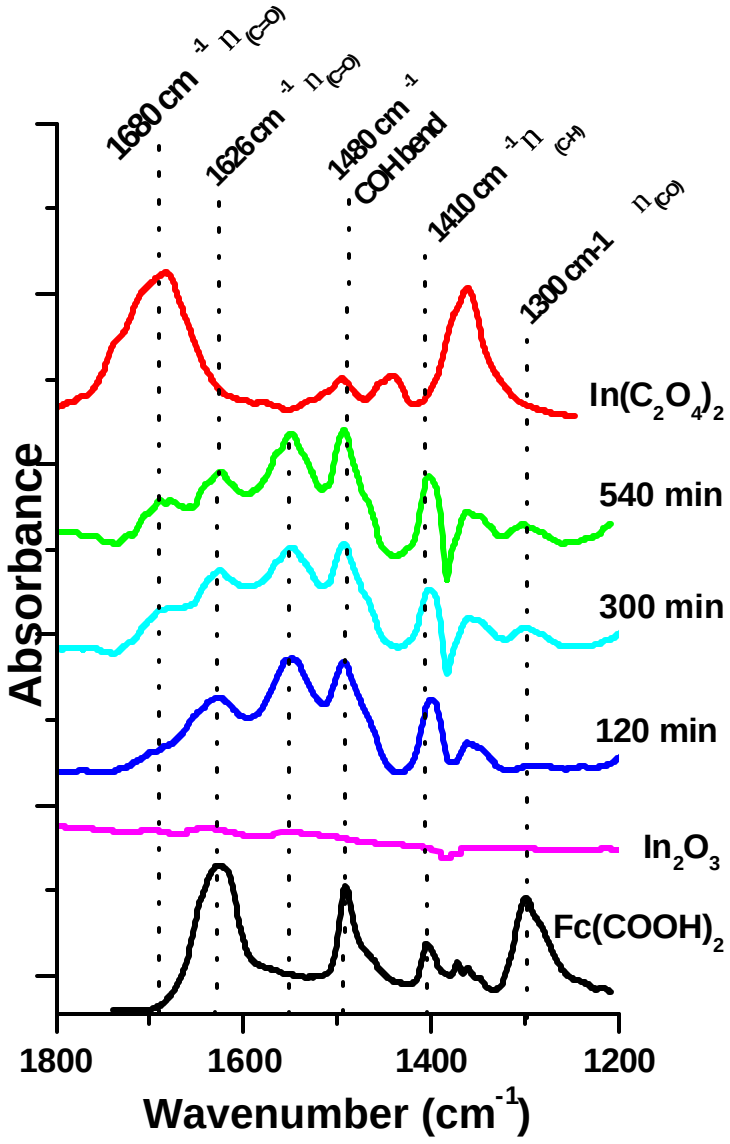

Figure 3.17 FTIR spectroscopic characterization of $Fc(COOH)_2$ modification on In_2O_3 powders with respect to immersion time. Also shown is the characterization neat $Fc(COOH)_2$, bottom spectrum, and $In(C_2O_4)_2$ shown as the top most spectrum. Peaks visible at 1626 cm^{-1} can be ascribed to the carbonyl stretching vibration $?_{(C=O)}$ of the carboxylic acid functionality, and those visible at 1480 cm^{-1} are due to the COH bending vibrations, 1410 cm^{-1} is the $?_{(C-H)}$ ring mode while the peak at 1300 cm^{-1} is ascribed to the $?_{(C-O)}$ stretch. The peak at ca. 1680 cm^{-1} is assigned to the $?_{(C=O)}$ of the complexed species and coincides with the step in Figure 3.16 indicating the formation of an In-$Fc(COOH)_2$ complex.

ascribed to the $\nu_{(C-O)}$ stretch. A control spectrum was taken utilizing the same modification steps as above, only devoid of the modifier and included In_2O_3 powder soaked in EtOH and dried before suspension in KBr. The spectrum is devoid of significant peaks in the 1550-1750 cm^{-1} range indicating no applicable contribution to the modification spectra. Samples with $Fc(COOH)_2$ incorporated into the regime, taken after a short modification times (ca. 5 min to 250 minutes), dried and suspended in KBr retain the $\nu_{(C=O)}$ stretch at 1625cm^{-1}, the COH bending at 1480cm^{-1}, $\nu_{(C-H)}$ ring modes at 1410cm^{-1}, and the $\nu_{(C-O)}$ stretch at 1290cm^{-1}. However, an additional peak at ca. 1560cm^{-1} appears, and can be ascribed to the $\delta_{(OH...H)}$ stretch that arises when the modifier hydrogen bonds[87-89] strongly with hydroxyl groups prevalent on the In_2O_3 surface. Additionally, the $\nu_{(C-O)}$ peak at 1290cm^{-1} for $Fc(COOH)_2$ is dramatically decreased after adsorption. It is unclear why this band decreases with adsorption but may suggest strong hydrogen bonding with both functionalities.

At longer modification times, those that coincide with the electron transfer rate increase step near $9x10^{-11}$ mols/cm^2 (300 minutes, Figure 3.15) a new peak begins to appear at 1680 cm^{-1}. This new peak is presumable due to the $\nu_{(C=O)}$ stretch of the complexed species.[84,87,88] This is verified by observing the $\nu_{(C=O)}$ of $In(C_2O_4)_2$, a species that is thought to be similar to the surface bound indium complex (top most spectra). The spectra shows a peak at 1680 cm^{-1} which is ascribed to the $\nu_{(C=O)}$ stretching vibration and can be matched exactly with the peak position of the newly formed peak. It may be expected that the shift in peak position would occur at a lower energy due to the acceptor nature of the indium ion, when in-fact, the actual peak positions are observed at a higher

energy. This type of behavior is typical for a back bonding scenario between the central atom and the ligand and is common in the formation of similar complexes of this type such as those formed with Al.[71]

The presence of this peak suggests that at long modification times the surface structure of ITO has rearranged itself enough to allow the formation of the surface complex between the carboxylic acid groups of the modifier and surface bound In groups. The formation of this species can then be used to explain the step in electron transfer rates. Likely, formation of a coordinated complex on the parent oxide creates additional active sites which allows for a change in the charge transfer dynamics of the electrode resulting in the observed increase in the effective rate coefficient.

Alternatively, there is evidence that mono-dentate carboxylic acid complexes which form on aluminum oxide surfaces are less stable than bi-dentate complexes and readily desorbs from the surface.[81-83] Modification of the ITO surface by molecules which may form less stable coordination complexes(mono-dentate) with a surface bound indium atoms such as 3-TAA or be sterically hindered (HBC-$(C_3COOH)_6$) can also be followed by a k_{eff} versus coverage plot. Figure 3.18a shows the effective electron transfer rate coefficient as a function of modifier coverage for HBC-$(C_3COOH)_6$. The step-like function previously associated with the $Fc(COOH)_2$ and $(p\text{-}OMe)_2$-TPD-X_2 is noticeably absent for this type of modifier. k_{eff} gradually increases with increasing modifier coverage until a steady state is reached at ca. $5.1x10^{-3}$cm s^{-1} or 40% of a compact monolayer. The initial increase in rate can still be attributed to a redox mediation in that the E° for the

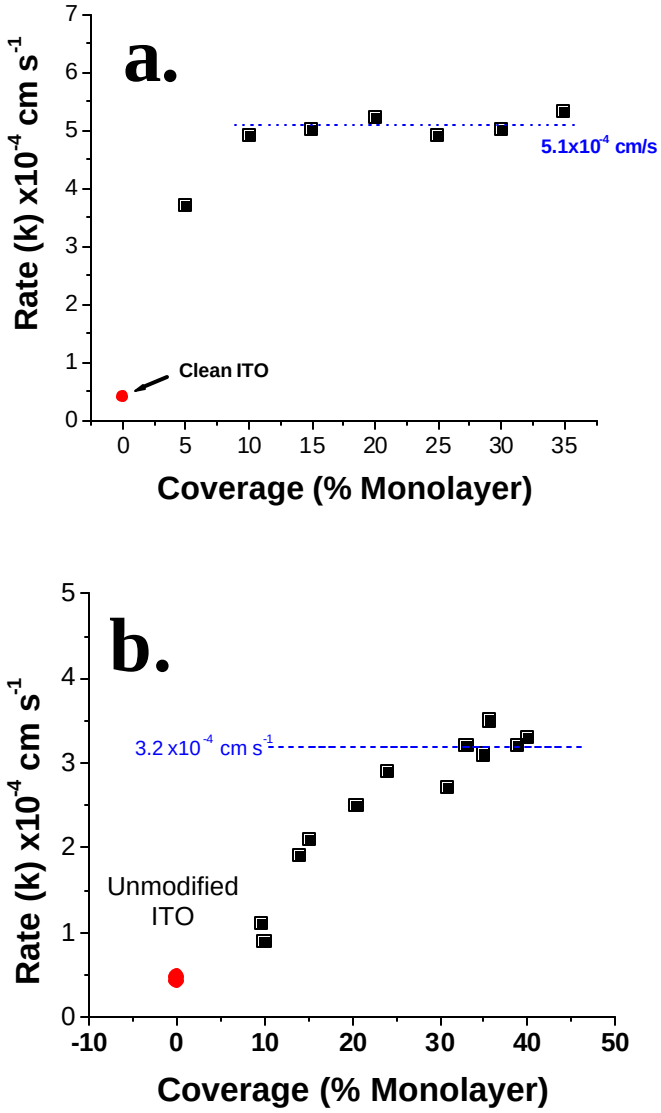

Figure 3.18 Effective electron transfer rate as a function of apparent small molecule modifier coverage for **(a)** HBC-$(C_3COOH)_6$ and **(b)** 3-TAA. Both are unlikely to form a stable surface indium complex as indicated by the absence of the step-like function seen in Figure 3.15. 3-TAA also is devoid of the steep initial increase, indicating electrocatalytic behavior is not present.

HBC-$(C_3COOH)_6$ molecule is approximately the same as that for the $Fc(COOH)_2$, 0.2 volts positive of the Fc probes E° and the oxidation peak is sufficiently broad.

Figure 3.18b describes the adsorption/rate profile for 3-TAA, a molecule which would have difficulty forming a stable surface complex (mono-dentate) as well as having an E° well positive that of the probe ca. 1.0 V vs. Fc. The consequence of the large E° is that virtually no oxidized material can exist at potentials where the probes are active and hence very unlikely to participate in electrocatalytic behavior. This can be seen in the resulting coverage/rate profile as a noticeable absence of the initial jump in k_{eff} (i.e. the initial k_{eff} of unmodified ITO and the 3-TAA modification is the same). The profile begins at nearly the same rate coefficient as that of clean ITO and gradually increases as the etching process becomes important before reaching a plateau at steady state.

3.3.4 Changes in Workfunction

Charge injection across the ITO/Organic interface plays a key role in the performance of organic thin-layer devices and is greatly dependant on the frontier orbital energies attributed to both the electrode and the adjacent material. Generally, an injection barrier is present at this interface and is determined by the energy difference between the highest occupied molecular orbital (HOMO) of the organic layer and the Fermi level (E_F) of ITO. Many studies have been concerned with this barrier and have attempted to reduce its magnitude by a variety of techniques.[6,18,20-21,25,29] The most

popular method to alter this barrier is by chemisorbing or covalently attaching an additional molecular species to the electrode, changing its electronic character. It is well known that some molecular species, particularly those possessing strong dipoles, when adsorbed to the surface of a metal may alter the effective work-function (F) or the energy required to move an electron from the Fermi level to the vacuum level (V_L). This effect can be illustrated by the adsorption of alkane-thiol monolayers on pristine gold surfaces, measured through UPS characterization, compared to the gold surfaces alone.

Measurements shown here are determined by UV-photoelectron spectroscopy using He(I) excitation source (21.2 eV) in an ultra-high vacuum environment (Kratos, Ultra). Figure 3.19a shows this effect by comparing the UPS spectra for increasing molucular weight alkane-thiol SAMs on bare gold, compared to samples of pristine gold.[72] As the alkane-thiol chain length increases from 8 to 18 substituents, the low energy kinetic energy edge of the spectra shifts ca. 1.5 eV lower, indicating a lowering of the vacuum energy associated with the new surface, decreasing the work-function of the SAM covered surface as the dipole gets larger. Alternatively, molecular components with a dipole in the opposite direction (fluorinated alkane-thiol) can have the opposite effect on the apparent vacuum level. This is illustrated in Figure 3.19b by the UPS spectra of increasingly flourenated alkane-thiol SAMs on gold surface(dipole in the opposite direction) again, compared to a pristine gold surface. The low kenetic energy egde of the spectrum shifts to higher kinetic energy with the increasing fluorination (increasing dipole) and indicates a slight increase of the vacuum energy associated with the new surface of ca. 1.0 eV.

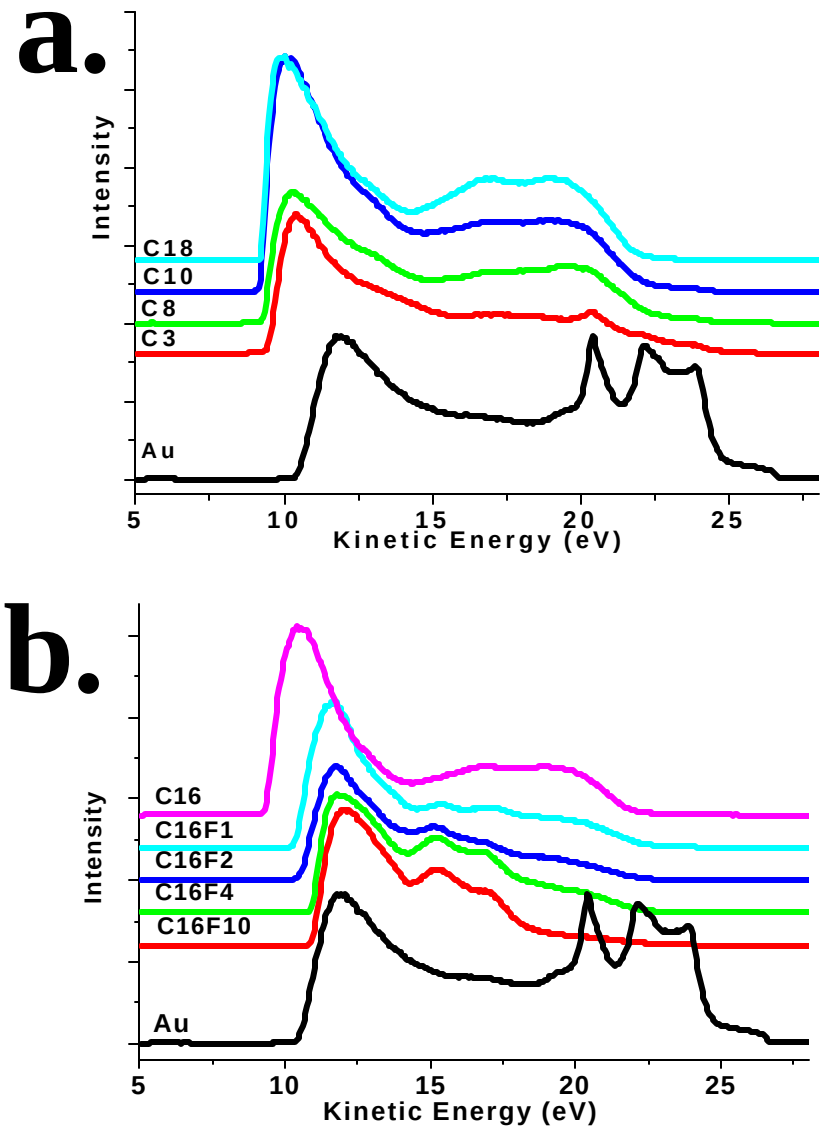

Figure 3.19 **a)** UPS spectra of alkane thiol SAM covered gold, showing the effect an increase the adsorbed dipole (number of carbon constituents) may have on the workfunction (shift in high binding energy edge). As carbon atoms increase from 3 to 18, the vacuum level shifts ca. 1.5 eV, lowering the workfunction. **b)** Similar spectra series for increasing degrees of fluorinated alkane thiol SAMs on gold, (opposite dipole) showing the opposite shift in workfunction. As the degree of fluorination increases, the vacuum level shifts ca. 1.0eV, raising the workfunction of the new surface. (adapted from Alloway *et. al.)*

This strategy can apply to any adsorbed species. However, small molecule modifications of ITO electrodes conducted above have produced only modest changes in effective work function. Generally, ITO thin films show widely varying work functions, depending upon source of ITO, surface cleaning procedures, modification with dipolar small molecule species, and with the addition of conducting polymer thin films, such as poly(3,4-diethoxy-thiophene)/poly-(styrene)-sulfonates (PEDOT:PSS).[32-37] In this case, $Fc(COOH)_2$ and other small molecules are absorbed to the surface through techniques previously described and the resulting workfunction was measured along with a control sample which was soaked in an ethanol solution devoid of any modifier. Figure 3.20 highlights the results of this work in which unmodified ITO samples are sputter cleaned by exposure to an argon ion source (750eV, 30 minutes) under vacuum. The rational for the sputtering process is to remove the first few layers of the oxide and expose a contaminant free surface, that presumably exists as the oxide terminated lattice. After sputter cleaning, samples were placed in modification solutions containing 0.01 M $Fc(COOH)_2$/EtOH, and a neat ethanol control in an inert atmosphere (glove bag attached to the vacuum chamber). The results were then plotted against a sputter cleaned ITO sample and any shift in the spectrum is observed. The Figure shows each sample, with the sputtered sample as the bottom, the $Fc(COOH)_2$ modified sample in the middle and the ethanol control as the top most spectra. Sputter cleaned ITO resulted in a low kinetic energy edge of ca. 7.6 eV, and a high edge of ca. 24.7 giving rise to an apparent work-function of ca. 4.1 eV. After modification, the $Fc(COOH)_2$ sample shows a shift of ca. 0.72 eV at the high kinetic energy cutoff. This indicates an increase of the apparent

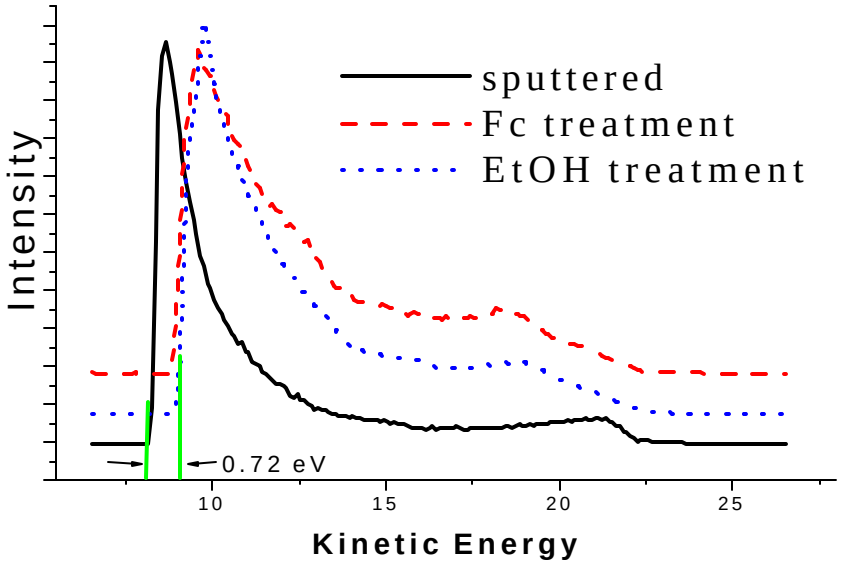

Figure 3.20 Ultraviolet photoelectron spectroscopy (UPS) of ITO surfaces which have been ***i)*** sputter cleaned, ***ii)*** been modified by the small molecule modifier $Fc(COOH)_2$ and ***iii)*** soaked in a EtOH control. A 0.72 eV shift in the high binding energy edge indicates an apparent vacuum shift of the sample when sputter cleaned ITO is exposed to water containing solvents (e.g. ethanol or $Fc(COOH)_2$ modification solutions) which leads to the hydrolysis of the surface and an apparent formation of a surface dipole resulting from the formation of $In(OH)_X$ moieties.

workfunction by the same amount to ca. 4.8 eV. However, the control sample, which was soaked in a neat ethanol solution devoid of modifier, also shows a shift in the high kinetic energy cutoff of the same amount. This indicates that the presence of the modifier does not significantly affect the vacuum levels and hence, workfunction of ITO. However, there is a substantial shift when sputtered ITO is exposed to ethanol solutions.

The most likely explanation for the observed shift involves the exposure of the sputtered oxide surface to solvent, which is likely contaminated with water, and results in the creation of surface dipoles sufficient to shift the vacuum level of the sample. Initially, ITO samples were sputter cleaned in high vacuum to remove contamination from the near surface. A consequence to this cleaning, was the reduction of the surface to a state resembling the native oxide, e.g. much of the surface confined $In(OH)_X$ material was removed (XPS of sputtered ITO). This is consistent with the measured work-function, which seemed low compared to solution cleaned samples. Upon exposure to the modification solvent (with or without the modifier), hydrolysis of the sputtered surface is likely creating a build up of the aforementioned $In(OH)_x$ material. This has been shown to occur spontaneously upon similar surfaces after a few minutes of exposure to atmosphere.[54] The build up of this material leads to an abundant concentration of hydroxide groups at the near surface which can be modeled by an adsorbed species with a heavy dipole. The observed shift (increase) in work-function is consistent with an adsorbed dipole in that direction, e.g. the fluorinated SAM. It is the change in the surface structure which results in the apparent difference of the measured workfunction and not the addition of the modifier.

However, few device construction schemes utilize sputter cleaned ITO directly, the continual washing with ethanol common in device construction effectively negates any effect from a workfunction shift, due to a sputter cleaned ITO electrode. Adsorption of all the small molecules summarized, has to date produced only minimal work function changes in ITO substrates, as revealed by UPS experiments, despite the fact that one may predict a small interface dipole effect from their chemisorption.[73] Larger changes have been noted for covalently bound modifiers by Schwartz and coworkers,[74-76] however their modifiers are attached at surface sites which do not necessarily provide direct electrical contact to the oxide lattice.

3.3.5 Contact Angle and Surface Wettability

The chemical compatibility of the ITO surface with the adjacent organic layers (created primarily from non-polar molecules) or conducting polymer thin films can be problematic in the planning and construction of organic thin layer devices. A major complication that must be addressed is the polarity of the adjacent material with respect to the ITO surface. Commercial polymer blends, meant to coat ITO electrodes, incorporate additives to help create highly polar solutions and aid in the spreading of the material. However, the addition of these materials is generally at the cost of decreased conductivity. Alternatively, molecular layers deposited in high vacuum environments may be entirely non-polar and lead to microscopic gaps and fissures in the deposited film.

The difference in polarity between these two major device making strategies makes the nature of the ITO surface extremely important in the planning and construction of organic thin-layer devices. Regardless of the adjacent material, hole-transport layers or conducting polymers, must maintain an intimate contact with the oxide surface, especially near electrode active sites, for maximum charge injection and device longevity. Previous work[77] initiated by Friend *et al.* has shown that the polarity of ITO surfaces can be influenced substantially by various pretreatments and cleaning procedures. In their work, the polarity of the surface is estimated by investigating the contact angles of various liquids by the sessile drop method[77-78] as a convenient way to estimate surface free energies and how the polarity of an ITO surface may be altered after treatment. The authors report a wide range of ITO surface polarity based on the particular treatment used, with oxygen plasma treatments showing highest polarity, while argon-plasma based treatments show the lowest surface polarity. This broad range suggests that the ITO surface can be manipulated in a manner to enhance its compatibility with any adjacent material, regardless of the type.

Studies shown here utilize sessile drop water contact angles on ITO surface to similarly investigate the changes (if any) that can be attributed to ITO modification by those methods previously discussed. In general, an increase the water contact angle is an indication of the decreased polarity of the ITO surface, while low contact angles indicate the drop is on a polar surface. If the modification preformed has rendered the surface more or less favorable to the addition of the adjacent organic layer, the resulting thin-film is expected to exhibit a proportional change in the amount of microscopic voids between

the ITO and the subsequent deposited organic layer that are present (Figure 3.21). A lack of surface wettability may manifest itself as a microscopic buckling of the film where the molecules are lifted away from the surface in order to relieve the built up repulsive energy.

Static sessile drop water contact angles were measured for several ITO samples, each exposed to a different modification procedure, identical to those described above, including: As received ITO (EtOH washed), air-plasma etched, Piranha treated, RCA treated, and the small molecule modifiers, $Fc(COOH)_2$, 3-TAA, HBC-$(C_3COOH)_6$ and (p-OMe)$_2$-TPD-X_2. Values were taken from the average of a series of measurements (ca. 20 measurements per sample), following the modification protocol, and are shown in Figure 3.22 and Table 3.2. The as-received ITO shows a moderate hydrophilicity with contact angles of ca. 31 ± 3°. The air-plasma etched samples are shown to have the highest hydrophilicity with contact angles of less than 5°. Piranha treated samples showed contact angles of ca. 16 ± 4°, with the RCA treatment producing ITO with water contact angles of ca. 35 ± 3°. These values complement earlier findings concerned with the amount of surface hydroxide present on ITO. Similar reports[77-78] show the amount of water-like groups on the ITO surface lead to more polar surfaces. Modification by small molecules show a substantial decrease in the surface polarity by nearly doubling the angles with respect to the as-received sample, $Fc(COOH)_2$, 3-TAA, HBC-$(C_3COOH)_6$ and (p-OMe)$_2$-TPD-X_2 show angles of 51 ± 5°, 62 ± 2°, 58 ± 2° and 56 ± 3° respectfully.

The addition of these small molecule modifiers significantly lowers the polarity of the ITO surfaces, although close packed layers of these materials might be expected (with

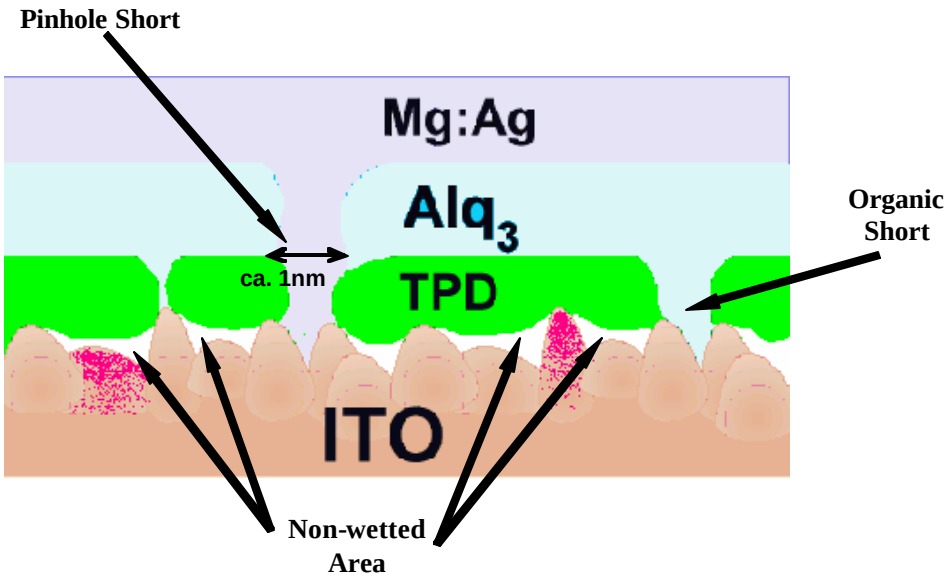

Figure 3.21 Representation of problems associated with non-polar molecules deposited on the ITO surface. The hydrophilic surface will resist uniform distribution of the organic during deposition. Incompatibility issues will manifest itself as a microscopic buckling of the film where the molecules are lifted away from the surface in order to relieve the built up repulsive force, leading to small cavities and various pinholes at the interface, and throughout the film.

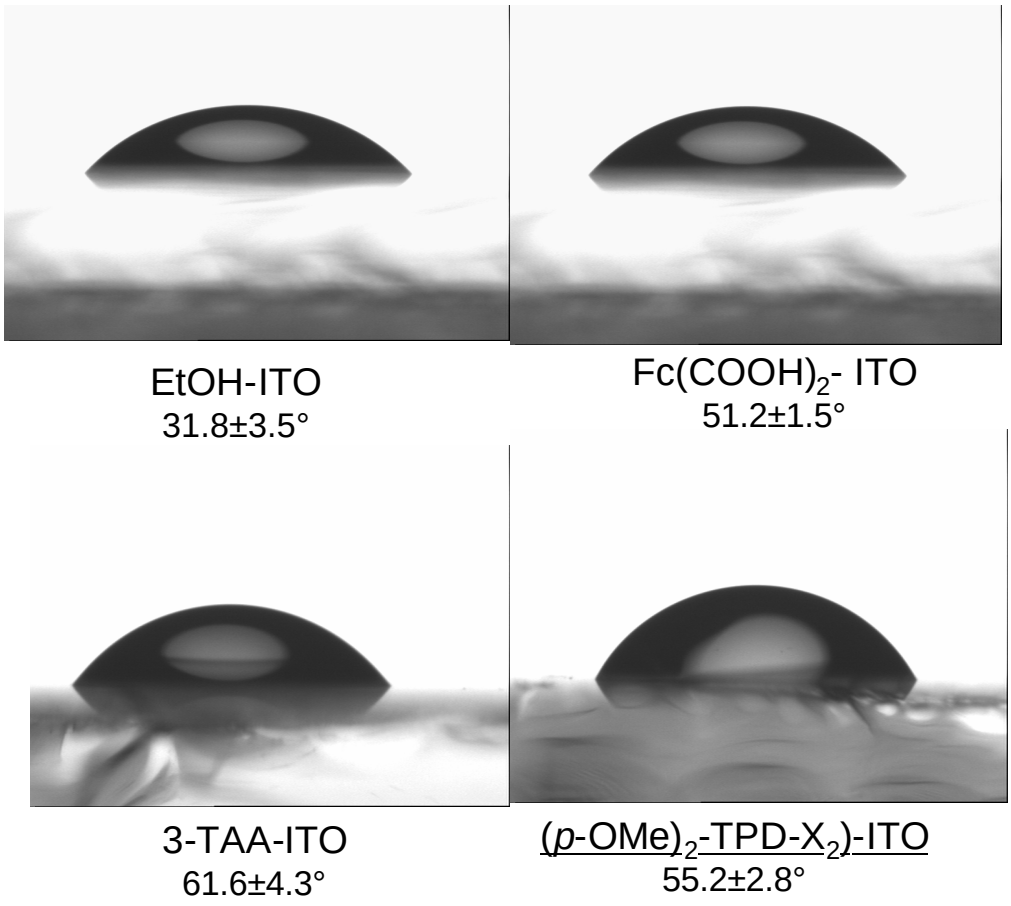

Figure 3.22 Water contact angle profiles showing the decreased polarity of the surface following modification of the ITO by small molecules. The contact angles progress from plasma etched ITO at <3°, non-modified but EtOH washed ITO at ca. 32°, $Fc(COOH)_2$, 3-TAA and (p-OMe)$_2$-TPD-X_2 display angles of 51.2°, 61.6° and 55.2° respectively.

Sample	Left	Right	Average
Plasma etched ITO	cannot measure >5		
EtOH washed ITO	30.8	32.7	**31.7**
Piranha treated ITO	15.9	16.2	**16.4**
RCA Cleaned	34.2	36.4	**35.1**
$(p\text{-}OMe)_2$-TPD-X_2	55.3	55.1	**55.2**
$Fc(COOH)_2$	51.2	51.2	**51.2**
3-TAA	61.8	61.4	**61.6**
HBC-$(C_3COOH)_6$	55.9	56.6	**56.2**
PEDOT:PSS	13.5	10.4	**11.9**
Undoped PEDOT	29.6	29.5	**29.5**
Doped PEDOT	38.1	40.9	**39.5**

Table 3.2 Average water contact angles for ITO surfaces after modification procedures as well as non-altered ITO samples.

chemisorption of all carboxylate groups to the oxide surface) to lead to contact angles closer to 80-90°. It is likely that lower angles are observed because modifier functional groups can be arranged spatially outward providing some interaction with the solvent, as well as the droplet inducing some amount of desorption from the surface.

It is clear that the polarity of the ITO surface is not static. Shown here, as well as previous reports indicate that the surface may be "tailored" for the optimal approach, i.e. more polar surfaces for the addition of commercial conductive polymer layers, and less polar for hydrophobic vapor deposited layers. Regardless of the approach, construction of these devices should involve careful consideration of the interfacial compatibility. This would help decrease microscopic gaps and fissures along the electrode/organic boundary prevalent in many devices. The benefits have the potential to be substantial including increased charge injection due to better wettability and added stability to device longevity.

It is interesting to note that plasma etched samples gave rise to very polar surfaces, less that 3º. However, many device protocols utilize freshly air or oxygen plasma etched ITO for immediate molecular deposition. This would suggest a poor scenario for direct application of organic layers on this surface. Judging from the results shown here, this practice is not advisable strictly from a wettability point of view and may lead to many of the delamination problems observed in current devices.

3.4 SPIN-CAST CONDUCTIVE POLYMER

Modification strategies have been employed for increasing the desirable attributes of an ITO electrode for some time. By far the most widely used method of modification is the spin casting of a conductive polymer directly on the ITO surface prior to device construction. The most common of these polymer layers is PEDOT:PSS. Typically, a sample is spin-cast and annealed on the ITO surface in order to create a stable conductive film covering the entire electrode.

3.4.1 Physical Characteristics

The casting of a thin conductive polymer layer over ITO changes the nature of the electrode considerably with respect to an unaltered sample. Typically, a thinned solution of PEDOT:PSS is spin cast onto a sample by flooding the surface with copious amounts of the casting solution, then rotating the sample at high speeds, (3000 rpm, 1 minute) and allowing the centripetal forces to dispose of the excess material, leaving behind a smooth, uniform film over the entire sample surface. Annealing conditions vary, but generally include sufficient time to drive off any residual water from the cast film (100° C, 1 hour). Thickness of a completed film is strongly dependant on casting conditions such as dilution of the parent solution, humidity, rotation speed, initial rotational acceleration, and duration of the rotation. Typically, a thickness of ca. 50 nm is preferred when constructing organic devices (measured by AFM or elipsometry) as increasing thickness

can lead to lower conductivity through the CP layer. Figure 3.23 displays an AFM image of a typical PEDOT:PSS coated and annealed ITO sample prior to device construction. The rms surface roughness, which for ITO averages ca. 1.5 nm, has increased slightly to ca. 3 nm for the spin cast polymer film. Contact angle measurements show the resulting film to be more polar than previously thought. Water contact angle measurements averaged at 11.9° ± 2.1° indicating a reasonable material for the wetting of the ITO surface. However, this also indicates compatibility problems may still exist between the primarily hydrophobic organic layer deposited directly adjacent to the film.

3.4.2 Electron Transfer Kinetics and Model of Advantages

Voltammetric methods to measure k_{eff} for Fc/Fc^{+} in acetonitrile were employed for PEDOT:PSS cast ITO samples in a similar manner to that described earlier. Figure 3.24 shows the voltammetric characterization of PEDOT:PSS coated ITO with respect to an unaltered ITO sample. As-received ITO, when characterized with an Fc/Fc+ probe results in a calculated k_{eff} of ca. 6.0×10^{-4} cm s^{-1}. With the addition of a cast and annealed thin layer of PEDOT:PSS, the voltammogram assumes a much more reversible form. The anodic/cathodic peak difference decreases substantially which translates to an effective electron transfer coefficient of ca. $k_{eff} = 1.6 \times 10^{-2}$ cm s^{-1}.

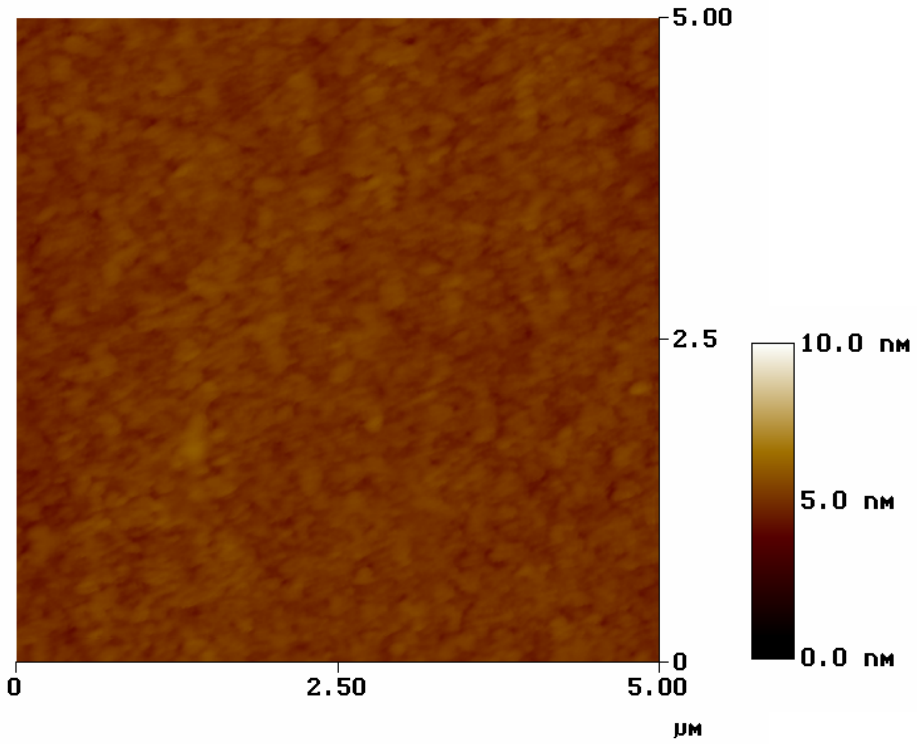

Figure 3.23 Tapping mode AFM image of PEDOT:PSS cast on ITO (after 1 hour anneal, 100° C, ca 50nm thick) showing a relatively defect free surface with a rms roughness of ca. 3 nm.

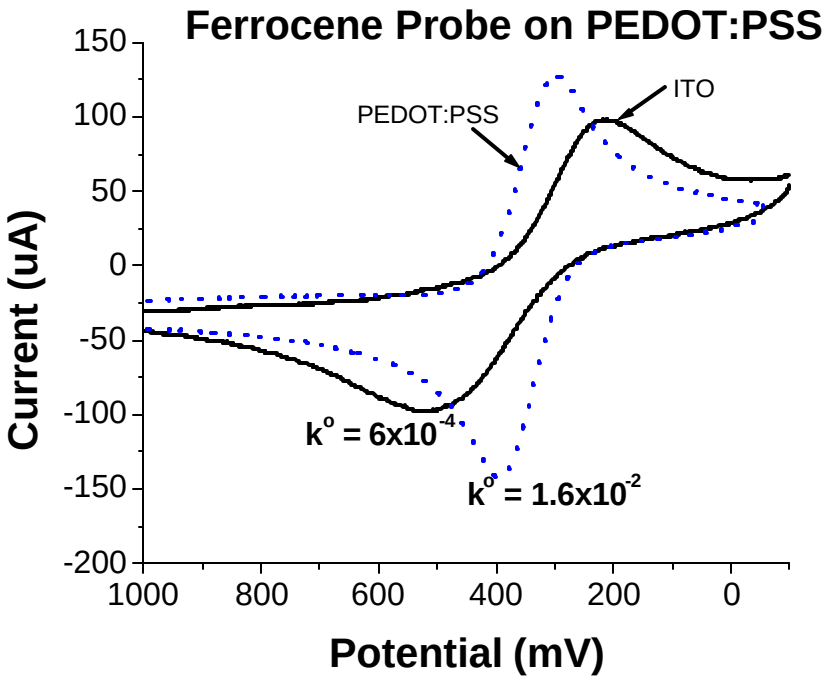

Figure 3.24 Voltammetric characterization of PEDOT:PSS coated ITO with respect to a cleaned ITO sample using the ferrocene/ferrocenium as a redox probe. PEDOT:PSS shows a large improvement of electron transfer characteristics with better reversibility and a rate coefficient of 1.6 x 10^{-2} cm s^{-1}(0.250 M $LiOCl_4$, 0.01V s^{-1}).

The increases in k_{eff} observed by simple casting of the PEDOT:PSS layer over the ITO electrode suggests a different mechanism for increased charge injection than that of the small molecule modifiers, as the surface of ITO was not significantly altered. Although there is undoubtedly better wetting of the ITO surface by the CP, the underlying surface chemistry of the ITO surface presumably remains the same e.g. still supports the insulating $In(OH)_X$ material thought to be blocking active surface sites and severely limiting electron injection. However, another explanation for the dramatic increase in charge injection can be proposed.

Figure 3.25 depicts the surface of ITO where a thin layer of PEDOT:PSS has been cast , compared to that of an unaltered ITO sample. On ITO, redox events rely on diffusion to carry probe molecules to a particular active site before charge transfer can occur. Surface conditions of the sample dictate nearly 99% of the surface is inactive, resulting in discrete areas of redox activity. By adding the conductive polymer layer (Figure 3.25b), the active sites on ITO are no longer spatially confined, e.g. while active sites do not move or increase in population, the polymer layer allows for "multiple paths" of charge transport from the polymer surface to each active site. Redox events that may have previously been restricted to short distances from a discrete active site, while on the unaltered ITO sample, may now be expanded through the conductivity of the polymer to a more homogeneous state. It is thought the overall effect of this delocalization would be similar to the addition of more active sites, and consequentially be manifest as an increase in the apparent charge injection as described by Comninellis, Bard and Swain.[49,52] The increase in the activity can be conveniently measured by adapting it to

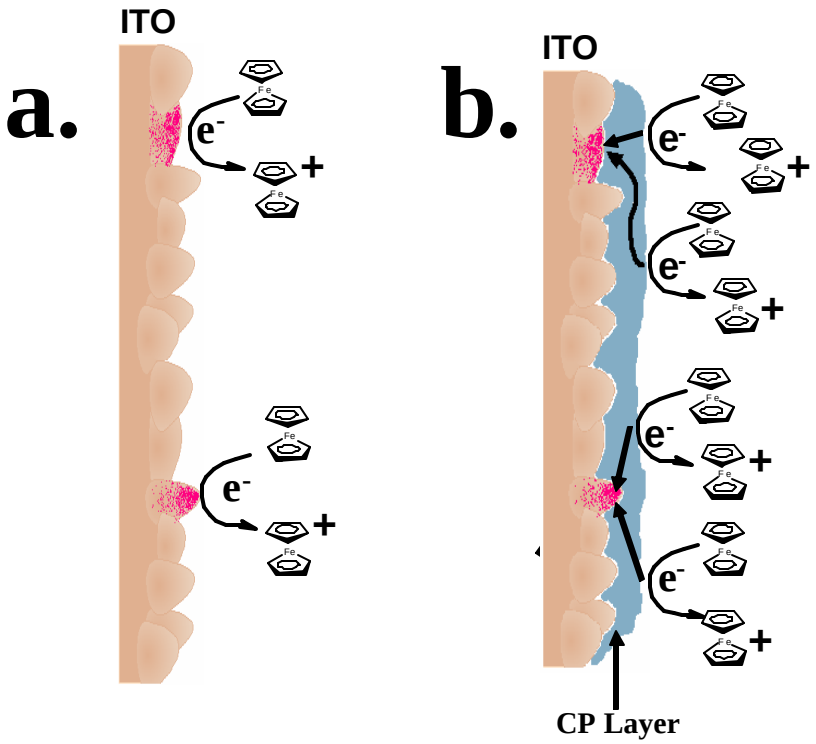

Figure 3.25 Cartoon of the surface of bare ITO, and ITO where a thin layer of PEDOT:PSS has been cast. Bare ITO active transport sites are laterally confined allowing only redox species in close proximity to transfer charge. With the addition of the conductive polymer layer, the active sites of ITO are no longer spatially confined allowing more redox events to occur by “multiple pathways.”

effective active surface area according to equation 4. PEDOT:PSS activity dramatically decreases the effective blocking area, or ca. 93% compared to ca. 99% for the unaltered ITO. It is important to note that the application of CP layers on ITO does not increase active sites as the comparison may imply, and as such, is susceptible to the limitations of ITO as a blocked electrode.

3.5 ELECTROCHEMICALLY GROWN CONDUCTIVE POLYMERS

The successful use of PEDOT:PSS as an electrode modification strategy has lead to the development of electrochemically grown conductive polymer films with the possibility that the individual chains grown radially from active sites, may show a greater increase in electroactivity than a spin cast film. i.e. surface wetting is not required as each individual chain is anchored to the active sites. The principle polymer utilized in these studies is a polythiophene derivative whose monomer is dioxy-ethyl thiophene (PEDOT) which is the main oligomer component in PEDOT:PSS. The strategy is designed so that the nucleation and propagation of the chains are electro-catalyzed on the surface of the electrode and propagate outwards with the application of potential. In this scheme, as much (or little) polymer is generated on the electrode surface to achieve optimal results. 3-TAA was chosen as the precursor to polymer growth and chemisorbed to the ITO sample according to the protocols described above. The thiophene derivative was chosen because of its ability to strongly chemisorb to the ITO surface and may act as a

nucleation site for the subsequent polymer growth with appropriate potentials applied, although no evidence for this has been found.

Figure 3.26 shows the resulting current stemming from the growth of the polymer during simple potential sweeps. In the first sweep, PEDOT is generated without the use of an adsorbed precursor. The nucleation process in this case requires a slight overpotential before growth is observed. However, when PEDOT is generated on a surface that has previously been treated with 3-TAA, polymerization happens more readily. This could be due to the modifier acting as nucleation sites, but likely is due to the slight activation of the surface due to the etching effect already discussed. After the desired growth time, the polymer is stepped to a potential where growth no longer occurs but the chain remains partially oxidized (doped) in order to retain conductivity of the polymer. This can be followed by observing the contact angle measurements listed in Table 3.2 which indicate the doped surface has a contact angle of nearly 10° lower than that of an undoped sample.

3.5.1 Physical Characteristics

Growth of the polymer occurs during application of positive potential in a monomer solution where the onset on clean ITO occurs at ca. 1.0 V vs. Fc/Fc^{+}. Films are generated by stepping the potential to a region where slow growth is observed, typically 0.7 V for the precursor modified ITO. Figure 3.27 shows an AFM image of an ITO sample for a progression of polymer growth times (height and phase images). The raised

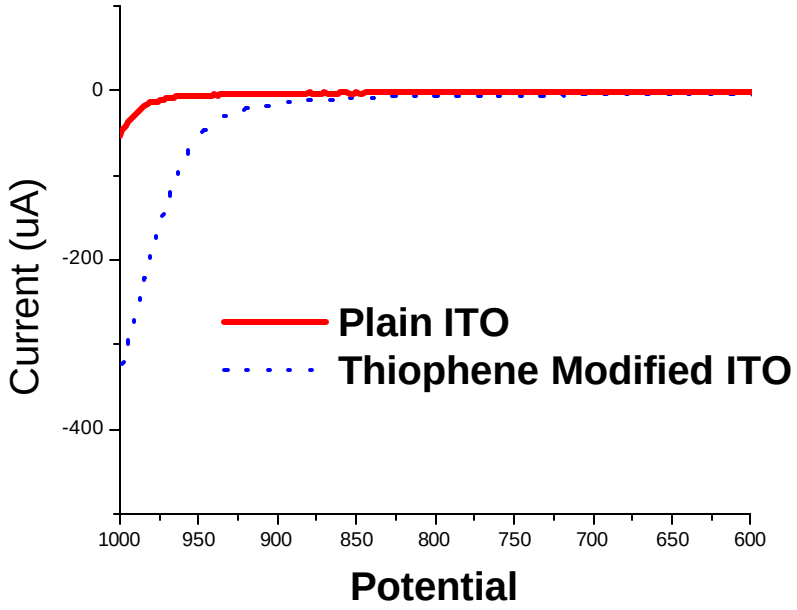

Figure 3.26 Voltammetric characterization of the enhancement in electropolymerization of PEDOT, shown on surfaces of clean ITO and ITO modified with 3-TAA. The sample with adsorbed 3-TAA shows a lowering of the potential needed for polymer nucleation and growth, likely indicating a more active surface created by light etching with 3-TAA modification.

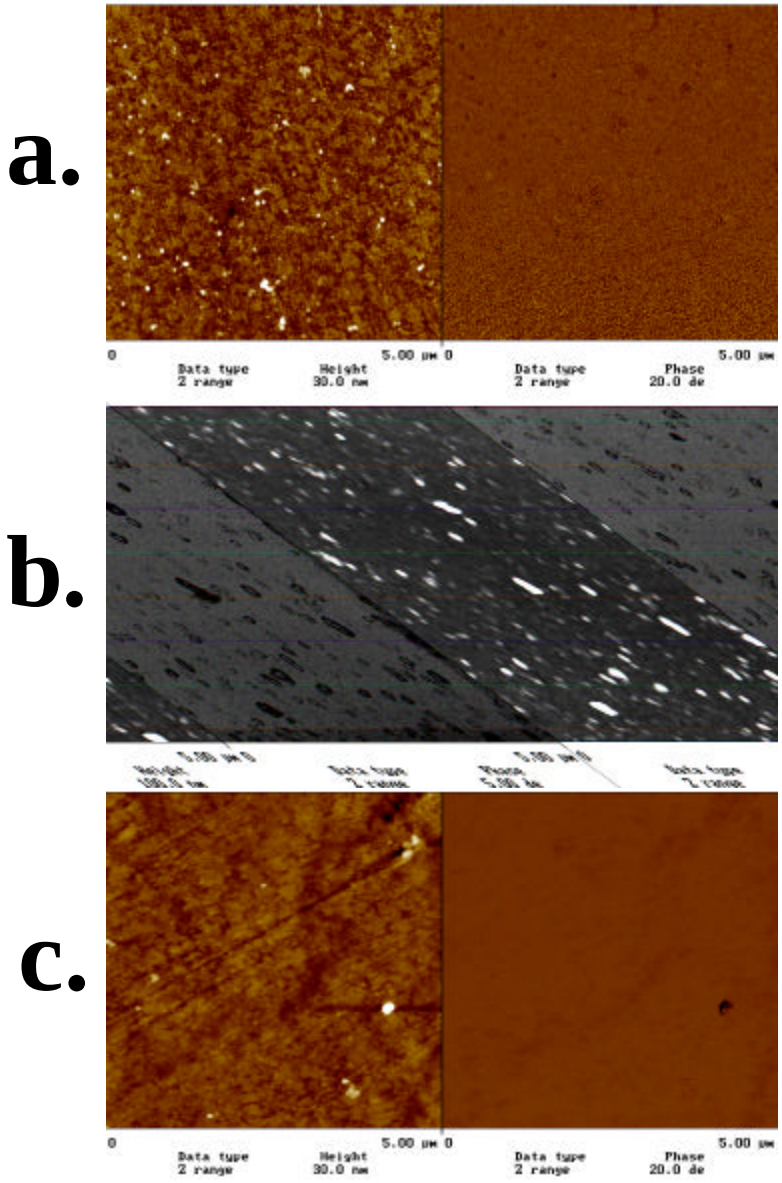

Figure 3.27 AFM images of electrochemically grown PEDOT on ITO surfaces. Images represent a progression of growth from 1 to 20 seconds growth time at 0.8 Volts vs. Ag/AgCl. At 1 second, **(a)** nucleation points scattered randomly across the surface indicate active sites present. **(b)** By 5 seconds growth, domes of expanding polymer continue to grow while less active nucleation sites are now visible. **(c)** At 20 seconds, the polymer has covered the surface together to create a semi-smooth film (rms roughness = 7) with a thickness of ca. 120nm

dome like features seen in the initial images are the expanding polymer chains radiating from the nucleation sites randomly distributed across the image. When compared to polymer growth on clean ITO samples, no difference was observed even though polymerization onset occurs at lower potentials for the precursor adsorbed samples. It is presumed that the presence of polymer growth at these isolated sites regardless of precursor used, is a consequence of ITO supporting limited numbers of active sites surrounded by electrically inactive areas and the main factor controlling the polymer nucleation is these active areas. Surface roughness of these types of films is generally high even when a complete film is grown (Figure 3.27c) with an RMS roughness of ca. 7.0 nm. This is a consequence of the radial growth of the polymer and may be problematic for the use in thin-film devices.

This type of surface can be explored using similar techniques as those described above to determine the effective rate coefficient of other modified ITO substrates. The calculated rate coefficient is similar to that observed for the PEDOT:PSS films at a k_s = 1.0×10^{-2} cm s^{-1}. Because PEDOT retains it conductivity, the same arguments made for the increase in the apparent rate coefficient and for the spin cast PEDOT:PSS films are valid. The domes of polymer allow for multiple paths for charge to transfer to the active sites across ITO, although thicker films are needed to achieve reasonable smoothness which likely leads to the lower rate coefficient.

3.6 CONCLUSIONS

ITO is far from the ideal TCO material used in the construction of organic thin-film devices as shown by the comparisons with platinum which revealed how poorly ITO behaves. However, ITO does possess the best combination of electrical and optical properties currently available for a transparent electrode, consequently devices will continue to rely on ITO as the transparent electrode material. This creates a challenge in working with a material of limited properties, while improving the application and design of novel organic thin-film devices.

These studies have shown that the strategic modification of ITO can have substantial effects on the areas known to contribute to charge transfer events at the electrode/organic interface. Based on the results observed, the simple modification scheme outlined here should have substantial effects when utilizing the modification schemes during the construction of simple organic thin-layer devices.

It has also been shown that the surface composition of ITO films is important to the electronic transfer properties between these types of electrodes and adjacent redox molecules. An incompatible interface likely creates microscopic voids between the electrode and the adjacent organic layers. The voids are problematic in that less electrode surface area is in direct contact with the organics and may focus transport events to areas with intimate contact. This can be somewhat alleviated by choosing a modification scheme for ITO which changes the nature of the surface functionalities such as the small

molecule modifiers described. Regardless of the scheme utilized, the success can be ascertained by observance of the water contact angle on the modified surface.

The state of the ITO surface chemistry is also an important factor to consider for the maximum increase in the observed electron transfer rate coefficient. In this case, chemisorbing small molecule modifiers illustrates the effect changing the surface chemistry can achieve on the overall electronic transfer process. ITO used directly is thought to have a limited number of active sites, presumably defects in the oxide structure, where charge can be transferred between the TCO and the redox molecules of interest. However, utilizing the small molecule modifiers, a light etching of the material opens the surface to allow for a higher population of active sites. This increase in the number of these sites is known to have a positive effect on the observed electron transfer rate coefficient and can be theoretically increased even more by using a modifier with a stronger etching behavior. The possibility to directly interact with the surface oxide is also present, as shown by the formation of a complex between surface bound indium and some of the modifiers used in these studies. The increase in the observed rate coefficients for this complex formation suggests that other ways of interacting with the ITO surface exist to enhance the electron transport properties.

Increasing the charge transport properties of ITO can successfully be achieved through the modification schemes outlined here. However, overall transport is a combination of factors that must be addressed individually. To this end, a method to probe active populations and charge transfer kinetics was developed. This used in conjunction with traditional techniques such as UPS and contact angle measurements

have allowed for the ramifications of modification strategies to be fully explored. This information is presumed to translate in some capacity to thin-film devices constructed utilizing the studied modification strategies.

CHAPTER 4

OPTIMIZED PERFORMANCE OF ORGANIC LIGHT EMITTING DIODES AND ORGANIC PHOTOVOLTIAC DEVICES

4.1 INTRODUCTION

Previous chapters have described the modification strategies and solution based characterization methods for modified ITO electrodes. It has been clearly shown that some of the modification strategies discussed here have the ability to alter the charge injection characteristics and hydrophobicity of ITO surfaces sufficiently that it appears such modifications would be conducive to significant improvements in performance of a solid state device. Both OLEDs and OPVs were therefore constructed with, and without the use of selected modification protocols, in an attempt to improve upon the use of ITO as the bottom contact in both technologies. The modifications discussed here include: ***i)*** Small surface modifying molecules with carboxylate functionalities chemisorbed to the electrode surface. ***ii)*** The growth or casting of conductive polymer thin-films such as EC PEDOT and PEDOT:PSS across over the ITO surface, and ***iii)*** a combination of (*i*) and (*ii*), where small molecule modified ITO samples have CP thin-films grown or spin cast over the modifier before additional device fabrication.

Each of these strategies is aimed at changing the surface chemistries of the ITO/organic interface by altering the properties contributing to total charge injection with

respect to a thin-layer device. Small molecule modification techniques have been shown to significantly alter the ITO surface in a variety of ways. These effects include: ***i)*** Enhancing the wettability of the ITO surface by altering the polarity of surface functional groups to be more compatible with the adjacent organic layers; ***ii)*** Inducing an increase in the population of available active sites across the ITO surface. These increases are likely brought about by a light etching of the electrode surface and subsequent removal of a slight amount of the insulating $In(OH)_X$ material abundant on the surface. ***iii)*** Increasing the in apparent charge injection rate coefficient (k_{eff}), achieved through an elecro-catalytic effect.

Conductive polymer modified electrodes have similarly shown significant increases in the effective charge injection rate. This is likely due to the conductivity of the polymer providing "multiple paths" for charge to diffuse toward just a few active sites on the unaltered ITO surface, increasing the effective electrode activity. CP layers have also been shown to have a polarity more compatible with organic hole transport materials and likely increase the wetting of the electrode surface.

4.2 ORGANIC LIGHT EMITTING DIODES (OLEDS)

Organic light emitting diode (OLED) devices provide a suitable platform for evaluating the effects of ITO modification on charge injection efficiency. These types of thin layer devices are well established, and the mechanisms of charge movement and injection have been thoroughly described.[1-12] Additionally, the incorporation of a

modification step is straightforward and allows for direct comparisons with devices created from unmodified ITO. This study includes modification of the ITO electrode by the small molecule modifiers previously studied: $Fc(COOH)_2$, (p-$OMe)_2$-TPD-X_2, and 3-TAA). Conductive polymer layers are also evaluated by their addition to both unaltered and small molecule modified surfaces consisting of ***i)*** commercially obtained PEDOT:PSS, and ***ii)*** in-house electrochemically grown films of poly(3,4-diethoxy-thiophene). All of these modifications have previously shown significant improvements in charge transfer characteristics with individual testing and are expected to relay these improvements to the solid state device.

4.2.1 OLED RC Circuit Model

In general terms, the simplified behavior of an OLED thin-film device, operating at DC potentials, can be modeled as a simple diode circuit described in Chapter 1 and represented by the RC circuit diagram in Figure 4.1a. This simple interpretation of the RC circuit can be expanded to allow for the elements in the device that may be altered following modification of the ITO surface. Figure 4.1b shows this expanded circuit and includes the addition of more resistance terms. First, the shunt resistance is likely altered by the changing polarity of the ITO surface with respect to organic layers at the electrode/organic interface and a new shunt resistance R_P' is added, where it is expected that $R_P' >> R_P$. As the ITO/organic interface is optimized, by the addition of a

hydrophobic modifier, for example, the population of film defects (and shorts) are reduced and this resistance term should increase, forcing more current to flow through the diode. This is also indicated by low leakage currents measured at low potentials, and reverse bias.

The series resistance term can be divided into several resistance terms, all in series with the diode and with each other. These include: ***i)*** a term related to the internal resistance of ITO (R_{ITO}). This term describes the semiconducting nature of the ITO material and its limitations as an electrode. R_{ITO} is especially problematic when utilizing large area devices where current must travel long distances within the ITO layer before reaching a more conducting contact. Researchers have attempted to limit this term by decreasing the size of the devices, and by the addition of metal "bus bars" deposited on the ITO in an effort to decrease the distance current must flow within the TCO. The magnitude of this term can be estimated based on four point probe measurements and is expressed as the sheet resistance. Modification does little to alter this term which cannot be

readily altered with commercially obtained ITO. However, it can be increased or decreased sharply depending on the source and sputter conditions when constructing the ITO film from scratch. This term is held static in these studies by utilizing similar ITO substrates from the same source sheet; ***ii)*** Electron injection between the electrode and the organic material has been generally neglected by the organic thin-layer device community. However, we suggest that this is an important parameter in the efficient

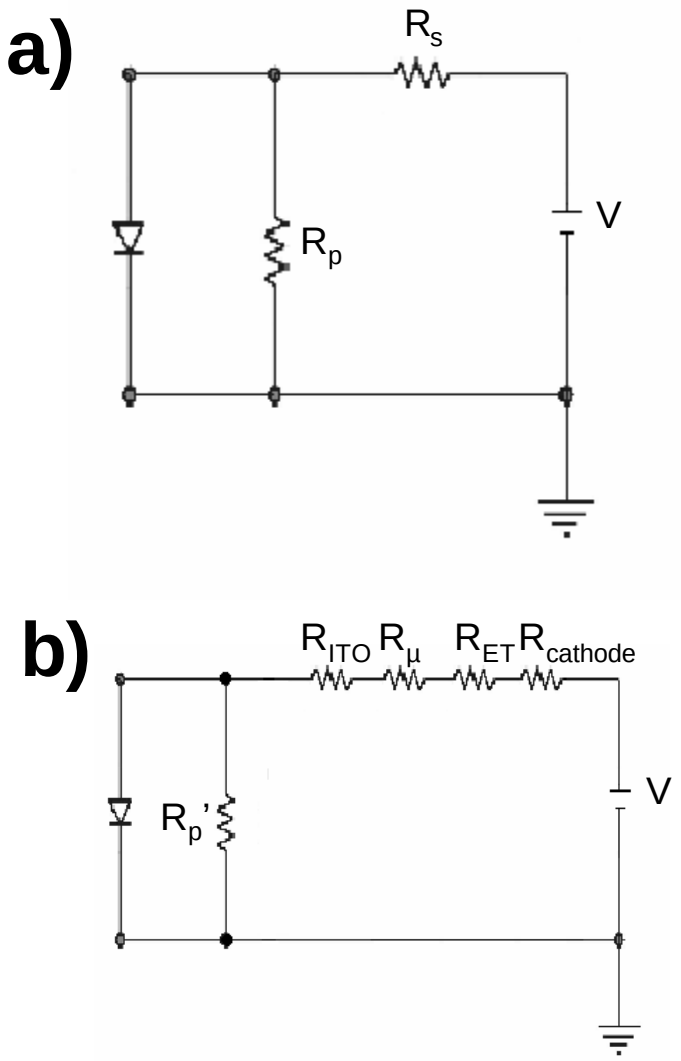

Figure 4.1 Modeling of an OLED thin layer device by simple RC circuit diagrams. **a)** equivalent circuit for a non-modified device showing shunt (R_p) and series (R_s) resistances and **b)** expanded circuit showing the possible effects modification generates in addition to series and shunt resistances, terms due to wettability (R_{wett}), internal nature of ITO (R_{ITO}), electron transfer (R_{et}), and the number of active sites accessible (R_n) can be asserted.

function of these types of devices and can be described as a separate series resistor element (R_{ET}). This is the term most readily altered by ITO surface modification and represents the effects of limited surface activity and slow electron transfer kinetics. R_{ET} is inversely proportional to the effective charge transfer rate coefficient (calculated from solution electrochemistry) and can be decreased dramatically by targeted modification techniques where improvement of electron transfer is two fold. First, etching of the surface may lead to the depletion of less stable $In(OH)_X$ material on the surface and a corresponding increase in the active area of the electrode. Second, certain modifications can lead to an increased intrinsic electron transfer rate coefficient. This may take place when the modifier oxidation potential sufficiently overlaps with oxidation potential of the adjacent organic molecules and act as an electron transfer mediator. The formation of a surface indium/modifier complex species may also result in a change of the rate coefficient, giving rise to an increased electron injection.

Alternatively, this term can be influenced by utilizing a conductive polymer layer on the ITO surface to allow an enhanced interaction with the limited number of accessible active sites on ITO by allowing multiple paths for charge transfer. ***iii)*** The third term represents the resistance due to charge mobility on the interior of the device (R_{μ}). The magnitude of this term is generally dependant on the materials and thickness used for the organic layers (HTL and ETL). These studies hold this term static by utilizing the same construction methods with exception to the addition of PEDOT:PSS layers ***iv)*** The last term described by the model represents those processes that occur at the complementary electrode junction ($R_{cathode}$). Fundamentally, the limitations described

for the ITO/organic junction are also valid for the cathode. This includes conductivity of the cathode as well as electron transfer kinetics with respect to the cathode material and the adjacent organic layer (ETL).

By adapting this new model, the effects modification can have on the modeled circuit can be clearly ascertained. For example, a change in the wettability of the electrode brought about by modification steps directly influences R_P', while changes in the electrode kinetics or active area influence R_{ET}. This allows for the characterization of the most influential terms, and hence, where to focus future research efforts.

4.2.2 OLED Device Construction

In order to ascertain whether modification strategies and the corresponding enhancements observed in solution studies translate directly to the solid state and organic thin-layer devices in general, the same modification schemes developed previously were utilized in the construction of OLED devices and compared to those devices utilizing no modification protocols. There are several types of OLED technologies which could be successfully used for this type of study.[2-6,8,9] However, the type of device constructed for application here were chosen so that any change in device output characteristics reflect the changes brought about by the ITO modification strategies only, and were not incidental to device artifacts and/or random fluctuations in device performance. This

generally limits the device type to those technologies that have been well established, but may not represent current "state-of-the-art" in OLED technology. Care must also be taken to provide ITO samples sufficiently similar for valid comparison. In general there are sufficient variations in ITO composition across a 12" x 12" sheet of this material that one cannot simply randomly acquire the ITO sections for each device. Careful visual inspections on each ITO sheet using reflected light to find regions which are similar in reflectivity and color were used to establish uniform electrochemical performance for TCO films.[30,42] Generally, five OLED devices can be built on each 1" x 1" ITO substrate (approximate area 0.250 cm^2) and the variation in response from device to device is within acceptable limits (less than 0.15 volt differences in onset bias, and less than 7.0 % differences in OLED device efficiencies). The variation in response between 4-5 1" x 1" ITO substrates is likewise less than the variations in response seen due to modification of the ITO substrates.

Figure 4.2 shows the general construction scheme of OLEDs utilized in these studies and as first developed by Tang *et al.*[8] Commercially obtained ITO covered glass was used as the bottom contact material. The completed device consists of two deposited organic layers, a hole transport layer of 4,4'-bis(*m*-tolylphenylamino)biphenyl (TPD) deposited adjacent to the ITO and an electron transport/emissive layer of aluminum quinolate (Alq_3) subsequently deposited, each 50 nm thick. These layers are then capped with a 250nm thick 10:1 Mg:Ag mixture to provide electrical contact as the cathode. Deposition conditions for each layer are strictly controlled for vacuum pressure, deposition rates, and layer thicknesses. This, combined with a rotating deposition stage

remotely located ca. 1 meter away from the source, allows for uniform, reproducible layers without heat damage to the organic layers after metal depositions. Additionally, the deposition chamber is coupled to an atmospherically controlled glove box where device testing occurs to insure against effects that may arise from reactions with oxygen or water. Figure 4.2b shows the finished set of devices on an ITO substrate. The metal band visible at the top is for contact with the ITO in order to decrease the effect of internal resistances. Also ITO samples have been heavily etched directly under the cathode contact points to remove the entirety of the ITO thin-film directly under the contact probes. This prevents "punch through" shorts by removing the possibility of incidental contact between the cathode contact probe, and the underlying ITO electrode if the organic layers are broken.

4.2.3 Small Molecule Modification Response

Modification of ITO substrates was carried out according to the steps outlined in appendix A.2 and are the same as those used in solution electrochemistry studies. Two layer devices were constructed on each modified substrate as well as on non-altered, but solution cleaned ITO samples for comparison. Devices were tested by ramping the bias between anode and cathode with a Keithly 2100 source meter, which monitors J/V

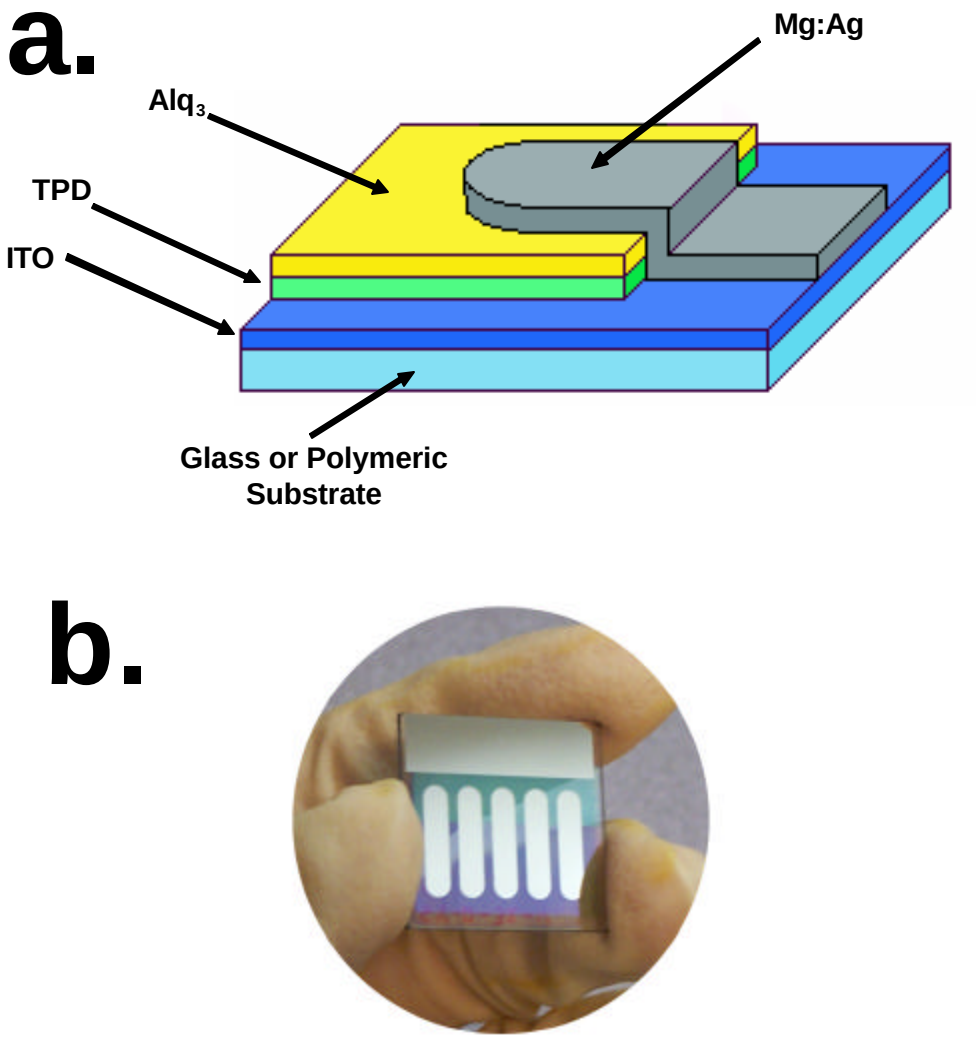

Figure 4.2 **a)** Two layer OLED structure consisting of glass or polymeric substrate, sputtered ITO film, TPD hole transport layer, Alq_3 electron transport and emissive layer, capped with a 10:1 Mg:Ag cathode. **b)** Finished device showing five separate OLEDs on one substrate.

characteristics, while simultaneously collecting any light output with a calibrated photodiode perpendicular to the device face. Luminance (L) verses bias as well as current density (J) vs. voltage plots and corresponding quantum efficiencies can be constructed for each device and analyzed for comparison purposes. Figure 4.3 shows the results for devices constructed with ITO samples and those modified with small molecules $Fc(COOH)_2$, $(p\text{-}OMe)_2\text{-}TPD\text{-}X_2$, and 3-TAA. Figure 4.3a shows the addition of any of the selected small molecule modifiers lowers the onset voltage for the appearance of an electroluminescence with respect to the non-altered ITO counterpart. In nearly all cases, the onset voltage is comparable, ca. 1.0 before the onset of the unaltered ITO device. The forward bias required to achieve ca. 50 cd/m^2 luminance (ca. 50% of average display brightness) is also reduced by 0.5-1.5 volts depending on the modifier used. However, $Fc(COOH)_2$ modified samples show the greatest increase, and a somewhat greater luminosity at the same voltage with respect to the other samples.

Figure 4.3b shows the corresponding current-voltage plots for the modifications of the same set, plotted as log(J) vs. voltage to maximize the contrast between the currents flowing prior to electroluminescence (leakage currents) and those flowing during production of a visible OLED response. At ca. 1.0 volts forward bias, the leakage current in the modified devices on average reach levels ca. 5×10^{-6} A/cm^2 to as low as 5×10^{-9} A/cm^2, as opposed to the unaltered ITO devices which show substantial leakage currents of ca. 1×10^{-2} A/cm^2. This contrast in low bias leakage is generally attributable to a lowering of the pinhole density in the vacuum deposited organic layers and appears to be

slightly better than the reduction in leakage currents achieved with spin-cast PEDOT:PSS layers described below. In addition, space charge limited current values are comparable across the bias potential even with the knowledge that the unaltered ITO devices consist of may pinholes and the associated excess current flow. The device efficiency, measured at a forward bias of 5 volts, nearly doubles when the small molecule modifiers are used (e.g. the efficiency for normally cleaned ITO is ca. 0.55 %; the efficiency for an OLED using either 3-TAA or (*p*-OMe)$_2$-TPD-X$_2$ as a modifier is ca. 0.98 %).

Diode-like behavior and resistance values (R_S, R_P) calculated for the unaltered device show R_S = 0.5 O, R_P = 25 KO, compared to the Fc(COOH)$_2$ modified device which is representative of the general effects seen for modification and shows values of R_S = 0.5 O, R_P = 185 KO. Values for the other small molecule modifications were similar and shown in Table 4.1. The results show a dramatic increase in the shunt resistance of the device, and a drop in the reverse saturation current of nearly 3 orders of magnitude (1.54×10^{-3} to 4.0×10^{-6} µA cm^{-2}). However, the series resistance which was expected to show large changes remained relatively unchanged between each sample (ca. 0.3 O).

These observed enhancements can be explained in a similar manner to those proposed during the solution electrochemical studies. Figure 4.4 illustrates the state of the device for modified ITO vs. non-modified ITO samples. For the non-modified device, the common problems described with incompatible surface conditions are present. This can be seen by the large void at the interface which disrupts the continuity of the film and introduces pinhole defects throughout the device which allow for current leakage and a

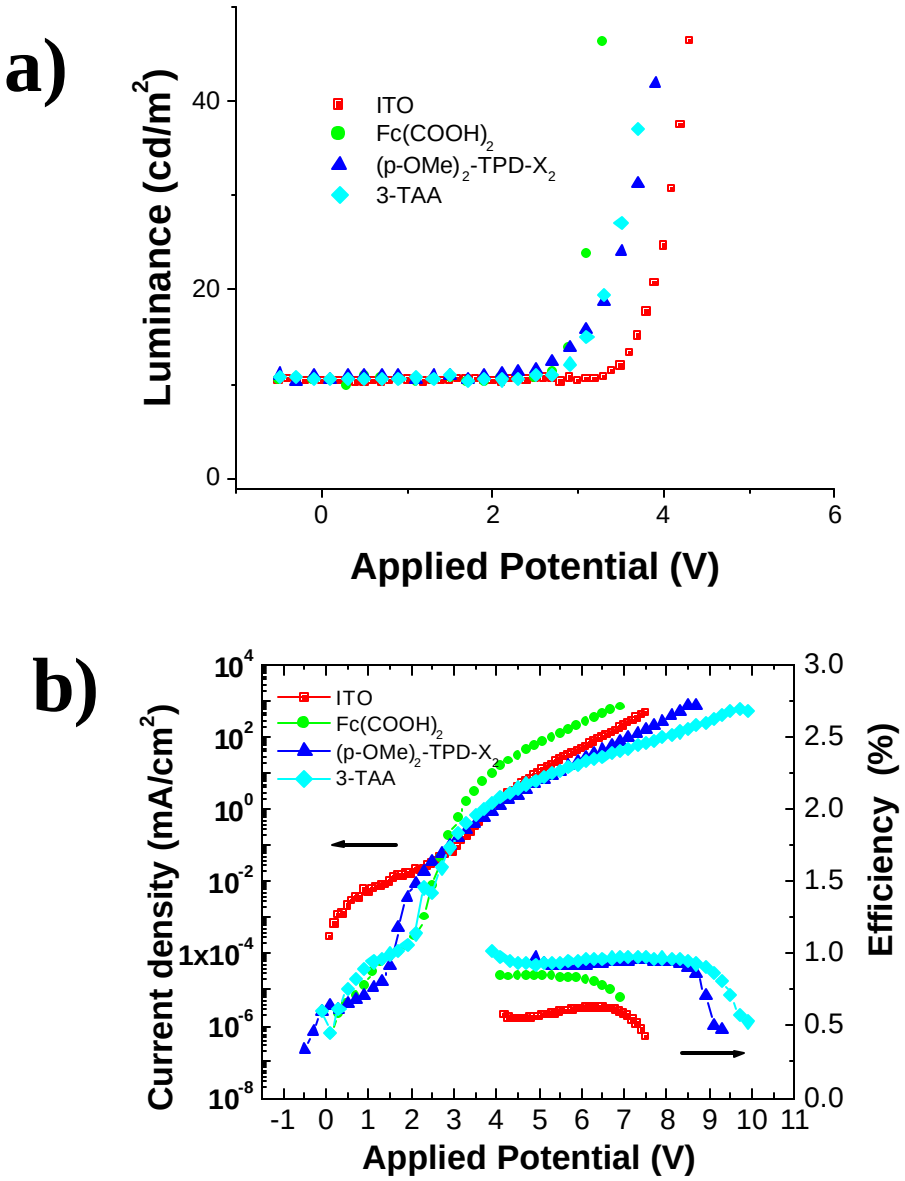

Figure 4.3 **a)** Luminance/Bias curves for OLED devices constructed on non-altered ITO, as well as ITO modified with $Fc(COOH)_2$, $(p\text{-}OMe)_2$-TPD-X_2, and 3-TAA. **b)** current density/Bias as well as quantum efficiency curves for the same samples.

	R_S (O)	R_P (O)	J_0 (μA/cm2)
Unmodified ITO	0.5	2.50E+04	1.54
$Fc(COOH)_2$	0.5	2.19E+05	0.0004
$(p\text{-}OMe)_2$-TPD-X_2	0.6	1.84E+05	0.0009
3-TAA	0.5	1.02E+06	0.0066
Unmodified ITO	0.5	2.50E+04	1.54
PEDOT:PSS	0.9	4.48E+05	0.0036
PEDOT:PSS	0.3	8.79E+02	0.0577
$Fc(COOH)_2$/PEDOT:PSS	0.2	1.18E+07	0.0152
$(p\text{-}OMe)_2$-TPD-X_2/PEDOT:PSS	0.3	4.55E+06	0.025
3-TAA/PEDOT:PSS	0.2	6.88E+06	0.0257

Table 4.1 Series (R_S), shunt (R_P) resistances and reverse saturation current (J_0) calculated from OLED device data for different modification procedures.

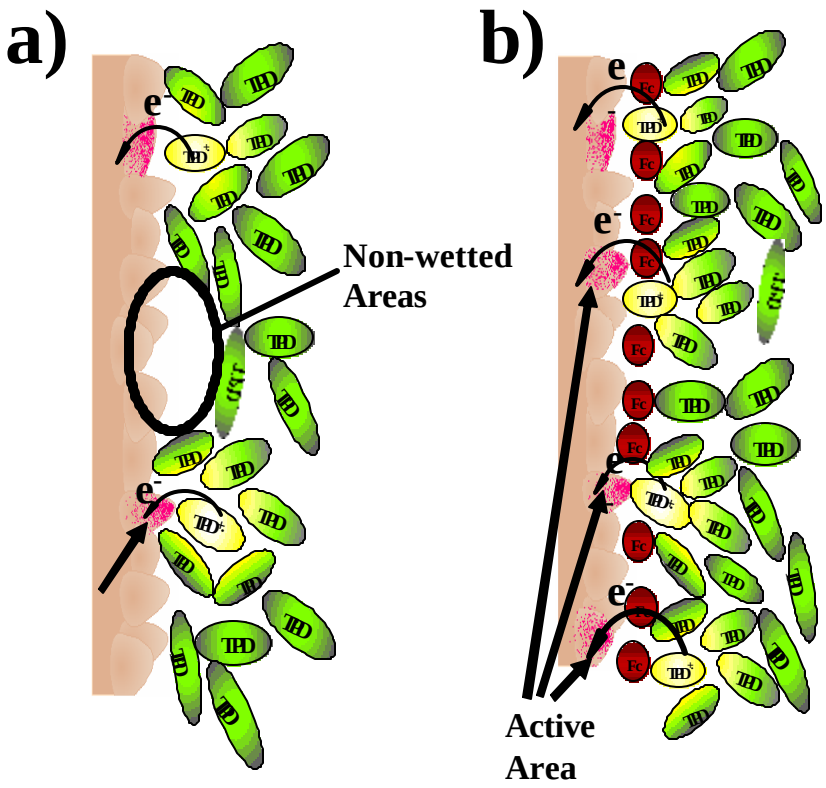

Figure 4.4. Cartoon representation of the ITO/TPD interface for two OLED devices: **a)** unaltered ITO device, which shows pinhole formation due to incompatibility of materials leading to high leakage current and **b)** $Fc(COOH)_2$ modified ITO devices, which show better wetting as well as an increase in charge injection sites.

decrease in the intimate contact between the electrode and organic layer. This is indicated by the large leakage currents (large J_0) that this device experiences at reverse bias. Upon modification the reverse saturation current is greatly reduced. This is most likely due to the modifier changing the polarity of the ITO surface to become more compatible with the adjacent organic, also shown by contact angle measurements, and allowing for a more defect free deposition of the organic film. The increased quality of the film carries over to each successive deposition and results in a lower defect device, in general. This is also evident in the increased efficiencies associated with the modified devices. Other advantages of modification likely include those seen with solution models including, a greater number of active surface sites and a mediated electron transfer rate.

Unfortunately, with the high level of the leakage currents (shorts) from non-modified ITO devices, it is difficult to extract comparable information from the space charge limited regime pertaining to active sites or injection rates. However, the comparable values measured for a pinhole infested device with respect to the modified devices make it likely that the space-charge limited current for the modified devices would be larger than non-modified counterpart due to the additional active transport sites and increased rate of electron transport as demonstrated with solution studies.

We expected to see a substantial decrease in R_S; however, these results indicate little to no change in the value. This is likely due to the large area of the devices without the use of additional bus bars. In this case, current from the device must travel within the resistant TCO film for comparatively long distances to complete the circuit. The effect is

a dominating R_{ITO} term and when combined with mobility resistances ($R\mu$) effectively mask any changes to R_{ET} that may be occurring.

4.2.4 PEDOT:PSS Modified Response

One of the most common ITO modification techniques in use is the casting of a thin layer of conductive polymer such as PEDOT:PSS over the electrode before the deposition of the subsequent organic layers. Solution electrochemical studies show that a large improvement should be anticipated when constructing a device with PEDOT:PSS opposed to one constructed with unaltered ITO. These devices are constructed according to the outline stated above except a ca. 50 nm PEDOT:PSS layer has been spin cast and annealed prior to placing in the deposition chamber as described in appendix A.2. Figure 4.5 shows the resulting L/V and J/V plots based on devices of this kind.

With the addition of the CP layer, the onset voltage for the electroluminescence to reach ca. 50 cd/m^2 luminance is reduced by nearly 2 volts. Additionally, at low biases, the ITO-only device again shows a large leakage current at nearly 5x10^{-2} A/cm^2, while the addition of PEDOT:PSS modifier, the leakage current decreases by nearly 3 orders of magnitude to ca. 5x10^{-5} A/cm^2 at 1 V bias. Reverse saturation current is also greatly decreased from 1.54 μA cm^{-2} down to 3.6 x 10^{-3} μA cm^{-2}. It is also interesting to note that

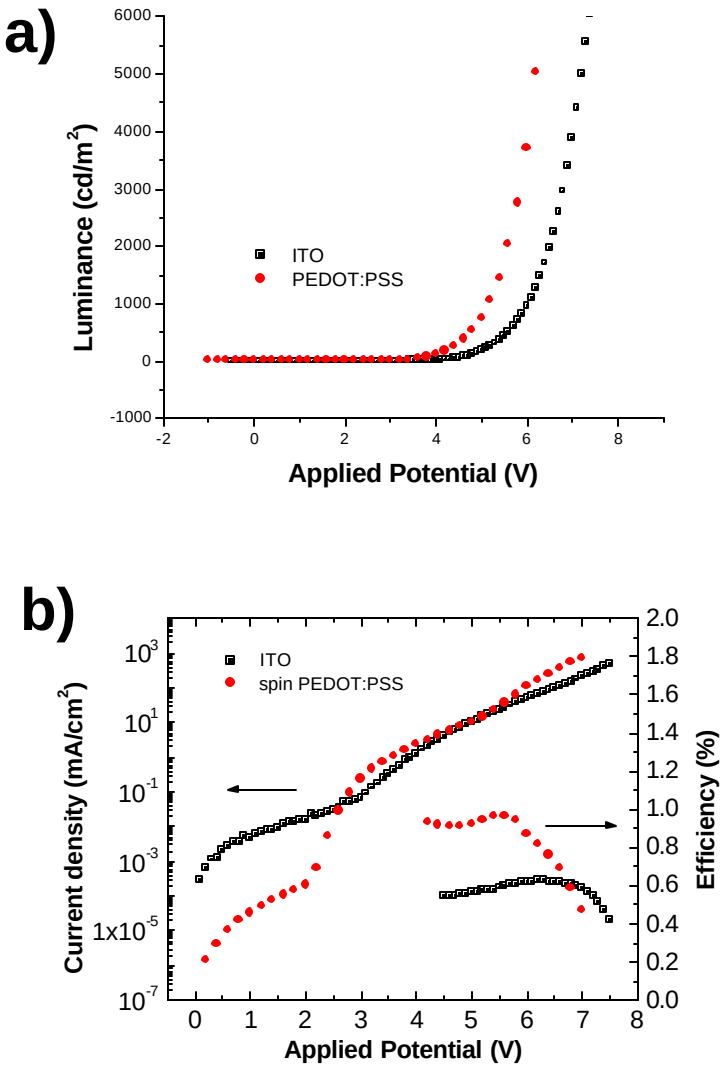

Figure 4.5 **a)** Luminance/Bias curves for OLED devices constructed on non-altered ITO, as well as ITO spin cast with PEDOT:PSS. **b)** current density/Bias as well as quantum efficiency curves for the same samples.

given the large leakage current present in the ITO-only device, the space charge limited current of the CP modified device is greater between biases of 3 and 7 volts. Device efficiency is also nearly double that (1.0% and 0.5% respectively) of the ITO-only device at its peak at a bias of ca. 5.5 V. However, R_S for the modified device increases by nearly double to 0.9 O from 0.5 O respectively. R_p also shows a substantial increase from 0.25 KO for the unmodified sample to ca. 4.5 KO for the PEDOT:PSS containing device.

The results seen here can be explained using a cartoon of the surface conditions, shown in Figure 4.6. The PEDOT:PSS layer, due to is polarity, is more compatible with the ITO surface forming a thin-film with less defects than direct deposition of organic molecules alone which creates defects and inconsistencies leading to pinholes and leakage current. The total level of leakage is still above that of the small molecule modifier based OLEDs which indicates some defects still exist. This is probably due to the polarity difference between the deposited organic molecules and CP cast on the ITO samples. Experiments show a difference of contact angle measurement of ca. 20°, where the small molecule modified ITO is considered a more compatible surface with respect to organic moieties than that of the CP.

Space charge limited current levels are also high even compared to the ITO-only device that exhibits known pinhole leakage. This can be explained again by the figure in which the CP allows multiple paths to the open active sites on the ITO surface. With the

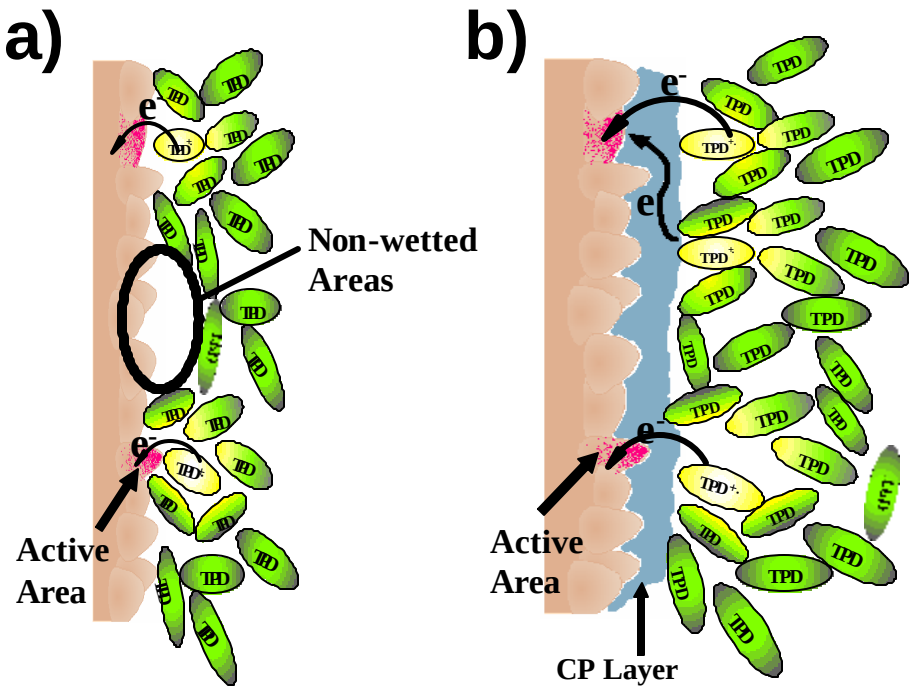

Figure 4.6. Cartoon representation of the ITO/TPD interface for two OLED devices: **a)** unaltered ITO device, which shows pinhole formation due to incompatibility materials leading to high leakage current and **b)** ITO spin cast with 50nm PEDOT:PSS showing better wettability and multiple pathways for charge injection.

relief of a lateral confinement, more current is allowed to flow through the device. This leads to greater efficiency as observed with the spincast CP modification scheme.

While an increase of R_S in this case might seem shocking, the increase was entirely expected. One of the drawbacks when utilizing PEDOT:PSS layers is the limited conductivity (with respect to thickness) these layers exhibit. The increased value is in line with the addition of a CP layer this thick.

4.2.5 Small Molecule Coupled with PEDOT:PSS Response

Figure 4.7 shows the L/V and J/V curves for a series of OLED devices created using ITO samples with a spin-cast PEDOT:PSS layer as well as ITO samples utilizing a combination of PEDOT:PSS layers applied after modification of the surface with the small molecule modifiers $Fc(COOH)_2$, 3-TAA and $(p\text{-}OMe)_2$-TPD-X_2. Similar to the previous use of small molecule modifiers, the bias required to meet a 50 cd/m^2 luminescence is decreased by nearly two volts when compared to the PEDOT:PSS counterpart. Additionally, the presence of the modifier lowered the leakage current at 1.0 V by a factor of 10 versus the PEDOT:PSS-alone treatment, and reverse saturation current reduced by half, 0.05 to 0.025 mA/cm^2 respectfully, as well as elevating the space charge limited current levels between 2 and 10 times as the bias is increased from

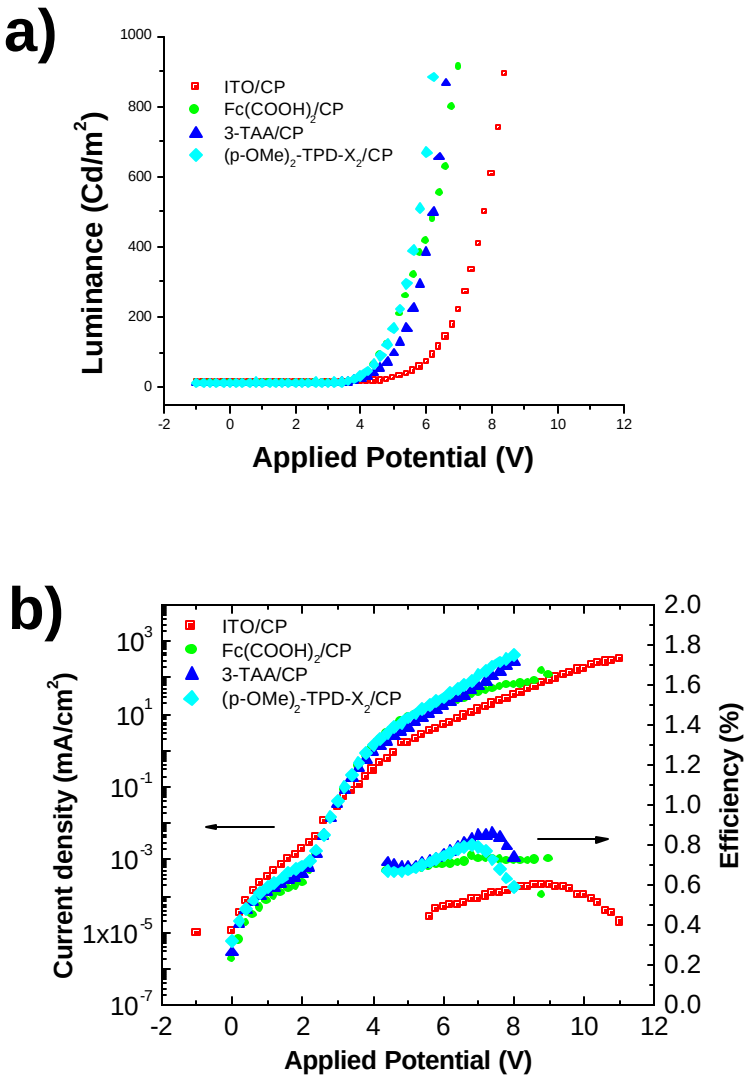

Figure 4.7 **a)** Luminance/Bias curves for OLED devices constructed on spin cast PEDOT:PSS film on non-altered ITO, as well as ITO modified with small molecules $Fc(COOH)_2$, $(p\text{-}OMe)_2$-TPD-X_2, and 3-TAA . **b)** current density/Bias as well as quantum efficiency curves for the same samples.

3.0 to 8.0 Volts. The presence of the small molecules also increased the total device efficiency by ca. 40-50% (0.65% to 0.9% efficiency) with respect to PEDOT:PSS only device. R_S values remained unchanged with respect to modifications with values of ca. 0.3 O for all samples. R_P however, increased from 0.85 KO to 4.5 KO and 10 KO for the (*p*-OMe)$_2$-TPD-X_2 and Fc(COOH)$_2$ respectfully.

It is clear that the presence of the small molecule as intermediate between the bare ITO surface and the conducting polymer can play an important role in device operation. The increase in device performance observed for this system can be seen as a combination of those factors discussed for the previous devices. Figure 4.8 outlines this in cartoon form. The lowering of the leakage current is evidence of a more pinhole free device. However, in this case the organic layers are not in direct contact with the ITO surface. This suggests that the PC film itself is affected by the changing of the ITO surface chemistry and is more susceptible to the polar ITO surface than originally thought. The increase in the space charge limited current can be seen as direct evidence for an enhancement in charge injection when utilizing these small molecule modifiers. Because there is no direct contact between the modifiers and the organic molecules, the effects seen arise due to either an increased population of active sites brought about by the light etching of ITO during the modification process and/or an increase in the apparent charge transfer rate coefficient. The increased current flow through the device leads to the ca. 2.0 V lower biases needed to achieve 50 cd/m^2, as observed.

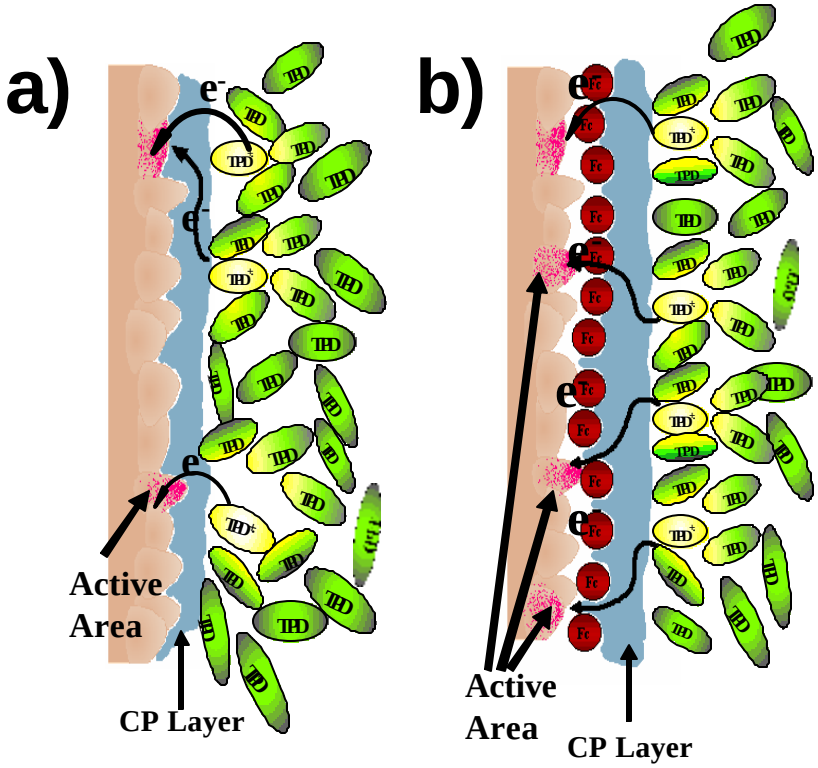

Figure 4.8. Proposed representation of the ITO/TPD interface for two OLED devices: **a)** Unaltered ITO with a 50 nm PEDOT:PSS spin cast and **b)** $Fc(COOH)_2$ modified ITO spin cast with 50 nm PEDOT:PSS.

It should also be noted that comparable changes in OLED performance, and "hole-only" organic diodes, have been noted with this same set of small molecule modifiers, in single layer devices.[44] In those experiments single layer OLEDs based on poly-vinylcarbazole (PVK) films, doped with high concentrations of Alq_3 or its sulfonamide derivative, $Al(qs)_3$, to form devices with the configuration ITO/PVK:Alq_3/Al, or just ITO/PVK/Al "hole-only" devices. In both device types addition of the small molecule modifier lowered the onset voltage for current flow in the forward bias direction, in the case of the OLEDs, these small molecule modifiers also lowered the "turn-on" voltage and increased the overall OLED device efficiency

4.3 ORGANIC PHOTOVOLTAIC CELLS (OPV)

Modification strategies can also be adapted for use in other organic thin layer devices. Organic photovoltaic cells represent another test bed for the modification strategies outlined here. The construction is similar to OLED technology and still allows modification to the substrate without affecting other device aspects.

4.3.1 RC Circuit Modeling of OPV Cells

A similar argument to the OLED equivalent circuit can be made for an equivalent RC circuit that describes an OPV. Standard and expanded circuit diagrams are shown in Figures 4.9a and 4.9b. Thin film OPV cells can be modeled as a simple photoactive diode as shown. R_S is again the series resistance and R_P is the shunt resistance as described earlier. Although it is clear that if pin-hole free films can be formed with materials which are poor dark conductors (high R_P values are achieved) that the observed photopotential will be dictated by the frontier orbitals of the organic constituents of the thin films, and the major loss of PV power will be through high values of R_S. This series resistance is expected to arise from ***i)*** the linear addition of contact resistances and the resistance to charge flow within the TCO film itself, ***ii)*** resistances arising from low charge mobilities within the thin organic layers, and ***iii)*** resistances arising from low rates of charge transfer at both the anode and cathode interfaces.

Similar arguments can be made for the splitting of R_p and R_s resistance values as shown in the Figure. Successful interface modifiers should decrease the terms R_{ET} leading to a lower total resistance in series with the diode, while an increase of R_P' should be observed. The portion of R_S contributed by slow heterogeneous charge transfer, R_{et} is again proportional to $1/k_{ET}$, where k_{ET} is the heterogeneous charge transfer rate coefficient (e.g. for oxidation/hole injection at the ITO/organic interface).[41] The primary role of the ITO surface modifiers discussed here can therefore be to increase k_{ET}, by both mediated

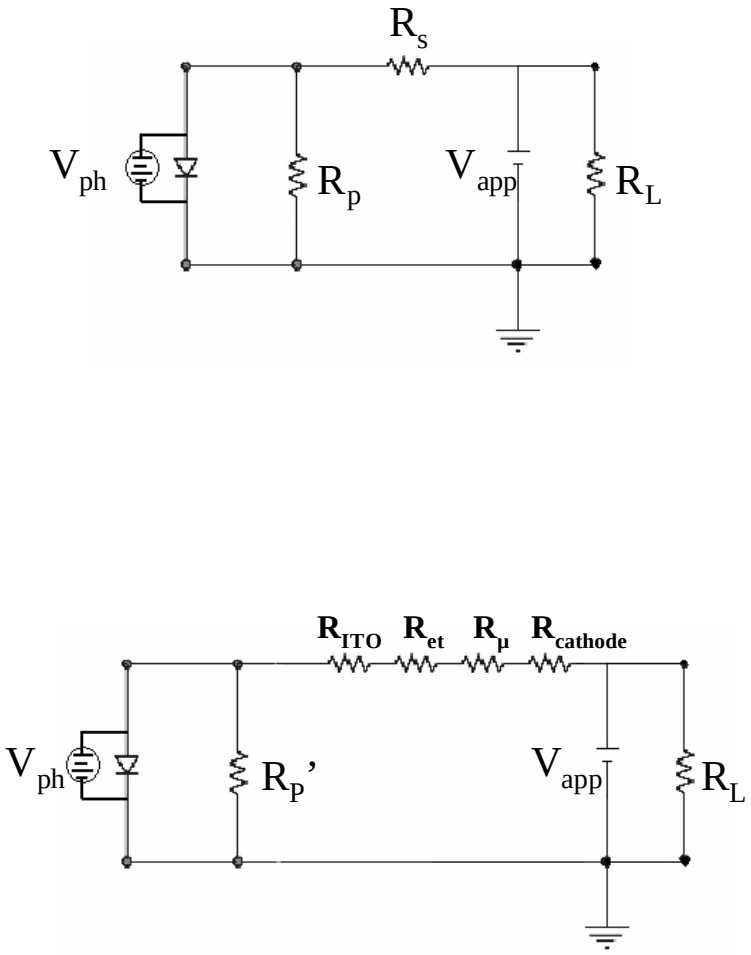

Figure 4.9. Modeling of an OPV thin layer device by simple RC circuit diagrams. a) equivalent circuit for a non-modified device according to simple photo active diode showing shunt (R_p) and series (R_s) resistances as well as the load resistance (R_L) and the applied voltage (V_{app}) and b) expanded circuit showing the possible effects modification generates in addition to the previous terms, elements due to wettability and surface activity (R_p'), internal nature of ITO (R_{ITO}), electron transfer (R_{et}), and the effects from the opposite contact ($R_{cathode}$) can be asserted.

electron transfer and/or increasing the number of active sites for electron transfer on the ITO surface, and lowering the reorganization energy for ET at the organic layer/ITO interface[42] as well as increasing R_P' by limiting the amount of pinholes formed.

4.3.2 Organic Photovoltaic Response

Characterization of these ITO substrates as anodes in an OPV cell configuration was carried out with a vacuum-deposited multilayer configuration as shown in Figure 4.10. Again, a well established OPV protocol, described by Forrest,[12] was chosen as the test bed. In this case, a phthalocyanine/C_{60} multilayer configuration was selected which had been shown to provide power conversion efficiencies of ca. 2–3.6 %, and which could be reproduced at lower, but consistent efficiencies. These multilayer cells were constructed in a vacuum chamber coupled to an Ar-glove-box characterization chamber to isolate atmospheric contamination. Base substrates were prepared by utilizing solution cleaned modified ITO substrates with the small molecule protocols as well as the unaltered ITO substrates, over which, either spin cast PEDOT:PSS layers, or electrochemically grown PEDOT:ClO or PEDOT:PSS layers were deposited and annealed. Following base preparation, sublimation-purified copper phthalocyanine (CuPc) (Aldrich), C_{60} (MER Corp.) and bathocuprine (BCP) (Aldrich) were vacuum deposited at ca. $1x10^{-6}$ Torr in a house built deposition chamber, for thicknesses of ca. 20 nm, 40nm and 10nm respectively. Following vacuum deposition of the final organic

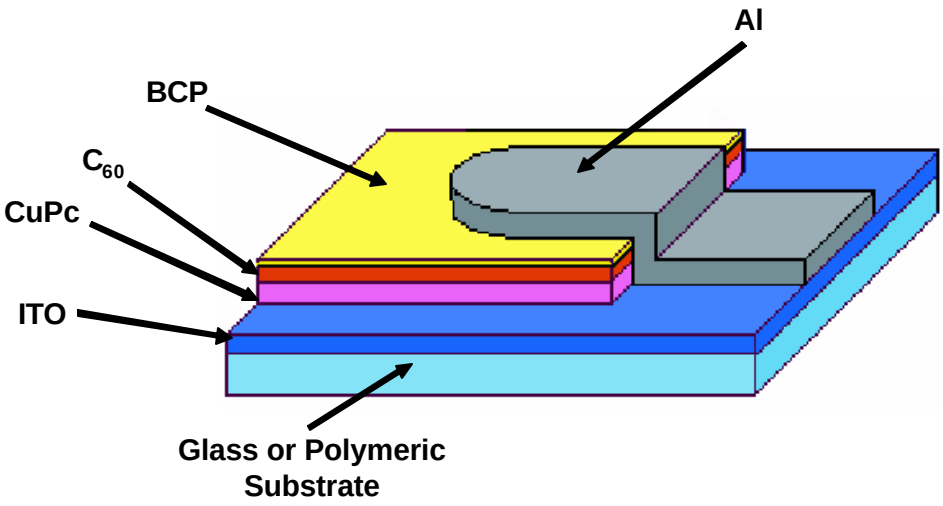

Figure 4.10 Device structure for OPV thin layer devices used here. Devices consist of a base of ITO sputter deposited on glass or polymeric material with a thin (ca. 50nm) CP layer, either spin cast PEDOT:PSS or electrochemically grown PEDOT:ClO_4^-, followed by vacuum deposited layers of copper phthalocyanine (20nm), C60(40nm) and bathocuperin(10nm). Capped with an aluminum anode (150nm).

layer, PV cells were exposed to glovebox atmosphere for ca. 5–10 min while a mask was fitted over the ITO substrate, the assembly was reintroduced to vacuum and an aluminum cathode (150 nm) was evaporated over the device. Characteristics of the devices varied within acceptable limits from device-to-device. Changes in current/voltage behavior, cell efficiency, etc. were tracked as a function of changes in ITO modification procedure.

Figure 4.11 a and b are typical for OPV data obtained for devices created on small molecule modified ITO, followed by spin-cast PEDOT:PSS layers. The Figure shows J/V plots for unaltered ITO/PDOT:PSS samples (Figure 4.11a) in the dark as well as 3 illuminations of white light, 25,50 and 75 mW/cm^2. Figure 4.11b shows that, modification of the ITO substrate with 3-TAA followed by spin-casting of the PEDOT:PSS layer leads to improved PV activity over that seen for the unmodified ITO substrates, at 50 mW/cm^2, $V_{O.C.}$ is increased slightly to ca. 0.414 volts, and $J_{S.C.}$ is increased from 0.26 to 3.4 mA/cm^2 (a relative increase of 31%). Although only modest increases in fill factor are seen (FF 0.38-0.40), the power conversion efficiency increases by ca. 40%, up to 1.14% for the 3-TAA modified devices. Also, higher short circuit currents are observable for higher light intensities with no loss of fill factor. Comparable responses were obtained for ITO substrates modified with $Fc(COOH)_2$ and (p-OMe)$_2$-TPD-X_2. These effects can be explained in a similar manner to those seen in OLED device configurations. A majority of the increases are obtained through the etching of the ITO during the modification process exposing a greater number of active transport sites as previously described, while a portion can be attributed to increased charge transfer rates.

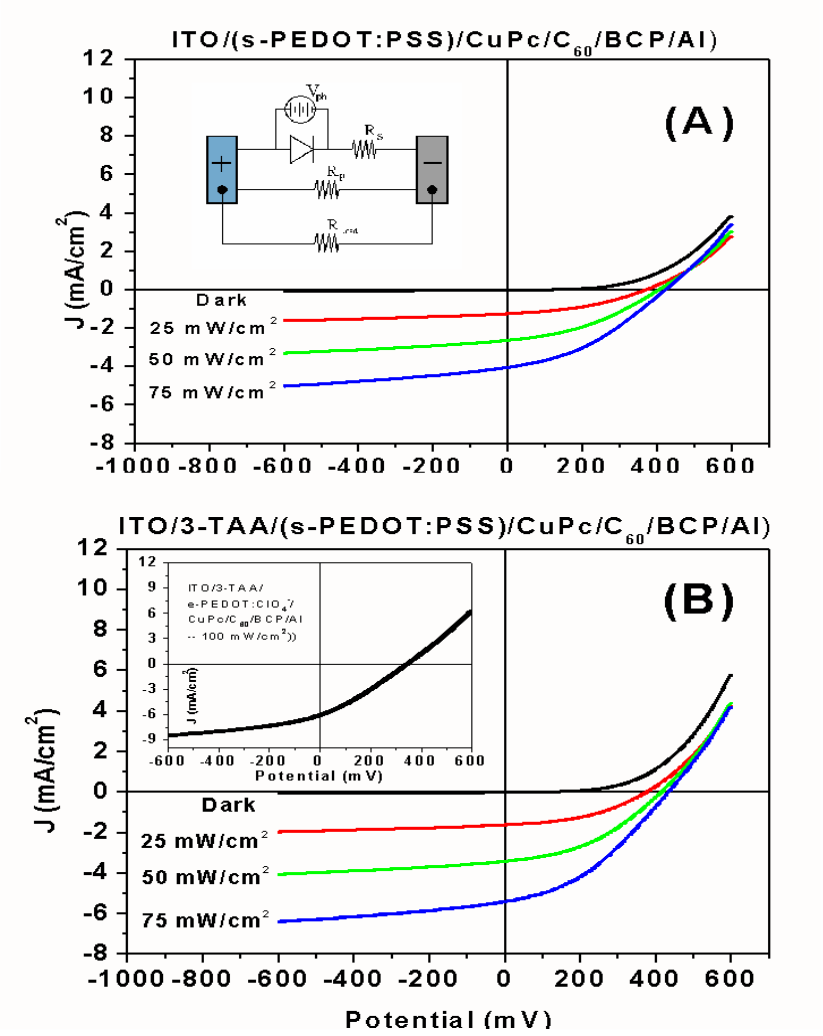

Figure 4.11 Current density vs. voltage plots for ITO/CuPc/C60/BCP/Al OPV cells under no, and 3 different white light illumination intensities. **a)** unaltered ITO substrates followed by spin casting of PEDOT:PSS and **b)** ITO substrates modified with the 3-TAA small molecule modifier.

Similar cells were constructed with electrochemically grown PEDOT films over the 3-TAA modifier, at both 2.5 and 5.0 second growth intervals. The *J/V* response shown in Figure 4.11b arises from a PEDOT film grown for 5.0 seconds, and shows comparable $J_{S.C.}$ values, but lower $V_{O.C.}$ values than even the unmodified ITO films. Thinner PEDOT films (2.5 seconds growth, Figure 4.11b inset), however, show a substantial improvement in response and at light intensities of 100 mW/cm^2, $V_{O.C.}$ is increased to ca. 0.35 volts, and $J_{S.C.}$ is increased to 6.1 mA/cm^2. As seen with many other organic PV cells,[31] highest fill factors (ca. 0.5) are seen at the lowest illumination intensities (dropping to ca. 0.3 for the 100 mW/cm^2 illumination), and R_S values can be cut from ca. 8 to 4 ohms by the prior modification of the ITO substrate. Such decreases in R_S on PV cells which only differ by the simple modification of the ITO substrate and/or electrodeposition vs. spin-casting of PEDOT layers, confirm how critical the electrical contacts of these organic layers are to the ITO substrates in these emerging technologies.

4.4 CONCLUSIONS

Transparent conducting oxide films are likely only to increase in their importance with emerging technologies based on energy conversion or display applications. Their surface chemistries, however, are complex, and begin changing immediately upon first atmospheric exposure following their deposition in high vacuum environments. In the case of commercially available ITO thin films, there is concern over the complexity of

their surface composition, the variability in work function, electrical activity, and the difficulties in obtaining reproducible electrical performance from these materials. Modification of these anodes with spin-cast conducting polymer films, such as PEDOT:PSS, has been an appealing short-term solution to this problem, and has made possible many of the recent successes in the optimization of OLED and OPV technologies. However, while these spin-cast films offer vast improvements over unaltered ITO, it is unlikely that these films take full advantage of the available, mediated transfer and/or electronically-active sites on the ITO surface. Unfortunately, current flow across the ITO/organic interface is still carried by only a fraction of the geometric area. Strategies designed to directly access the electronically active sites on the ITO surface, and to maximize the density of those sites, are clearly desirable. This is accomplished by the use of small molecule modifiers which lightly etch the surface to expose greater populations of active transfer sites, form surface bound complexes with lattice indium for increased transfer rates, mediate charge across the interface, and provide better wetting surfaces with respect to the adjacent organic layers.

By combining small molecule modification procedures with current CP based techniques, the potential to gain full advantage of the known enhancements can be realized. This is shown clearly above and indicates the importance the surface chemistry of ITO is, with respect to this type of technology. More importantly, it has been shown that solution based characterization procedures can be correlated to devices built in the solid state. This is an important aspect of this work as the device operations can successfully be broken down to individual components. This allows for a more

systematic approach to the enhancement of the ITO electrode and organic electronic devices in general.

CHAPTER 5

ELECTROCHEMICALLY GROWN POLYMER NANOSTRUCTURES: DIFFRACTION GRATINGS

5.1 INTRODUCTION

There has recently been substantial interest in the characterization and exploitation of certain materials where changes in electrochemical and optical properties may be induced as a function of the chemical composition of the surrounding environment.[1-16] In a variety of formats, electrochemically-formed polymeric materials may be effective transducers of an environmental stimulus and have the potential to modulate the optical and electrochemical response of the polymer, showing potential as both chemical and/or biochemical sensors.[4,6,17-21] However, changes in the index of refraction (*n*) for the material may also represent a promising indicator for environmental stimulus.[22-25] Changes in *n* may be brought about by environmental conditions which alter the dielectric constant of the bulk material by displacing interstitially packed entities, such as electrolyte ions, and replacing them with either higher or lower index materials. The changes in *n* resulting from this displacement would seem readily accessible for measurement and analysis purposes. However, only a limited assortment of techniques, aside from surface plasmon resonance, have taken advantage of the changing index of refraction to study environmental stimulus with respect to these types

of materials. This chapter outlines a promising technique which takes advantage of changes in potentiometric character, refractive index and adsorptivity to probe changes in the surrounding environment.

It has long been known that microscopic structures on smooth surfaces can be constructed with micro contact printing (μCP) techniques. Patterned SAMs formed by μCP have many applications, including microfabrication,[26-31] wetting and cellular adhesion,[34] as well as analytical studies involving scanning electron microscopy,[32] or scanning probe microscopies.[33] One of the most popular applications of μCP is the stamping of alkane-thiol SAMs onto gold surfaces to create intricately patterned surfaces. In this process, alkane-thiol moieties chemisorb spontaneously onto the gold surface, following the loss of the sulfur bound hydrogen, to form a stable, adsorbed, alkane-thiolate. Additionally, a wide variety of organic functional groups can be incorporated into this surface (or on the interior of a stamped monolayer) depending on the alkane-thiol used. SAMs produced in this way can therefore be tailored to provide a wide variety of material properties, wettability, and protection against chemical etchants; and are especially relevant to many applications.

Alternatively, if the alkane chain utilized has significant insulating properties, these SAMs can be used to pattern the electrochemical reactivity of the gold surface. In this fashion, polymer structures based on simple embossed structures such as blazed angle diffraction gratings, can be constructed using micro-contact printing processes followed by the electro-catalyzed polymerization (μCP-EP) of either polyethylenedioxythiophene (PEDOT) or polyanaline (PANI) to form diffraction grating-

like structures with sub-micron features. These grating-like structures can then be studied by observing the modulation of diffracted light with respect to an environmental stimulus which may affect the efficiency of the diffracted light by altering the absorptivity, and/or index of refraction of the polymer. We show that this process can complement SPR as a method to exploit refractive index changes brought about by changes in potential and analyte concentrations.

5.2 DIFFRACTION GRATINGS

Simple diffraction of light may occur when a wavefront of monochromatic light strikes a barrier containing a narrow aperture or slit. In the process of passing through the slit, the wavefront spreads out, creating well known diffraction patterns. If a number of these slits are introduced into the barrier, constructive and destructive interference is set up between the waves passing through each slit, resulting in a diffraction pattern which can be characterized by equation 1:

$$m\lambda = a\ (\sin\ q_i) \qquad (1)$$

Where m represents the order of the diffracted light, λ indicates the wavelength of the light, a is the space between the slit and q_i the angle of diffracted light. This pattern (Fraunhofer diffraction) is characterized by a central intense band (zero order) bordered

on each side by bands of decreasing intensity, with each band separated by areas devoid of light. With the addition of polychromatic light, the diffraction equation dictates that each wavelength must be separated into different diffraction angles giving rise to multiple patterns of separated wavelength bands. This same simple description can be expanded for a reflective, ruled structure (grating) where each groove simulates a separate diffracting slit. The most common type of these structures is a diffraction grating where features are mechanically embossed into a reflective surface such as metal or glass, although this treatment applies to many other types of gratings as well.

5.2.1 Blazed Gratings

Figure 5.1a illustrates the general geometry of a blazed angle diffraction grating. Modern gratings are characterized by a number of angled bevels equidistant across the grating face. Typically, spacing is on the order of 1000-10000 features per millimeter with variable angles ranging from 5° to 40° depending on the application.[35] In this case, light impinges upon the faces of the grating and is reflected across the edge of the bevel, this close interaction sets up interference patterns which dictate that when the difference between light from adjacent bevels equals some integral multiple of the wavelength λ of the light, the light will be "in phase" leading to constructive interference; and at all other

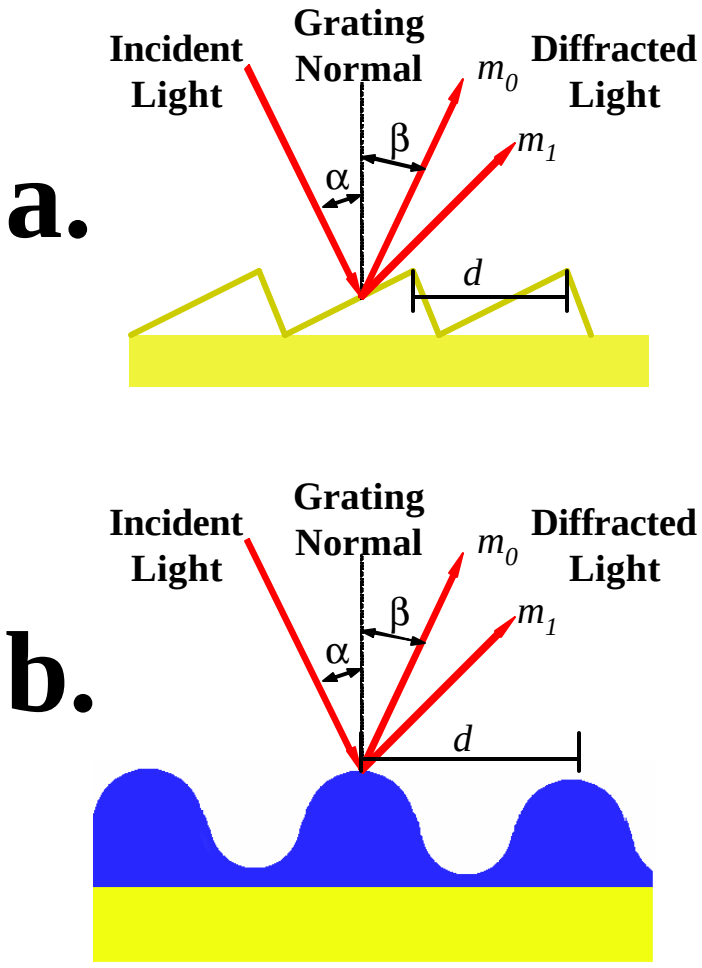

Figure 5.1 Ray diagram showing the diffraction of light on (a) simple blazed diffraction grating where diffraction properties are primarily due to interference patterns from the feature edges, and (b) a holographic grating consisting of a base of reflective gold and features of photoresist.

angles, there is some measure of destructive interference. This behavior is expressed by the common grating equation:

$$m\lambda = d\,(\sin\alpha + \sin\beta) \qquad (2)$$

Where the integer m is the order of diffraction, λ is the wavelength of the light, α and β are the angles of incident and diffracted light respectively, and d is the spacing between the bevels. The efficiency of these gratings is typically limited by the reflectivity of the grating material and the quality of the surface, generally ranging between 70-90%. However, other types of gratings incorporate absorptive materials as a portion of the grating, generally the ruled features, and the resulting structure must abide by the properties of the material used.

5.2.2 Holographic Gratings

A grating structure may be formed by the interference fringe field of two parallel lasers whose standing wave pattern is exposed to a polished substrate coated with photo resist. Processing of the exposed structure, results in a pattern of straight lines with a sinusoidal cross section, described as a holographic diffraction grating (Figure 5.1b).

Diffraction of light by these gratings is roughly the same as blazed angle gratings. However, due to the uniformity of the features, holographic gratings produce less stray light than ruled gratings. They can also be produced with large numbers of grooves per millimeter (ca. 10,000) for greater theoretical resolving power, and production costs for this type of structure are generally lower than traditional gratings. However, due to their sinusoidal cross section, holographic gratings cannot be easily blazed and their efficiency is usually considerably less than a comparable ruled grating, limiting their use to applications where throughput is not an issue.

5.2.3 Mixed Media Gratings

Complications arise when mixing a highly reflective grating surface with rule materials that exhibit light absorbing properties. This type of structure, shown in Figure 5.2, illustrates the additional interaction light undergoes during the diffraction process for these structures. In this case, the grating consists of a substrate (gold) coated with a thin film of material (conductive polymer) patterned as sequential rules. Due to the absorptive nature of the rule material, these gratings create a modulation in the complex index of refraction ($\boldsymbol{n}(x,\lambda)$) as defined by Equation 3:

$$\boldsymbol{n}(x,\lambda) = n(x,\lambda) + ik(x,\lambda) \qquad (3)$$

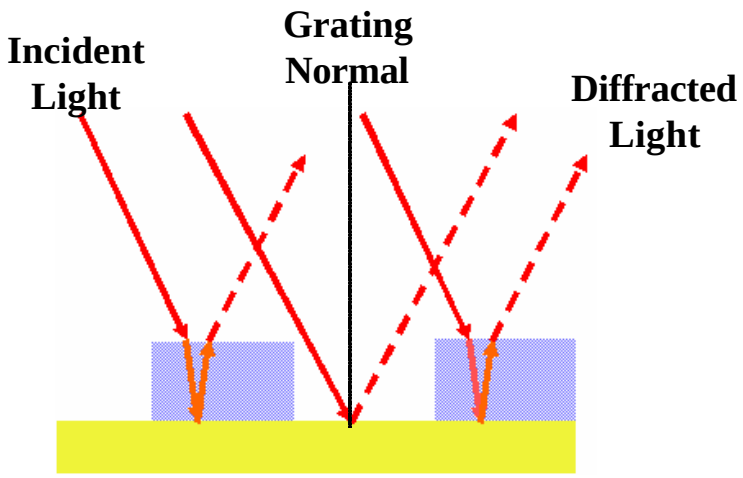

Figure 5.2 Mixed-media grating consisting of a base of reflective gold and features of conductive polymer. Properties of this type of grating are dependant not only on the interference patterns governed by the grating equation but also the optical properties (*n* and *k*) of the feature material.

where *n* and *k* represent the real and imaginary components of the refractive index at any position (x) along the grating respectively. Both values are wavelength dependant and *k* is defined as the absorptivity of the grating material at the position (x) and λ. Diffraction behaves similarly, according to the diffraction equation, however the efficiency of this type of grating is more complex. Strictly, the efficiency is defined by the sum of the diffracted light intensities over the intensity of incident light.

$$DE = \Sigma I_{diff} / I_0 \qquad (4)$$

Fayer and co-workers[36,37] have shown that the diffraction efficiency for a grating produced when a variation of *k* and/or *n* is involved can be approximated by Equation 5.

$$DE_{(l)} = e^{\frac{-2.303OD(l)}{\cos q}}\left[\frac{T}{l\cos q}\right]\left[?k_{(?)}{}^2 + \Delta n_{(l)}{}^2\right] \qquad (5)$$

Where OD(λ) is the optical density at a given wavelength, which can be approximated by the average absorptivity at λ, Δ*k* is the difference in absorptivity between the surrounding medium and the material making up the rules of the grating, Δ*n* is the difference in refractive index, again between the feature material (conductive polymer) and the surrounding medium; λ is the wavelength of light, q is the angle of incidence, and T is the grating thickness in nanometers.

In this equation, $\Delta k(l)$ and $\Delta n(l)$ both correspond to the difference in the absorptivity and refractive index of the grating material i.e. an electrochemically grown polymer and the surrounding electrolyte solution, at wavelength l. Further, it has been shown that switching the electrochemical potential of the polymer may induce a change in either $k(l)$ and/or $n(l)$ values.[38-41] It is therefore conceivable that the diffraction efficiency of a mixed-media grating, comprised of conductive polymer structures on gold, will change if the redox (or doping) state of the material is altered. This strategy may be useful for applications corresponding to chemical sensors where an analyte may induce a similar change in optical properties and is discussed below.

5.3 MICRO-CONTACT PRINTING

Microcontact printing (μCP) is increasingly being used for the structuring of complex patterns onto various types of surfaces. Several applications of this technique have been described[5-7, 42-51] in the literature; the most common of which involves the stamping of a generic alkane-thiol on gold surfaces in order to create a complex patterned surface. The same procedure can be used in the creation of diffraction gratings incorporating conductive polymer (PANI, PEDOT) structures on gold. Figure 5.3 illustrates the schematic of the μCP-EP process starting with sub-micron featured grating masters. In this case, a conventional Au-coated blazed angle grating (1200 lines per millimeter, blaze angle = 36º, grating depth = ca. 180 nm) was used as the master, and

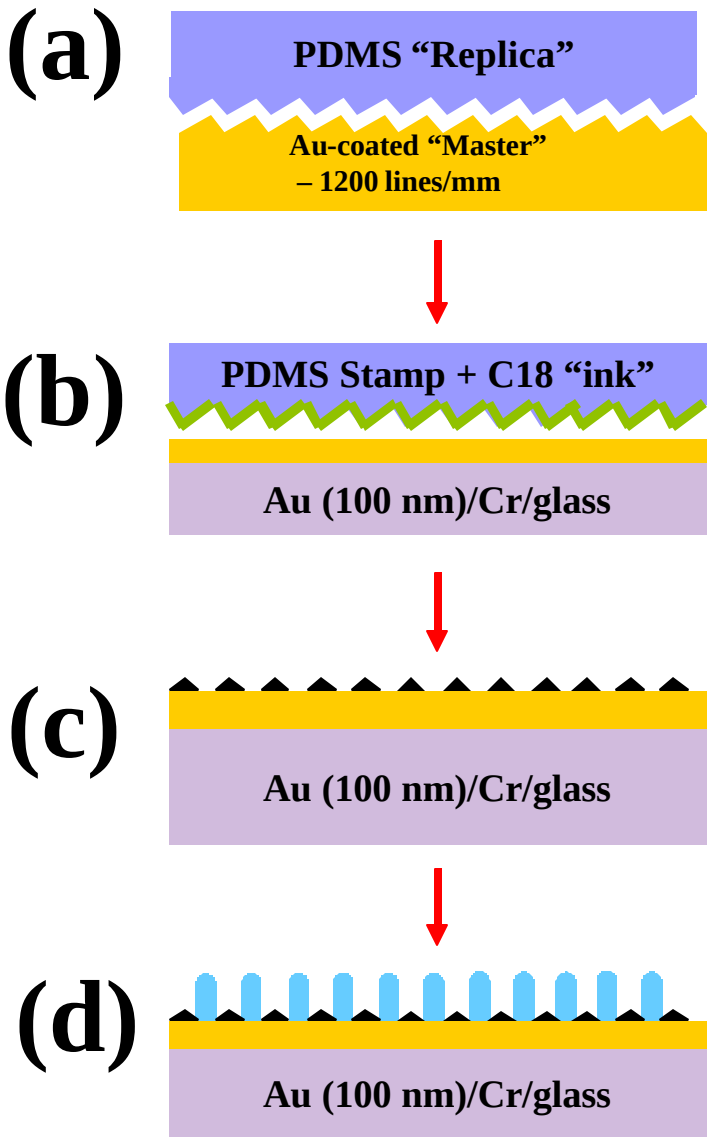

Figure 5.3 Micro-contact printing (μCP) of a gold coated substrate for the formation of electrochemically grown polymer diffraction gratings. (a) The creation of the PDMS stamp on the image of a common diffraction grating. (b) The inking of the stamp, 0.1mM octadecanethiol/ethanol. (c) Following stamping, the alkanethiol pattern on gold reflect the inverse of the grating master. (d) following electro-polymerization, PANI or PEDOT features are isolated to the regions between the stamp, creating the diffraction grating.

soft-polymer stamps were fabricated from its image by casting polydimethylsiloxane (PDMS) from the master grating.

This stamp is constructed by placing the grating master in a level container where a 10:1 (w:w) mixture of SYLGARD silicone elastomer 184 and SYLGARD 184 curing agent (DOW Corning Corporation) is poured over and envelopes the master (Figure 5.3a). The encoated grating is allowed to degas at room temperature for 1-2 hours until the elastomer pour is free of visible air bubbles then allowed to further cure for 12 hours at ca. 90° C. Following the curing of the elastomer, the PDMS can be gently peeled back from the grating master and cut to size with a razor. The resulting stamp replicates the inverse of the features on the grating master ie. raised portions on the grating master correspond to the recessed regions of the stamp. Figure 5.4 shows an AFM image of the PDMS stamp on a 1 x 1μm scale as well as the corresponding SEM image of the grating master showing the sharp ruled edges, but also includes many surface irregularities visible across the grating.

In preparation for stamping, Figure 5.3b, the PDMS stamp can be "inked" by exposing the face of the stamp to a 0.1 mM solution of octadecanethiol/ethanol, which is then allowed to stand 1 minute and is then dried in a stream of nitrogen. The stamping process is accomplished by transferring the "ink" to a gold substrate using a house-built apparatus which allows for constant vertical alignment with the surface to be stamped (a gold substrate) to ensure normal, even stamping, with constant pressure across the entire stamped surface. The inked and dried stamp is brought into contact with a freshly cleaned Au thin film with a force of ca. 1-2 kg per cm^2, for 5 seconds, then allowed to rest for an

a.

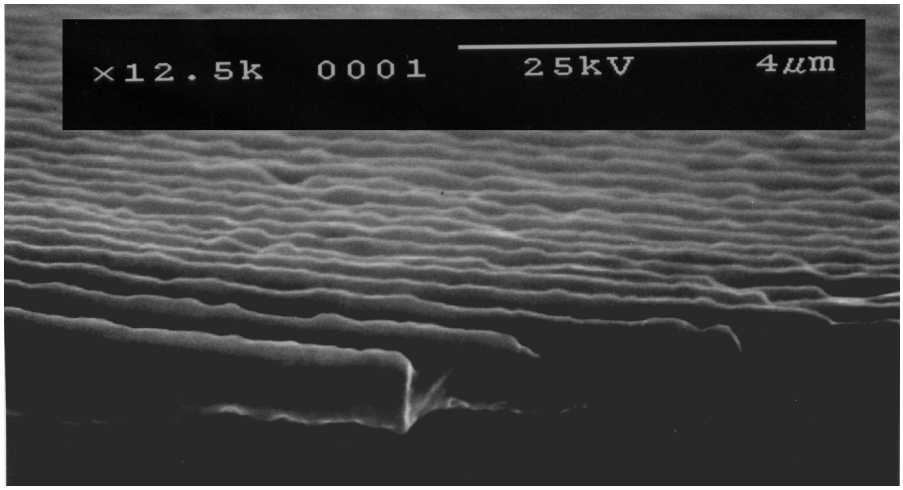

b.

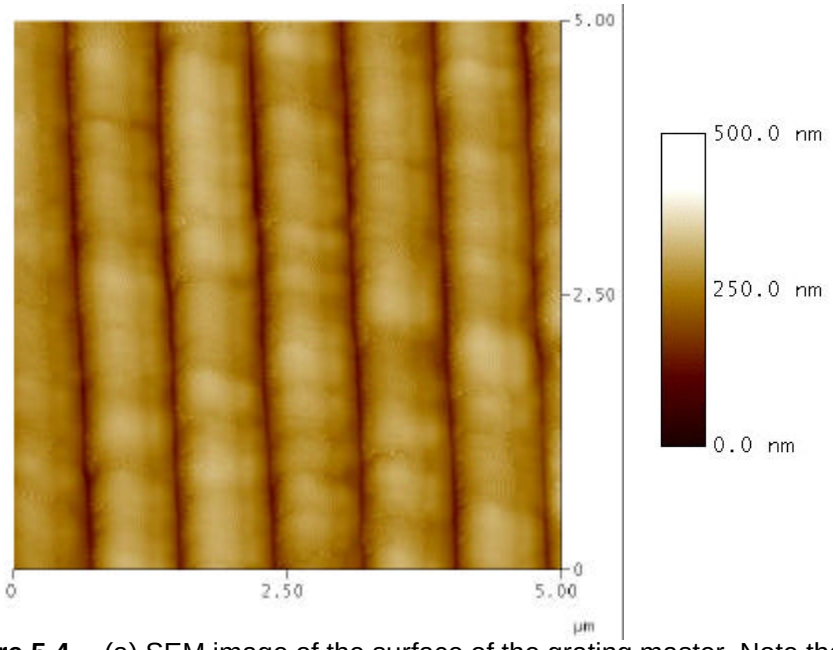

Figure 5.4 (a) SEM image of the surface of the grating master. Note the irregularities in the feature which may lead to irregularities in the stamp. (b) AFM image of the resulting PDMS stamp.

additional 5 seconds before the stamp is separated from the gold surface, rinsed with EtOH and dried in a stream of N_2, leaving behind a patterned gold surface (Figure 5.3c). Concerns that poor integrity of stamped features on a gold surface due to flow of the alkane-thiol solution away from the point of contact, appear to be overcome with this stamping approach. The concern stems from the SEM images of Figure 5.4b showing regions where the flow of alkane-thiol ink from each contact region might occur due to irregularities created in the stamp. However, reproducible pressures on the stamp for 5 seconds, and leaving the stamp on the gold electrode surface for an additional ca. 5 seconds, provides for excellent integrity of the stamped region. It is possible that the irregularities in the stamped region are minimal as pressure applied to the stamp causes deformations in the elastomer, which bulges under pressure to cover concave defects.

Figure 5.5 shows the result of the patterning of the gold surface by the alkane-thiol "ink" via AFM. Stripe features ca. 2.5 nm high can be observed across the gold sample which are the stamped regions ascribed to the presence of alkane-thiol. Widths of the alkane-thiol stripes between ca. 200-600 nm can be obtained, and wider alkane-thiol stripes can be obtained with greater force applied to the stamp. The center-to-center spacing, however, remains constant at ca. 833 nm. Feature quality varied greatly upon the smoothness of the stamped surface; and best results were found with Au samples where the grain roughness did not exceed 1 nm rms.

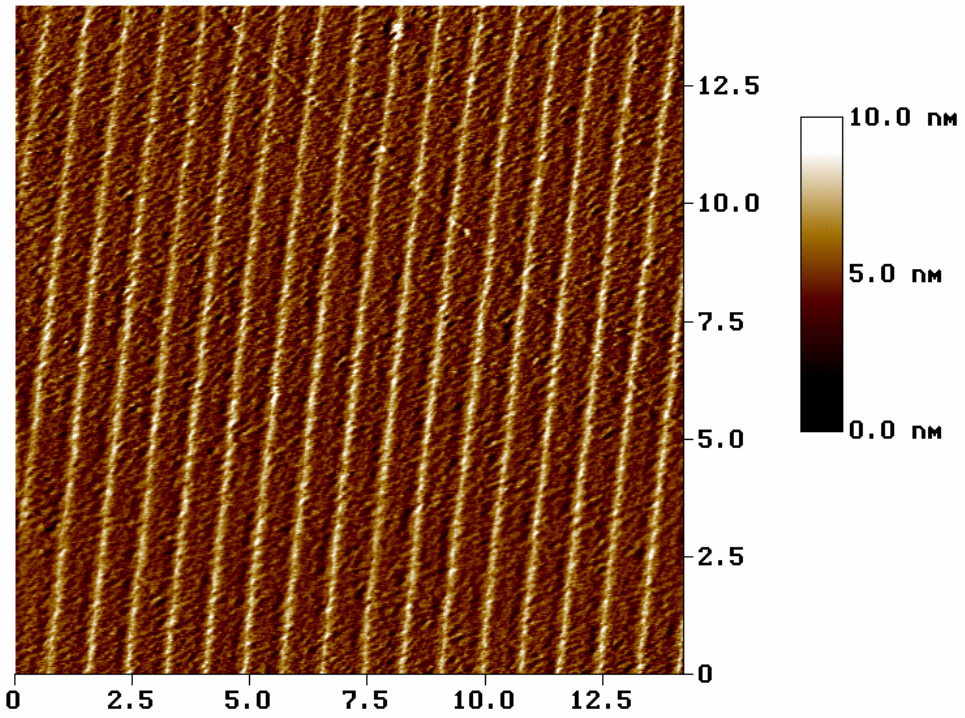

Figure 5.5 Gold surface after stamping. Light regions represent the alkane-thiolate transferred to the gold from the PDMS stamp while the darker regions are indicative of the bare gold surface. Feature widths are dependant on stamping pressure and range from 200-600nm with the spacing a constant 833nm.

5.4 POLYMER GROWTH AND GRATING FORMATION

Polymeric stripes were subsequently grown in the "bare" gold regions, between these alkane-thiol patterned regions, by using either voltammetry, or constant potential coulometry on the gold substrate (Figure 5.3d) However, the electropolymerized features suggest that alkanethiol coverage may be more complete at the center of each stamped region and may taper outward from that point. Good uniformity of grating features, over electrode areas of ca. 1 cm^2, were achieved by using a semi-transparent ITO/glass counter electrode directly opposite the gold working electrode, in a specially designed small volume electrochemical cell (Appendix A5.3). Additionally, this cell design allowed several different solutions to be brought into contact with the grating, without need to change the position of the cell. The semi-transparent counter electrode allowed optical characterization of the diffraction efficiency during grating formation, and during/after exposure to different electrolyte solutions as described below.

To observe the growth of these structures, patterned PEDOT films were potentiostatically or voltammetrically deposited from either methanol/water solutions, or from acetonitrile solutions in a solution cell suitable for AFM imaging of the gold surface. The images in Figure 5.6 were obtained by cycling the potential of the patterned gold surface with simultaneous characterization by *in situ* tapping mode AFM (methanol/water; 10% v/v MeOH; 0.1M $LiClO_4$; 0.01 M EDOT monomer).

For each voltammetric cycle, the potential was swept past the onset for polymer formation (ca. 0.9 volts vs. Ag/AgCl) and returned to its initial potential. In Figure 5.6a a

contrast between the clean gold and alkanethiol-stamped gold regions is observed prior to onset of polymer formation, with the stamped regions lightly elevated. With the first voltammetric cycle (Figure 5.6b) a sufficient thickness of PEDOT film is grown to bring the alkanethiol-stamped and polymer-coated regions of the entire film to approximately the same height, and the initial image contrast disappears (5.5×10^{-5} coul/cm^2 of PEDOT deposition has occurred, providing for patterned features of ca. 2 nm thickness). For additional voltammetric cycles the image contrast improves (Figure 5.6c) as PEDOT thickness increases, and after 5 cycles (2.7×10^{-4} coul/cm^2) the patterned films are ca. 12 nm in height (Figure 5.6d). PEDOT growth is not initially uniform and polymer growth is controlled by nucleation at specific sites under these growth conditions.[52,53]

As polymer growth continues, the original nucleation sites coalesce as conductive polymer converges into the bare gold regions. A similar growth mechanism for patterned PANI films was inferred from AFM characterization of films where growth was stopped at apparent grating depths of ca. 5 nm to 150 nm. Closely spaced columnar deposits of PANI with an average diameter 175 nm, growing vertically from similar sized nuclei, comprise most of the PANI film, with occasional nuclei growing faster than others. Mature gratings of both PEDOT and PANI can be seen in Figure 5.7. These images show a 5x5 μm section of grating with a height scale of 150 nm. Here, the growth of the PANI grating can be clearly seen; also present, is the presence of polymer embedded in the stamped region. This may occur due to an aberration in the alkanethiolate SAM before growth, or may represent a partial loss of the SAM film during growth conditions.

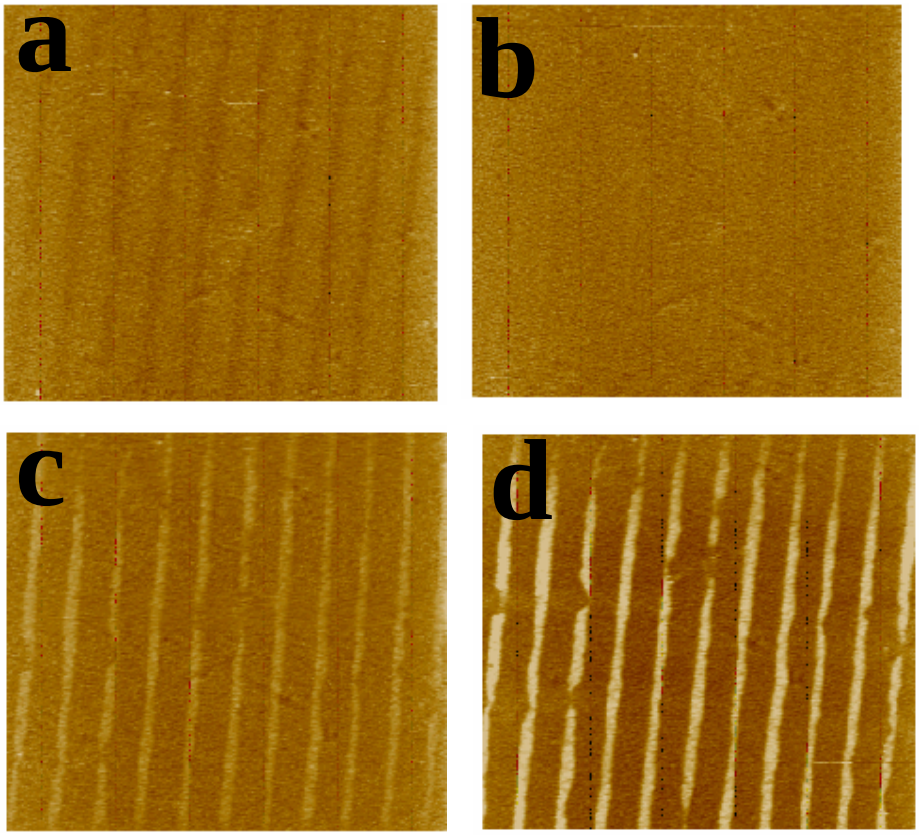

Figure 5.6 characterization of grating growth by *in situ* tapping mode AFM (methanol/water; 10% v/v MeOH; 0.1M LiClO4; 0.01 M EDOT monomer). Potential was swept past the onset for polymer formation (ca. 0.9 volts vs. Ag/AgCl) and returned to its initial potential. (a) the contrast between the clean gold and alkanethiol-stamped gold regions prior to onset of polymer formation. (b) first voltammetric cycle brings the alkanethiol-treated and polymer-coated regions of the entire film to approximately the same height ($5.5x10^{-5}$ coul/cm^2 of PEDOT deposition has occurred, providing for patterned features of ca. 2 nm thickness). (c) and (d) additional voltammetric cycles PEDOT thickness increases, and after 5 cycles (2.7x10-4 coul/cm^2) the patterned films are ca. 12 nm in height

Regardless of the cause, the presence of these non-uniformities likely lead to the demise of the diffraction grating after sufficient intrusion into the SAM.

Evaluation of grating growth can also be monitored by observing the first order diffraction efficiency (DE) of a laser through the semitransparent electrode in the growth cell, Figure 5.8. Patterned polymer film growth using potential steps (Figure 5.8a (PEDOT) and 5.8b (PANI)) show a steady increase in DE of up to ca. 14.6 % (PEDOT) and ca. 26.1% (PANI) whereupon, the DE gradually decreases for both PEDOT films, and sharply decreases for the PANI films. DE was measured with 633 nm (5 mW He-Ne) excitation, s- or p-polarization, incident at 45° or 90° to the surface normal, at the first order (m = 1 or m = -1) diffraction spot. However, AFM images slightly past the growth peak do not indicate poor quality gratings. The initial decrease in DE can be explained by the geometry of the structure based on Equation 5.

Figure 5.9 shows a simulation of DE versus grating depth for standard grating features with optical constants: $n = 1.7$, $k = 0.14$, on a Au substrate; superstrate optical constants $n = 1.4$, $k = 0.0$.[54] The simulated DE plot was normalized to the maximum predicted efficiency, and to the grating depth providing that maximum efficiency (t/t_{max}). These simulations show that diffraction gratings of this type are expected to increase in efficiency with increasing grating depth, up to a maximum grating depth of 75-150 nm (depending upon the relative optical properties of the grating and substrate materials), and will then decrease until the grating depth increases to twice that where the first maximum was observed. DE is expected to continue to increase beyond that point.[55] The fact that these electrochemically grown gratings show significant decreases in efficiency

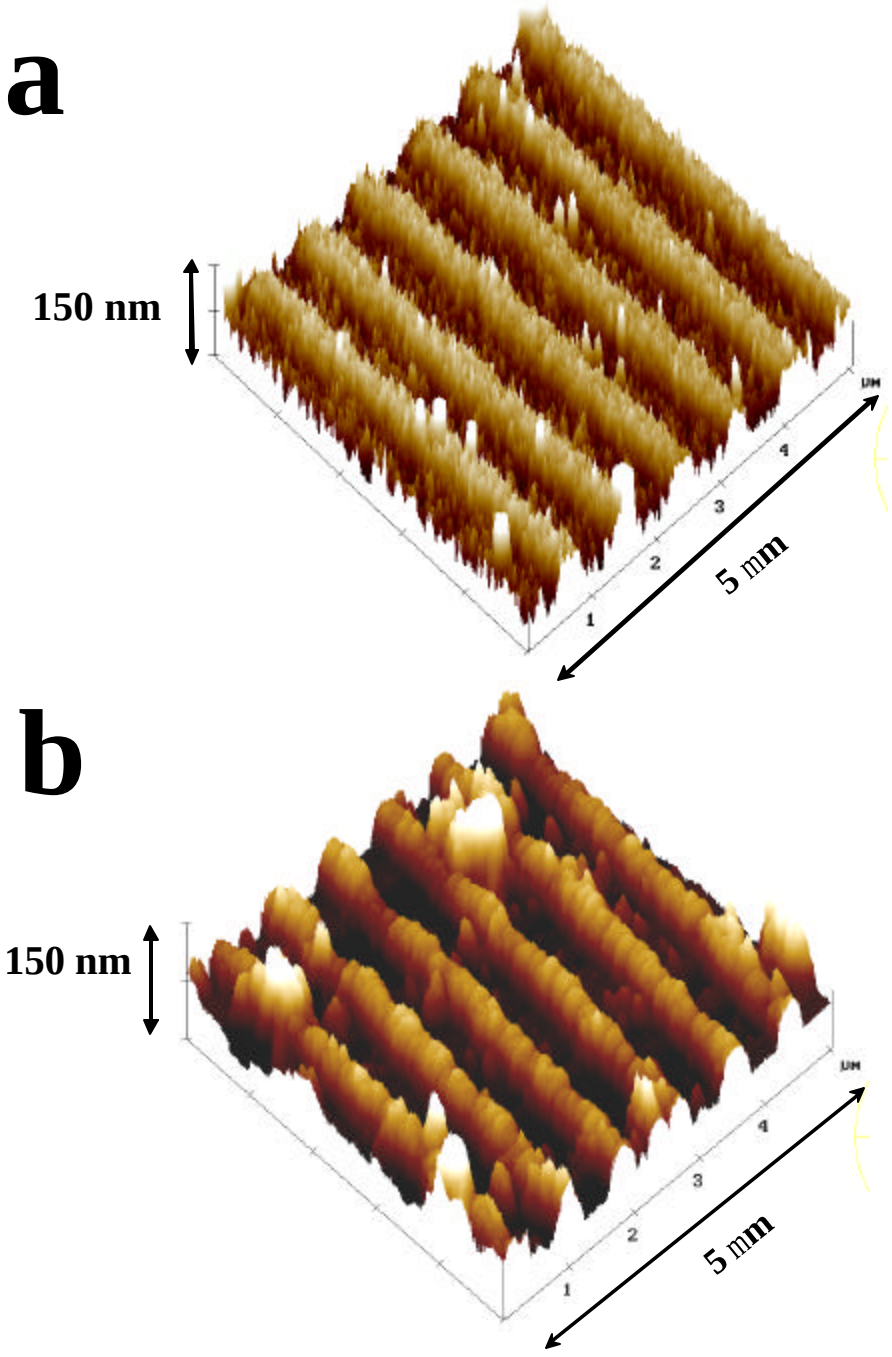

Figure 5.7 Mature gratings with growth arrested just past maximal DE. **(a)** PEDOT and **(b)** PANI. Nucleation sites are visible along the feature rules, and both show beginning growth of polymer anomalies in the stamped regions (between the rules).

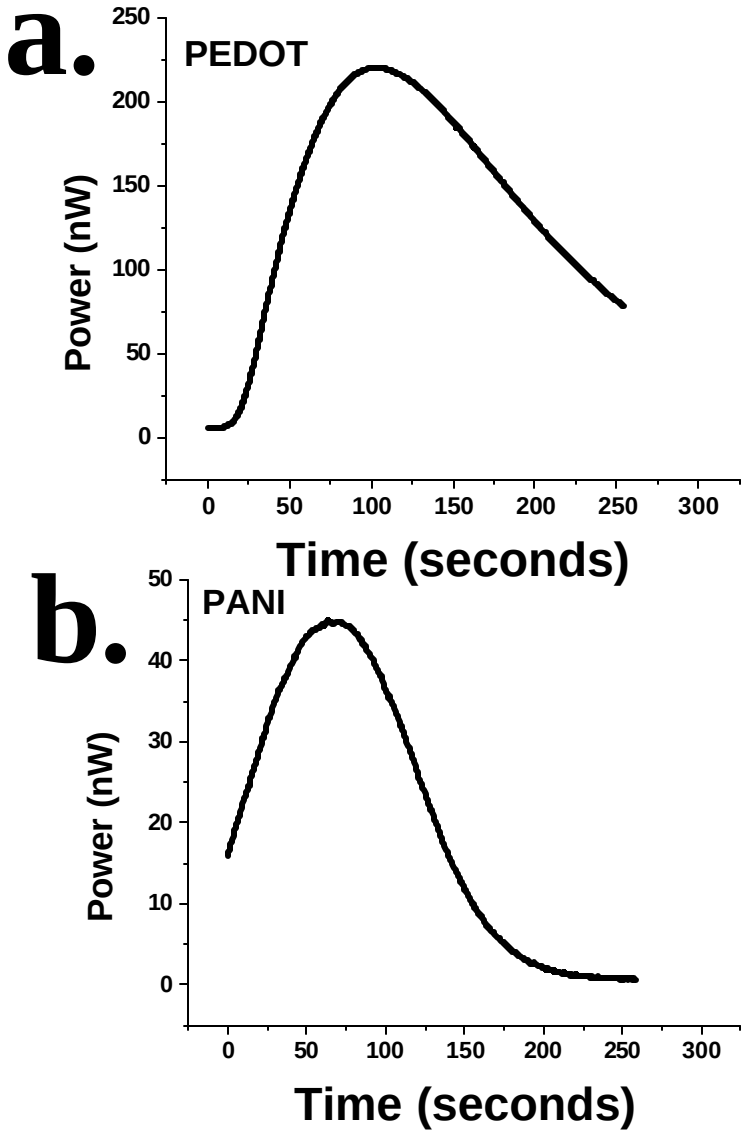

Figure 5.8 Grating growth monitored by the first order diffraction efficiency (DE) of a laser during a potential step through the semitransparent electrode in the growth cell. **(a)** PEDOT and **(b)** PANI show a steady increase in DE of up to ca. 14.6 % (PEDOT) and ca. 26.1% (PANI) whereupon, the DE gradually decreases for both films.

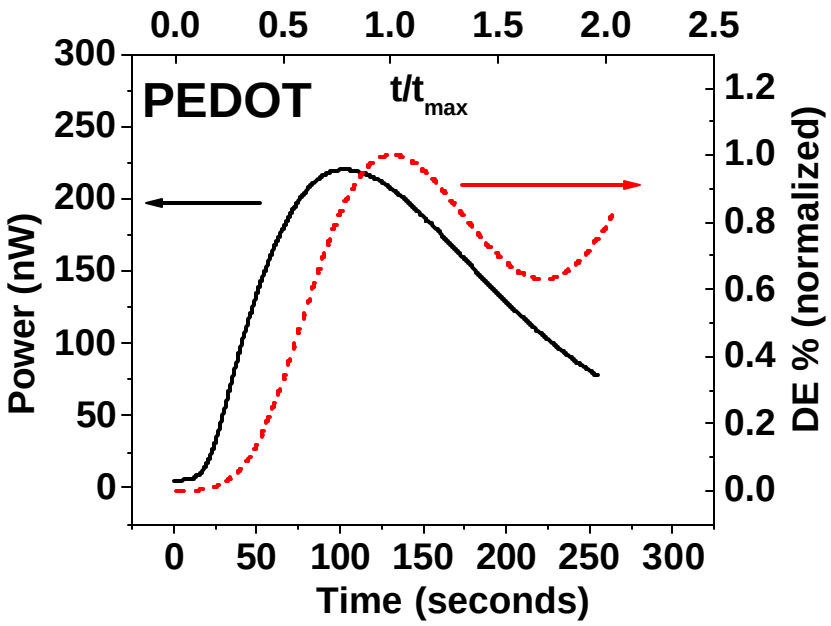

Figure 5.9 Growth curve for PEDOT with a superimposed simulation of DE versus grating depth for standard grating features with optical constants: n = 1.7, k = 0.14; solution: n = 1.4, k = 0.0. DE is expected to increase in efficiency with increasing grating depth, up to a maximum at grating depths of 75-150 nm (depending upon the relative optical properties of the grating and substrate materials), then decrease until the grating depth increases to twice that where the first maximum was observed occurred, then continue to increase beyond that. Continual decrease of the PEDOT indicates overgrowth has occurred.

beyond the thickness of maximum efficiency where DE is expected to increase, is consistent with the gradual loss of polymer patterning, most likely due to overgrowth of the conductive polymer regions. This overgrowth was confirmed by AFM characterization of several patterned films for potentiostatic growth times beyond 200 seconds and shown in Figure 5.10. It is noteworthy, however, that until this overgrowth occurs, we routinely produce diffraction gratings with efficiencies exceeding 13%, which leads to easily visible first and second order diffraction features from white light sources as shown in Figure 5.11a.

A comparison of DE versus wavelength for PEDOT gratings, with respect to the master grating used to make the PDMS stamp, is shown in Figure 5.11b. It is observed that the PEDOT gratings have a strong wavelength dependence in diffraction efficiency, peaking at ca. 500nm, and at their maximum, their efficiencies are approximately double those of the master grating. This is reasonable as the rules of a mature polymer grating are ca. 50% larger than the bevels on the master grating. PANI gratings have a similar wavelength dependence also peaking at ca. 500nm. This is consistent with wavelength behavior most gratings undergo, as diffraction efficiency is known to be wavelength dependant according to the grating equation.

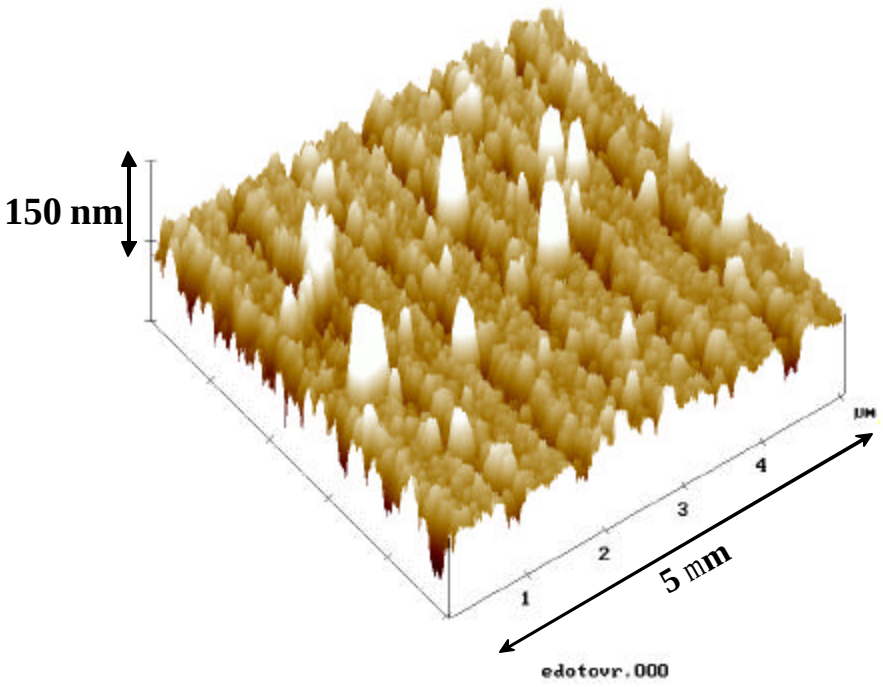

Figure 5.10 Mature grating where overgrowth is substantial (growth times greater than 200 seconds) leading to polymer growth between the rules, the merger of some polymer features and a corresponding reduction of DE.

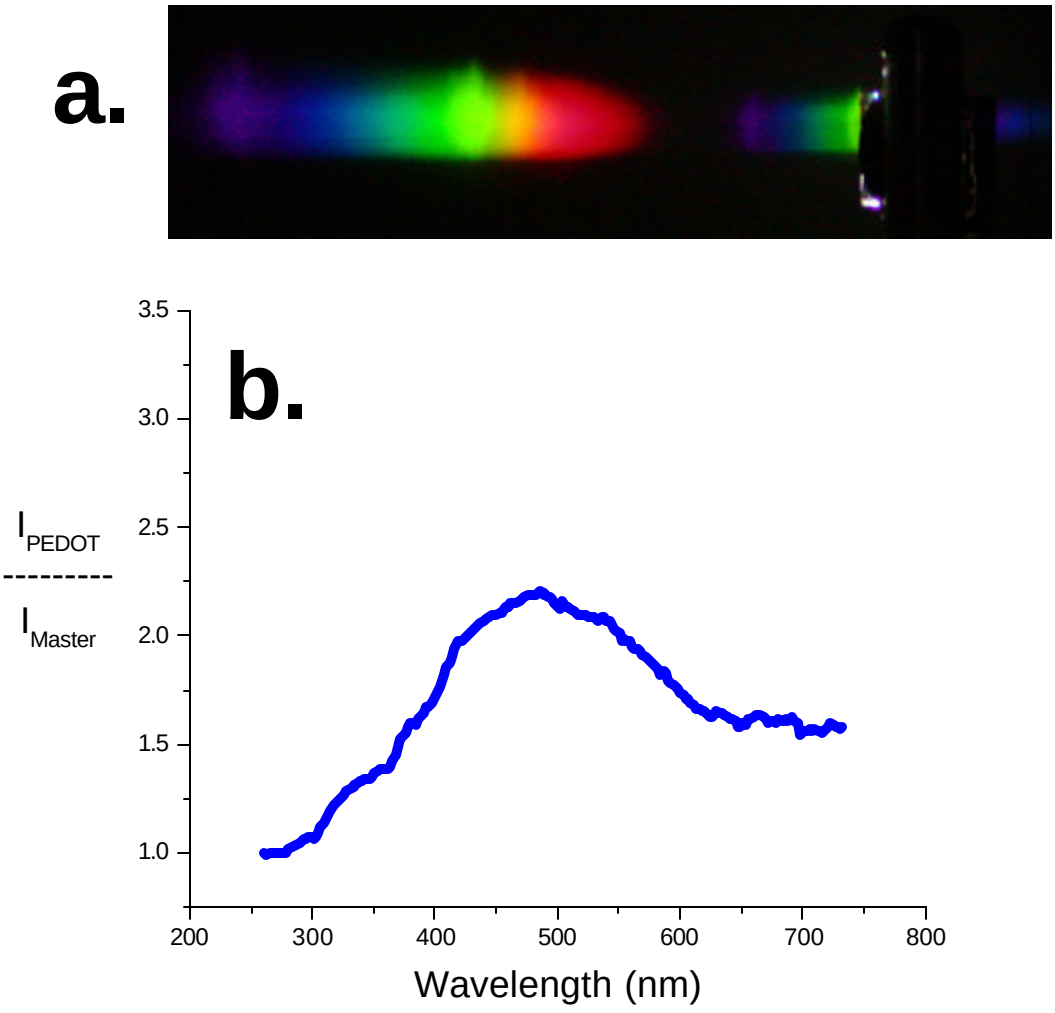

Figure 5.11 **(a)** Diffraction of white light by mature PANI grating. First order diffraction is visible to the left while a second order diffraction can be made out near the grating itself. **(b)** strong wavelength dependence of PEDOT grating, peaking at ca. 500nm, with efficiencies are approximately double those of the master grating. PANI gratings have a similar wavelength dependence also peaking at ca. 500nm.

5.5 PHYSICAL RESPONSE TO ENVIRONMENTAL CHANGES

For polymer structures such as these, changes in DE are anticipated as a result of changes in both the real (n) and imaginary (k) components of refractive index. Due to the mixed media aspect of the grating, DE becomes a function of both the absorptivity (k) and the refractive index (n) of the material according to the relation as given in equation 5. However, if the polymer can take on different forms with respect to changing environmental conditions, the equation can be written in terms of the change in DE (ΔDE) which takes into account initial and final states the polymer and can be represented by Equation 6:[56-57]

$$\Delta DE_{(l)} = \left[\frac{p}{l\cos q}\right]\left\{T_i e^{\frac{-2.303OD(l)}{\cos q}\left[?k_{f(?)}{}^2 + \Delta n_{f(l)}{}^2\right]} - T_f e^{\frac{-2.303OD(l)}{\cos q}\left[?k_{i(?)}{}^2 + \Delta n_{i(l)}{}^2\right]}\right\} \quad (6)$$

This form of the equation states a change in the diffraction efficiency should be observed when conditions dictate a change in the absorptive and/or refractive index of the polymer features based on surrounding stimulus. However, it has been recently demonstrated that the diffraction efficiencies of patterned polymer films will be significantly more sensitive to changes in n than k.[5] Further, there is generally a tight coupling of changes in n and changes in k. As noted above, it is well-known that these materials exhibit a change in absorptivity during a change in the redox state.[38] However, the refractive index of a material will also change with the changing redox state. This is

due to the close relationship between the absorptivity and the refractive index.[39-41] The Kramers-Kronig relation allows for the calculation of this change in refractive index (n) induced by a change in the absorptivity of a material expressed by Equation 7.[58,59]

$$\Delta n(w') = \frac{c}{p}\int_0^{\infty} \frac{\Delta a(w)}{w^2 - w'^2}\partial w \qquad (7)$$

Where $\omega = 2\pi c/\lambda$ and $\Delta\alpha = 2\pi k/\lambda$ represents the change in the absorptivity the polymer undergoes with the changing redox state. The solution to the integral can be modeled numerically, substituting in the change in absorptivity (Δk), to solve for the change in n (?n). For example, a change in absorptivity that leads to a Gaussian shaped perturbation of absorbance, the index of refraction will increase to the red of the maximum in the Δk curve (where Δk is positive) and decreases to the blue.[60] If a decrease in absorptivity is observed, the sign of the perturbation (Δk) is changed, and changes in n are reversed to increases to the blue and decreases to the red peak of the change.

Modeling experiments also indicate that ?DE/?n will be maximized for gratings with depths less than half that required for optimum DE.[55] The pH dependence of the DE of PANI as well as potentiometric dependence by PEDOT gratings was therefore explored with gratings potentiostatically grown to depths yielding 25-50% of maximum DE.

5.5.1 Evaluation of PANI Diffraction Gratings Under pH Control

It is well known PANI exhibits a broad range of conjugated states determined by the oxidation state, the degree of protonation of the polymer, or both. It is also known that each of these states display a unique combination of physical properties including the conductivity of the polymer and its optical properties. Further, this polymer is capable of changing its state based on the exposure to environmental conditions such as pH as well as applied potential.[61] These forms, as well as their transition points are outlined in Figure 5.12. At low potentials, those below ca. 0.14 volts versus Ag/AgCl reference, the polymer exists exclusively in the leucoemeraldine form (LE). A colorless, fully reduced state, which exists as the protonated form (e.g. the polymer is not pH active.) Moving to higher potentials, those between 0.14 and 0.45 volts versus Ag/AgCl, PANI exists as the characteristically green, partially oxidized, most conductive form, in either the protonated emeraldine salt (ES) form or the less conducting emeraldine base (EB), depending on the pH (pK_a = 2-3). At higher potentials, those above ca. 0.45 volts versus Ag/AgCl, PANI exists as the fully oxidized and less conductive forms, the pernigraniline base (PB) and pernigraniline salt (PS) forms for the non-protonated and protonated forms respectively.

These forms can be followed spectroscopically by controlling both the oxidation state of the polymer, by the application of fixed potential to a thin film of polymer on a gold substrate, and the degree of protonation, by adjusting the pH of the solution the film is exposed to with calibrated buffer solutions introduced to the film. Figure 5.13 describes these forms as the reflection-absorption spectra of a thin film PANI sample on a

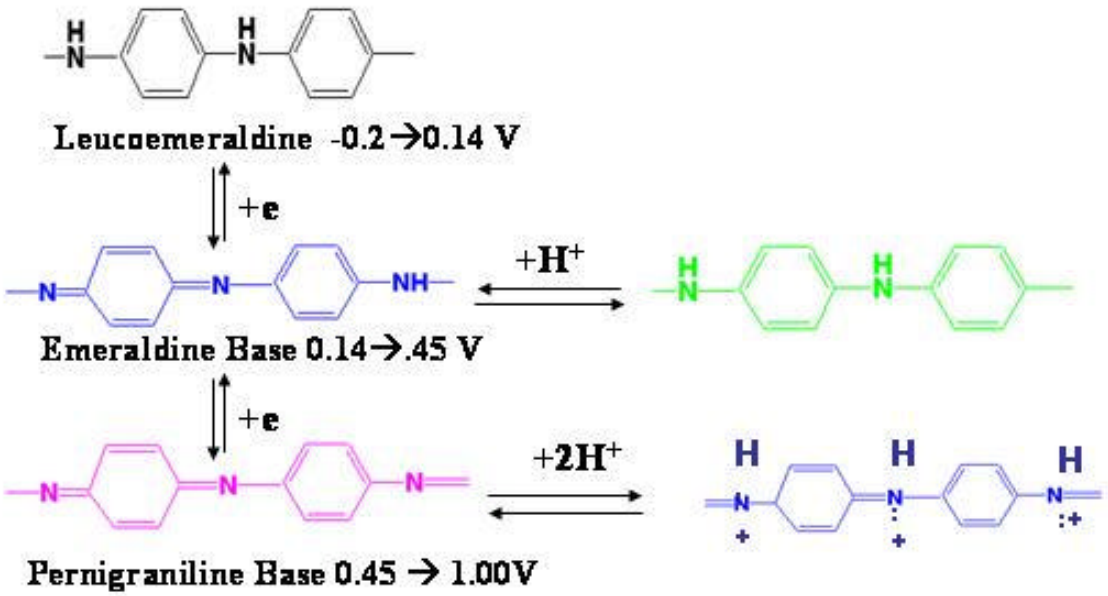

Figure 5.12 Oxidation and protonation states for PANI. At low potentials, below ca. 0.14 volts, PANI exists exclusively in the Leucoemeraldine form. At higher potentials, between 0.14 and 0.45 volts, PANI exists as the characteristically green, partially oxidized form, in either the emeraldine base or emeraldine salt (protonated form) depending on the pH (pKa = 2-3). At higher potentials, those above ca. 0.45 volts, PANI exists as the fully oxidized state or the pernigraniline base and pernigraniline salt forms for the non-protonated and protonated forms respectively.

gold substrate with differing buffer solutions of incremental pH values at three different potentials: open circuit potentials, 0.0 volts, and +0.4 volts potential control.

Figure 5.13a shows the spectrum of a PANI film held at a fixed potential of 0.0 volts vs. Ag/AgCl. At this potential, PANI exists almost exclusively in the LE form as noted by the lack of absorbance throughout the visible region. As pH is increased via the introduction of successive buffer solutions, the spectrum remains unchanged between pH values of 2-5. In more alkaline solutions, pH values ≥ 5, a change in the spectrum occurs. It is unlikely that deprotonation is occurring, however, a change in the absorbance is apparent suggesting that this somewhat unstable PANI form is becoming oxidized in these conditions and reverting to the emeraldine base form, giving rise to the broad absorption peak observed at ca. 600 nm. It is known that oxidation potential of PANI shifts negatively with increasing pH, which will explain the conversion to EB even at 0.0 volts versus Ag/AgCl reference.[17] It is also possible that at higher pH values the films become electroinactive which results in the loss of potential control.

When the potential is held at a fixed 0.45 volts, (Figure 5.13b) low pH values tend to show broad absorption peaks near 850 nm, presumably due to the ES form of the polymer. Changing the buffer to higher pH values results in a spectrum similar to those seen for alkaline solutions at 0.0 potentials, showing a broad absorption peak at ca. 600 nm, which increases until a solution pH of 5 is reached, above which, the spectrum

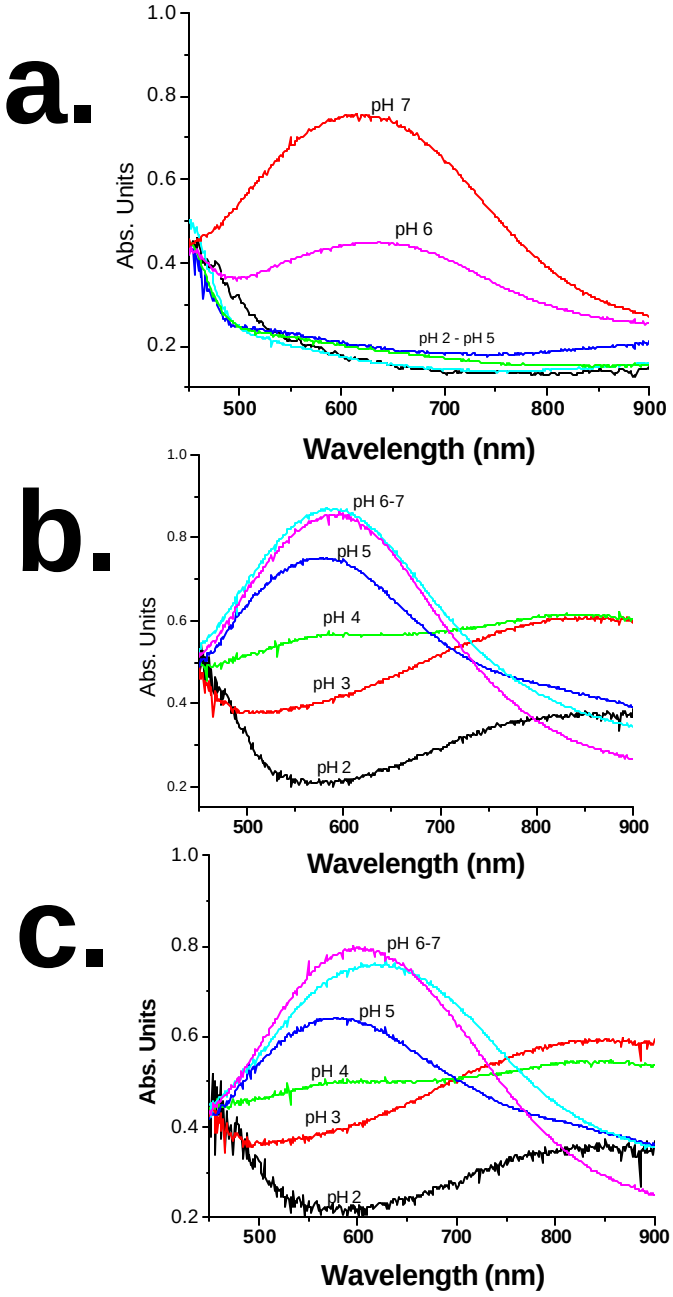

Figure 5.13 Reflection absorption spectra of PANI thin film on Au with variations in the pH of a surrounding buffer solution. (a) Film potential held at 0.0 volts vs. Ag/AgCl. (b) Film potential held at 0.4 volts vs. Ag/AgCl and (c) Film left at open potential.

remains unchanged. This is indicative of the emeraldine salt transitioning to the emeraldine base forms of PANI as the pH is changed. At open-circuit, (Figure 5.13c) the spectrum resembles that seen at 0.45 volts. This suggests that the emeraldine form of PANI is retained once formed.

Polyaniline has properties that are not often found with other conducting polymers, the polymer exists in a variety of forms which differ in degree of oxidation or extent of protonation and is colored with a dependence on the state it exists in, as described above. Additionally, a change in the refractive index can be inferred for the film by observing the change in the absorbance during the emeraldine salt to emeraldine base transition as pH increases from 2-8 units. Figure 5.14 displays the Kramers-Kronig relation for this transition. It can be seen that the perturbation in absorbance leading to the Δk curve induces a change in the refractive index of the PANI film. The result of the Δn curve is similar to that observed elsewhere[6] and is characterized by a substantial decrease in n at ca. 500 nm, a peak increase near 700 nm, and an increase of ca. 0.4 where diffraction efficiency is observed at 633nm. The combination of this shift in absorptivity and the change in refractive index combine to create a material with nearly ideal sensing properties with respect to changing the environmental conditions. To this end, PANI diffraction gratings were constructed to study the changes in diffraction efficiencies that can be accomplished by changing the oxidation states and/or degree of protonation by a changing chemical environment (i.e. varied buffer solutions).

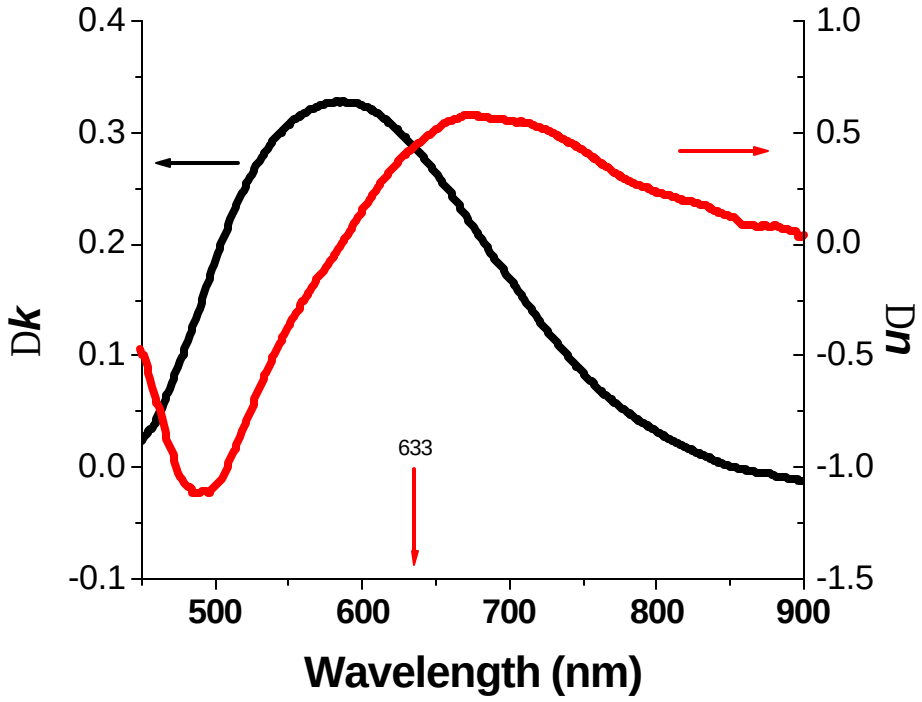

Figure 5.14 Change in absorptivity (Δ*k*) for a PANI thin-film during the leucoemeraldine to emeraldine transition brought about by altering the pH of the surrounding buffer solution from 2-7 pH units (at 0.4 volts fixed potential) and the Kramers–Kronig transformation which gives the coresponding change in refractive index (Δ*n*).

PANI diffraction gratings were grown to create rule depths of ca. 30% those required for maximal DE before polymer overgrowth for optimal sensing (see above). The Au electrode/grating substrate was then monitored by observing the first order DE with potentials held at 0.0 volts, +0.4 volts, and at open circuit while the pH of the surrounding solution was changed. To alter the pH, various buffer solutions, successively increasing in value, were introduced into the growth cell, without changing the grating position between pH 2 – pH 8. Both s- and p-polarization of the incident He-Ne laser were used, with incident angles of both 0° and 45° -- results using p-polarization of the incident beam are shown in Figure 5.15. In general, a higher DE is observed for 45° versus 0° incidence of the He-Ne laser, although the absolute changes remain nearly the same. Also, p-polarized light indicated a larger change in ΔDE over s-polarized light. This trend can be explained by the difference in the refractive index the polymer exhibits between each polarization. This has been shown for other species,[54,55] and is presumably the case here.

At potentials held at 0.0 volts vs. Ag/AgCl there is little dependence of DE vs. pH, regardless of polarization or incident angle (Figure 5.15), until pH = 5 is reached, whereupon there is an abrupt rise in DE. This is similar to the reflection-absorption spectrum observed for PANI films fixed at this potential. This type of behavior is easily explained by the change in oxidation state of the PANI. At low pH values, and at a 0.0 volts fixed potential, the polymer exists almost exclusively in the LE form. For this oxidation state, changing the pH has little effect until values reach ca. pH 5. At this

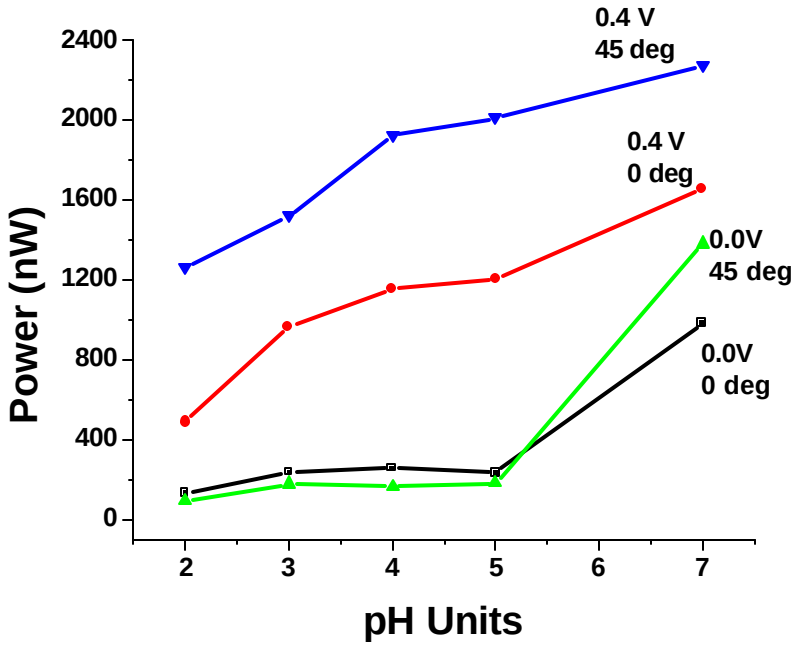

Figure 5.15 Diffraction power of PANI gratings with the changing pH of the surrounding buffer solution at fixed potentials of 0.0 and 0.4 volts vs. Ag/AgCl respectively, and at 0 and 45° incidence.

point, the polymer becomes oxidized in the alkaline solution as shown by the changing absorption spectrum discussed above, causing a significant change in the optical constants. The DE response of a He-Ne laser at 633 nm throughout the pH range for samples held at this potential are shown in the figure. Low pH values have little change in the oxidation state of PANI therefore little change in the absorptivity or the refractive index. At values of pH 5 and above, the oxidation of PANI results in the EB form, with the accompanied change in absorptivity. The refractive index is also presumed to change according to the Kramers-Kronig relation (ca. 0.1) resulting in the sharp increase in diffraction efficiency observed.

For PANI gratings held at +0.4 volts, there is a monotonic rise in DE with pH, DE increases by 2x to 3x as pH is increased from 2 to 7, This can be explained by the degree of protonation experienced by the emeraldine form of the polymer grating. At a fixed potential of 0.4 volts and low pH values, a majority of the polymer is in the ES form. However, as pH increases, the fraction of PANI in the EB form also increases. This can be seen in the absorption spectrum by a decrease in the peak at ca. 850 nm and an increase in the peak at ca. 600 nm. The resulting change in composition likely affects both the dielectric constant of the material and the absorptivity leading to the increasing DE. This can be seen in the Kramers-Kronig relation discussed above for this transition. Between the initial states (pH 2) and the final state (pH 8) a total Δn of ca. 0.5 is anticipated from the analysis of these spectra. This is consistent with the increase in DE observed according to Equation 6. PANI held at open circuit (not shown) indicated similar increases in DE as a function of pH. A similar argument can be made for this

response noting a fraction of the polymer may be in other oxidation states ie. the leucoemeraldine form.

5.5.2 Evaluation of PEDOT Diffraction Gratings Under Potential Control

The optical properties of nanostructured conductive polymers are also easily modulated by changes in redox state caused by changes in applied potential. PEDOT may undergoe reduction to the neutral state which consequently leads to large changes in absorptivity and has increased interest in PEDOT as an electrochromic material.[8,10-11] The change in absorptivity is characterized by observing the reflection-absorption spectrum for a thin film of the polymer on a gold substrate under potential control, shown in Figure 5.16. This figure details the change in the absorptivity of the material at potentials between 0.4 and 0.4 volts negative, potentials known to bracket the range where the PEDOT film transitions between its partially oxidized and neutral forms.[62] The figure indicates that at positive potentials (0.1-0.4 volts) PEDOT has no noticeable changes in the absorptivity and is characterized by a single broad absorption at ca. 850 nm, presumable due to the persistence of the partially oxidized form (polaron state). However, upon applying negative potentials, a reduction of PEDOT is observed leading to the appearance of a broad absorbance peak at ca. 575nm while the peak at ca. 850 is decreased substantially, indicating a change in polymer to the neutral form as shown.

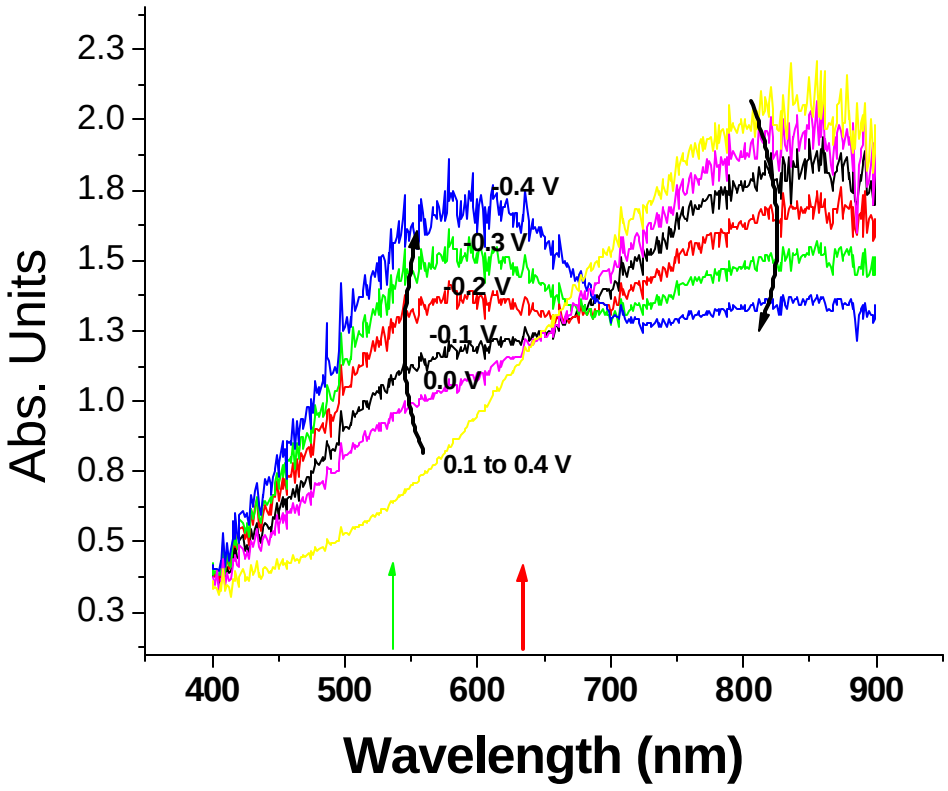

Figure 5.16 Reflection-absorption spectra of a PEDOT thin-film surveyed at potentials from 0.1 to 0.4 volts vs. Ag/AgCl reference and 0.0 to -0.4 volts vs. Ag/AgCl. At positive potentials (0.1-0.4 volts) PEDOT has no noticeable changes in the absorptivity and is characterized by a single broad absorption at ca. 850 nm, presumable due to the partially oxidized form. At negative potentials (0.0 to -0.4) the appearance of a broad absorbance peak at ca. 575nm is observed while the peak at ca. 850 is decreased substantially indicating a transition to the neutral state.

The change in absorptivity can also be analyzed to find the anticipated change in refractive index of the polymer during this transition by using the Kramers-Kronig relation similarly to that described above. Figure 5.17 shows both the resulting curve for Δk and the corresponding curve for Δn. The changing absorptivity can be characterized by a broad increase in absorbance near 550 nm as well as a decrease at ca. 800 nm. This change in absorptivity the leads to a drop in the refactive index at ca. 500 nm with a maximum increase at ca. 675 nm respectively.

In order to test the potentiometric sensing capabilities of PEDOT, polymer diffraction gratings were grown in acetonitrile (0.1 M $LiClO_4$) and characterized in a similar manner to the gratings described above. Figure 5.18 shows the changes in DE versus applied potential for a patterned PEDOT film, after its initial growth, using both 534 nm and 633 nm laser sources (p-polarization, 45° incident angle). Similar changes were noted for a PEDOT films grown in $MeOH/H_20$, but were larger and better defined for PEDOT polymers grown in the nonaqueous solvent. The DE vs. potential changes shown in Figure 5.18 were reproduced exactly as shown as potential was cycled in a triangular wave several times from 0.0 volts to +0.2 volts then negative to -0.2 volts before completing the cycle again at 0.0 volts vs. $Ag/AgCl^+$, however, for clarity only one cycle is shown. During the positive portion of the sweep, little change is observed in the DE as a function of potential at either wavelength, 633nm or 534 nm. However, as the potentials begin the negative sweep, a ca. 17% increase in the DE is observed at 534 nm as the potential cycles to -0.2 volts and back while ΔDE for the 633 nm laser show a slight decrease ca. 6% before returning to the initial value at the end of the sweep.

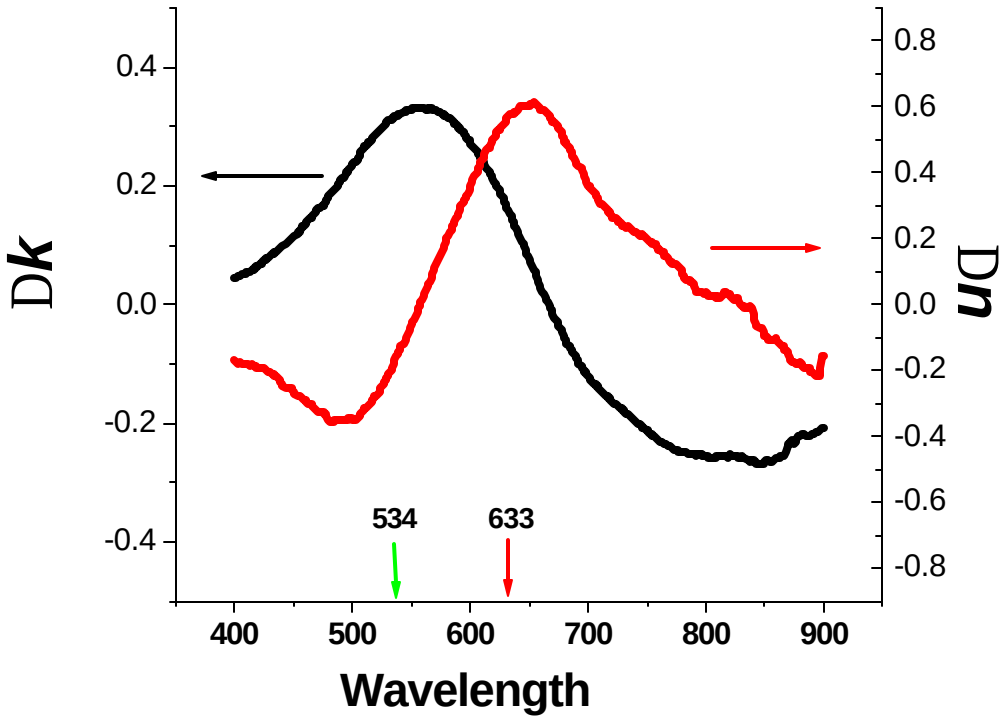

Figure 5.17 Change in absorptivity (Δ*k*) for a PEDOT thin-film during the transition brought about by cycling the potential between 0.0 and -0.4 volts vs. Ag/AgCl and the Kramers–Kronig transformation which gives the corresponding change in refractive index (Δ*n*) for the transition.

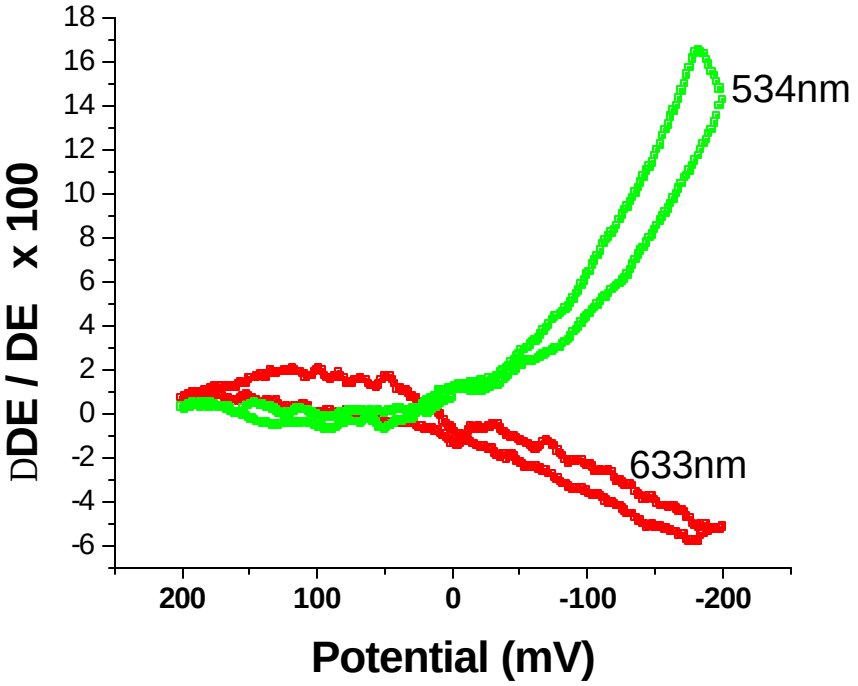

Figure 5.18 Change in the first order diffraction efficiency of a PEDOT grating observed with at 633 nm and 534 nm laser spots during cyclic potentials vs. Ag/AgCl. Sweeping positive, little change is observed in the DE as a function of potential at either wavelength, 633nm or 534 nm. At negative sweep potentials, a ca. 17% increase in the DE is observed for 534 nm and a slight decrease, ca. 6% for 633 nm laser show before returning to the initial value at the end of the sweep

It is interesting to note that the DE of the PEDOT grating markedly increases at 534 nm which corresponds to a large increase in the absorbance of the PEDOT as the electrode potential is cycled from the partially-oxidized state of PEDOT to its neutral state, while the DE at 633 nm decreases during these same potential changes even though the spectrum indicates a small increase in absorbance. Further, the Kramers-Kronig relation predicts a decrease of ca. 0.2 in n for the film at 534 nm, but an increase of ca. 0.6 at 633 nm. However, upon further calculations, ΔDE at 534 nm is expected to increase ca. 11%, according to equation 6 (at 534 nm: superstrate; $k = 0$, $n = 1.4$, PEDOT in neutral form;[54] $k = 0.17$, $n = 1.2$ with T = 100 nm) which corresponds well to the actual increase if an allowance is made for the swelling of the polymer upon reduction. It is unclear why a decrease is observed in DE at 633 nm, calculations indicate virtually no (less than 3%) increase should be observed (at 633 nm: superstrate; $k = 0$, $n = 1.4$, PEDOT in neutral form;[54] $k = 0.28$, $n = 1.08$ with T = 100 nm). It has been recently suggested that conductive polymer optical constants, PEDOT in particular, show a great sensitivity to ions on the interior of the polymer film.[63] It is possible that these variations change the refractive index in a manner not predictable by the Kramers-Kronig relation and the actual refractive index at 633nm is sufficient to give the observed results. In any case, potentiometric sensing by the PEDOT grating has been achieved.

5.6 CONCLUSIONS

It has been shown that polymer nanostructures, based on the image of a common diffraction grating can be constructed utilizing micro-contact printing techniques followed by the electro-catalyzed polymerization of the conductive polymers PANI and PEDOT can be successfully created. Further, these structures can be formed to produce features on a sub-micron scale, which exhibits surprising efficiency, nearly double that of the grating master. In both cases, features up to 180 nm in height can be created before overgrowth of the grating (growth in the stamped regions) leads to a drop in the DE and ultimately loss of diffraction.

It has also been demonstrated that gratings created using PANI as the grating features, show sensitivity to pH perturbations of the surrounding environment. This sensitivity has lead to the development of a working pH sensor based on the modulation of the DE with changing pH. Similarly, gratings which utilize PEDOT as the rule features show sensitivity to potentiometric influences, where the DE may be observed to change as potentials are decreased dictating a change in the polymer form. The sensing of environmental changes by these polymer diffraction gratings, described here, is a result of the unique properties displayed by the polymer material under environmental changes. In most cases, changes in the absorptivity and the refractive index of the material lead to the observed changes in the diffraction efficiency. However, changes in refractive index are the dominant factor for ΔDE observed, these devices can be viewed as one of the few

analytical technique which utilizes changes in the refractive index as the sensing element and complements SPR as an analytical tool.

CHAPTER 6

CONCLUSIONS AND FUTURE DIRECTIONS

6.1 ITO SURFACE CHEMISTRY AND MODIFICATION

The research presented here displays the importance interfacial chemistry plays in the development of organic thin-layer technologies, especially where designs dictate that a TCO is to be used as an active electrode. It has been shown through rigorous surface analysis that the heterogeneity of commercially available ITO is substantial, and likely represents many problems associated with ITO use. To this end, understanding ITO surface chemistry and how it can be altered with respect to changes in the surrounding environment has been investigated. The studies presented here have led to the development of a working model of how specific surface chemistry affects the electronic properties of ITO. Furthermore, through the application of various solution pretreatments, ITO has shown to be variable in its composition in a dynamic manner, with respect to the chemistry of the environment. Unfortunately, commercial manufacturing and storage conditions are extremely variable and this dynamic nature only compounds the large variations in device performance parameters common in organic thin-film devices.

Evidence of this heterogeneity is clarified by the application of solution electrochemistry techniques to investigate ITO surfaces with respect to their charge transfer characteristics. This electrochemical treatment has made exploration of small

molecule electron transfer modifiers and the evaluation of active site populations possible. Additionally, these studies have demonstrated a link between solution electrochemistry and solid state device performance. Hence, electrode evaluations can be carried out in a more practical manner than constructing complete thin-layer devices and attempting to extrapolate the effects arising predominantly from the electrode.

The development of the surface model has been crucial with respect to strategies aimed at improving the charge transfer characteristics of ITO by providing a pathway to improved device performance. Although ITO substrates are not strictly homogeneous in composition, application of solution pretreatments has been a first step in the progression toward a well behaved electrode interface. These studies have shown that the exposure of ITO to various chemical agents has a profound effect on both the surface chemistries and the corresponding electron transfer characteristics. This is seen in the surface XPS data for the various pretreatments as well as the effective electron transfer rates of an adsorbed probe molecule. Although the results obtained with solution pretreatments have not readily been observable in completed devices, the increases in electron transfer rates show that the modification of the ITO surface can indeed impact the efficiency of a completed device. However, care must be taken when selecting pretreatments as it was shown that some small molecules or polymers have the potential to negatively impact the charge transfer characteristics and should be avoided.

The concepts presented here have already been extended beyond the scope of this dissertation. Follow-up studies have selected more rigorous pretreatments in which to subject ITO surfaces to. Figure 6.1 illustrates this by work from Adam Simmonds *et al*

where conducive tip AFM images of as-received ITO are compared with ITO samples which have been treated with 12 M HCl, and 0.2 M $FeCl_3$.[1-2] It is clear that the surface resistance of the treated sample has decreased dramatically after pretreatment. It is likely that the performance of such a surface, when incorporated into a device, is also greatly enhanced due to the increased area of activity shown. In the long term, other solution pretreatments can be envisioned which target the polymeric $In(OH)_x$ material directly and more completely without negatively impacting the lattice of the oxide.

Alternatively, one can envision a treatment that may provide a protecting character to the native oxide shortly after sputtering/etching has occurred to inhibit the hydrolysis of the surface. This may be partially realized by subjecting the ITO samples to modification protocols utilizing small molecules with carboxylic acid functionalities. Thw behavior should be explored more thoroughly through conductive tip AFM studies where various pretreatment protocols are ascertained for the effectiveness at increasing the electronic character of the ITO sample. Presumably, the treatments which have shown to remove substantial amount of hydroxide coverage and show increased solution electron transfer rates would also indicate this as increased active area under imaging. Furthermore, the pretreatments which are found to give the best results should be combined with a surface modification aimed at blocking the hydrolysis of the sample by strongly bonding to surface functional groups in high coverages. Ideally, a sputter cleaned ITO sample (found to be low in relative hydroxide concentration) should be subjected to small chain acids with bi-functional character such as succinic acid before exposure to atmosphere which may

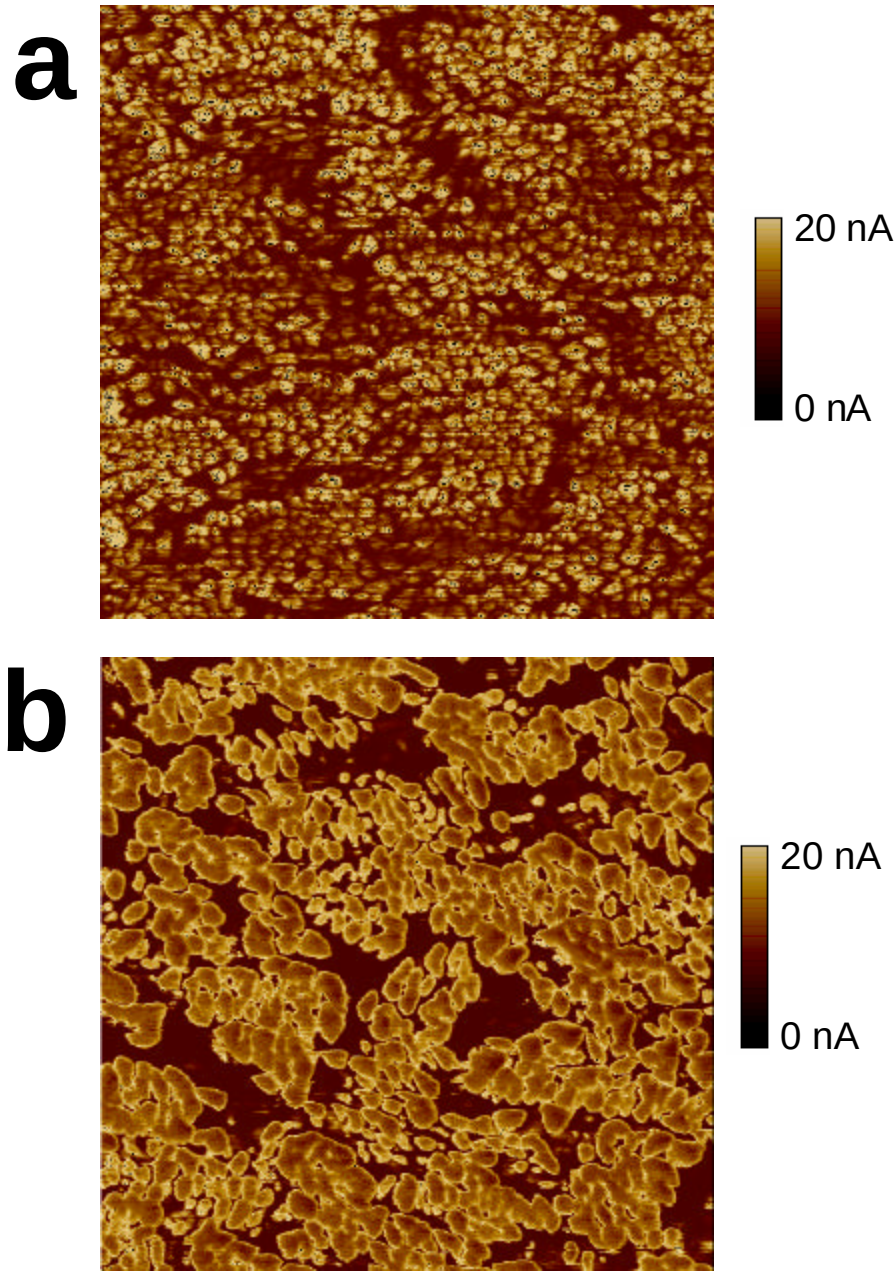

Figure 6.1 Conductive tip AFM images of ITO samples a) as received ITO, and b) ITO which has been pretreated with 12 M HCl 0.2 M /$FeCl_3$ solution for 15 seconds.

provide some protection from the immediate hydrolysis of the surface. Another approach that seems feasible is the application of a densely packed SAM layer to the ITO surface. Currently, a variety of SAMs are being explored as possible modifications to ITO[3-5] and include species such as docosyltrichlorosilane ($CH_3(CH_2)_{20}CH_2SiCl_3$) and 1-decanethiol ($HS(CH_2)_9CH_3$). However, most studies utilize this layer to enhance wettability or tune the ITO workfunctions rather than focus on changing (or limiting the change in) surface chemistry. Insights from this research suggest that these layers may potentially employed to reduce hydrolysis of the surface by acting as a blocking layer to water. The full potential of these layers can only be realized if less insulating (shorter or conjugated chains) SAMs are applied directly on heavily etched or sputtered ITO surfaces.

In the short term, techniques borrowed from other oxide surfaces could be employed to enhance as-received ITO. Processing of aluminum electrodes in the manufacture of electrolytic capacitors experience a similar problem with the spontaneous growth of $Al(OH)_3$.[6] Strategies developed to address this problem should be considered for ITO surfaces and include washing with warm benzoic acid to inhibit hydroxide formation, and dehydration of the surface under high heat and vacuum.

In any case, the build up of $In(OH)_X$ is likely the largest problem facing ITO, not withstanding inherent film resistances, for the further development of organic electronic devices. It is this author's opinion that research should be directed at removing this material as a first step to achieving higher efficiencies of these types of devices.

6.2 SMALL MOLECULE MODIFICATION

These studies have also shown that simple modification of the ITO surfaces can been achieved through the absorbance of small molecules, functionalized with strong hydrogen bonding groups which interacts directly with the ITO surface chemistry. The result of which, is a change in the surface nature of the sample, both physically and electrically after modification protocols are complete. In this approach, the alteration of the ITO surface leads to enhanced characteristics in both solution electron transfer and completed device characteristics. The underlying principles that govern the observed enhancements can be explained by the following processes: ***i)*** Etching of the electrode surface to expose an increased population of active transfer sites. ***ii)*** The increase the wettability between the electrode and an adjacent organic layer, based on changing the polarity of exposed terminal functional groups across the electrode, and to a lesser degree, ***iii)*** creating an electrocatalytic effect, brought about by select modifiers acting as a charge transport mediator between the electrode material and the adjacent organic layers. ***iv)*** The ability to change the apparent work function of the ITO material by inducing a dipole upon chemisorption which leads to a vacuum shift dependant of the magnitude of the dipole (not explored here).

Success in any one of these processes, have the potential to significantly change the electronic properties of a given device. Likely, the resulting increase in charge injection observed is a combination of these factors and cannot be attributed to simply one factor as discussed below.

6.2.1 Active Sites of Transfer

Perhaps the most important factor in the transfer of charge between ITO and an adjacent organic layer is the population of active sites across the electrode. It has been shown that ITO exhibits a heterogeneous conductivity map which includes sites where electron transfer is prevalent, and areas where the electron transfer is nearly non-existent.[1-2,7-9] The limited population of these active sites is problematic in that charge injection is also limited based on the number of active sites in contact with the organic layers. This research has presented evidence for the increase of the active area based on the apparent increase in solution electrochemical rate coefficients. Working from the surface model developed previously, ITO relies on defect sites in the lattice to initiate charge transfer events. However, the formation of a $In(OH)_x$ material, possibly by the hydrolysis of the lattice, creates an insulating barrier where charge is isolated from passing between the electrode and the organic essentially blocking the active site. Indeed, there is a strong correlation between the amount of $In(OH)_x$ material present and the electron transfer rate coefficients. It is thought that the increase in the active area observed may occur by a light etching mechanism of the ITO surface.

This light etching surface occurs through the modification process by breaking up of the surface confined $In(OH)_x$ groups which are thought to exist on the ITO surface in an abundant amount. In this model, the modifier approaches the $In(OH)_x$ network and

initiates a complex with indium. The resulting complex formation leaves the O-In-O bond severed. By repeated complex formation, the network is broken enough to where a fraction of the material can be washed away. This reduction in $In(OH)_x$ material allows for an increased exposure to redox active events. The result is a surface that has a dramatic decrease in the insulating material. While the process outlined is capable of removing the insulating material, only a fraction of the insulating material is actually lost. It is important that future studies incorporate a more aggressive removal scheme to maximize the active area exposed to the organic surface as previously outlined.

6.2.2 Wettability of ITO

The data set forth in this dissertation has also shown the wettability of an ITO surface with respect to a hydrophobic organic moiety is enhanced following small molecule modification procedures. In fact, OLED device data has shown the increase in shunt resistance ascribed to better wetting of the ITO surface leads to substantially more efficient devices. The extent of this enhancement can be quite large judging from the water contact angles measured, from less than 3° for plasma etched ITO to greater that 60° for the HBC modified surface. The consequence of this increase in contact angle is a better integration between the electrode surface and the adjacent organic layers, increasing the surface area where the electrode and the organic layer are in electrical

contact, and improving adhesion which may help stem delamination effects after device service as well as reducing the number of device pinholes, enhancing the efficiency.

Unfortunately, the nature of the oxide surface is inherently incompatible with hydrophobic organic molecules and these modifications only relieve a fraction of the stress incurred. Future considerations should include efforts to increase contact angles to values approaching 90%. This may be accomplished by the use of a SAM with a more hydrophobic head-group; or one can envision a SAM deposited on the surface which may covalently link with the organic layer in a polymeric form. This may include specific modifier functionalities that adsorb strongly to ITO then polymerize with specially synthesized organic layers, or polymers locking them to the surface.

Alternatively, the self assembly of entire device structures is promising and should be explored more fully. This is partially being realized by current efforts[10] stemming from the research presented here where muli-layer structures are self assembled to provide custom surfaces. Electrochemical studies on these surfaces are promising and show a clear enhancement of the electrode characteristics which do not suffer from substrate etching that may occur with application of PEDOT:PSS layers. Additionally, as the this technology matures, one can envision "built-in" functional layers which likely could lead to a surface or complete device engineered for specific purposes or self assembly.

6.2.3 Electron Transfer Kinetics

Through the course of this work, it has been shown that with select modification of the ITO surface, enhancement of electron transfer kinetics can occur. The modest increase observed in the electron transfer rate coefficient is attributed to a variety of mechanisms. First, select molecules have the potential to undergo a slight electrocatalytic effect where the surface bound modifier acts as a charge transport mediator between the electrode and the redox couple present in the adjacent evaluation solution and presumably those present in an organic layer. Although only a few of the studied modifiers could exhibit this behavior, it is believed that this route has to potential to be extremely effective if a suitable mediator is found. Second, light etching and subsequent removal of insulating material from the surface of the electrode results in the exposure more active area across the electrode. This increase is shown to have substantial effects on the observed electron transfer rate coefficient when compared with the initial sample. This result is arguably the largest contributor to the increases seen in these studies and should be a focal point for future explorations. Lastly, there is evidence that long term exposure to select modification solutions may etch the oxide lattice itself, creating additional defect sites in the surface increasing the electronic nature of the electrode. This is found when prolonged exposure leads to complex formation between the small molecule modifier and surface bound indium groups. The coupling of the modifier with the oxide leads to a lattice defect and as a result, additional electron transfer sites.

Based on this more complete understanding of how ITO behaves, future projects should focus on mapping the conductivity changes of ITO after modification protocols and finding more potent electro-catalytic materials compatible with the desired device materials.

6.2.4 Device Thermodynamics

Although the modification schemes outlined here did not substantially change the observed work function of the ITO electrode, the importance of this aspect should not be overlooked. Thermodynamic properties such as the electrode's workfunction/vacuum level are viable options depending on the chemistry of the surface. This has been demonstrated by the simple absorption of ethanol to a sputter-cleaned ITO surface changing the effective vacuum level. Other well known studies have established this further by changing vacuum levels routinely by the absorbtion molecules with strong dipoles. Following these examples, modification has the ability to strategically shift the apparent workfunction of ITO to be more compatible with organic materials or to provide a larger internal bias for photovoltaic cells. Future work is needed to identify appropriate candidates that may achieve the desired shift in vacuum level as well as incorporate those advantages discussed above.

6.3 INTERNAL RESISTANCE OF ITO

In all these studies, the inherent internal resistance due attributed to the ITO material was fixed as a function of the source of ITO. Because of this limitation, little could be done to study this factor. New TCO construction techniques and materials are being developed in an effort to improve electrical characteristics within the device. This is particularly important in the development organic thin-layer technology as ITO is known to be limited by high resistance values (compared with other conductors). As this technology matures, efforts should concentrate on the control of ***i)*** the composition of ITO, with regards to the purity, and dopant levels of both indium and oxygen. ***ii)*** The crystalline nature of the sample, low grain boundaries and complete crystal faces are desirable. ***iii)*** The construction of new TCO materials which may surpass ITO as the TCO of choice, such as indium doped zinc oxide (IZO) which are currently being explored.[11-12] Efforts in this region should focus on lowering the internal resistance of the material while retaining a high optical transmission and electrical properties.

6.4 CONCLUDING REMARKS

The accomplishments presented are several-fold and may lead to important discoveries and advancements for the design and manufacture of organic thin-film device structures. The strategic modification of TCO electrodes such as ITO can provide a

method to effectively increase the observed electron transfer at the ITO/organic interface. This increase is achieved by the ability pretreatments and modification protocols have to alter the physical and electrical aspects of the ITO electrode and hence, improve upon the performance aspects of organic thin film devices. However, it is difficult to correlate any beneficial effects observed strictly to an individual factor. Current techniques for the study of interface charge transfer events, is primarily through regression from a completed device measurement. This is problematic in that measurements of this type cannot resolve between individual factors contributing to the observed change in charge transfer. However, Successful alterations can be monitored by pre-device electrochemical methods, which allow for the direct inquiry of electrode kinetic aspects without back projection. This provides a tool for ascertaining the effectiveness of electrode modification strategies without complications of addressing the device as a whole. The combined effect is method for the evaluation and optimization of organic thin-film device operation and performance.

Overall, this research has set forth the ground work and methods for future investigations aimed at improving the TCO/organic interface. While the results shown are provocative and present a modest improvement, the work is intended to be a "proof of concept" and is by no means conclusive. More work is needed to build on the methods and concepts outlined particularly in advancing ITO surface modification to address the $In(OH)_x$ material. In conclusion, these studies will help to overcome the many challenges that exist for the development and large scale commercialization of organic thin-layer devices.

6.5 CONDUCTIVE POLYMER NANOSTRUCTURES

The research presented in this dissertation illustrates the successful formation of conductive polymer nanostructures constructed through a combination of micro-contact printing and electro-catalyzed polymer growth of either PEDOT or PANI monomers. Furthermore, these structures have been shown to have remarkable definition with moderate polymer growth and can achieve repeating feature resolution on a sub-micron scale. The end result has been the formation of conductive polymer diffraction grating with relatively high efficiencies and the potential to respond to chemical stimulus in the immediate environment.

Also shown here is the development of working chemical sensors based on these microstructures in a diffraction grating format where the basic sensing element can be described by changes in adsorptivity and refractive index induced by environmental stimulus. The first of these working sensors is a pH sensor were response to changing pH was documented by the change in diffraction efficiency of the PANI structure. Additionally, a potentiometric changes induced a response in the diffraction efficiency for gratings with PEDOT structures.

Although the presented work displays this achievement, the actual boundaries of the size scale have not been explored. Future endeavors should probe the potential of this system to reduce the scale further to determine the point where polymer/substrate contrast

is lost. Other endeavors should include the growth of polymer in other patterned features as an initial step toward converting this technology to nano-device technology. To this end, the study has set the ground work needed to utilize this technology for nano-electronics where the potential of patterned conductive channels to act as nano-wires is feasible. One can even envision large scale organic circuitry built in this manner to produce working devices on nano-distance scales.

Additionally, the sensing capability of these structures can be expanded beyond the simple elements shown here. Future work in this area may refine the structures to include acceptor moieties specific to a given sensing target where changes induced by their union may be visible in the gratings characteristics.

APPENDIX A

EXPERIMENTAL METHODS

A1 ITO CHARACTERIZATION

A1.1 Microscopy of ITO Surfaces

Surface images of ITO samples were taken with a Nanoscope II atomic force microscope operating in tapping mode. Samples were cleaned by rubbing with Triton X-100 detergent and rinsed with copious amounts of water followed by rinsing in ethanol. Samples where then dried in a stream of nitrogen and mounted to a magnetic sample stage with double sided tape. Images were taken across the sample, in a minimum of 4 placements to insure homogeneous samples. A representative image was then selected from those collected to represent the sample. Roughness measurements were found through the software provided by the manufacturer over large areas (greater than 10 μm^2) with any obvious anomalies removed.

A1.2 Electron Spectroscopy of ITO Surfaces

XPS studies were conducted with a Kratos Axis-Ultra X-ray photoelectron spectrometer equipped with a monochromatic Al Kα source at 1486.6 eV. For all the

data presented here, the analyzed spot size was 300 x 700 microns, with an analyzer pass energy of 20 eV. UPS spectra were obtained with a pass energy of 5 eV and 21.2 eV He (I) excitation (Omicron VUV Lamp HIS 13). For all UPS analyses, a 5 volt bias was applied to improve the transmission of low KE electrons and to improve the determination of the energy of the low KE edge. The Fermi edge for these ITO samples was determined by extensive sputter cleaning of an ITO sample, until sufficient reduction of the surface was achieved to clearly see ionization from the Fermi edge of this material. We insured that the absolute kinetic energy of this edge was the same as seen for clean gold samples, i.e. the ITO samples were in electronic equilibrium with the spectrometer. Samples were cleaned and modified according to the experimental designs. Samples were then mounted on a sample stage with double sided tape and grounded by the application of silver conductive paint, or a metal surface clip. Once introduced into the analysis chamber, electron signal was maximized for the C 1s photoelectrons for both 0° and 75° takeoff angles.

XPS of SAM covered gold was carried out by exposing 3.0 grams of In_2O_3 powder (450 m^2 surface area, ca. 150 m^2 per gram) to ITO modification solutions similar to those used for ITO (0.01 M). In_2O_3 powders have been shown to be similar in composition to ITO but provide high surface areas to maximize the $In(OH)_x$ material that may potentially be lost to solution. After sufficient elapsed time to achieve equilibrium had passed, (approximately 8 hours) the solution was collected, double filtered, and exposed to gold samples which had previously been modified with an alkane-thiol carboxylic acid,

($SH(CH_2)_{12}COOH$). The carboxylic acid functionalized SAM was utilized to complex with, and pre-concentrate, any indium or indium carboxylate-like complex present in the modification solution, capturing any etched material in the thin film suitable for analysis by XPS. The gold samples were allowed to soak overnight in the collected modification solutions before rinsing with ethanol and placing under vacuum. The results are shown by the XPS spectra of the SAM covered gold substrates after immersion in modification solutions collected over powder exposed to $Fc(COOH)_2$ as well as a control group where the powder was exposed to EtOH only.

A1.3 Ultraviolet Photoelectron Spectroscopy of ITO

Samples were introduced to the analysis chamber after thorough cleaning by sonication in successive solutions of Triton X-100/water, water, and ethanol. Samples were then sputter cleaned with an argon ion source (750 eV) for 45 minutes to insure contaminant free surfaces. Analysis was then conducted on the cleaned surface. Select samples were then transferred to an atmosphere controlled glove-bag filled with dried argon attached directly to the chamber entrance as to avoid exposure with laboratory atmosphere. Modification of samples was then conducted within the bag according to predetermined modification protocols as discussed below. Samples were then re-introduced into the chamber where additional analysis could be conducted on the now

modified surfaces. Control samples were implemented in the form of ***i)*** no modification, and ***ii)*** submersion into neat ethanol to accompany the modified samples.

A1.4 Static Drop Contact Angle Measurements

Static water contact angle measurements were taken from at least 10 separate droplets per sample utilizing a Kruss DSA 1.7 drop shape analyses instrument that allows for automated delivery and calibrated volumes (50uL) to maximize reproducibility. Samples were prepared according to protocols for modified and non-modified surfaces and placed on the mobile sample stage where a series of droplets of filtered water (Millipure filtering system, 18MΩ) were deposited laterally across the sample surface. Each droplet was then imaged by the onboard camera and measured for contact angle on both sides through the software package supplied by the manufacturer. Careful attention was given to the time drops were analyzed, imaging was limited to a few elapsed seconds to avoid significant interaction between the chemisorbed small molecules and the water droplet and evaporation/or effects.

A2 MODIFICATION OF ITO SAMPLES

ITO/glass films used in these studies were obtained from Colorado Concept Coatings Limited, (Denver Colorado) with a sheet resistance of ca. 13 Ω/cm^2. All ITO samples were initially cleaned by scrubbing with a soft cloth and a Triton X-100/water solution, followed by ultrasonic cleaning in successive solutions of Triton X-100/water, water, and ethanol for at least 15 minutes each and then dried in a stream of nitrogen.

A2.1 Solution Pretreatment of ITO

Additional pretreatment/cleaning procedures were then conducted according to the following protocols: 1) *Air plasma cleaning* (Herrik, 60 watts for 5-15 minutes), for most devices, and for all of the ITO films which were modified by small molecule dopants and/or electropolymerized conducting polymer films this air plasma cleaning step immediately preceded the modification and creation of a device. 2) *Piranha treatment*, adapted from Wilson and Schiffrin,[28] consisted of three steps: *i)* heating the ITO in a 10 mM solution of NaOH for 4 hours at 80°C, *ii)* soaking the ITO in piranha (4:1 H_2SO_4: H_2O_2) for 1 minute, and *iii)* heating the ITO to ca. 160°C for 2 hours. The ITO was rinsed with copious amounts of water between each step and dried with nitrogen. 3) *RCA treatment* involved heating the ITO in a 1:1:5 solution of NH_4OH : H_2O_2 : H_2O for 30 minutes at 80°C, rinsing thoroughly with water, and drying with a

stream of nitrogen gas. 4) Certain ITO samples were also *argon-ion sputtered* at 750eV for 45 minutes with an argon pressure of $6.5*10^{-7}$ torr, which were conditions estimated to remove some carbonaceous impurities and surface hydroxides, but which would not lead to extensive oxide reduction and lattice damage.

A2.2 Modification of ITO Surfaces

Several different small molecules were adsorbed to ultrasonically-cleaned, plasma etched ITO thin films, and then either used for the formation of vapor deposited thin-layer devices, or further modified with either spin-cast PEDOT:PSS (commercially available as Baytron-P (EL grade)), or with electrochemically grown PEDOT:ClO_4^- or PEDOT:PSS layers. Four different small molecule modifiers were evaluated: ferrocene dicarboxylic acid ($Fc(COOH)_2$), 3-thiophene acetic acid (3-TAA) (both from (Aldrich, used without further purification), a hexa-carboxylic acid derivative of hexabenzocoronene, (HBC-$(C_3COOH)_6$) and a modified version of the hole transport agent, TPD (4,4'-Bis(*m*-tolylphenlyamino)biphenyl) functionalized with two *para*-methoxy substituents and two six-carbon alkoxy side chains, terminated in carboxylic acids (6-{4-[{4'-[[4-(5-Carboxy-pentyloxy)-phenyl]-(4-methoxy-phenyl)-amino]-biphenyl-4-yl}-(4-methoxy-phenyl)-amino]-phenoxy}-hexanoic acid, (p-OMe)$_2$-TPD-X_2, and HBC). Adsorption of onto ITO was achieved by soaking cleaned ITO samples in a 1

mM solution of the small molecule, in pure ethanol, for 8 hours and then rinsing briefly with acetonitrile followed by drying the sample in a stream of nitrogen.

Electrochemical characterization of the adsorbed monolayers was carried out by standard cyclic voltammetry. All electrochemistry was done with a saturated Ag/AgCl or a Ag wire reference electrode, a platinum counter electrode, and the modified ITO as the working electrode in a custom built electrochemical cell. The potential axis of all voltammograms are reported versus the parent (ferrocene/ferrocinium (Fc/Fc^{+})) redox couple, which has an E^{o} in acetonitrile of 0.159V vs. S.C.E. (31). The solvent for all the electrochemical studies of adsorbed small molecules was acetonitrile with a supporting electrolyte of 0.1 M tetrabutylammonium hexafluorophosphate.

Conductive polymer thin films were grown on the ITO substrate solutions of 10mM 2,3-dihydrothieno[3,4-b]-1,4-dioxin (EDOT) and 100mM counter ion ($LiClO_4$) or 5mg/ml polystyrene sulfonate in acetonitrile. The potential was stepped to 1.1 volts vs. Fc/Fc+ for periods of a few seconds. After electropolymerization was stopped the potential was stepped back to +0.6 volts, a value greater than that required to electrochemically dope PEDOT films but a value at which further PEDOT will not form. The modified ITO substrate was then immersed under potential control, rinsed in ethanol, and dried in a stream of nitrogen.

Thin films of commercial PEDOT:PSS were established by spin coating techniques. The cleaned samples were mounted to a rotary stage where the surface was flooded with the polymer solution (Baytron P, EL grade) and allowed to sit for 30 second. The sample is then brought up to rotating speed quickly to ca. 3000 rpm for 60

seconds. Upon completion of the films, films are annealed in a vacuum oven for 2 hours at 100° C to drive off any residual water.

A3 CHARGE TRANSFER MEASURMENTS

Charge transfer kinetic studies utilized cyclic voltammetry of a well established probe couple, ferrocene/ferrocinium (Fc/Fc^+), at varying sweeprates in order to estimate electron transfer rate coefficients. Cyclic voltammograms were acquired with an EG&G Instruments 283 potentiostat, with samples placed in a custom designed and house built 3 port electrochemical cell incorporating a freshly prepared Ag/AgCl pseudoreference electrode, and a Pt counter electrode, in N_2-degassed solutions containing tetrabutylammonium-hexafluorophosphate (TBAHFP) or lithium perchlorate ($LiOCl_4$) supporting electrolyte at high concentrations 0.250 M. All solvents were purified by distillation and stored over activated alumina to remove impurities and trace water. Prior to creating analyte solutions, the distilled solvent was run through a fresh column of activated alumina to insure clean solvents.

Prior to cleaning, ITO samples for electrochemical experiments were masked off and etched with 15% HCl solution heated to 80°C to create a 2x10mm band electrode (0.2 cm^2), with contact pads to reduce radial diffusion effects. Voltammograms of the probe where taken at regular intervals of 5, 7.5, 10, and 15 mV/s. Slower sweeprates resulted in deformed voltammograms due to mass transport effects, while sweeprates

faster resulted in anodic/cathodic peak separations too large to be evaluated. Samples with excessively slow rate coefficients were analyzed with a regression to determine suitable anodic/cathodic peak separations at lower sweeprates. Electron transfer rate coefficients were then estimated based on the method described by Nicholson et al.

A4 ORGANIC THIN-LAYER DEVICES

ITO-coated glass was obtained commercially (Colorado Concept Coatings LLC; Longmont, CO) and cut to the appropriate device size prior to cleaning. Samples for a particular set of devices or electrochemical experiments were selected to be adjacent to each other on the larger sheet of ITO, to minimize variations in the device and electrochemical properties, which arise due to small variations in ITO processing Prior to cleaning, ITO samples for OLED and OPV devices were masked and either etched as described previously, or coated in select regions with an insulating layer of SiO to create a contact pad for a device area of ca. 0.2 cm^2.

Each ITO sample was then taken through a series of cleaning steps: *i)* samples were first rubbed with a soft cotton cloth saturated with soapy water and thoroughly rinsed with filtered water (Millipore filtering system – 18 MO); *ii)* samples were cleaned in an ultrasonic bath (30 minutes each cycle) in filtered water/Triton X-100, filtered water, and finally pure ethanol. Samples were then dried in a stream of nitrogen and *iii)*

etched in an air-plasma cleaner (Harrick – 60 watts) for 5 minutes just prior to surface modification and/or device preparation

A4.1 OLED Construction

After cleaning and/or modification steps select ITO samples were placed in a custom-designed high vacuum deposition chamber, base pressure ca. 10^{-8} torr (Kurt J. Lesker Corp.). Once at the desired pressure successive layers of TPD and Alq_3 were vacuum deposited through a mask on a rotating stage to achieve 50nm thickness for each layer. The two layer device was then masked under vacuum and deposited with a co-deposit of 10:1 Mg:Ag (100nm) for the cathode material. OLED devices were transferred to a Vacuum Atmospheres glove box (less than 1 ppm O_2, H_2O) without exposure to laboratory atmosphere. Both current-voltage and luminance-voltage measurements were made with a Keithly 2400 SourceMeter and a calibrated photodiode positioned perpendicular to the device face (calibrated to provide correct luminance measurements at 540 nm).

A4.2 OPV Construction

A multilayer OPV cell configuration was selected which had been shown to provide high efficiency, and which could be reproduced at lower, but consistent efficiencies in our labs. Multilayer cells were constructed in a vacuum chamber coupled to an Ar-glove-box/characterization chamber, so that atmospheric exposure could be avoided. Vacuum deposited sublimation-purified copper phthalocyanine (CuPc) (Aldrich), C_{60} (MER Corp.) and bathocuprine (BCP) (Aldrich) at thicknesses of 20nm, 40nm, and 10nm respectively was deposited at pressures below at ca. $1x10^{-6}$ torr, on various cleaned and pretreated ITO substrates. Following deposition of the final organic layer, the sample was moved to the glove box and masked for an aluminum cathode to be evaporated over the device. The OPV cell was then immediately transported from the vacuum deposition environment into the glove box for characterization. Illumination of the device was achieved using a tungsten-halogen light source, filtered to provide ca. 100 mW/cm^2 across the visible wavelength region.

A4.3 Device Testing

Device substrates were seated into a custom-built clamp, which facilitates electrical contact to the cathodic contacts of the four devices and the ITO anode. In addition, this clamp facilitates the coupling of photodiode detectors (Hamamatsu The

photodiode current was passed through a current-to-voltage amplifier (Newport, Model 1815-C), and a Keithly 2400 SourceMeter was used to control bias voltage and measure device current. The entire measurement package was computer-interfaced to a LabView program (National Instruments) that controls the SourceMeter and measures device current and intensity.

A5 CONDUCTIVE POLYMER NANOSTRUCTURES

A5.1 Substrate Cleaning

Cleaning of the Au surface is an essential first step prior to stamping, and was achieved by either a) rinsing in a piranha solution for 1 minute, followed by rinsing in triply distilled water, or b) by electrochemically cleaning the Au electrodes by cycling their potential from 0.0 to +1.4 volts, vs. Ag/AgCl, in the supporting electrolyte solution, forming and reducing the gold surface oxide.

A5.2 Micro-Contact Printing

Stamps were created by utilizing conventional Au-coated blazed grating (1200 lines per millimeter, blaze angle = 35º, grating depth = ca. 100 nm) as a master form,

soft-polymer stamps were fabricated from its image by casting polydimethylsiloxane (PDMS) on the master grating. This stamp is constructed by placing the grating master in a level container where a 10:1 (w:w) mixture of SYLGARD silicone elastomer 184 and SYLARD 184 curing agent (DOW Corning Corporation) is poured over and envelopes the master. The encoated grating is allowed to degas at room temperature for 1-2 hours until the elastomer pour is free of visible air bubbles then allowed to cure for 8 hours at ca. 90° C. Following the curing of the elastomer, the PDMS can be gently peeled back from the grating master and cut to size with a razor. The resulting stamp replicates the inverse of the features on the grating master ie. raised portions on the grating master correspond to the recessed regions of the stamp.

Substrate cleaning processes were followed immediately by rinsing with triply distilled water, drying and stamping with the C_{18}-alkanethiol solution, in a laminar flow hood environment, which kept dust particles from adsorbing to the electrode surface. Rinsing with water immediately before stamping was found to be particularly important as the residual water on the surface is thought to help to distribute C_{18} fully along the stamp.

The stamping process is accomplished by transferring the “ink” to a gold substrate using a house built apparatus which allows for constant vertical alignment with the surface to be stamped (a gold substrate) to ensure normal, even stamping, with constant pressure across the entire stamped surface. The inked and dried stamp is brought into contact with a freshly cleaned Au thin film with a force of ca. 1-2 kg per cm^2, for one minute, then quickly separated from the gold surface, rinsed and dried leaving behind a

patterned gold surface. Concerns that poor integrity of sub-micron stamped features on a gold surface due to flow of the alkanethiol solution away from the point of contact, appear to be overcome with this stamping approach.

A5.3 Electro-Catalyzed Polymer Growth

Diffraction gratings were grown in a custom designed electrochemical cell using potential step techniques. The cell is designed to house a small cavity of ca. 2ml that incorporates apposing ports where the space can be flooded with outside solutions allowing for studies without changing the alignment of the grating. The gold surface resides at the back of the cell with indiumtinoxide coated glass directly opposite to function as a counter electrode. The cell front incorporates a wide horizontal cutout to allow unobstructed viewing at large diffraction angles. An additional small port, houses a Ag/AgCl pseudoelectrode used as the referance electrode. Potential-step growth of polymer gratings is achieved by filling the cell with growth solution (PANI: 0.5M H_2SO_4; 0.05M Aniline, PEDOT: methanol/water; 10% v/v MeOH; 0.1M $LiClO_4$; 0.01 M EDOT monomer or acetonitrile; 0.1M $LiClO_4$; 0.01 M EDOT monomer) and stepping the potential (for PEDOT – 1.0 volts vs. Ag/AgCl -- Fig. 3b; for PANI – 0.7 volts vs. Ag/AgCl – Fig. 3c) for a predetermined amount of time. Growth of a grating is monitored by observing the diffraction power from to a 2mW HeNe laser trained on the gold sample with a photo diode/power meter combination. With this method, samples can be grown to: some percentage before maximum diffraction, maximum diffraction, or

after maximum diffraction (overgrown state). Gratings grown voltammetrically are similar except potential is cycled to a point just past the redox potential for the monomer until desired region is reached.

Wavelength dependant efficiency diagrams were created by removing the OEM grating from a commercial monochromator and replacing it with either a PEDOT, PANI or stamp mater grating mounted on a glass slide. The wavelength scale was calibrated using two lasers (633nm, 532nm) while scanning the monochrometer with time. Once the scale was set, a Ar/Xe arc lamp provided the white light source(slits at 0.5mm) for diffraction. The ratio of the polymer to master output was plotted to remove features that arose from the lamp itself.

In situ grating growth observed by AFM was accomplished by placing a stamped gold sample under an electrochemically compatible AFM scanning stage provided by Digital Instruments. Tapping mode AFM image scans in this liquid stage were taken before and after each of a series of cyclic voltammetry scans with a potential range of 0.0V to 1.1V.

A5.4 Polymer Diffraction Grating pH Sensing

pH profiles for PANI gratings were generated by growing PANI gratings as described above then flushing the growth solution in the cell with KHP buffer solutions made up to be different values of pH, numerically from 1-6 pH units. Grating diffraction

was measured for each solution at laser incident angles of 0 and 45 degrees normal to the surface, in both S and P polarized rotations of the laser. To monitor reproducibility, the buffer series was re-introduced and compared with initial findings.

A5.5 Polymer Diffraction Grating Potentiometric Sensing

Cyclic diffraction of PEDOT gratings was achieved by potentiostatically growing a grating as described above to ca. 30% of the expected diffraction efficiency. At this point the growth solution was exchanged for a 0.1M $LiOCl_4$/MeCN electrolyte solution. The first order (m = +1,-1) diffraction spot from a 2mW HeNe(633nm) laser, trained on the grating, was monitored while the potential of the grating was ramped in a cyclic fashion beginning at 0.0V scanning forward to +0.2V and then reversing to –0.2V and then back to 0.0V. Diffraction spot was evaluated using a photodiode/power meter combination during the scan. The process was repeated to obtain data at a different wavelength GeNe laser at 532nm. Cycles for both lasers were repeated twice to ascertain degradation effects upon cycling.

REFERENCES

CHAPTER 1

1. Bao, Z. N. "Materials and Fabrication Needs for Low-Cost Organic Transistor Circuits," *Adv. Mater.* 2000, *12*, 227.

2. Bao, Z. N.; Rogers, J. A.; Katz, H. E. "Printable Organic and Polymeric Semiconducting Materials and Devices," *J. Mater. Chem.* 1999, *9*, 1895-1904.

3. Brabec, C. J.; Sariciftci, N. S.; Hummelen, J. C. "Plastic Solar Cells," *Adv. Funct. Mat.* 2001, *11*, 15-26.

4. Greenham, N. C.; Moratti, S. C.; Bradley, D. D. C.; Friend, R. H.; Holmes, A. B. "Efficient Light-Emitting Diodes Based on Polymers with High Electron Affinities," *Nature* 1993, *365*, 628-630.

5. Friend, R. H.; Gymer, R. W.; Holmes, A. B.; Burroughes, J. H.; Marks, R. N.; Taliani, C.; Bradley, D. D. C.; Dos Santos, D. A.; Bredas, J. L.; Logdlund, M.; Salaneck, W. R. "Electroluminescence in Conjugated Polymers," *Nature* 1999, *397*, 121-128.

6. Gustafsson, G.; Cao, Y.; Treacy, G. M.; Klavetter, F.; Colaneri, N.; Heeger, A. J. "Flexible Light-Emitting Diodes Made from Soluble Conducting Polymers," *Nature* 1992, *357*, 477-479.

7. Tang, C. W.; Vanslyke, S. A. "Organic Electroluminescent Diodes," *Appl. Phys. Lett.* 1987, *51*, 913-915.

8. Tang, C. W.; Vanslyke, S. A.; Chen, C. H. "Electroluminescence of Doped Organic Thin-Films," *J. Appl. Phys.* 1989, *65*, 3610-3616.

9. Shi, J.; Tang, C. W. "Doped Organic Electroluminescent Devices with Improved Stability," *Appl. Phys. Lett.* 1997, *70*, 1665-1667.

10. Chen, C. H.; Tang, C. W. "Efficient Green Organic Light-Emitting Diodes with Stericly Hindered Coumarin Dopants," *Appl. Phys. Lett.* 2001, *79*, 3711-3713.

11. Baldo, M. A.; Thompson, M. E.; Forrest, S. R. "High-Efficiency Fluorescent Organic Light-Emitting Devices Using a Phosphorescent Sensitizer," *Nature* 2000, *403*, 750-753.

REFERENCES (CONTINUED)

12. Adachi, C.; Baldo, M. A.; Thompson, M. E.; Forrest, S. R. "Nearly 100% Internal Phosphorescence Efficiency in an Organic Light-Emitting Device," *J. Appl. Phys.* 2001, *90*, 5048-5051.

13. Lamansky, S.; Djurovich, P.; Murphy, D.; Abdel-Razzaq, F.; Lee, H. E.; Adachi, C.; Burrows, P. E.; Forrest, S. R.; Thompson, M. E. "Highly Phosphorescent Bis-Cyclometalated Iridium Complexes: Synthesis, Photophysical Characterization, and Use in Organic Light Emitting Diodes," *J. Am. Chem. Soc.* 2001, *123*, 4304-4312.

14. Slooff, L. H.; Polman, A.; Cacialli, F.; Friend, R. H.; Hebbink, G. A.; van Veggel, F.; Reinhoudt, D. N. "Near-Infrared Electroluminescence of Polymer Light-Emitting Diodes Doped with a Lissamine-Sensitized Nd3+ Complex," *Appl. Phys. Lett.* 2001, *78*, 2122-2124.

15. Cleave, V.; Yahioglu, G.; Le Barny, P.; Friend, R. H.; Tessler, N. "Harvesting Singlet and Triplet Energy in Polymer Leds," *Adv. Mater.* 1999, *11*, 285-288.

16. Shaheen, S. E.; Jabbour, G. E.; Kippelen, B.; Peyghambarian, N.; Anderson, J. D.; Marder, S. R.; Armstrong, N. R.; Bellmann, E.; Grubbs, R. H. "Organic Light-Emitting Diode with 20 Lm/W Efficiency Using a Triphenyldiamine Side-Group Polymer as the Hole Transport Layer," *Appl. Phys. Lett.* 1999, *74*, 3212-3214.

17. Shaheen, S. E.; Kippelen, B.; Peyghambarian, N.; Wang, J. F.; Anderson, J. D.; Mash, E. A.; Lee, P. A.; Armstrong, N. R.; Kawabe, Y. "Energy and Charge Transfer in Organic Light-Emitting Diodes: A Soluble Quinacridone Study," *J. Appl. Phys.* 1999, *85*, 7939-7945.

18. Kafafi, Z. H.; Murata, H.; Picciolo, L. C.; Mattoussi, H.; Merritt, C. D.; Iizumi, Y.; Kido, J. "Electroluminescent Properties of Functional Pi-Electron Molecular Systems," *Pure Appl. Chem.* 1999, *71*, 2085-2094.

19. Yang, Y.; Jiang, H.; Liu, S.; Zhou, X.; Wu, F.; Tian, W.; Ma, Y.; Shen, J. "Photoluminescence and Electroluminescence Properties of Dye-Doped Polymer System," *Synth. Met.* 1997, *91*, 335-336.

20. Note: Companies Include Pioneer, Philips, Cambridge Display Technologies, Uniax, Kodak, Etc.

REFERENCES (CONTINUED)

21. Lim SF, Wang W, Chua SJ "Degradation of organic light-emitting devices due to formation and growth of dark spots" *Materials Science and Engineering B-Solid State Materials for Advanced Technology* 85 (2-3): 2001 22 154-159

22. Yamashita K, Mori T, Mizutani T "Encapsulation of organic light-emitting diode using thermal chemical-vapour-deposition polymer film" *Journal of Physics-Applied Physics* 2001 34 (5) 740-743

23. Carrard M, Goncalves-Conto S, Si-Ahmed L, et al. Improved stability of interfaces in organic light emitting diodes with high T-g materials and self-assembled monolayers *Thin Solid Films* 1999 352 (1-2): 189-194

24. Giorgetti E, Margheri G, Delrosso T, et al. A study of the degradation of poly(3-octylthiophene)-based light emitting diodes by Surface Enhanced Raman Scattering *Applied Physics B- Lasers and Optics* 2004 79 (5) 603-609

25. Xu G Study of degradation mechanism and packaging of organic light emitting devices *Chinese Journal of Polumer Science* 2003 21 (5): 527-531

26. Chen Z, Cotterell B, Wang W The fracture of brittle thin films on compliant substrates in flexible displays *Engineering Fracture Mechanics* 2002 69 (5): 597-603

27. Sturm JC, Wilson W, Iodice M Thermal effects and scaling in organic light-emitting flat-panel *displays IEEE Journal of Selected Topics in Quantum Electronics* 1998 4 (1): 75-82

28. Gong JR, Wan LJ, Lei SB, et al. Direct evidence of molecular aggregation and degradation mechanism of organic light-emitting diodes under joule heating: an STM and photoluminescence study *Journal of Physical Chemistry B* 2005 109 (5): 1675-1682

REFERENCES (CONTINUED)

29. Popovic ZD, Aziz H Reliability and degradation of small molecule-based organic light-emitting devices (OLEDs*) IEEE Journal of Selected Topics in Quantum Electronics, 2*002 8 (2): 362-371

30. Lim SF, Wang W, Chua SJ "Degradation of organic light-emitting devices due to formation and growth of dark spots" *Materials Science and Engineering B-Solid State Materials for Advanced Technology* 2001 85 (2-3): 154-159

31. Liu G, Kerr JB, Johnson S "Dark spot formation relative to ITO surface roughness for polyfluorene devices *Synthetic Metals* 2004 144 (1) 1-6

32. Yan L, Mason MG, Tang CW, et al. "Photoemission study of energy alignment at the metal/Alq(3) interfaces" *Applied Surface Science* 2001 175: 412-418

33. Schlaf R, Parkinson BA, Lee PA, et al. "Determination of frontier orbital alignment and band bending at an organic semiconductor heterointerface by combined X-ray and ultraviolet photoemission measurements" *Applied Physics Letters* 1998 73 (8): 1026-1028

34. Hung LS, Chen CH "Recent progress of molecular organic electroluminescent materials and devices" *Materials Science and Engineering R-Reports* 2002 39 (5-6): 143-222

35. Barth S, Muller P, Riel H, et al. "Electron mobility in tris(8-hydroxy-quinoline)aluminum thin films determined via transient electroluminescence from single- and multilayer organic light-emitting diodes" *Journal of Applied Physics* 2001 89 (7): 3711-3719

36. Burrows PE, Gu G, Bulovic V, et al. "Achieving full-color organic light-emitting devices for lightweight, flat-panel displays" IEEE *Transactions on Electron Devices* 1997 44 (8): 1188-1203

37. Brunner, K; van Dijken, A; Borner, H; et al. "Carbazole compounds as host materials for triplet emitters in organic light-emitting diodes: Tuning the HOMO level without influencing the triplet energy in small molecules" *Journal of the American Chemical Society*, 2004, 126 (19): 6035-6042

REFERENCES (CONTINUED)

38. Inomata, H; Goushi, K; Masuko, T; et al. "High-efficiency organic electrophosphorescent diodes using 1,3,5-triazine electron transport materials" *Chemistry of Materials*, 2004 16 (7): 1285-1291

39. Duong, HM; Bendikov, M; Steiger, D; et al. "Efficient synthesis of a novel, twisted and stable, electroluminescent "Twistacene" *Organic Letters*, 2003 5 (23): 4433-4436

40. Lin, XQ; Chen, BJ; Zhang, XH; et al. "A novel yellow fluorescent dopant for high-performance organic electroluminescent devices" *Chemistry of Materials*, 2001 13 (2): 456-458

41. Mason MG, Hung LS, Tang CW, et al. "Characterization of treated indium-tin-oxide surfaces used in electroluminescent devices" *Journal of Applied Physics* 1999 86 (3): 1688-1692

42. Gainutdinov IS, Nesmelov EA, Aliakberov RD, et al. "Influence of surface conductivity on the optical properties of tin-doped indium oxide films" *Journal of Optical Technology* 2005 72 (10): 787-791

43. Warschkow O, Miljacic L, Ellis DE, et al. "Interstitial oxygen in tin-doped indium oxide transparent conductors" *Journal of the American Ceramic Society* 2006 89 (2): 616

44. Yagi T, Tamano K, Sato Y, et al."Analysis on thermal properties of tin doped indium oxide films by picosecond thermoreflectance measurement" *Jornal of Vacuum Science and Technology* A 2005 23 (4): 1180

45. Mehl, W.; Buchner, W. Krist. Z. *Phys. Chem.* 1965, 47, 76.

46. Pope, M., Magnante P., Kallmann, H.P. "Electroluminescence in Organic Crystals" *Journal of Chemical Physics* 1963, 38 (8): 20428.

47. Helfrich, W.; Schneider, W. G. "Recombination of Radiation in Anthracene Crystals" *Phys. Rev. Lett.* 1965, 14, 229.

48. Tang, C. W.; Van Slyke, S. A. "Organic Electroluminescent Diodes" *Applied physics Letters*, 1937, 51 (12) 913

REFERENCES (CONTINUED)

49. Hung LS, Chen CH "Recent progress of molecular organic electroluminescent materials and devices" *Materials Science and Engineering R-Reports* 2002, 39 (5-6): 143-222

50. Friend RH, Gymer RW, Holmes AB, et al. "Electroluminescence in conjugated polymers" *Nature* 1999, 397 (6715): 121-128

51. Blom PWM, Vissenberg MCJM "Charge transport in poly(p-phenylene vinylene) light-emitting diodes" *Materials Science and Engineering R-Reports* 2000, 27 (3-4): 53-94

52. Hung LS, Chen CH "Recent progress of molecular organic electroluminescent materials and devices" *Materials Science and Engineering R-Reports* 2002 39 (5-6): 143-222

53. Li XC, Sun JZ, Ma YG, et al. "Electroluminescent and displaying devices based on semi-conducting polymers" *Chemical Journal of Chinese Universities* 1999 20 (2): 309-314

54. Hung LS, Liao LS, Lee CS, et al. "Sputter deposition of cathodes in organic light emitting diodes" *Journal of Applied Physics* 1999 86 (8): 4607-4612

55. Han SJ, Huang CJ, Lu ZH "Color tunable metal-cavity organic light-emitting diodes with fullerene layer " *Journal of Applied Physics* 97 (9): Art. No. 093102 2005

56. Chuen CH, Tao YT "Highly-bright white organic light-emitting diodes based on a single emission layer" *Applied Physics Letters* 81 (24): 4499-4501 2002

57. Adamovich V, Brooks J, Tamayo A, et al. "High efficiency single dopant white electrophosphorescent light emitting diodes" *New Journal of Chemistry* 26 (9): 1171-1178 2002

58. Shaheen SE, Kippelen B, Peyghambarian N, et al. "Energy and charge transfer in organic light-emitting diodes: A soluble quinacridone study" *Journal of Applied Physics* 85 (11): 7939-7945 1999

59. J. Kido, and Y. Iizumi, "Fabrication of highly efficient organic electroluminescent devices" *Applied Physics Letters* 73, 2721, 1998.

REFERENCES (CONTINUED)

60. M. A. Baldo, V. G. Kozlov, P.E. Burrows, M.E. Thompson, and S. R. Forrest, V.S. Ban, B. Koene, and M. E. Thompson, *Appl. Phys. Lett.* 76, 4, 1997.

61. H. F. M. Schoo, R. C. J. E. Demandt, J.J.M. Vleggaar, C.T. H. Liendenbaum, P. van de Weijer, and Y. Croonen, *Materials Research Society Meeting Spring 1998*, San Francisco, California, paper G1.1., 1998.

62. Peumans P, Yakimov A, Forrest SR "Small molecular weight organic thin-film photodetectors and solar cells" Jornal of Applied Physics 93 (7): 3693-3723 2003

REFERENCES (CONTINUED)

CHAPTER 2

1. Dunphy, D.R.; Mendes, S.B.; Saavedra, S.S.; Armstrong, N.R., *Interfacial Electrochemistry: Theory, Experiment, and Applications;* Wiechowski, A., Ed.; Marcel Dekker, Inc.: New York, 1999; 513

2. Dunphy, D.R.; Mendes, S.B.; Saavedra, S.S.; Armstrong N.R. "The Electroactive Integrated Optical Waveguide: Ultrasensitive Spectroelectrochemistry of Submonolayer Adsorbates" Darren R. Dunphy, Sergio B. Mendes, S. Scott Saavedra, and Neal R. Armstrong *Analytical Chemistry* 69, 3086, 1997

3. Kim, J.S.; Ho, P.K.H.' Thomas, D.S.; Friend, R.H.' Cacialli, F.; Vao, F.-W.' Li, S.F.Y. "X-ray photoelectron spectroscopy of surface-treated indium-tin oxide thin films" *Chem. Phys. Lett*., 315, 307, 1999

4. Kim, J.S.' Cacialli, F.; Granstrom, M.; Friend, R.H.; Johansson, N.; Salaneck, W.R.; Daik, R.;Feast, W.J. *Synthetic Metals*, 101, 1999, 111

5. Kim, H.; Gilmore, C.M.; Pique, A.; Horowitz, J.S.; Mattoussi, H.; Murata, H.; Kafafi, Z.H.; Chrisey, D.V. "Electrical, optical, and structural properties of indium–tin–oxide thin films for organic light-emitting devices"*J. Appl. Phys*., 86, 6451, 1999

6. Mason, M.G.; Hung, L.S.; Tang, C.W.; Lee, S.T.; Wong, K.W.; Wang, M. *J. Appl. Phys*, "Characterization of treated indium–tin–oxide surfaces used in electroluminescent devices" *86*, 1688-1692, 1999

7. Brabec, C.J.; Sariciftci, N.S.; Hummelen, J.C. *Adv. Funct. Mater.* "Plastic Solar Cells" *11*, 15-26, 2001

8. Milliron, F.J.; Hill, I.G.; Shen, C.; Kahn, A.; Schwartz, J. Surface oxidation activates indium tin oxide for hole injection" *J. Appl. Phys*, *87*, 572-576, 2000

9. Nuesch, F.; Rothberg, L.J.; Forsythe, E.W.; Le, Q.T.; Gao, Y. "A photoelectron spectroscopy study on the indium tin oxide treatment by acids and bases" *Appl. Phys. Lett*., *74*, 880-882, 1999

REFERENCES (CONTINUED)

10. Le, Q.T.; Forsythe, E.W.; Nuesch, F.; Rothberg, L.J.; Yan, L.; Gao, Y. "Interface formation between NPB and processed indium tin oxide" *Thin Solid Films, 363*, 42-46, 2000

11. Kim, J.S.; Granstrom, M.; Friend, R.H.; Johansson, N.; Salaneck, W.R.; Daik, R.; Feast, W.J.; Cacialli, F. "Indium–tin oxide treatments for single- and double-layer polymeric light-emitting diodes: The relation between the anode physical, chemical, and morphological properties and the device performance" *J. Appl. Phys*., 1998, *84*, 6859-6870.

12. Yulong Shen, Daniel B. Jacobs, George G. Malliaras, Goutam Koley, Michael G. Spencer, and Andronique Ioannidis, *Adv. Mater.* 2001 13(16) 1234.

13. Karg, S.; Scott, J.C.; Salem, J.R.; Angelopoulos, M., "Increased brightness and lifetime of polymer light-emitting diodes with polyaniline anodes" *Synth. Met*. *80*, 111-117, 1996

14. Carter, S.A.; Angelopoulos, M.; Karg, S.; Brock, P.J.; Scott, J.C.; "Polymeric anodes for improved polymer light-emitting diode performance" *Appl. Phys. Lett. 70*, 2067, 1997

15. Li, W.; Wang, Q.; Cui, J.; Chou, H.; Shaheen, S.W.; Jabbour, G.E.; Anderson, J.D.; Le, P.A.; Kippelen, B.; Peyghambarian, N.; Armstrong, N.R.; Marks, T.J. *Adv. Mater.* 1999, *11*, 730-734.

16. VanderKam, S.K.; Gawalt, E.S.; Schwartz, J.; Bocarsly, A.B. "Electrochemically Active Surface Zirconium Complexes on Indium Tin Oxide" *Langmuir* 1999, *15*, 6598-6600.

17. Purvis, K.L.; Lu, G.; Schwartz, J.; Bernasek, S.L. "Surface Characterization and Modification of Indium Tin Oxide in Ultrahigh Vacuum" *J. Am. Chem. Soc. 122*, 1808-1809, 2000.

18. U. Manna, H.M. Kim, M. Gowtham, J. Yi, Sunyoung Sohn, Donggeun Jung; "Enhanced carrier injection of organic light emitting devices using self assembled monolayer in the cathode/organic interface" *Thin Solid Films* 495 380 – 384, 2006

REFERENCES (CONTINUED)

19. Ishida, T.; Kobayashi, H.; Nakato, Y. " Structures and properties of electron-beam-evaporated indium tin oxide films as studied by x-ray photoelectron spectroscopy and work-function measurements" *J. Appl. Phys*, *73*, 4344-4350, 1993

20. Nelson, A.J.; Aharoni, H. *J. Vac. Sci. Technol. A*, 1987, *5*, 231-233.

21. Hartnagel, H.L.; Dawar, A.L.; Jain, A.K.; Jagadish, C. *Semiconducting Transparent Thin Films. Bristol: Institute of Physics Publishing*, 1995, pp 13-15, 175-187, 265-282.

22. Bender, M.; Seelig, W.; Daube, C.; Frankenberger, H.; Ocker, B.; Stollenwerk, J. "Dependence of oxygen flow on optical and electrical properties of DC-magnetron sputtered ITO films" *Thin Solid Films* 326 (1998) 72–77

23. Utsumi, K.; Iigusa, H.; Tokumaru, R.; Song, P.K.; Shigesato, Y. "Study on In_2O_3–SnO_2 transparent and conductive films prepared by d.c. sputtering using high density ceramic targets" *Thin Solid Films* 445 229–234, 2003

24. Bhatti, M. Tariq; Rana, anwar manzoor; Khan, Abdul Faheem, *Materials Chemistry and Physics* 84 (2004) 126–130

25. Strumpfel, J.; May, C "Low ohm large area ITO coating by reactive magnetron sputtering in DC and MF mode" *Vacuum* 59 (2000) 500-505

26. Schiller, S.; Heisig, U.; Dorndorfer, Chr.; Beister, G.; Reschke, J.; Steinfelder, K.; Strumpfel, "Reactive d.c. high-rate sputtering as production technology" *J. Surface and Coatings Technology*, 33, 405-423, 1987

27. Utsumi, K.; Liqusa, H.; Tokumaru, R.; Song, P.K.; Shigesato, Y.; "Study on In_2O_3–SnO_2 transparent and conductive films prepared by d.c. sputtering using high density ceramic targets" *Thin Solid Films* 445 229–234, 2003

28. Amaral, A.; Brogueira, P.; Nunes de Carvalho, C.; Lavereda, G. *Optical Materials* 17, 291-294, 2001

29. Seki, S.; Sawada, Y.; Ogawam M.; Yamamoto, M.; Kagota, Y.; Shida, A.; Ide, M. "Highly conducting indium-tin-oxide transparent films prepared by dip-coating with an indium carboxylate salt" *Surface and Coatings Technology* 169 –170 525–527, 2003

REFERENCES (CONTINUED)

30. Alam, M.J.; Cameron, D.C. "Characterization of transparent conductive ITO thin films deposited on titanium dioxide film by a sol–gel process" *Surface and Coatings Technology* 142-144 (2001) 776-780

31. P.K. Song, Y. Shigesato, I. Yasui, C.W. Ow-Yang, D.c. Paine, Study on Crystallinity of Tin-Doped Indium Oxide Films Deposited by DC Magnetron Sputtering" *Jpn. J. Appl Phys., Part 1* 37 1870, 1998

32. T.J. Vink, W. Walrave, J.L.C. Daams, P.C. Baarslag, J.E.A.M. van der Meerakker, "On the homogeneity of sputter-deposited ITO films Part I. Stress and microstructure" *Thin Solid Films* 266 (1995) 145.

33. C.H. Yi, Y. Shigesato, I. Yasui, S. Takaki, "Microstructure of Low-Resistivity Tin-Doped Indium Oxide Films Deposited at 150~200°*C*" Jpn. *J. Appl. Phys.*, Part 2 34 (1995) L244.

34. M. Higuchi, M. Sawada, Y. Kuronuma, "Microstructure and Electrical Characteristics of Sputtered Indium Tin Oxide Films" *J. Electrochem. Soc*., 140 (1993) 1773

35. H. Higuchi, S. Uekusa, R. Nakano, K. Yokogawa, "Micrograin structure influence on electrical characteristics of sputtered indium tin oxide films" *J. Appl. Phys.*, 74 6710, 1993

36. M. Hoheisel, A. Mitwalsky and C. Mrotzek, "Microstructure and etching properties of sputtered indium - tin oxide (ITO)" *Phys. Status Solidi A,* 123 (1991) 461.

37. Y. Shigesato, D.C. Paine, "A microstructural study of low resistivity tin-doped indium oxide prepared by d.c. magnetron sputtering" *Thin Solid Films,* 238 44, 1994

38. J. H. W. De Witt, J. *Solid State Chem*. 8, (1977) 143

39. J. H. W. De Witt, J. *Solid State Chem*. 13, (1973) 142

40. J. H. W. De Witt, J. *Solid State Chem*. 20, (1975) 192

41. J. H. W. De Witt, G. van Unen, M. Lahey, "Electron concentration and mobility in In_2O_3" *J. Phys. Chem. Solids* 38, (1977) 819

REFERENCES (CONTINUED)

42. E. C. Subbarao, P. H. Sutter, J. Hrizo, "Defect Structure and Electrical Conductivity of ThO_2-Y_2O_3 Solid Solutions " *J. Am. Ceram. Soc.* 48 (1965) 443

43. G. Frank, H. Kostlin, "Electrical properties and defect model of tin-doped indium oxide layers" *Appl. Phys A: Solids Surf.* 27 (1982) 197

44. R.B.H. Tahar, T. Ban, Y. Ohya, Y. Takahashi, "Tin doped indium oxide thin films: Electrical properties" *J. Appl. Phys*, 83, 2631, 1998

45. Scott H. Brewer, Stefan Franzen, "Calculation of the electronic and optical properties of indium tin oxide by density functional theory" *Chemical Physics* 300, 285, 20004

46. O.N. Mryasov, A.J. Freeman, "Electronic band structure of indium tin oxide and criteria for transparent conducting behavior" *Physical Review B*, 64 (2001) 233111

47. Zhong ZY, Zhong YX, Liu C, et al. "Study on the surface wetting properties of treated indium-tin-oxide anodes for polymer electroluminescent devices**"** *Physica Status Solidi A-Applied Research* 198 (1) 197-203, 2003

48. K. Siegbahn, Nobel Prize for Physics 1981

49. Ishii H, Sugiyama K, Yoshimura D, et al. "Energy-level alignment at model interfaces of organic electroluminescent devices studied by UV photoemission: trend in the deviation from the traditional way of estimating the interfacial electronic structures" *IEEE Journal of Selected Topics in Quantum Electronics* 4 (1): 24-33 1998

50. Fan, J.C.C.; Goodenough, J.B. "X-ray photoemission spectroscopy studies of Sn-doped indium-oxide films" *J. Appl. Phys*., 48, 3524, 1977

51. Major, S.; Kumar, S.; Bhatnagar, M.; Chopra, K.L. "Effect of hydrogen plasma treatment on transparent conducting oxides" *Appl. Phys. Lett*., 49 (1986), 394.

52. Hill, I.G.; Milliron, D.; Schwartz, J.; Kahn, A. "Organic semiconductor interfaces: electronic structure and transport properties" *Appl. Surf. Sci*. 2000, *166*, 354-362.

53. Fan, J.C.C.; Goodenough, J.B. *J. Appl. Phys*. X-ray photoemission spectroscopy studies of Sn-doped indium-oxide films" *48*, 3524-3531, 1977

REFERENCES (CONTINUED)

54. Liau, Y.H.; Scherer, N.F.; Thodes, K. "Nanoscale Electrical Conductivity and Surface Spectroscopic Studies of Indium-Tin Oxide" *Journal of Physical Chemistry B;* 105, 3282, 2001

55. Zotti, G.; Schiavon, G.; Zecchin, S.; Berlin, A.; Pagani, G. 'Adsorption of Ferrocene Compounds on Indium-Tin-Oxide Electrodes. Enhancement of Adsorption by Decomposition of Ferrocenium Molecules by Oxygen" *Langmuir,* 14 (1998) 1728

56. Ganzorig C, Kwak KJ, Yagi K, et al. «Fine tuning work function of indium tin oxide by surface molecular design: Enhanced hole injection in organic electroluminescent devices" *Applied Physics Letters* 2001 79 (2): 272-274

57. Gardner, T.J.; Frisbie, C.D.; Wrighton, M.S. "Systems for orthogonal self-assembly of electroactive monolayers on Au and ITO: an approach to molecular electronics" *J. Am. Chem. Soc.*, 117, 6927, 1995

58. Berlin, A.; Zotti, G. "Self-assembly of mono- and multilayers of polyconjugated conducting polymers" *Macromol. Rapid Commun*. 21, 2000, 301

59. Donley C.L. Dissertation Thesis, 2005, University of Arizona

60. Dua, A. Fujishima, Ch. Comninellis, "Electron transfer kinetics on composite diamond (sp^3)–graphite (sp^2) electrodes" *Electrochemistry Communications*, 5 (8) 695

61. Ishida T, Kuwabara K, Koumoto K Journal of the Ceramic Society of Japan 106 (4): 381-384 1998

62. Thompson LCA, Pacer R *J. of Inorganic and Nuclear Chem.* 25 (8): 1041-1044 1963

63. Biedermann G, *Arkiv. For. Kemi.* 9 (3): 277-293 1956

64. Song JE, Lee DK, Kim HW, et al. "Preparation and characterization of monodispersed indium–tin oxide nanoparticles" *Colloids and Surfaces A* 257: 539-542 Sp.

65. Wilson, R.; Schiffrin, D. J. "Kinetic determination of propyl gallate in edible and cosmetic oils with sensitized terbium(III) luminescence detection" *Analyst* 1995, *120*, 175-178.

REFERENCES (CONTINUED)

66. Donley, C.L.; Carter C. *Unpublished Results*

67. Baes, C.F. Jr.; Mesmer, R.E. *The Hydrolysis of Cations*. John Wiley & Sons: New York, 1976; p 319-327, 349-357.

68. Laviron, E. "General expression of the linear potential sweep voltammogram in the case of diffusionless electrochemical systems" *J. Electroanal. Chem*., 101 1979, 19

69. Y. Shigesato, I. Yasui, Y. Hayashi, S. Takaki, T. Oyama, M. Kamei, "Effects of water partial pressure on the activated electron beam evaporation process to deposit tin-doped indium-oxide films" *J. Vac. Sci. Technol. A*, 13, 1995, 268

70. R. Wilson, D.J. Schiffrin, *J. Electroanal. Chem.* "Electrochemically oxidized ferrocenes as catalysts for the chemiluminescence oxidation of luminal" 448, 125 (1998).

71. C. Donley, D. Dunphy, D. Paine, C. Carter, K. Nebesny, P. Lee, D. Alloway, N. R. Armstrong, "Characterization of Indium-Tin Oxide Interfaces Using X-ray Photoelectron Spectroscopy and Redox Processes of a Chemisorbed Probe Molecule: Effect of Surface Pretreatment Conditions", *Langmuir* 2002, *18*, 450.

72. Veneman, A.; Brumbach, M.; Simmonds, A.; Armstrong N. R. *Manuscript in Preparation*

REFERENCES (CONTINUED)

CHAPTER 3

1. C. Donley, D. Dunphy, D. Paine, C. Carter, K. Nebesny, P. Lee, D. Alloway, N. R. Armstrong, Characterization of Indium-Tin Oxide Interfaces Using X-ray Photoelectron Spectroscopy and Redox Processes of a Chemisorbed Probe Molecule: Effect of Surface Pretreatment Conditions*" Langmuir 18,* 450, 2002

2. J. S. Kim, M. Granstrom, R. H. Friend, N. Johansson, W. R. Salaneck, R. Daik, W. J. Feast, F. Cacialli, "Indium–tin oxide treatments for single- and double-layer polymeric light-emitting diodes: The relation between the anode physical, chemical, and morphological properties and the device performance" *Journal of Applied Physics, 84,* 6859, 1998

3. J. S. Kim, B. Lagel, E. Moons, N. Johansson, I. D. Baikie, W. R. Salaneck, R. H. Friend, F. Cacialli, "Kelvin probe and ultraviolet photoemission measurements of indium tin oxide work function: a comparison" *Synthetic Metals 111*, 311, 2000

4. J. S. Kim, R. H. Friend, F. Cacialli, "Surface energy and polarity of treated indium–tin–oxide anodes for polymer light-emitting diodes studied by contact-angle measurements" *Journal of Applied Physics, 86,* 2774, 1999

5. C. Ganzorig, M. Fujihira, "Improved drive voltages of organic electroluminescent devices with an efficient *p*-type aromatic diamine hole-injection layer" *Applied Physics Letters 77*, 4211, 2000

6. C. Ganzorig, K. J. Kwak, K. Yagi, M. Fujihira, "Fine tuning work function of indium tin oxide by surface molecular design: Enhanced hole injection in organic electroluminescent devices" *Applied Physics Letters 79,* 272, 2001

7. Veinot JGC, Yan H, Smith SM, et al. "Fabrication and Properties of Organic Light-Emitting "Nanodiode" Arrays" *Nano Letters* 2 (4): 333, 2002

8. T. Kugler, W. R. Salaneck, H. Rost, A. B. Holmes, "Polymer band alignment at the interface with indium tin oxide: consequences for light emitting devices" *Chemical Physics Letters, 310,* 391, 1999

REFERENCES (CONTINUED)

9. G. Greczynski, T. Kugler, M. Keil, W. Osikowicz, M. Fahlman, W. R. Salaneck, "Photoelectron spectroscopy of thin films of PEDOT–PSS conjugated polymer blend: a mini-review and some new results" *Journal of Electron Spectroscopy and Related Phenomena 121*, 1, 2001

10. J. S. Kim, B. Lagel, E. Moons, N. Johansson, I. D. Baikie, W. R. Salaneck, R. H. Friend, F. Cacialli, "Kelvin probe and ultraviolet photoemission measurements of indium tin oxide work function: a comparison *Synthetic Metals" 111*, 311, 2000

11. Q. T. Le, F. Nuesch, L. J. Rothberg, E. W. Forsythe, Y. L. Gao, "Photoemission study of the interface between phenyl diamine and treated indium–tin–oxide" *Applied Physics Letters 75*, 1357, 1999

12. Q. T. Le, F. M. Avendano, E. W. Forsythe, L. Yan, Y. L. Gao, C. W. Tang, **"**X-ray photoelectron spectroscopy and atomic force microscopy investigation of stability mechanism of tris-(8-hydroxyquinoline) aluminum-based light-emitting devices" ***Jo****urnal of Vacuum Science & Technology a-Vacuum Surfaces and Films 17*, 2314, 1999

13. R. A. Hatton, M. R. Willis, M. A. Chesters, F. J. M. Rutten, D. Briggs, "Enhanced hole injection in organic light-emitting diodes using a SAM-derivatised ultra-thin gold anode supported on ITO glass" *Journal of Materials Chemistry 13*, 38, 2003

14. V. Christou, M. Etchells, O. Renault, P. J. Dobson, O. V. Salata, G. Beamson, R. G. Egdell, "High resolution x-ray photoemission study of plasma oxidation of indium–tin–oxide thin film surfaces" *Journal of Applied Physics 88*, 5180, 2000

15. E. W. Forsythe, M. A. Abkowitz, Y. L. Gao, "Tuning the Carrier Injection Efficiency for Organic Light-Emitting Diodes" *Journal of Physical Chemistry B 104*, 3948, 2000

16. D. J. Milliron, I. G. Hill, C. Shen, A. Kahn, J. Schwartz," Surface oxidation activates indium tin oxide for hole injection" *Journal of Applied Physics 87*, 572, 2000

17. K. L. Purvis, G. Lu, J. Schwartz, S. L. Bernasek, "Surface Characterization and Modification of Indium Tin Oxide in Ultrahigh Vacuum" *Journal of the American Chemical Society, 122*, 1808, 2000

REFERENCES (CONTINUED)

18. E. L. Bruner, N. Koch, A. R. Span, S. L. Bernasek, A. Kahn, J. Schwartz, "Controlling the Work Function of Indium Tin Oxide: Differentiating Dipolar from Local Surface Effects" *Journal of the American Chemical Society 124*, 3192, 2002

19. K. Sugiyama, H. Ishii, Y. Ouchi, K. Seki, "Dependence of indium–tin–oxide work function on surface cleaning method as studied by ultraviolet and x-ray photoemission spectroscopies" *Journal of Applied Physics*, *87*, 295, 2000

20. J. A. Chaney, P. E. Pehrsson, "Work function changes and surface chemistry of oxygen, hydrogen, and carbon on indium tin oxide" *Applied Surface Science 180*, 214, 2001

21. J. Cui, A. Wang, N. L. Edleman, J. Ni, P. Lee, N. R. Armstrong, T. J. Marks, **"**Indium Tin Oxide Alternatives - High Work Function Transparent Conducting Oxides as Anodes for Organic Light-Emitting Diodes" *Advanced Materials 13*, 1476, 2001

22. J. E. Malinsky, J. G. C. Veinot, G. E. Jabbour, S. E. Shaheen, J. D. Anderson, P. Lee, A. G. Richter, A. L. Burin, M. A. Ratner, T. J. Marks, N. R. Armstrong, B. Kippelen, P. Dutta, N. Peyghambarian, *Chemistry of Materials 14*, 3054, 2002

23. Y. H. Liau, N. F. Scherer, K. Rhodes, "Nanoscale Electrical Conductivity and Surface Spectroscopic Studies of Indium-Tin Oxide" *Journal of Physical Chemistry B 105*, 3282, 2001

24. R. Schlaf, H. Murata, Z. H. Kafafi, "Work function measurements on indium tin oxide films" *Journal of Electron Spectroscopy and Related Phenomena 120*, 149, 2001

25. H. Y. Yu, X. D. Feng, D. Grozea, Z. H. Lu, R. N. S. Sodhi, A. M. Hor, H. Aziz, "Surface electronic structure of plasma-treated indium tin oxides" *Applied Physics Letters 78*, 2595, 2001

26. F. Nüesch, F. Rotzinger, L. Si-Ahmed and L. Zuppiroli, "Chemical potential shifts at organic device electrodes induced by grafted monolayers" *Chemical Physics Letters* 288 (5-6): 861 1998

27. F. Nüesch, K. Kamarás and L. Zuppiroli, "Protonated metal-oxide electrodes for organic light emitting diodes" *Chemical Physics Letters* 283 (3-4): 194 1998

REFERENCES (CONTINUED)

28. J.S. Kim, F. Cacialli, M. Granström, R.H. Friend, N. Johansson, W.R. Salaneck, R. Daik and W.J. Feast, *Synthetic Metals* 101 (1-3): 111 1999

29. F. Garten, J. Vrijmoeth, A.R. Schlatmann, R.E. Gill, T.M. Klapwijk and G. Hadziioannou, "Light-emitting diodes based on polythiophene: influence of the metal workfunction on rectification properties" *Synthetic Metals* 76 (1-3): 85 1996

30. J. S. Kim, M. Granstrom, and R. H. Friend, N. Johansson and W. R. Salaneck R. Daik and W. J. Feast "Indium–tin oxide treatments for single- and double-layer polymeric light-emitting diodes: The relation between the anode physical, chemical, and morphological properties and the device performance" *Journal of Applied Physics* 84, 6859, 1998

31. C.C. Wu, C. I. Wu, J.C. Sturm, and A. Kahn, "Surface modification of indium tin oxide by plasma treatment: An effective method to improve the efficiency, brightness, and reliability of organic light emitting devices" *Applied Physics Letters*. 70, 1348, 1997

32. Greczynski, G; Kugler, T; Keil, M; et al. 'Photoelectron spectroscopy of thin films of PEDOT–PSS conjugated polymer blend: a mini-review and some new results" *Journal of Electron Spectroscopy and Related Phenomena*, 121 (1-3): 1-17 2001

33. Dhanabalan, A; van Duren, JKJ; van Hal, PA; et al. **"**Synthesis and Characterization of a Low Bandgap Conjugated Polymer for Bulk Heterojunction Photovoltaic Cells" *Advanced Functional Materials*, 11 (4): 255 2001

34. Chen, ZK; Huang, W; Wang, LH; et al. "A Family of Electroluminescent Silyl-Substituted Poly(*p*-phenylenevinylene)s: Synthesis, Characterization, and Structure-Property Relationships" *Macromolecules*, 33 (24): 9015-9025 NOV 28 2000

35. de Jong, MP; van IJzendoorn, LJ; de Voigt, M. "Stability of the interface between indium-tin-oxide and poly(3,4-ethylenedioxythiophene)/poly(styrenesulfonate) in polymer light-emitting diodes" *Applied Physics Letters*, 77 (14): 2255 2000

REFERENCES (CONTINUED)

36. Brown, TM; Kim, JS; Friend, RH; et al. "Built-in field electroabsorption spectroscopy of polymer light-emitting diodes incorporating a doped poly(3,4-ethylene dioxythiophene) hole injection layer" *Applied Physics Letters*, 75 (12): 1679, 1999

37. Aedotron^{TM} polymers, TDA Research, Golden Co.

38. M. P. de Jong,, L. J. van IJzendoorn, M. J. A. de Voigt, "Stability of the interface between indium-tin-oxide and poly(3,4-ethylenedioxythiophene)/poly(styrenesulfonate) in polymer light-emitting diodes" *Applied Physics Letters* 77, 2255, 2000

39. G. Sauer, M. Kilo, M. Hund, A. Wokaun, S. Karg, M. Meier, W. Riess, M. Schwoerer, H. Suzuki, J. Simmerer, H. Meyer, and D. Haarer, *J. Anal. Chem*. USSR 353, 642, 1995

40. J. C. Scott, J. H. Kaufman, P. J. Brock, R. DiPietro, J. Salem, and J. A. Goitia, "Degradation and failure of MEH-PPV light-emitting diodes" *Journal of Applied Physics* 79, 2745, 1996

41. W. Brütting, M. Meier, M. Herold, S. Karg, and M. Schwoerer, "Doping in PPV light-emitting devices fabricated on different substrates" *Chemical Physics* 227, 243, 1997

42. M. Meier, S. Karg, and W. Riess, "Light-emitting diodes based on poly-p-phenylene-vinylene: II. Impedance spectroscopy" *Journal of Applied Physics* 82, 1961, 1997

43. S. Karg, M. Meier, and W. Reiss, "Light-emitting diodes based on poly-p-phenylene-vinylene: I. Charge-carrier injection and transport" *Journal of Applied Physics* 82, 1951, 1997

44. M. P. de Jong, D. P. L. Simons, M. A. Reijme, L. J. van IJzendoorn, A. W. Denier van der Gon, M. J. A. de Voigt, H. H. Brongersma, and R. W. Gymer, "Indium diffusion in model polymer light-emitting diodes" Synthetic *Metals* 110, 1, 1999

45. Armstrong NR, Carter C, Donley C, et al. "Interface modification of ITO thin films: organic photovoltaic cells" *Thin Solid Films* 445 (2): 342, 2003

REFERENCES (CONTINUED)

46. Zotti G, Schiavon G, Zecchin S, Berlin A, Pagani G "Adsorption of ferrocene compounds an indium-tin-oxide electrodes. Enhancement of adsorption by decomposition of ferrocenium molecules by oxygen" *Langmuir* 14 : 1728, 1998

47. Nicholson, R, Shain S; "Theory of Stationary Electrode Polarography. Single Scan and Cyclic Methods Applied to Reversible, Irreversible, and Kinetic Systems." *Analytical Chemistry* 36 (4): 706& 1964

48. El-Metwally, M; Youssef Ibrahim, G; M, Tayon, N. *Collect. Czech. Chem. Commun*. 62, 1690, 1997

49. Holt, K; Bard, A; Show, Y; Swain, G; "Scanning Electrochemical Microscopy and Conductive Probe Atomic Force Microscopy Studies of Hydrogen-Terminated Boron-Doped Diamond Electrodes with Different Doping Levels" *Journal of Physical Chemistry B, 108,* 15117, 2004

50. Buchi F, Bond A.; "Interpretation of the electrochemistry of cytochrome c at macro and micro sized carbon electrodes using a microscopic model based on a partially blocke" *Journal of Electroanalytical Chemistry* 314 (1-2): 191 1991

51. Holt, K; Bard, A; Show, Y; Swain, G; "Scanning Electrochemical Microscopy and Conductive Probe Atomic Force Microscopy Studies of Hydrogen-Terminated Boron-Doped Diamond Electrodes with Different Doping Levels" *Journal of Physical Chemistry B, 108,* 15117, 2004

52. I. Duo, A. Fujishima, Ch. Comninellis "Electron transfer kinetics on composite diamond (sp^3)–graphite (sp^2) electrodes" *Electrochemistry Communications* 5 695–700, 2003

53. Carter C. Armstrong N.R. *Unpublished Results*

54. C. Donley, C. Carter, *Unpublished Results*

55. R. Wilson,; D.J. Schiffrin, "Kinetic determination of propyl gallate in edible and cosmetic oils with sensitized terbium(III) luminescence detection" *Analyst* 1995, *120*, 175-178

REFERENCES (CONTINUED)

56. Anderson JD, McDonald EM, Lee PA, et al. "Electrochemistry and Electrogenerated Chemiluminescence Processes of the Components of Aluminum Quinolate/Triarylamine, and Related Organic Light-Emitting Diodes" *Journal of the American Chemical Society* 120 (37): 9646, 1998

57. Neophytides, S.G, Vayenas, C. G. "TPD and Cyclic Voltammetric Investigation of the Origin of Electrochemical Promotion in Catalysis" *Journal of Physical chemistry* 99 (47): 17063 1995

58. T.O. Mason , G.B. Gonzalez , D.R. Kammler , N. Mansourian-Hadavi , B.J. Ingram "Defect chemistry and physical properties of transparent conducting oxides in the CdO-In_2O_3-SnO_2 system" *Thin Solid Films* 411 (2002) 106–114

59. Beatty AM "Open-framework coordination complexes from hydrogen-bonded networks: toward host/guest complexes" *Coordination Chemistry Reviews* 246 (1-2): 131 2003

60. Tong ML, Zheng SL, Chen XM; "Synthesis and structures of two-dimensional coordination polymers constructed by metal salts and 4,4'-bipyridine" *Polyhedron* 19 (15): 1809, 2000

61. Radhouane Bel Hadj Tahar,a) Takayuki Ban, Yutaka Ohya, and Yasutaka Takahashi "Tin doped indium oxide thin films: Electrical properties" *Journal of Applied Physics* 83, 2631, 1998

62. Yuzo Shigesato, Satoru Takaki, and Takeshi Haranoh "Electrical and structural properties of low resistivity tin-doped indium oxide films" *Journal of Applied Physics*, 71, 1 3356 1992

63. Ingram, B. Gonzales, D, Dammler, M, Bertoni, M, Mason, T; "Chemical and Structural Factors Governing Transparent Conductivity in Oxides" *Journal of Electroceramics*, 13, 167, 2004

64. Odaka, H, Shigesato, Y, Murakam, T, Iwata, S; "Electronic Structure Analyses of Sn-doped In_2O_3" *Jpn. J. Appl. Phys.* Vol. 40 . 3231, 2001

65. Moeller T, "Chemistry of Indium - A Colorimetric Method for the Estimation of Small Amounts of Indium" *Industrial and Engineering Chemistry-Analytical Edition* 15: 270 1943

REFERENCES (CONTINUED)

66. Moeller T, "Contribitions to the chemistry of indium. VI. The effects of certain hydroxy anions upon the precipitation of hydrous indium hydroxide" *Journal of Physical Chemistry* 46 (7): 794 1942

67. Stary, Jirf "Systematic study of the solvent extraction of metal oxinates" *Analytica Chemica Acta,* 28, 132, 1962

68. T. Kebede K V Ramana M S Prasida *Proc. Indian Acad. Sci.* (*Chem. Sci.*), Vol. 113, No. 4, 2001, pp 275–284

69. R. Kettler, D. A. Palmer, D.J. Weslowski., Geological Society of America *Abstracts with Programs*, Vol. 37, No. 7, p. 380

70. J. van den Brand, O. Blajiev, P. C. J. Beentjes, H. Terryn, and J. H. W. de Wit *"Interaction of Anhydride and Carboxylic Acid Compounds with Aluminum Oxide Surfaces Studied Using Infrared Reflection Absorption Spectroscopy" Langmuir 20*, 6308, 2004

71. Pandey PC, Upadhyay BC; "Role of Palladium in the Redox Electrochemistry of Ferrocene Monocarboxylic Acid Encapsulated Within ORMOSIL Networks" *Molecules* 10 (6): 728 2005

72. Carter C., Armstrong, N.R. manuscript in preparation

73. (a) H. Ishii, K. Sugiyama, E. Ito, K. Seki, **"**Energy Level Alignment and Interfacial Electronic Structures at Organic/Metal and Organic/Organic Interfaces" *Advanced Materials* 1999, 11, 605-625; (b) D. Cahen, A. Kahn, "Electron Energetics at Surfaces and Interfaces: Concepts and Experiments**"** *Advanced Materials*, *15,* 271, 2003

74. D. J. Milliron, I. G. Hill, C. Shen, A. Kahn, J. Schwartz, "Surface oxidation activates indium tin oxide for hole injection" *Journal of Applied Physics 87*, 572, 2000

75. K. L. Purvis, G. Lu, J. Schwartz, S. L. Bernasek, "Surface Characterization and Modification of Indium Tin Oxide in Ultrahigh Vacuum" *Journal of the American Chemical Society 122,* 1808, 2000

REFERENCES (CONTINUED)

76. E. L. Bruner, N. Koch, A. R. Span, S. L. Bernasek, A. Kahn, J. Schwartz, "Controlling the Work Function of Indium Tin Oxide: Differentiating Dipolar from Local Surface Effects" *Journal of the American Chemical Society 124*, 3192, 2002

77. J. S. Kim, R. H. Friend, and F**. "**Caciallia Surface energy and polarity of treated indium–tin–oxide anodes for polymer light-emitting diodes studied by contact-angle measurements" *Journal of Applied Physics* 86, 2774, 1999

78. S. Wu, *"Polymer Interface and Adhesion"* ~Marcel Dekker, New York, 1982, 178–181.

79. Schneider, B. PhD Thesis, University of Saarland, 2001.

80. Schneider, B.; Possart, W. *Journal of Adhesion*, in press.

81. J. van den Brand, O. Blajiev, P. C. J. Beentjes, H. Terryn, J. H. W. de Wit, *Langmuir* "Interaction of Anhydride and Carboxylic Acid Compounds with Aluminum Oxide Surfaces Studied Using Infrared Reflection Absorption Spectroscopy" *20*, 6308, 2004

82. Buckland, A. D.; Rochester, C. H.; Topham, S. A. **"**Infrared study of the adsorption of carboxylic acids on haematite and goethite immersed in carbon tetrachloride" *Journal of the Chemical Society, Faraday Transactions 1, 76* 302-313, 1980

83. Hill, I. R.; Levin, I. W. "Vibrational spectra and carbon–hydrogen stretching mode assignments for a series of *n*-alkyl carboxylic acids" *Journal of Chemical Physics* 1979, *70* (2), 842-851.

84. Teddington: Middlesex, Roeges, N. P. G. *A; "Guide to the Complete Interpretation of Infrared Spectra of Organic Structures"* Wiley: Chichester, 1994.

85. Evans, H. E.; Weinberg, W. H. "A comparison of the vibrational structures of ethanol, acetic acid, and acetaldehyde adsorbed on alumina" *Journal of Chemical Physics, 71* (12), 4789, 1979

REFERENCES (CONTINUED)

86. Alexander, M. R.; Payan, S. "Interfacial interactions of plasma-polymerized acrylic acid and an oxidized aluminium surface investigated using XPS, FTIR and poly(acrylic acid) as a model compound" *Surface Interface Analysis 26* (13), 961, 1998

87. Hu, H.; Saniger, G.; Garciaalejandre, J.; Castano, V.M. "Fourier transform infrared spectroscopy studies of the reaction between polyacrylic acid and metal oxides" *Materials Letters 12* (4), 281, 1991

88. Allara, D. L.; Nuzzo, R. G. "Spontaneously organized molecular assemblies. 2. Quantitative infrared spectroscopic determination of equilibrium structures of solution-adsorbed n-alkanoic acids on an oxidized aluminum surface" *Langmuir 1* (1), 52, 1985

89. Nuesch F, Rotzinger F, Si-Ahmed L, et al. "Chemical potential shifts at organic device electrodes induced by grafted monolayers" *Chemical Physics Letters* 288 (5-6): 861, 1998

REFERENCES (CONTINUED)

CHAPTER 4

1. Hung LS, Chen CH “Recent progress of molecular organic electroluminescent materials and devices” *Materials Science and Engineering R-Reports* 39 (5-6): 143-222 DEC 1 2002

2. Patel NK, Cina S, Burroughes JH “High-efficiency organic light-emitting diodes” *IEEE Journal of Selected Topics in Wuantum Electronics* 8 (2): 346-361 MAR-APR 2002

3. Berner D, Houili H, Leo W, et al. “Insights into OLED functioning through coordinated experimental measurements and numerical model simulations” *Physica Status Solidi A-Applied Research* 202 (1): 9-36 JAN 2005

4. Chen CH, Shi JM “Metal chelates as emitting materials for organic electroluminescence” *Coordination Chemistry Reviews* 171: 161-174 APR 1998

5. Greenham, N. C.; Moratti, S. C.; Bradley, D. D. C.; Friend, R. H.; Holmes, A. B. "Efficient Light-Emitting Diodes Based on Polymers with High Electron Affinities," *Nature* 1993, *365*, 628-630.

6. Friend, R. H.; Gymer, R. W.; Holmes, A. B.; Burroughes, J. H.; Marks, R. N.; Taliani, C.; Bradley, D. D. C.; Dos Santos, D. A.; Bredas, J. L.; Logdlund, M.; Salaneck, W. R. "Electroluminescence in Conjugated Polymers," *Nature* 1999, *397*, 121-128.

7. Gustafsson, G.; Cao, Y.; Treacy, G. M.; Klavetter, F.; Colaneri, N.; Heeger, A. J. "Flexible Light-Emitting Diodes Made from Soluble Conducting Polymers," *Nature* 1992, *357*, 477-479.

8. Tang, C. W.; Vanslyke, S. A. "Organic Electroluminescent Diodes," *Appl. Phys. Lett.* 1987, *51*, 913-915.

9. Tang, C. W.; Vanslyke, S. A.; Chen, C. H. "Electroluminescence of Doped Organic Thin-Films," *J. Appl. Phys.* 1989, *65*, 3610-3616.

10. Shi, J.; Tang, C. W. "Doped Organic Electroluminescent Devices with Improved Stability," *Appl. Phys. Lett.* 1997, *70*, 1665-1667.

REFERENCES (CONTINUED)

11. Chen, C. H.; Tang, C. W. "Efficient Green Organic Light-Emitting Diodes with Stericly Hindered Coumarin Dopants," *Appl. Phys. Lett.* 2001, *79*, 3711-3713.

12. Baldo, M. A.; Thompson, M. E.; Forrest, S. R. "High-Efficiency Fluorescent Organic Light-Emitting Devices Using a Phosphorescent Sensitizer," *Nature* 2000, *403*, 750-753.

REFERENCES (CONTINUED)

CHAPTER 5

1. Sonmez G, Schottland P, Reynolds JR "PEDOT/PAMPS: An electrically conductive polymer composite with electrochromic and cation exchange properties" *Synthetic Metals* 155 (1): 130 2005

2. Godovsky DY "Device applications of polymer-nanocomposites" *Advances in Polymer Science* 153: 163-205 2000

3. Gustafsson JC, Inganas O, Andersson AM "Conductive Polyheterocycles as Electrode Materials in Solid-State Electrochromic Devices" *Synthetic Metals*, 62 (1): 17, 1994

4. Christie S, Scorsone E, Persaud K, et al. "Remote detection of gaseous ammonia using the near infrared transmission properties of polyaniline" *Sensors and Actuators B - Chemical* 90 (1-3): 163 2003

5. Kirk S. Schanze, Troy S. Bergstedt, Brain T. Hauser, and Carla S. P. Cavalaheiro "Photolithographically-Patterned Electroactive Films and Electrochemically Modulated Diffraction Gratings" 795 *Langmuir* 2000, *16,* 795-810

6. Aaron M. Massari, Keith J. Stevenson, Joseph T. Hupp "Development and application of patterned conducting polymer thin films as chemoresponsive and electrochemically responsive optical diffraction gratings" *Journal of Electroanalytical Chemistry* 500, 185, 2001

7. Kirk S. Schanze, Troy S. Bergstedt, and Brian T. Hauser Photolithographic "Patterning of Electroactive Polymer Films and Electrochemically Modulated Optical Diffraction Gratings" *Adv. Mater.* 1996,8, No. *6 531*

8. Pei QB, Zuccarello G, Ahlskog M, et al. "Electrochromic and Highly Stabile Poly(3,4-Ethylenedioxythiophene) Switches Between Opaque Blue-Black and Transparent Sky Blue" *Polymer* 35 (7): 1347-1351 1994

9. Sapp SA, Sotzing GA, Reynolds JR "High contrast ratio and fast-switching dual polymer electrochromic devices" *Chemistry of Materials* 10 (8): 2101-2108 AUG 1998

REFERENCES (CONTINUED)

10. Kumar A, Welsh DM, Morvant MC, et al. "Conducting poly(3,4-alkylenedioxythiophene) derivatives as fast electrochromics with high-contrast ratios" *Chemistry of Materials* 10 (3): 896 1998

11. Sapp SA, Sotzing GA, Reddinger JL, et al. 'Rapid switching solid state electrochromic devices based on complementary conducting polymer films" *Advanced Materials* 8 (10), 808, 1996

12. DeLongchamp D, Hammond PT, "Layer-by-Layer Assembly of PEDOT/Polyaniline Electrochromic Devices" *Advanced Materials* 13 (19): 1455, 2001

13. Admassie S, Inganas O O "Electrochromism in diffractive conducting polymer gratings" *Journal of the Electrochemical Society* 151 (6): H153 2004

14. Barbero C, Miras MC, Schnyder B, et al. "Sulfonated polyaniline films as cation insertion electrodes for battery applications. Part 1.—Structural and electrochemical characterization" *Journal of Materials Chemistry* 4 (12): 1775 1994

15. Jelle BP, Hagen G, "Transmission Spectra of an Electrochromic Window Based on Polyaniline, Prussian Blue and Tungsten-Oxide" *Journal of the Eectrochemical Society* 140 (12): 3560, 1993

16. Somani P, Mandale AB, Radhakrishnan S., "Study and development of conducting polymer-based electrochromic display devices" Acta Materialia 48 (11): 2859 2000

17. Pringsheim E, Terpetschnig E, Wolfbeis O.S, "Optical sensing of pH using thin films of substituted polyanilines" *Analytica Chimica Acta*, 357 (3): 247 1997

18. Lindfors T, Ivaska , "Calcium-selective electrode based on polyaniline functionalized with bis[4-(1,1,3,3-tetramethylbutyl)phenyl]phosphate)" *Analyitca Chimica Acta*, 37 (2): 171 2001

19. Bendikov TA, Harmon TC "Long-lived solid state perchlorate ion selective sensor based on doped poly(3,4-ethylenedioxythiophene) (PEDOT) films" *Analytica Chimica Acta* 551 (1-2): 30 2005

REFERENCES (CONTINUED)

20. Sotzing GA, Briglin SM, Grubbs RH, et al "Preparation and Properties of Vapor Detector Arrays Formed from Poly(3,4-ethylenedioxy)thiophene-Poly(styrene sulfonate)/Insulating Polymer Composites" *Analytical Chemistry* 72 (14): 3181 2000

21. Michalska A, Maksymiuk K, "All-plastic, disposable, low detection limit ion-selective electrodes" *Analytica Chimica Acta* 523 (1): 97 2004

22. T.S. Bergstedt, B.T. Hauser, K.S. Schanze, "Microstructured Photopolymer Films of a Ruthenium(II) Polypyridine Complex. Fabrication of an Electrochemically Switchable Phase Grating" *Journal of the American Chemical Society* 116, 8380, 1994

23. K.S. Schanze, T.S. Bergstedt, B.T. Hauser, **"**Photolithographic patterning of electroactive polymer films and electrochemically modulated optical diffraction gratings" *Advanced Materials* 8 531. 1996

24. F. Nakajima, Y. Hirakawa, T. Kaneta, T. Imasaka, "Diffractive Optical Chemical Sensor Based on Light Absorption" *Analytical Chemistry* 71, 2262, 1999

25. A.B. Bocarsly, C.C. Chang, Y. Wu, E.P. Vicenzi, "Inorganic Photolithography: Interfacial Multicomponent Pattern Generation" *Journal of Chemical Education* 74 663 1997

26. Kumar A and Whitesides G M "Features of gold having micrometer to centimeter dimensions can be formed through a combination of stamping with an elastomeric stamp and an alkanethiol ``ink" followed by chemical etching" *Applied Physics Lettters* 63, 2002, 2003

27. Kumar A, Biebuyck H A and Whitesides G M "Patterning Self-Assembled Monolayers: Applications in Materials Science" *Langmuir* 10 1498, 1994

28. Kim E, Kumar A and Whitesides G M "Combining Patterned Self-Assembled Monolayers of Alkanethiolates on Gold with Anisotropic Etching of Silicon to Generate Controlled Surface Morphologies" *Journal of the Electrochemical Society* 142 (2) 628, 1995

29. Biebuyck H A and Whitesides G M "Self-Organization of Organic Liquids on Patterned Self-Assembled Monolayers of Alkanethiolates on Gold" *Langmuir* 10 2790, 1994

REFERENCES (CONTINUED)

30. Xia Y, Mrksich M, Kim E and Whitesides G M "Microcontact Printing of Octadecylsiloxane on the Surface of Silicon Dioxide and Its Application in Microfabrication" *Journal of the American Chemical Society* 117, 9576, 1995

31. Wilbur J L, Kim E, Xia Y and Whitesides G M "Lithographic molding: A convenient route to structures with sub-micrometer dimensions" *Advanced Materials* 7 649–52 1995

32. Singhvi R, Kumar A, L´opez G P, Stephanopoulos G N, Wang D I, Whitesides G M and Ingber Science D E 1994

33. Wilbur J L, Biebuyck H A, MacDonald J C and Whitesides G M "Scanning Force Microscopies Can Image Patterned Self-Assembled Monolayers" *Langmuir* 11 825 1995

34. Singhvi R, Kumar A, L´opez G. P., Stephanopoulos G N, Wang D I, Whitesides G M and Ingber D E *Science* 264 696, 1994

35. *Spectra-Physics*, Newport Corp.

36. Fayer, M. D." Dynamics of Molecules in Condensed Phases: Picosecond Holographic Grating Experiments" *Annu. Rev. Phys. Chem.*, *33*, 63 1982

37. Nelson, K. A.; Casalegno, R.; Miller, R. J. D.; Fayer, M. D. "Laser-induced excited state and ultrasonic wave gratings: Amplitude and phase grating contributions to diffraction" *J. Chemical Physics*, *77*, 1144-1152, 1982

38. Monk, P. M. S.; Mortimer, R. J.; Rosseinsky, D. R. *Electrochromism: Fundamentals and Applications*; VCH: Weinheim, 1995.

39. Redondo, A.; Ticianelli, E. A.; Gottesfeld, S. "Ellipsometric studies of conducting polymers" *Synthetic Metals 29*, E265, 1989

40. Gottesfeld, S.; *"Electroanalytical Chemistry*, *15*, 143-265.1989

41. Redondo, A.; Ticianelli, E. A.; Gottesfeld, S. *Mol. Cryst. Liq.Cryst. 160*, 185, 1988

REFERENCES (CONTINUED)

42. Saalmink, M; van der Marel, C; Stapert, HR; et al. "Positive Microcontact Printing with Mercaptoalkyloligo(ethylene glycol)s" *Langmuir*, 22 (3): 1016, 2006

43. Kim, HS; Bae, YM; Kim, YK; et al "Antibody layer fabrication for protein chip to detect E. coli O157 : H7, using microcontact printing technique" .*Journal of Microbiology and Biotechnology*, 16 (1): 141, 2006

44. Park, KS; Seo, EK; Do, YR; et al. "Light stamping lithography: Microcontact printing without inks" *J. Am. Chem. Soc*., 128 (3): 858, 25 2006

45. Wang, LK; Feng, XZ; Hou, S; et al. . "Microcontact printing of multiproteins on the modified mica substrate and study of immunoassays" *Surface and Interface Analysis*, 38 (1): 44 2006

46. Kane, RS ; Takayama, S; Ostuni, E; et al. . "Patterning proteins and cells using soft lithography" *Biomaterials*, 20 (23-24): 2363 1999

47. Bernard, A; Delamarche, E; Schmid, H; et al. "Printing Patterns of Proteins" *Langmuir*, 14 (9): 2225 1998

48. Mrksich, M; Chen, CS; Xia, YN; et al. "Controlling cell attachment on contoured surfaces with self-assembled monolayers of alkanethiolates on gold" *Proceedings of the National Academy of Sciences of the United States of America*, 93 (20): 10775-10778 OCT 1 1996

49. Mrksich, M; Whitesides, GM "Using self-assembled monolayers to understand the interactions of man-made surfaces with proteins and cells" *Annual Review of Biophysics and Bimolecular Structures*, 25: 55-78 1996

50. Jachman, RJ; Wilbur, JL; Whitesides, GM "Fabrication of Submicrometer Features on Curved Substrates by Microcontact Printing" *Science*, 269 (5224): 664-666 AUG 4 1995

51. Wilbur, JL; Kumar, A; Kim, E; et al. "Microfabrication by Microcontact Printing of Self-Assembled Monolayers" *Advanced Materials*, 6 (7-8): 600-604 JUL-AUG 1994

REFERENCES (CONTINUED)

52. Li, F.; Albery, W. J. "A novel mechanism of electrochemical deposition of conducting polymers: two-dimensional layer-by-layer nucleation and growth observed for poly(thiophene-3-acetid acid)" *Electrochimica Acta, 37*, 393. 1992

53. Hillman, A. R.; Mallen, E. F. "Nucleation and growtn of polythiophene films on gold electrodes" *J. Electroanalytical Chem., 220*, 351 1987

54. L.A.A. Pettersson, T. Hohansson, F. Carlsson, H. Arwin, O, Inganas, "Anisotropic optical properties of doped poly(3,4-ethylenedioxythiophene)" *Synthetic Metals* 101, 198 1999

55. Simulation of diffraction grating features, unpublished

56. K.A. Nelson, R. Casalegno, R.J.D. Miller, M.D. Fayer, "Laser-induced excited state and ultrasonic wave gratings: Amplitude and phase grating contributions to diffraction" *Journal of Chemical Physics* 77 1144 1982

57. M.D. Fayer, "Dynamics of Molecules in Condensed Phases: Picosecond Holographic Grating Experiments" Annual Review Physical Chemistry 33, 63 1982.

58. F. Wooten, *"Optical Properties of Solids"*, Academic Press, NewYork, 1972.

59. G.R. Olbright, N. Peyghambarian, "Interferometric measurement of the nonlinear index of refraction, n_2, of CdS_xSe_{1-x}-doped glasses" *Applied Physics Letters* 48, 1184, 1986

60. K.S. Schanze, T.S. Bergstedt, B.T. Hauser, C.S.P. Cavalaheiro, "Photolithographically-Patterned Electroactive Films and Electrochemically Modulated Diffraction Gratings" *Langmuir* 16 795, 2000

61. Jaroslav S, Pavel K, Jenkins, A.; Collect. *Czech. Chem. Commun.* 6, 1747 1995

62. Ahonen HJ, Lukkari J, Kankare J "n- and p-Doped Poly(3,4-ethylenedioxythiophene): Two Electronically Conducting States of the Polymer" *Macromolecules* 33 (18): 6787, 2000

63. Fukumi K, Chayahara A, Kitamura N, Horino Y, Sodeoka S, Yamanaka H, Nishii "Chemical State and Refractive Index of Mg-Ion-Implanted Silica Glass" *J. Jap J. of App. Phys* 2002 41 (12): 7447-7452

REFERENCES (CONTINUED)

CHAPTER 6

1. Simmonds, A.; Armstrong N. R. *Manuscript in Preparation*

2. Veneman, A..; Armstrong N. R. *Manuscript in Preparation*

3. U. Manna, H.M. Kim, M. Gowtham, J. Yi, Sunyoung Sohn, Donggeun Jung, *Thin Solid Films* 2006 495 380– 384

4. Breen TL, Fryer PM, Nunes RW, et al. "Patterning Indium Tin Oxide and Indium Zinc Oxide Using Microcontact Printing and Wet Etching" *Langmuir*, 18 (1): 194 2002

5. Jorge Morgado, Nunzio Barbagallo, Ana Charas, Manuel Matos, Lu´ýs Alc´acer, Franco Cacialli J. *Phys. D: Appl. Phys.* 36 (2003) 434–438

6. Stol, R. J., van Helden, A. K., and de Bruyn, P. L. *The Surface Chemistry of Aluminum Oxides and Hydroxides,* 1976

7. C. Donley, D. Dunphy, D. Paine, C. Carter, K. Nebesny, P. Lee, D. Alloway, N. R. Armstrong, "Characterization of Indium-Tin Oxide Interfaces Using X-ray Photoelectron Spectroscopy and Redox Processes of a Chemisorbed Probe Molecule: Effect of Surface Pretreatment Conditions" *Langmuir* 18, 450, 2002

8. C. Carter, M. Brumbach, C. Donley, R. D. Hreha, S. Marder, B. Domercq, S. Yoo, B. Kippelen, N. R. Armstrong *J. Phys Chem. Submitted*

9. Heh-Nan L.; Sy-Hann C.; Gung-Yeong P.; Show-An Chen *J. Appl. Phys.* 2001 89, (7) 1

10. Marikkar S.; Armstrong N. R. *Manuscript in Preparation*

11. Brumbach, M; Armstrong N. R. *Manuscript in Preparation*

12. Goyal DJ, Agashe C, Takwale MG, et al. "Development of transparent and conductive ZnO films by spray pyrolysis" *Journal of Materials Science* 27 (17): 4705 1992

Finis